DYNAMIC PROPERTIES OF SUPERCONDUCTING MICROBRIDGES

A Dissertation

Presented to the Faculty of the Graduate School

of

Yale University

in Candidacy for the Degree of

Doctor of Philosophy

by

Mark David Feuer

December 1980

ABSTRACT

DYNAMIC PROPERTIES OF SUPERCONDUCTING MICROBRIDGES

Mark David Feuer

Yale University

1980

Superconducting microbridges of Pb alloys have been studied in both the uniform-thickness and variable-thickness geometries. Variable-thickness microbridges of pure In have also been studied, to investigate the effect of a long electron mean free path and a long superconducting coherence length. Measurements of the time-averaged voltage as a function of the current bias, performed at various power levels of microwave irradiation, yield information about the Josephson effect, Joule heating, and other phenomena of the dynamic (i.e. finite-voltage) state. Critical current data, representative of the static state, have also been studied. A new photolithographic process incorporating ion-beam etching techniques has been developed to permit fabrication of microbridges with all bridge dimensions less than or equal to 50 nm.

Uniform-thickness microbridges of $Pb_{0.7}Bi_{0.3}$ and $Pb_{0.9}In_{0.1}$ alloys have been fabricated using optical projection lithography and metal-liftoff techniques. A special technique of through-the-substrate projection exposure has been developed to ensure successful liftoff of microbridges narrower than 0.5 μm. The uniform-thickness microbridges studied were roughly hyperbolic in shape, ranging from 0.2 μm to 1.9 μm in width and from 25 nm to 90 nm in thickness. The critical currents and the current-voltage curves of these microbridges have been compared to the uniform-depairing and vortex-flow theories of microbridge behavior. The data do not show clearly the predicted transition from

the uniform-depairing regime to the vortex-flow regime as a function of bridge width. The Josephson effect response of these alloy microbridges is similar to that of larger microbridges of elemental superconductors, except that the high device resistances of the alloy bridges, which range from 1 ohm to 8 ohms, are better suited to efficient microwave coupling. Both the temperature range and voltage range of operation of these uniform-thickness microbridges are limited by Joule heating, as in uniform-thickness microbridges of elemental superconductors.

Variable-thickness microbridges of $Pb_{0.9}In_{0.1}$ alloy and unalloyed In have been fabricated by a new technique, step-edge lithography. Microbridges ranging from 40 nm to 200 nm in width, with comparable lengths and bank thicknesses up to 600 nm, have been produced. The critical currents of the variable-thickness microbridges are found to be linear in temperature over a fairly wide range near the critical temperature. The magnitude of the critical current decreases smoothly as the cross-sectional area of the microbridge is reduced, approaching the theoretical, small-bridge limit for the narrowest microbridges tested. As expected, the Joule-heating limits are much less severe for the variable-thickness microbridges than for the uniform-thickness microbridges. The Joule heating also shows a strong dependence on bridge cross-sectional area: narrower microbridges show less severe heating effects. Boundary scattering in the narrow bridge region, quite significant in the pure In microbridges, is observed to increase the device resistance and reduce the Joule heating effects. For the narrowest In microbridge, microwave steps are observed to 1.9 mV and no hysteresis is observed down to 1.3 K, the lowest temperature tested. Other dynamic-state effects are discussed, including energy-gap-related

structure, microwave enhancement of the critical current, and a microwave-induced asymmetry of the current-voltage curves which has not been previously reported in microbridge studies. The overall trends of the data on variable-thickness microbridges indicate that very small, high-resistivity bridges with thick, low-resistivity banks offer the greatest promise for high-frequency device applications.

ACKNOWLEDGEMENTS

The debts of gratitude incurred during four years of dissertation research are myriad, so with apologies to those whose names are omitted, I will mention just a few here. From the first, equipment and experience have been generously shared by Dr. R. C. Barker and his students, including Dr. Armand Tanguay, Dr. Paul Dressendorfer, and Dr. Stefan Lai. Junior students in our lab, including James Cogdell and Clarence Teng, have made valuable contributions to the microfabrication effort. Special thanks are due to Dr. Alan Pooley of the Peabody Museum at Yale, for assistance and instruction in the art of scanning-electron microscopy, and to Clifford Sneider, for technical expertise ranging from construction of Dewar stands to design of vacuum systems. Among the many enlightening discussions which contributed to this work, particularly helpful conversations with Dr. Nicholas Giordano, Dr. Richard Howard and Dr. Miguel Octavio are gratefully recalled.

The financial support of Yale University and of the National Science Foundation, and the use of semiconductor clean-room facilities at Yale provided the necessary groundwork for this research.

In the preparation of this dissertation, I have relied heavily on the typographical skills of June Yarosh and the draftsmanship of Jim Brosious, for which many thanks. I also wish to thank Sara Batter, whose watchful eye and helping hand have kept me in harmony with the bureaucracy of the University and the Graduate School. From Bruce Dalrymple, I gratefully acknowledge not only assistance in proofreading and loan of precision drafting equipment, but also generous donation of many (whole-wheat) calories to the greater glory of science.

Many thanks go to my advisor, Dr. Daniel Prober, for helpfulness

and consideration beyond the call of duty, as well as excellent professional guidance.

Finally, I would like to share the credit for this work with my parents, who provided support in all possible forms, and with my wife Liz, whose contribution was the gift of confidence.

TABLE OF CONTENTS

Table of Contents (continued) Page

Table of Contents (continued)

LIST OF FIGURES AND TABLES

List of Figures and Tables (continued)

List of Figures and Tables (continued)

List of Figures and Tables (continued)

LIST OF SYMBOLS

Frequently-used symbols and abbreviations are defined here; symbols which occur in only one or two contiguous paragraphs are defined immediately preceding or following their first appearance. Standard abbreviations for units, such as cm and Ω, are used without explicit definition, as are the standard for the chemical elements, such as Pb.

Symbol	Meaning
a	normalized width of hyperbolic bridge, $a \equiv (W/2\xi(T)\sin(\theta_{max}))$
$\vec{A}$	electromagnetic vector potential
$\vec{b}$	local magnetic flux density
c	speed of light in vacuum
C	capacitance
d	thickness of bridge region in VTB; thickness of both bridge and banks in UTB
D	thickness of banks in VTB
e	charge on the electron; also used for the base of the natural logarithm
f	frequency
f_c	characteristic frequency of a microbridge, $f_c \equiv (2eI_cR/h)$
f_J	fundamental frequency of the Josephson oscillation, $f_J \equiv (2e\bar{V}/h)$
F_k	force exerted on the kth vortex
GL	Ginzburg-Landau (theory)
h	Planck's constant
$\hbar$	$\hbar \equiv (h/2\pi)$
i	$\sqrt{-1}$
I	current, often bias current through a microbridge

List of Symbols (continued)

Symbol	Meaning
I_b	current through accelerator supply of ion gun
I_c	critical current (≡ maximum zero-voltage current)
I_d	downset current (≡ minimum finite-voltage current in a hysteretic device)
I_∞	normalization current, see eq. (II-13)
$\tilde{I}$, I_{ac}	ac bias current
$I_c^{(fil)}$	I_c of a one-dimensional superconducting filament, see eq. (II-12)
ΔI	shift in effective I_c due to heating
ΔI_n	width in current of the nth microwave step, see Fig. II-3
$\delta I(\bar{V})$	asymmetry current at voltage $\bar{V}$
$\vec{J}$	current density
$\vec{J}_s$	supercurrent density
$\vec{J}_b$	current density of ion beam
ℓ	mean free path for elastic scattering of electrons
ℓ_{bank}	effective mean free path in the banks of a microbridge
ℓ_{bridge}	effective mean free path in the bridge region
L	length of a microbridge
m	mass of the electron; also used for an arbitrary integer
n	an arbitrary integer, also used for refractive index in chapter III
n_s	superconducting pair density
P	power dissipated in a microbridge
P_o	characteristic power for Joule heating defined by Tinkham et. al. (1977)
PR	photoresist
$\vec{r}$	position vector

List of Symbols (continued)

Symbol	Meaning
R	resistance, usually of a microbridge
R_d	characteristic device resistance, $R_d \equiv R_{min}$ at $t = 0.995$ for UTBs, $R_d \equiv R_{min}$ at $t = 0.99$ for VTBs.
R_D	differential resistance of the $\bar{V}(I)$ curve, $R_D = (d\bar{V}/dI)$
R_f	differential resistance of the low-voltage foot
R_{min}	minimum differential resistance of the $\bar{V}(I)$ curve above the foot region
R_o	characteristic vortex-flow resistance, see eq. (II-44)
R_{th}	thermal resistance (= temperature drop ÷ heat flow)
R_{tot}	total resistance of the bridge plus banks just above T_c
$R_\square$	resistance per square of thin film, $R_\square \equiv (\rho/d)$
RFI	radio-frequency interference
RSJ	resistively-shunted junction (model)
$\hat{s}$	unit vector normal to superconductor-insulator boundary
S_k	polarity of the kth vortex
SEM	scanning-electron microscope
SNS bridge	microbridge with superconducting banks and a non-superconducting bridge region
SQUID	superconducting quantum interference device
$S_cS_dS_c$ bridge	all-superconducting microbridge with a shorter mean free path in the bridge region than in the banks; also called clean-dirty-clean bridge
t	normalized (or reduced) temperature $t \equiv (T/T_c)$
t_B	normalized bath temperature $t_B = (T_B/T_C)$
T	temperature
T_B	bath temperature
T_C	critical temperature for superconductivity

List of Symbols (continued)

Symbol	Meaning
$T_{eff}(\vec{r})$	local effective temperature in the Joule-heating theory
ΔT	temperature difference, often $T_{eff} - T_B$
$\Delta T_{no\ hyst}$	hysteresis-free temperature range
ΔT_{sgs}	temperature shift inferred from energy-gap-related structure
TDGL	time-dependent Ginzburg-Landau (theory)
usa	ultrasonic agitation
UTB	uniform-thickness microbridge
v_f	Fermi velocity
v_s	effective velocity of superfluid flow
V	voltage
$\bar{V}$	time-averaged voltage
V_c	characteristic voltage, $V_c \equiv I_c R$
V_f	maximum voltage of low-voltage foot
V_{max}	voltage of the highest observable microwave step
V_o	characteristic voltage for vortex flow defined by Aslamazov and Larkin (1975), $V_o = (8/\pi^2) I_c R_o$
VTB	variable-thickness microbridge
W	width of microbridge at narrowest point
x	Cartesian position coordinate
x_k	position of the kth vortex
β	exponent in the relation $I_c \propto (T_c - T)^{\beta}$
Γ	linewidth of the Josephson oscillation
$2\Delta, 2\Delta(T)$	superconducting energy gap
η	thermal healing length in a thin film; also used for vortex viscosity

List of Symbols (continued)

Symbol	Meaning
θ	coaltitude angle of evaporation or SEM viewing
$2\theta_{max}$	asymptotic angle filled by one bank of a hyperbolic, planar microbridge
κ	thermal conductivity
$\lambda, \lambda(T)$	magnetic-field penetration depth
λ_{eff}	effective penetration depth, $\lambda_{eff} \equiv \max\{\lambda, \lambda_{\perp}\}$
λ_{GL}	Ginzburg-Landau penetration depth
$\lambda_{GL}(0)$	Ginzburg-Landau penetration depth, extrapolated to T = 0
λ_{L}	London penetration depth
λ_{Q}	quasiparticle diffusion length
$\lambda_{\perp}$	thin-film penetration depth, $\lambda_{\perp} \equiv \frac{2\lambda^2}{d}$
$\xi, \xi_{GL}(T)$	Ginzburg-Landau coherence length
$\xi_{GL}(0)$	Ginzburg-Landau coherence length, extrapolated to T = 0
ξ_{BCS}	BCS coherence length
ρ	normal state resistivity
τ	time variable
τ_{E}	inelastic electron-scattering time
τ_{o}	characteristic quasiparticle scattering time of Kaplan et. al. (1976), $\tau_{o} \approx 8.4\tau_{E}$; also used for the period of cyclic vortex motion
τ_{Δ}	order-parameter relaxation time in TDGL theory, see eq. (II-28)
ϕ	phase of the macroscopic wavefunction; also used for azimuth angle
$\Delta\phi$	phase difference (usually across a microbridge)
Φ_{o}	magnetic flux quantum, $\Phi_{o} \equiv (hc/2e)$ in cgs Gaussian units, $\Phi_{o} \equiv (h/2e)$ in mks units.
$\psi(\vec{r}), \psi$	Macroscopic wavefunction

List of Symbols (continued)

Symbol	Meaning
$\lvert\psi_\infty\rvert$	magnitude of ψ in the absence of fields or currents
Ω	solid angle for hot-electron diffusion subtended by the banks

I. INTRODUCTION

This thesis describes studies of superconducting microbridges carried out at Yale University between August 1976 and June 1980. These studies were undertaken to improve our understanding of the dynamic (time-dependent) state of microbridges, in which the Josephson effect and nonequilibrium superconductivity play prominent parts. In addition to the general scientific investigation of time-dependent phenomena in microbridges, we have tried to understand quantitatively the limits on the Josephson-effect in these devices, limits which are important in assessing the utility of microbridges in applications such as low-noise, mm-wave mixers.

I.A Microbridges and the Josephson Effect

A microbridge may be defined as a planar or quasi-planar structure consisting of two broad films of superconductor (banks), separated by a narrow insulating gap which is bridged by a single narrow piece of superconducting film (bridge) connecting the two banks. In some theoretical treatments, microbridges are classed with ideal point contacts, and the term "constriction weak link" or simply "constriction" is used. For the purposes of this thesis, the unmodified term "microbridge" implies that uniform material is used for the bridge and banks. Structures incorporating more than one material, such as a normal (i.e. non-superconducting) bridge with superconducting banks, are referred to by more specific titles, such as "SNS microbridge".

Superconducting microbridges are often divided into two classes, depending on geometry. If the bank films are the same thickness as the bridge, as in Fig. I-1a, the device is a uniform-thickness microbridge (UTB). The dimensions of a UTB are the bridge length L, the bridge

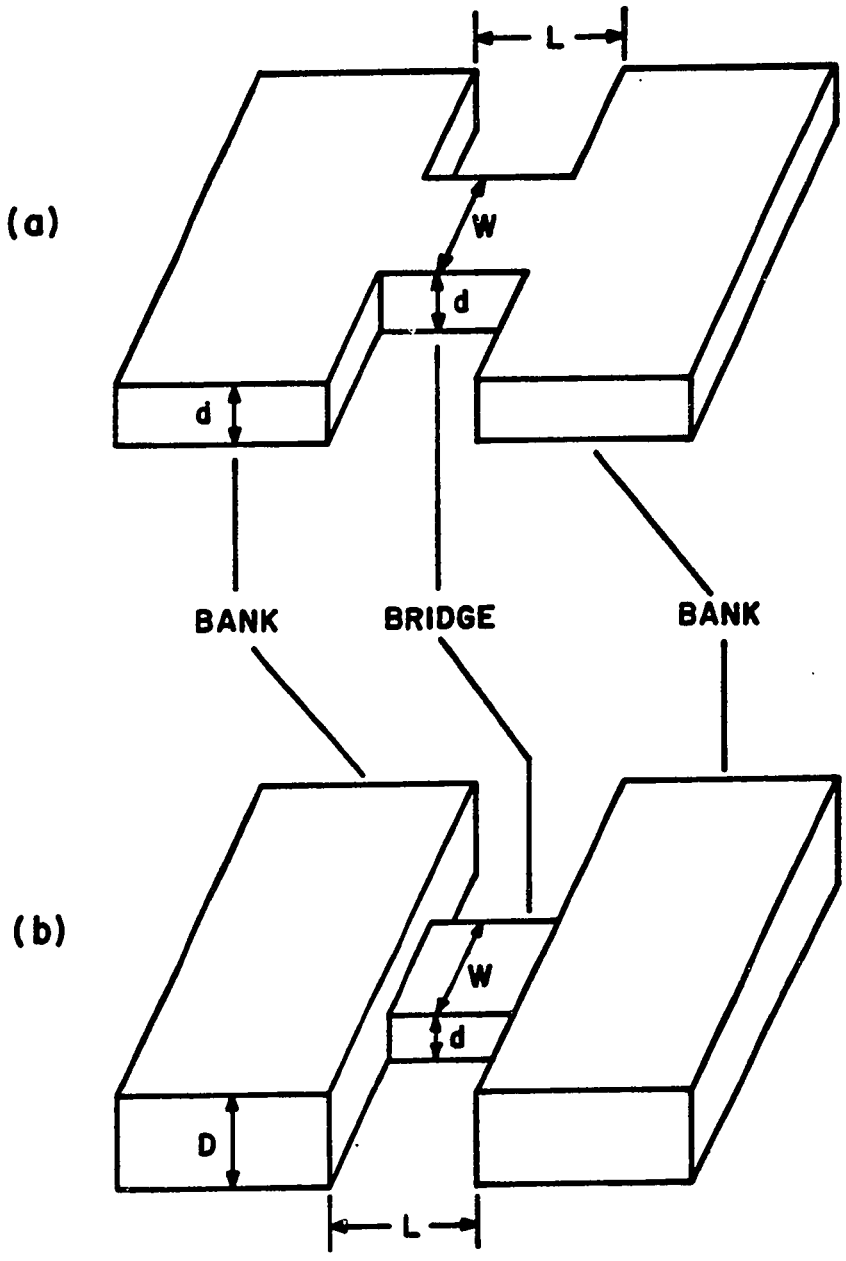

FIG. I-1. Idealized geometry of superconducting microbridges. (a) Uniform-thickness microbridge (UTB). (b) Variable-thickness microbridge (VTB). When current is passed from one bank to the other, the high current density in the bridge region causes a partial breakdown of the superconductivity there.

width W, and the film thickness d (both bridge and banks). If the banks are made thicker than the bridge region, as in Fig. I-1b, the device is a variable-thickness microbridge (VTB). In this case, d is the thickness of the bridge region and D is the bank thickness. As discussed in sections II.D and II.E, the VTB has practical advantages over the UTB, although its fabrication is usually more complicated.

A continuing source of interest in microbridge devices has been their behavior as Josephson-effect weak links. The modern history of such weak links begins in 1962, when Brian Josephson (1962) calculated that significant supercurrents (i.e. zero-voltage currents), due to tunneling of superconducting electron pairs, could flow through a thin, insulating oxide barrier between two superconductors.[1] Josephson recognized that the pair-tunneling supercurrent would be driven by differences in the phase of the macroscopic wave function of the two superconductors. Once Anderson and Rowell (1963) had actually observed the Josephson effect, this phase sensitivity was rapidly exploited in a wide variety of dc and ac applications.

Almost immediately after the tunnel junction experiments of AR (1963), it was discovered by Anderson and Dayem (1964) that superconducting microbridges, then in use by Parks and Mochel (1964) to study flow of magnetic flux vortices, showed microwave-induced, con-

---

[1] Previous to Josephson's work, it had been thought that the probability of such pair tunneling would be the square of the (very small) probability for single-particle tunneling, so that the pair-tunneling current would be unmeasurably small. Josephson, and later Philip Anderson, developed the idea that pairs could tunnel coherently, as single units, and found that the pair-tunneling supercurrent could be comparable in magnitude to the normal, single-electron tunneling current.

stant-voltage steps in the $\bar{V}(I)$ curve, one of the hallmarks of the Josephson effect. Although Anderson and Dayem explained their results with a semi-quantitative vortex-flow model, they correctly pointed out the fundamental relationship of their results to the Josephson effect observed in tunnel junctions. Eventually, the other key phenomena of the Josephson effect, including operation of a Superconducting Quantum Interference Device (SQUID, Fulton and Dynes (1970)) and direct observation of the Josephson radiation (Gubankov et. al. (1975)) were observed in superconducting microbridges.

A theoretical breakthrough in understanding the Josephson effect in microbridges came when Aslamazov and Larkin (1969) calculated the effect of current-induced depairing in a narrow superconducting constriction. They found that when an electric current is passed from one bank to the other, the high current density in the bridge region causes depairing, a partial breakdown of the superconductivity, there. If the weakened region is short and narrow compared to the superconducting coherence length, the Josephson effect results.

AL (1969) showed that small, dirty constriction-type weak links obey the same relations as tunnel junctions when they are in the static (i.e. zero-voltage) state at a temperature T near the critical temperature T_c. That is:

$$I = I_c \sin\Delta\phi \tag{1}$$

$$I_c R = (635\ \mu V/K)(T_c - T) \tag{2}$$

where I is the current, I_c is the maximum zero-voltage supercurrent, usually called the critical current, R is the resistance of the device in the nonsuperconducting state, and $\Delta\phi$ is the phase difference be-

tween the banks. Equations (1) and (2), together with the phase precession equation:

$$\hbar \frac{d(\Delta\phi)}{d\tau} = 2\, e\, V(\tau) \qquad (3)$$

can be used in the two-fluid picture to describe the key Josephson-effect phenomena mentioned above. (The phase precession equation (3) applies to all coherent superconducting systems. As elsewhere in this thesis, the time variable is denoted τ.)

Despite the similarities noted above, there are significant differences between microbridges and oxide-barrier tunnel junctions. One difference is that microbridges are much more strongly coupled devices, with critical current densities of 10^7 A/cm^2 or more. These large critical current densities imply small RC times (see Tinkham (1978)) which make microbridges attractive for high-frequency operation. In practice, however, R may be too low for efficient rf coupling. In addition, the high current densities present in microbridges can cause significant depairing and nonequilibrium effects in the banks. A second difference between microbridges and oxide-barrier junctions is that in the former, the weak region is typically longer than the electron mean free path ℓ. This means that the properties of the weak region can enter the calculations in much more complex form than the simple transmission coefficient which is adequate for basic tunneling theory. This complexity is largely responsible for the fact that sustained research has not yet been able to establish a microscopic theory of superconducting microbridges which is as complete as the microscopic theory of tunnel junctions.

Another Josephson-effect device which is closely related to the microbridge is the superconducting point contact. A clean point con-

tact, formed by pressing a sharply pointed superconducting wire against a superconducting block, is believed to consist of a simple metallic contact with a cross-sectional area of only a few thousand nm^2 (Tinkham et. al. (1977)). The current flow, concentrated in the small contact area, causes depairing and the Josephson effect in strict analogy to the operation of a variable-thickness microbridge. The point contact shares the small RC time of the microbridge, and it can be adjusted for high device resistance, so it has been widely used for SQUIDs and higher-frequency applications. However, most point contacts are not reproducible after thermal cycling or do not show the full value of the I_cR product (eq. (2)). If variable-thickness microbridges could be made with the tiny contact area and thick banks of a point contact, they might be expected to show the same excellent high-frequency performance, in a reproducible, thin-film device.

I.B Microbridges and Non-Equilibrium Superconductivity

Whenever a microbridge sustains a finite nonzero voltage, there is precession of the phase difference (eq. (3)) and temporal variation of the fractional depairing. Thus, operation at a finite voltage implies a dynamic state of the superconductor. The superconducting pair density, the superconducting energy gap, and the numbers and energy distributions of phonons and quasiparticles will vary in time, producing a complex problem in nonequilibrium superconductivity.

One can treat the lowest-order effects of this dynamic state by using the theory of Joule heating to account for power dissipation within the superconductor. In the Joule-heating picture, it is assumed that the phonons and quasiparticles are in local equilibrium at all points. The local temperature at each point $T_{eff}(\vec{r})$ is determined by

applying classical heat flow calculations to distributions of power dissipation, which may be postulated on physical grounds or may be computed self-consistently with the heat-flow calculations. Joule-heating theories have been very successful in describing deviations of microbridge behavior from the basic resistively-shunted-junction (RSJ) model (see section II.B.2) which occur at moderate-to-high levels of power dissipation.

Even when Joule heating is not significant, however, microbridges do not follow exactly the RSJ model predictions. Early attempts to account for microbridge behavior in terms of the finite relaxation time of the superfluid density (see the discussion of the TDGL model in section II.B.2) met with limited success, and recent work has focussed on the role of quasiparticle relaxation. Theories based on quasi-particle disequilibrium have been successful in describing phase-slip behavior in one-dimensional filaments and very long, narrow microbridges (see Kadin et. al. (1978)), and encouraging progress has been made in explaining microwave enhancement of the critical current (Klapwijk et. al. (1977b)) and low-voltage "foot" structures in the $\bar{V}(I)$ curves of microbridges (Schmid, et. al. (1980)). As microbridge studies are extended to a wider range of material and device parameters, these studies will serve as a proving ground for theories of quasiparticle disequilibrium and nonequilibrium superconductivity in general.

I.C Practical Application and the Effect of Microbridge Size

Josephson-effect devices have been used or proposed for use in a wide variety of practical applications. (See, for example, the proceedings of the 1978 Charlottesville conference on "Future Trends in Superconductive Electronics", AIP Conf. Proc. 44 (1978).) Most of

these can be put into three categories:

(1) Superconducting Logic Circuits

(2) SQUID Devices

(3) High-Frequency Detectors and Mixers.

Superconducting logic has been rapidly developed in recent years by the large program at IBM. (For a state-of-the-art survey, see the March 1980 issue of the IBM Journal of Research and Development.) Although the IBM technology using hysteretic circuitry is satisfactory, microbridge type devices could conceivably be useful in future generations of nonhysteretic logic with improved reproducibility after thermal cycling.

Successful low-noise SQUIDs have been made using both point contacts and shunted oxide-barrier tunnel junctions, but the highest energy sensitivity reported to date has been achieved for a two-junction SQUID incorporating very narrow Nb microbridges (Voss et. al. (1980)). Which type of Josephson-effect device will ultimately be preferred for SQUIDs is not yet clear.

In the field of high-frequency Josephson-effect detectors and mixers, oxide-barrier tunnel junctions are handicapped by their large intrinsic RC times, which limit operating bandwidth. Thus point contacts or microbridges are preferable for these applications.

While microbridges show promise as high-frequency devices, they have so far been limited by low device resistance and severe Joule heating. The device resistance is typically slightly less than the resistance of the structure in the normal state. For efficient, broadband, microwave coupling at frequencies $\gtrsim$ 100 GHz, a device resistance $\gtrsim 10\,\Omega$ is needed, whereas resistances of typical microbridges of pre-

vious studies have been $\lesssim 1\ \Omega$. The problem of Joule heating arises when finite-voltage operation leads to power dissipation in the microbridge. This power dissipation, concentrated around the bridge region, raises the temperature of that region until phase coherence is lost and the Josephson oscillation ceases. Thus, Joule heating of the bridge causes a maximum time-averaged voltage at which the Josephson effect and related phenomena can be observed. Through eq. (3), it can be shown (section II.B.2) that the voltage limit implies a frequency limit, which is usually the most important restriction on the operating frequency of a microbridge.

The calculation of Aslamazov and Larkin (1969) predicting tunnel-junction-like behavior for microbridges applies only to bridges whose length and width are small compared to the superconducting coherence length $\xi(T)$. (We make the conventional assumption that $d < W$.) If the bridges are made longer than a few coherence lengths, but still narrow, the $I(\Delta\phi)$ relation replacing eq. (1) becomes multivalued and the simple Josephson-effect behavior is lost (Likharev and Yakobson (1976a)). If the bridges are made wider than a few coherence lengths, but still short, the entire theoretical picture must be changed and new calculations based on flow of magnetic flux vortices become relevant (Likharev (1972)). These vortex-flow calculations, discussed in section II.C, predict dynamic effects reminiscent of, though distinct from, the ac Josephson effect.

Although the coherence length diverges near T_c, microbridge lengths and widths should be $< 5\text{-}10\xi(T = 0)$ if ideal junction-like operation is desired at $T < 0.9T_c$. For typical thin films of nominally pure Sn and In, $\xi(T = 0) \gtrsim 100$ nm, so it is necessary to use fabri-

cation techniques capable of achieving submicron dimensions. Furthermore, $\xi(T = 0)$ decreases as either T_c or the normal-state resistivity ρ increases, so the demands on fabrication techniques are even more stringent for high-resistivity or high-T_c materials.

Now let us consider the problem of increasing microbridge resistance. The bridge length may not be increased beyond a few coherence lengths, so the resistance must be increased by decreasing the cross-sectional area or increasing the resistivity of the bridge material. In the present study, we have concentrated on the latter option, but have also investigated the former.

I.D Motivation and Development of the Present Work

In this work, we have studied high-resistance (R = 1-8 Ω) microbridges in both the uniform-thickness and variable-thickness geometries fabricated from high-resistivity Pb alloys. The effect of boundary scattering in extremely narrow ($W \lesssim 40$ nm) VTBs of nominally pure In has also been investigated. Measurements of the time-averaged voltage $\bar{V}$ as a function of the current bias I, performed at various power levels of microwave irradiation, yield information about the Josephson effect, Joule heating, and other phenomena of the dynamic (i.e. finite-voltage) state.

In the first part of this work (chapters III and IV), UTBs of $Pb_{0.7}Bi_{0.3}$ and $Pb_{0.9}In_{0.1}$ alloys were studied. The UTBs were roughly hyperbolic in shape (see Fig. III-6), with minimum bridge widths ranging from 0.2 μm to 1.9 μm and device resistances ranging from 1 Ω to 8 Ω. The coherence length and bridge dimensions are such that measurements are practical in both the uniform-depairing and the vortex-flow regimes of operation. These investigations of high-resistance UTBs were carried

out with the aim of evaluating their potential for practical applications, and a specific point of interest was whether the vortex-flow theory of Aslamazov and Larkin (1975) provided an adequate description of the dynamic state for these microbridges.

The results obtained for the UTBs showed that high-resistivity microbridges suffered from Joule-heating limitations similar to those of pure-Sn UTBs of comparable normalized width (Skocpol (1974)). It became clear that reduction of Joule heating in microbridges required the use of the variable-thickness geometry (Klapwijk and Mooij (1975), Octavio et. al. (1977)) and the fabrication of bridges with still smaller dimensions (Tinkham et. al. (1977)). After considerable work and some unsuccessful preliminary attempts, we developed a novel VTB fabrication technology capable of meeting these needs, and high-resistivity microbridges of $Pb_{0.9}In_{0.1}$, with lengths and widths as small as 40 nm,were made and studied. In the end, the high resolution of the fabrication process made it possible to investigate high-resistance bridges of pure In, in which the high device resistance is provided predominantly by boundary scattering in the narrow bridge region.

Although the focus of the VTB experiments was on the Joule-heating limitation of the Josephson-effect response, observations on several other dynamic-state phenomena are reported in chapter VI. It is hoped that these data on low-voltage "foot" structure, energy-gap related structure,microwave-induced enhancement of the critical current and microwave-induced asymmetry of the $\bar{V}(I)$ curves will contribute to the theoretical understanding of nonequilibrium superconductivity which is currently being developed.

I.E A Note on Fabrication

In the course of this work, we have invested considerable time and effort in microfabrication techniques. This is not unprecedented in microbridge studies because the stringent limits on microbridge size require state-of-the-art lithography. In 1963, when the semiconductor industry was using a standard linewidth of 30 μm, Anderson and Dayem (1964) used photolithography to fabricate UTBs of 3 μm width. Superconducting microbridges were among the first electronic devices to be fabricated by electron-beam lithography (Lukens et. al. (1978)), and today microbridges are being fabricated with ultra-high resolution by contamination e-beam lithography (Laibowitz et. al. (1979)). Although much important work has been accomplished using microbridges produced by scribing techniques (for a very limited sample, see Chiao et. al. (1974), Gregers-Hansen et. al. (1972), and Octavio et. al. (1977)), we believe that the future belongs to lithographic techniques, which can now produce bridges of even smaller dimensions, with thick banks, more reproducibly than scribing methods.

The step-edge process for VTB fabrication described in chapter V is relatively unconventional. It is one of a number of quasi-planar processes introduced in recent years to provide smaller structures or more precise alignment of related parts. In these quasi-planar processes, the third dimension (i.e. the thickness of a film or an etch depth) is used to construct devices with details finer than those which can be attained by direct planar lithography. An early example of such a quasi-planar process is provided by the short-gate ($\approx$ 1 μm) FET process of Dean and Matarese (1975), in which the thickness of a photoresist layer is projected onto a planar substrate by evaporation

at an angle. Examples of quasiplanar processes used in superconducting device research include the work on small tunnel junctions by Dolan (1977), Havemann (1978), and Heiblum et. al. (1978).

Our microbridge process involves two innovative features. First, the vertical step is ion-beam etched into the substrate, rather than deposited on top of it. The ion-beam etching process yields a sharp, square, reproducible step profile. Second, this microbridge fabrication process is the only process known to us in which two-dimensional shadowing is used to provide two very small dimensions. In the process described in chapter V, none of the microbridge dimensions (L, W, d, D) is limited by optical diffraction or the resolution of the optical system.

Of course, the utility of step-edge fabrication is not limited to superconducting microbridges. One spinoff from the microbridge work, fabrication of ultrafine (nonsuperconducting) metal wires, has already been used in the study of electron localization in one-dimensional structures. (See Giordano, Gilson and Prober (1979), Prober, Feuer and Giordano (1980), and Giordano (1980).)) Work on other simple step-based microstructures is currently proceeding, both in this laboratory and elsewhere (White and Flanders (1980), Claassen (1980)).

I.F Outline of the Thesis

In this first chapter, we have introduced the concept of a microbridge and briefly discussed its scientific and technological interest. In chapter II, microbridge theories relevant to these experiments are described, and the results of different theories are compared. The applicability of the uniform-depairing and vortex-flow theories to the

actual experimental situation is assessed. Chapter III discusses the general experimental procedures used in the study, including shielding of the measurement apparatus and the photolithographic processes used to fabricate uniform-thickness microbridges (UTBs). Special attention is given to through-the-substrate projection exposure, a technique developed in this work to ensure successful liftoff processing for microbridges narrower than 0.5 μm. The results of the studies on uniform-thickness bridges are discussed in chapter IV. The critical currents of the bridges and the Josephson-effect response to microwave radiation are investigated, and the Joule heating is used to make a bolometric calibration of the absolute microwave sensitivity of several bridges. Chapter V treats the step-edge techniques developed to fabricate variable-thickness microbridges (VTBs) in which both the length and width of the bridge region is $\lesssim$ 50 nm. Ion-beam etching and evaporation shadowing are discussed at some length, with attention to the details of surface topography. The results of the studies on very small, variable-thickness microbridges are discussed in chapter VI. Critical currents and Joule-heating parameters are studied as functions of bridge dimensions for VTBs of Pb-In alloy and of nominally pure In. Spontaneous structure in the $\bar{V}(I)$ curves and microwave-induced effects are also discussed. Chapter VII summarizes our conclusions about the dependence of the various phenomena on bridge geometry and material parameters, and compares our results with those of previous workers.

Preliminary reports of some of this work have been published by Feuer, Prober, and Cogdell, AIP Conf. Proc. 44, 317 (1978); and by Feuer and Prober, IEEE Trans. MAG-15, 578 (1980) and Appl. Phys. Lett. 36, 226 (1980).

II. THEORY OF MICROBRIDGES

II.A. Ginzburg-Landau Theory

Virtually all theories of microbridge behavior are based on the Ginzburg-Landau (GL) theory of the macroscopic wavefunction or extensions of this theory. The GL theory was originally developed as a phenomenological description of the superconducting phase transition, but Gorkov (1959) showed that it could be derived as a limiting case of the BCS microscopic theory, valid near the critical temperature T_c when the supercurrent and superconducting pair density vary slowly in space and time. Many authors have discussed this theory, and derivations of general results which are quoted here without proof can be found in the text by Tinkham (1975).

The fundamental entity in the GL theory is the order parameter or pseudowave function $\psi(\vec{r})$. ψ is a complex quantity. The square of its magnitude is proportional to n_s, the density of superconducting pairs, while the gradient of its phase ϕ gives rise to superconducting currents. The pseudowave function is determined from the two GL differential equations:

$$\psi - \frac{|\psi|^2}{|\psi_\infty|^2}\psi + \xi^2 \left(\frac{\vec{\nabla}}{i} - \frac{2\pi}{\Phi_o}\vec{A}\right)^2 \psi = 0 \qquad (1)$$

and

$$\frac{c}{4\pi}(\vec{\nabla} \times \vec{b}) = \vec{J}_s = \frac{e\hbar}{2mi}(\psi^*\vec{\nabla}\psi - \psi\vec{\nabla}\psi^*) - \frac{e^2}{mc}\vec{A}\,\psi^*\psi \qquad (2)$$

in conjunction with the boundary condition:

$$\left(\frac{\hbar}{i}\vec{\nabla} - \frac{2e}{c}\vec{A}\right)\psi \cdot \hat{s} = 0 \qquad (3)$$

at the insulating boundary of the superconductor, where $\hat{s}$ is a unit vector normal to the boundary.

Boundary conditions must also be imposed within the superconductor itself, to specify, for example, the total current through a microbridge. In the above equations, $|\psi_\infty|^2$ is the density of superconducting pairs in the absence of currents or fields, $\Phi_o = \frac{hc}{2e}$ is the flux quantum, $\vec{A}$ is the electromagnetic vector potential, $\vec{b}$ is the magnetic flux density, $\vec{J}_s$ is the superconducting current density, and e and m are the charge and mass, respectively, of the electron. In Eq. (2), the Maxwell equation for the current is applied to the static case, so that the time derivative $\frac{d\vec{E}}{d\tau} = 0$ and $\vec{J} = \vec{J}_s$. The parameter

$$\xi \equiv \xi_{GL}(T) = \xi_{GL}(0)\ (1 - t)^{-1/2} \tag{4}$$

the Ginzburg-Landau coherence length, gives the characteristic scale of variations in ψ. In eq. (4), we have used the reduced temperature $t \equiv T/T_c$, where T_c is the critical temperature. There is a second length:

$$\lambda(T) = \left(\frac{mc^2}{8\pi e^2|\psi_\infty|^2}\right) = \lambda(0)\ (1 - t)^{-1/2} \tag{5}$$

the magnetic-field penetration depth, which gives the characteristic scale of variations in $\vec{b}$. When a magnetic field is applied perpendicular to a thin film ($d << \lambda$), the relevant depth is increased to:

$$\lambda_\perp = \frac{2\lambda^2}{d} \tag{6}$$

as shown by Pearl (1964).

The object of much of microbridge theory is to solve the GL equations for $\psi(\vec{r})$ with the appropriate boundary conditions. Due to the nonlinearity of the equations, exact solutions have not been obtained for the relatively complex geometry of the real microbridge. Approximate solutions have been obtained as extensions of two well-known

problems with simpler boundary conditions. The first approach, discussed in section II.B below, is based on the problem of current-induced depairing in a one-dimensional superconducting filament. The second approach, discussed in section II.C, is based on the vortex solution to magnetic flux penetration in a thin film. The calculations discussed in sections II.B - II.E apply to microbridges in the dirty limit (i.e. microbridges for which the mean free path ℓ is the smallest length involved). Clean microbridges are discussed briefly in section II.F.

II.B Uniform-Depairing Models of Microbridge Behavior[1]

II.B.1 Static Behavior

A superconducting filament of infinite length may be considered one-dimensional if its cross-sectional area is less than both ξ^2 and λ^2. In this case, the pseudowave function will be essentially constant across the filament cross-section. Assuming that the cross section is constant along the length of the filament, one can construct a translationally invariant solution:

$$\psi(x) = |\psi| e^{ikx} \tag{7}$$

which obeys the one-dimensional GL equation:

$$\psi + \frac{|\psi|^2}{|\psi_\infty|^2}\psi - \xi^2 \frac{d^2\psi}{dx^2} = 0. \tag{8}$$

The term in $\vec{A}$ has been omitted since the wire diameter is much less than λ so that self-fields are not important. $|\psi|$ is thus determined as a function of k:

---

[1] In the models treated in this section, the degree of depairing (and thus the superfluid density) is uniform across the midplane of the bridge. Physically, such an assumption is justified when vortex formation (see section II.C.) is energetically unfavorable.

$$|\psi|^2 = |\psi_\infty|^2 (1 - \xi^2 k^2) \tag{9}$$

where $|\psi_\infty|^2$ is the density of superconducting pairs in the absence of fields or currents. Then the current density in the filament is:

$$J = 2e|\psi_\infty|^2 \frac{\hbar}{2m} k(1 - \xi^2 k^2) = 2e\, n_s v_s. \tag{10}$$

The physical explanation of this result is that the current density is the product of a carrier (pair) density n_s and a velocity v_s. As the velocity becomes large, pair-breaking occurs and the carrier density decreases. Eventually, further increases in velocity lead to decreases in the current density.[2]

The maximum of the above function gives the depairing critical current:

$$I_c^{(fil)} = \frac{\hbar e}{m}|\psi_\infty|^2 \left(\frac{2Wd}{3\sqrt{3}\,\xi} \right) = \frac{c\Phi_o\, d}{12\sqrt{3}\,\pi^2\,\lambda^2} \frac{W}{\xi} \quad . \tag{11}$$

We may write this as:

$$I_c^{(fil)} = \frac{2}{3\sqrt{3}} I_\infty \frac{W}{\xi} \tag{12}$$

where:

$$I_\infty = \frac{c\Phi_o d}{8\pi^2\lambda^2} \tag{13}$$

is a useful normalization current. Near the critical temperature, both λ and ξ diverge as $(1 - t)^{-1/2}$, so the critical current of a long filament has the temperature dependence:

---

[2] After many years, the stability of the two superconducting solutions under current bias is still a matter of active research. See, for example, Kramer and Baratoff (1977).

$$I_c^{(fil)} \propto (1 - t)^{3/2} . \tag{14}$$

Note that this result is different from the temperature dependence associated with a Josephson tunnel junction:

$$I_c^{(jct)} \propto (1 - t)^{1} . \tag{15}$$

As we will see, some microbridges are found to have a junction-like dependence, while others are characterized by a depairing or "bulk-like" dependence (i.e. that of the infinite filament).

To apply these one-dimensional methods to microbridge structures, it is necessary to impose boundary conditions at some finite length. The simplest are rigid boundary conditions, in which the banks (see fig. I-1) are assumed to experience no depairing whatsoever. That is, the pair density $|\psi|^2$ at the ends of the bridge is required to equal the zero-current pair density of the banks. Likharev and Yakobson (1976a) have given a thorough discussion of this approach. The static solutions for $\psi(x)$ may be expressed in terms of elliptic functions, but numerical calculations are required to obtain $I(\Delta\phi)$ or $\bar{V}(I)$ relations for the case of arbitrary length. If the bridge length L is much less than the coherence length ξ, simple analytic solutions are found:

$$I = I_c \sin \Delta\phi \tag{16}$$

$$I_c = I_\infty - \frac{W}{L} = \frac{3\sqrt{3}}{2} \frac{\xi}{L} I_c^{(fil)} \tag{17}$$

Using the normal-state resistance of the bridge region, one can define a characteristic voltage:

$$V_c \equiv I_c R_N = \frac{c\Phi_o \rho}{8 \pi^2 \lambda^2} \approx 635 \frac{\mu V}{K} (T_c - T) \tag{18}$$

where ρ is the normal-state resistivity. We have used the dirty-limit formulas, appropriate when the electron mean free path ℓ is much less than the coherence length and the bridge dimensions, to obtain the last expression. Note that V_c is independent of material, as well as dimensions, as long as $\ell \ll L \ll \xi$. Interestingly, both the form of the $I(\Delta\phi)$ relation and the magnitude of I_c exactly match the static results for Josephson tunnel junctions for $T \approx T_c$. This fact is one of the strongest arguments in favor of the universality of Josephson-effect behavior among weak links which are well-localized in space.

Using numerical methods, LY(1976a) also obtained the $I(\Delta\phi)$ relations appropriate to longer bridges. Examples are reproduced in Fig. II-1. As the bridge is made longer, the $I(\Delta\phi)$ relation becomes more and more skewed, eventually becoming reentrant at $L = 3.5\xi$. The critical current decreases smoothly to approach the constant value of the one-dimensional filament. The characteristic voltage, however, increases monotonically, becoming proportional to the length for very long bridges.

From the work of Aslamazov and Larkin (1969), we know that the short-bridge results given above are generally associated with sharply localized depairing, and do not reflect peculiarities of the rigid boundary conditions. By assuming that the gradient term must dominate the GL equation for microbridges which are sufficiently small, AL (1969) were able to obtain a sinusoidal $I(\Delta\phi)$ relation with $V_c = 635\ \mu V/K$ without adopting any explicit geometry for the constriction. One slight difference between the conclusions of AL (1969) and LY (1976a) occurs in the definition of the resistance. AL (1969) use the normal-state resistance of the constriction as a whole, <u>including the resistance of the banks</u>, while LY (1976a) use the resistance of the bridge region

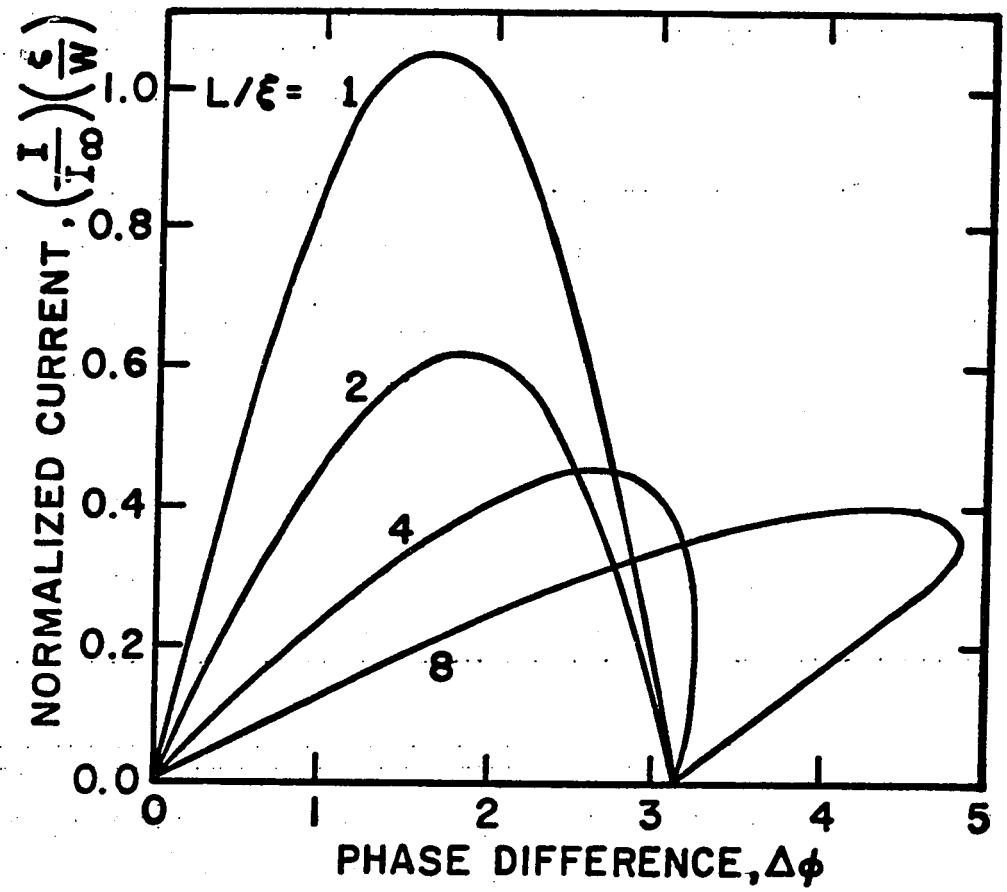

FIG. II-1. Normalized current as a function of phase difference (after Likharev (1976a)). The $I(\Delta\phi)$ relationship is nearly sinusoidal for $L/\xi(T) = 1$, but becomes increasingly skewed for longer bridges. This calculation, made under the assumption of rigid boundary conditions, predicts that the $I(\Delta\phi)$ relation becomes multivalued for $L/\xi(T) \gtrsim 3.5$.

alone. In fact, one should probably use an intermediate value, including the resistance of whatever portion of the banks undergoes significant depairing. Within the two-fluid picture which gives rise to the RSJ model, this resistance should be experimentally accessible as the minimum differential resistance of the $\bar{V}(I)$ curve at finite voltage.

The filament model with rigid boundary conditions does not consider depairing or phase gradients in the banks, though such depairing is likely to be important when the bridge region is short ($L \ll W$) or when the banks widen only gradually. The role of bank depairing has been theoretically investigated by Volkov (1973), Kulik and Omelyanchuk (1976), and Mooij and Dekker (1978). Volkov considered (two-dimensional) hyperbolic planar structures, obtaining analytic results appropriate for very narrow bridges ($W \ll \xi$), and Kulik and Omelyanchuk obtained similar results for (three-dimensional) hyperboloidal structures with axial symmetry. Mooij and Dekker combined analytical approximations and numerical methods to calculate the properties of both two- and three-dimensional constrictions. For planar hyperbolic structures, the dimensions are the width W, the film thickness d (assumed to be $\ll W$), and the asymptotic angle filled by one bank $2\theta_{max}$. For the three-dimensional hyperboloids, the diameter W and the asymptotic angle θ_{max} are the only two dimensions.

Mooij and Dekker found the full solution of the two-dimensional[3] GL equations too awkward, even by numerical methods, so several approximations were used in the model. In addition to neglecting the

---

[3] Since the three-dimensional structure has axial symmetry, it also involves two-dimensional equations.

vector potential term, they assumed that:

(1) The direction of current flow at all points in the bridge was the same as it would be if the bridge were in the normal state. (The magnitude of the current was allowed to vary however.)

(2) The gradients of ψ perpendicular to the current flow were negligible.

In this way, the bridge was divided into a number of arbitrarily narrow, microbridge-like channels. The one-dimensional equation for each channel was then solved, including nonlinear terms, and the solutions were chosen which led to self-consistency with the above approximations. Good self-consistency was obtained when:

$$a \equiv \frac{W}{2\xi \sin(\theta_{max})} \lesssim 0.5. \tag{19}$$

For the three-dimensional constrictions with $a < 0.1$, the critical current was found to agree with the junction-like behavior of AL (1969), using the total resistance of the infinite structure. For wider three-dimensional constrictions, the critical current density smoothly approached the infinite filament result. (Due to the nonuniform current distribution, the total critical current was found to depend on θ_{max} as well as Wd.) The $I(\Delta\phi)$ relation was found to be sinusoidal for narrow bridges, becoming reentrant for $a > 1$.

The critical current for the two-dimensional constriction was found to be well-approximated by:

$$I_c = I_\infty \frac{\theta_{max}}{\text{arcsinh}\ (1/a)} \tag{20}$$

for all values of a in the self-consistent range. This agrees with the analytic result of Volkov (1973) for small a. It is interesting to note that the characteristic voltage $V_c = I_c R$ agrees with that of

AL (1969) if only the resistance within a length $\frac{\xi}{2}$ of the bridge midline is included. The $I(\Delta\phi)$ relation is difficult to define for a two-dimensional constriction, because the total phase change includes the phase gradients in the banks and therefore diverges logarithmically as the measurement point is moved out to infinity. One possibility is to subtract out the phase difference which would occur in the absence of depairing, i.e.:

$$\Delta\phi = \frac{m}{\hbar e} \int_{-\infty}^{\infty} J_s \left(\frac{1}{|\psi|^2} - \frac{1}{|\psi_\infty|^2} \right) d\ell \ . \tag{21}$$

By this definition, the $I(\Delta\phi)$ relation found by MD (1978) for small a is skewed to the left, peaking at a value less than $\Delta\phi = \pi$. A sinusoidal $I(\Delta\phi)$ relation is obtained if only the phase winding within a length ξ of the midline is included:

$$\Delta\phi = \frac{m^*}{\hbar e^*} \int_{-\xi/2}^{\xi/2} \frac{J_s}{|\psi|^2} \, d\ell \ . \tag{22}$$

In brief, the critical current and net $I(\Delta\phi)$ relation of a small, hyperbolic planar constriction may be calculated as though it consisted of a core of length ξ with ideal Josephson behavior, connected to rigid banks which experience no depairing. It should be remembered, however, that the actual spatial dependence of $|\psi|^2$ and ϕ is quite different.

II.B.2 Dynamic Behavior

The discussion so far has centered on the static, or time-independent, behavior of microbridge structures. As in any system maintaining superconducting phase coherence, this static state is equivalent to the zero-voltage state. To be more precise, the potential of the superconducting pairs must be uniform in space if the superconducting phase is

to be constant in time. Conversely, finite voltages are associated with finite rates of phase variation according to the Josephson relation:

$$\frac{1}{\hbar}\frac{d(\Delta\phi)}{d\tau} = 2eV \tag{23}$$

where $\Delta\phi$, as before, represents the phase difference between two points and V represents the difference between the pair potentials of the points. The equation holds quite generally, as long as local equilibrium permits definition of the pair potential.

The simplest way to incorporate time dependence into weak link behavior is to treat the static $I(\Delta\phi)$ as instantaneously valid. To account for the quasiparticle current which appears at finite voltage, one may introduce the two-fluid ansatz:

$$I_{tot} = I(\Delta\phi) + \frac{V}{R} \tag{24}$$

By assuming a simple sinusoidal form for the $I(\Delta\phi)$ relation, one arrives at the most widely applied model of weak link dynamics, the Resistively-Shunted Junction (RSJ) model.

The RSJ model is the basis of most of our qualitative understanding of Josephson elements in ac circuits, and it has often been applied in a quantitative fashion as well. Substituting a time-independent voltage into the RSJ equations (23) and (24) one easily displays the well-known Josephson current oscillations:

$$I_{tot}(\tau) = \frac{V}{R} + I_c \sin(2\pi f_J \tau) \tag{25}$$

where the frequency of oscillation is:

$$f_J = \frac{2e}{h} V. \tag{26}$$

The proportionality constant is 484 MHz/μV, and typical experimental

frequencies are on the order of 10 GHz and above. In practice, it is impossible to obtain perfect constant-voltage bias for the enormous range of frequencies involved, while good constant-current bias is easily achieved by providing a high source impedance at low frequencies and using inductive leads. The RSJ model predicts that constant-current bias will lead to voltage oscillations with high harmonic content, at a frequency given by eq. (26) applied to the time-averaged voltage $\bar{V}$. In the present work, we have not measured the time-dependent voltage directly, but have drawn our conclusions from measurements of the time-averaged or dc component.

The time-averaged V-I curves predicted by the RSJ model are shown in Fig. II-2. (In part (a), $\bar{I}$ is plotted versus the dc voltage bias, while in part (b), $\bar{V}$ is plotted versus the dc current bias.) Note the substantial differences between the voltage-biased and current-biased curves. This strong dependence on source impedance may be viewed as a reflection of the "extra" variable in the system, the superconducting phase difference. In general, ac source currents and reactive source impedances lead to a very complex problem requiring numerical solution or analog simulation. (See, for example, Auracher and Van Duzer (1973) or Claassen and Richards (1978).) The simplest cases involving ac sources are those in which a perfect voltage or current source produces a sinusoidal ac signal superimposed on the dc bias:

$$I_{tot}(\tau) = I_{dc} + \hat{I} \sin(2\pi f \tau). \tag{26a}$$

Due to the low resistance typical of microbridges, the current-biased case is usually more relevant to the actual experiments. Numerical and simulator solutions for this case have been obtained by many workers,

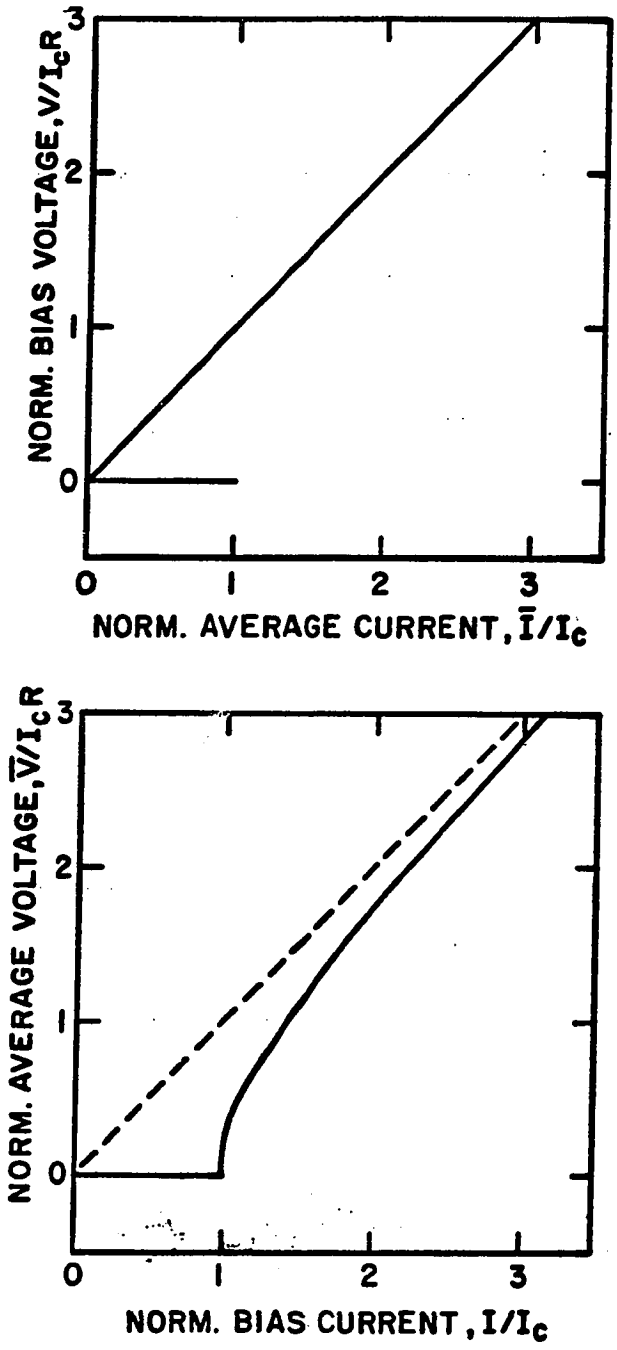

FIG. II-2. Current-voltage characteristics predicted by the resistively-shunted junction (RSJ) model. (a) Time-averaged current as a function of dc voltage bias (b) Time averaged voltage $\bar{V}$ as a function of dc bias current I. The difference between the voltage-biased and current-biased curves reflects the presence of an extra variable, the superconducting phase difference ϕ, in the problem.

including Russer (1972) and Henry et. al. (unpublished). As shown in Fig. II-3, constant-voltage plateaus are induced in the time-averaged $\bar{V}(I)$ characteristic when the Josephson oscillations are in resonance with the ac source signal. These are called Shapiro steps or simply microwave steps. The width (in current) of the step ΔI_n depends on the amplitude of the ac signal in a quasiperiodic fashion, shown in Fig. II-4. Even the critical current, which may be viewed as the zeroth step, shows the oscillatory behavior. To normalize the calculations, currents are scaled to I_c, voltages are scaled to $V_c = I_c R$, and frequencies are scaled to $f_c = \frac{2e}{h} V_c$. Although the intrinsic bandwidth of the junction is on the order of f_c, the bandwidth can be decreased by shunt capacitance or series inductance.

The use of the RSJ model, described above, is founded on the generality of the time-independent $I(\Delta\phi)$ relation. In fact, a microbridge biased at a finite voltage is undergoing periodic changes in the value of the energy gap; the total density, energy distribution and spatial distribution of the quasiparticles; and the density and distribution of phonons. When the operating frequency (proportional to voltage) becomes high enough, the finite relaxation rates of these quantities will become apparent, and the static $I(\Delta\phi)$ will fail. Time-dependent $I(\Delta\phi)$ relations can sometimes be introduced for some specific range of operation (see, for example, Jensen and Lindelof (1976)), but it is more common to solve directly for the $\bar{V}(I)$ curve.

The relaxation of the order parameter has been widely studied through the use of the time-dependent Ginzburg-Landau (TDGL) theory, which is based on the equations:

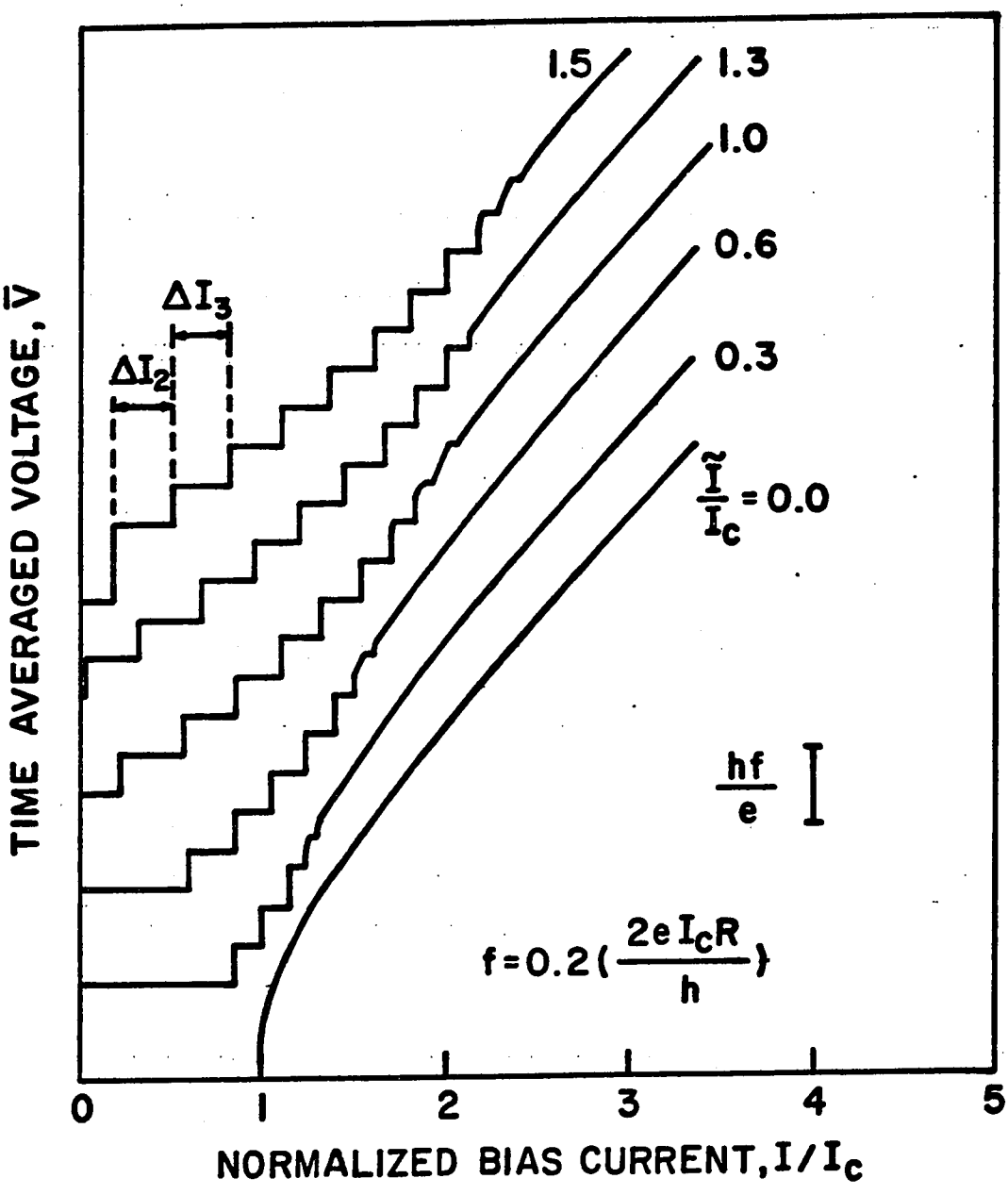

FIG. II-3. Microwave-induced constant-voltage steps in the $\bar{V}(I)$ curve, as predicted by the RSJ model. These curves are computed for a normalized frequency $\frac{hf}{2eI_cR} = 0.2$.

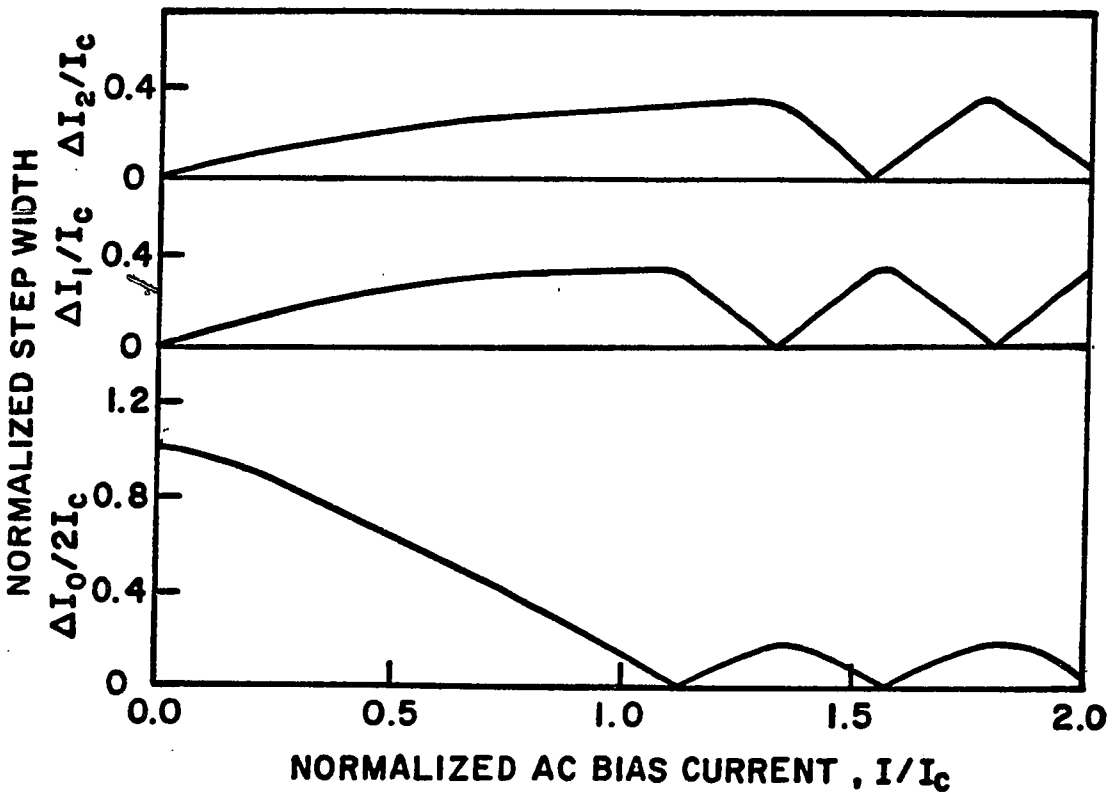

FIG. II-4. Microwave step widths ΔI_n versus microwave current, as predicted by the current-biased RSJ model. These curves are computed for a normalized frequency $\frac{hf}{2eI_cR} = 0.2$.

$$\tau_\Delta \left(\frac{d\psi}{d\tau} + i\mu \frac{2e}{\hbar} \psi \right) = \left(1 - \frac{|\psi|^2}{|\psi_\infty|^2}\right)\psi + \xi^2 \nabla^2 \psi \tag{27a}$$

$$\vec{J} = \frac{e\hbar}{2mi} \left(\psi^* \vec{\nabla}\psi - \psi \vec{\nabla}\psi^*\right) - \vec{\nabla}\mu/\rho \tag{27b}$$

τ_Δ is the Ginzburg-Landau relaxation time and μ is the electrostatic potential. Gorkov and Eliashberg (1968) showed that these equations should describe the relaxation of the order parameter in gapless superconductors, but the theory has been widely applied to ordinary superconductors as well. For gapless superconductors (strong depairing limit), the GL relaxation time is:

$$\tau_\Delta = \frac{12}{f_c} \tag{28}$$

where the tunnel-junction or short-bridge result for f_c is used. For ordinary (weak depairing) superconductors, the numerical coefficient is reduced to 5.79, but other terms should be included in the equations as well (Baratoff and Kramer (1977)).

Likharev and Yakobson (1976b) studied the finite-voltage properties of superconducting microbridges using one-dimensional TDGL theory with rigid boundary conditions. One striking feature of their results is the universal high-voltage asymptote:

$$V = (I - 0.75\ I_c)\ R. \tag{29}$$

Neither the relaxation time nor the bridge length enters into this formula, though the parameter:

$$\eta \equiv \gamma \frac{I}{I_c} \equiv 2\pi f_c \tau_\Delta \left(\frac{L}{\xi}\right)^2 \frac{I}{I_c} \tag{30}$$

determines when this asymptotic region is reached. LY (1976b) also

obtained the $\bar{V}(I)$ characteristic for a short bridge biased at a current just above I_c. The curve has a hyperbolic (RSJ-like) shape with a smaller effective resistance:

$$\bar{V} = (I^2 - I_c^2)^{1/2} R (1 + \gamma/15). \tag{31}$$

This adjustment is likely to be difficult to observe experimentally.

To solve the TDGL equations for arbitrary bias currents, numerical methods must be used. The most extensive calculations have been presented by Baratoff and Kramer (1977). By such direct calculations, BK (1977) showed that previous work by Jensen and Lindelof (1976) has overestimated the range of applicability of the analytic approximations. BK (1977) also discovered that extremely long relaxation times (not predicted by any microscopic theory) could lead to hysteresis in the $\bar{V}(I)$ curve at the voltage onset. Such long relaxation times reduce the amplitude of the Josephson oscillations at high frequencies, so the hysteresis may be analogous to that produced by shunt capacitance in the RSJ model (McCumber (1968), Stewart (1968)).

II.C Vortex-Flow Models of Microbridge Behavior

The earliest experiments performed on superconducting microbridges (see Parks and Mochel (1964), Anderson and Dayem (1964)) were explained in terms of motion of flux vortices in the bridge. Flux vortices in a thin film consist of a cylindrical region of zero-gap material, sometimes called the "normal core", through which the magnetic flux $\vec{b}$ penetrates, surrounded by circular currents which screen out the field in the rest of the superconductor. Under the influence of the transport current in the microbridge, these vortices experience a Lorentz force which drives them across the bridge. When a vortex

carrying total flux Φ crosses the bridge, the phase of the pseudowave function must change by an amount:

$$\delta(\Delta\phi) = 2\pi \frac{\Phi}{\Phi_o} \tag{32}$$

where

$$\Phi_o = \frac{hc}{2e} = 2.07 \times 10^{-7} \text{ gauss-cm}^2 \tag{33}$$

is the flux quantum. Since the rate of phase change is proportional to the voltage across the bridge (eq. (23)), we conclude that a bridge containing moving flux vortices will sustain a finite voltage, implying power dissipation $\overline{IV}$. This dissipation will actually take place in and around the vortex cores, where quasiparticle currents flow when the vortices move.

The physical reality of vortex flow in large, thick, type-I ($\lambda_{GL} < \xi_{GL}/\sqrt{2}$) microbridges has been graphically demonstrated by Chimenti and Huebner (1977), who used magneto-optical techniques to visualize the vortices. For type-II materials or sufficiently thin[4] films of type-I materials, however, the vortex-wall energy is negative, so the smallest vortices possible, those carrying a total flux $\Phi = \Phi_o$, are the only ones which are stable. These type-II vortices are too small to visualize by magneto-optical means, so supporting evidence for vortex flow has been indirectly obtained from V-I characteristics. In interpreting the V-I curves, some workers (e.g. Guthmann et. al. (1974), Klapwijk et. al. (1977a)) have used models based on pinning-limited vortex flow, which is probably inappropriate for small micro-

---

[4] The critical film thickness for type-II behavior is difficult to compute exactly. Typically, experimental values are on the order of the coherence length.

bridges. Simple models of pinning-limited vortex flow yield a finite $\frac{d\bar{V}}{dI}$ at the voltage onset. Unfortunately, the more sophisticated models described below yield $\bar{V}(I)$ curves much more similar to those predicted by the uniform-depairing models discussed in the previous section.

Figure II-5 shows schematically the structure of a vortex in a thin film of infinite extent. In more complex topologies, involving finite films and/or thickness variations, vortices may lose their circular symmetry. The region of currents and magnetic fields is characterized by a dimension $\lambda_{eff} \equiv \max \{\lambda, \lambda_{\perp}\}$, while the region of reduced superfluid density is characterized by the coherence length ξ.

Coherent vortex flow can give rise to ac effects reminiscent of the ac Josephson effect. For example, if a chain of vortices, each carrying one flux quantum, moves coherently across the bridge, an ac voltage at the frequency $f = (2e/h)V$ will be generated (cf. eq. (26)). Furthermore, an ac component of the bias current can synchronize vortex motion or nucleation, producing constant-voltage steps similar to the microwave steps discussed in the previous section.

For strongly type-II materials ($\lambda_{GL}/\xi_{GL} >> 1$) or very thin films, the normal core is relatively small and may be neglected for some calculations. Then n_s is constant everywhere and the supercurrent conservation equation:

$$\vec{\nabla} \cdot \vec{J}_s = 0 \tag{34}$$

implies:

$$\nabla^2 \phi = 0 \tag{35}$$

where we have made the gauge choice:

$$\vec{\nabla} \cdot \vec{A} = 0. \tag{36}$$

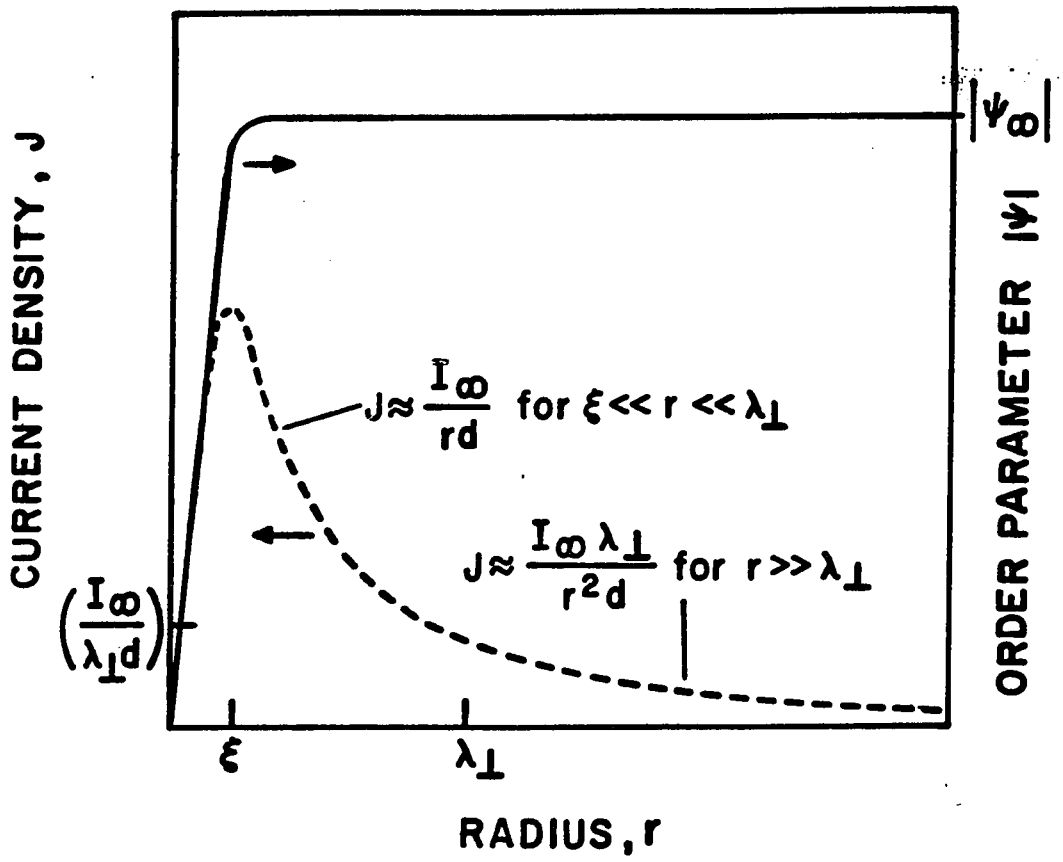

FIG. II-5. Schematic structure of an isolated vortex in a thin superconducting film. The magnitude of the order parameter $|\psi|$ rises to nearly its full value over a radius on the order of $\xi(T)$, but the circulating currents extend over a larger radius on the order of $\lambda_\perp(T) = \frac{2\lambda^2}{d}$. This example is sketched for the case $\lambda_\perp(T)/\xi(T) = 5$.

Within this approximation, a vortex is simply the solution of Laplace's equation for the phase of the wavefunction associated with a point singularity. A multiple-vortex state consists of a linear superposition of such solutions, which leads to a relatively simple model of vortex-vortex interactions. In principle, the motion of the vortices, and thus the voltage-current characteristics of the microbridge, could be calculted as follows:

(1) Solve Laplace's equation with the appropriate boundary conditions to obtain ϕ.

(2) Solve the integral equation for the current:

$$\vec{J}_s(\vec{r}) = \left(\frac{c\Phi_o}{8\pi^2\lambda^2}\right)\left[\vec{\nabla}\phi - \frac{2\pi}{c\Phi_o}\int \frac{J(\vec{r}')}{|\vec{r}-\vec{r}'|}\, d^3r'\right]. \qquad (37)$$

(3) Use this current distribution to compute the free energy according to the Ginzburg-Landau theory.

(4) Differentiate the energy with respect to vortex positions to obtain the forces on the vortices.

(5) Integrate the equation of motion to obtain the time dependence of the vortex positions.

(6) A viscous damping term must be included as an ansatz to the equation of motion to account for the power dissipation in the cores of moving vortices.

In practice, the analytical solution of this problem in a microbridge geometry is facilitated by two additional simplifications, made under the assumption that both the length and width of the bridge are much less than the effective penetration depth ($L,W \ll \lambda_{eff}$). Due to the short length, vortices in the bridge region will be repelled by the banks and may be expected to move across the bridge only at its mid-

line. The Lorentz force is perpendicular to the current, so the imposition of a net transport current through the bridge will not upset this conclusion. Due to the narrow width, the vector potential $\vec{A}$ is nearly uniform across the bridge region and may be neglected, as it was in the uniform-depairing models discussed above. This leads to the truncation of equation (37) above:

$$\vec{J}_S(\vec{r}) = \frac{c\Phi_o}{8\pi^2\lambda^2}\vec{\nabla}\phi \quad . \tag{38}$$

With the above simplifications, the problem is made tractable.

II.C.1 Method of Images

Likharev (1972) was the first worker to use the scheme described above to obtain analytic and numerical results for the V-I curves of microbridges in the vortex-flow regime. His calculations were made for rectangular VTBs, using the rigid boundary condition:

$$\phi = \text{constant} \tag{39}$$

along each bridge-bank interface and:

$$\vec{\nabla}\phi \cdot \hat{s} = 0 \tag{40}$$

at the bridge-vacuum interfaces. The solution of Laplace's equation for this geometry was attempted by the method of image vortices, analogous to the image-charge method of electrostatics. Image vortices projected into the banks are of the same polarity as the source vortex, so they repel it, holding it on the bridge midline. Image vortices projected into the vacuum regions are of opposite polarity from the source vortex, so they attract it, moving it toward whichever edge is nearest. This attraction toward the bridge edges constitutes a barrier to vortex entry which gives rise to a finite

critical current. Unfortunately, this method of solution requires a difficult double summation of single-vortex wavefunctions. Likharev (1972) approximated the first summation in a way which yields a force of vortex-vortex interaction which is independent of separation. Then he truncated the second summation after the zeroth term, leading to a complete loss of vortex-edge interactions. By means of some ad hoc (and nonphysical) assumptions about the current distribution in the bridge, a vortex-edge interaction was regained. It was a linear function of x, the distance from the center of the bridge to the vortex singularity.

The force equation derived by Likharev (1972) is:

$$F_k = \frac{\phi_o^2}{4\pi\lambda_\perp L} S_k \{ \frac{LI}{\pi W I_\infty} - (\frac{HWL}{\phi_o} - S_k)(\frac{2x_k}{W}) + \sum_{m \neq k} S_m (\frac{2x_m}{W} + \text{sign}(x_k - x_m)) \}. \tag{41}$$

In this equation, x_k is the position of the k^{th} vortex, H is the external magnetic field, and $S_k = \pm 1$ represents the polarity of the vortex. The critical current with no externally applied magnetic field is:

$$I_c(H=0) = \frac{\pi W}{L} I_\infty. \tag{42}$$

The dependence of I_c on the magnetic field is a function with periodic zeros, very similar to the $I_c(H)$ curve for an oxide-barrier tunnel junction.

When the bias exceeds the critical current, vortices of opposite polarity simultaneously enter the bridge from opposite edges, move across the bridge, and annihilate at the center. (This assumes that the bridge is symmetrical, and that H = 0.) The force equation given above is substituted into the viscous motion equation:

$$\frac{d}{d\tau}(x_k) = \frac{F_k}{\eta} \tag{43}$$

to obtain the vortex velocities, and thus the voltage across the bridge, as a function of the bias current. η is the viscosity of vortex flow.

The finite-voltage part of the $\bar{V}(I)$ curve has a vertical onset (i.e., $\frac{d\bar{V}}{dI} \to \infty$ as $\bar{V} \to 0$), followed by a region of decreasing differential resistance which reaches a minimum of:

$$R_{min} = 1.58 \left(\frac{2\Phi_o^2}{c^2 \eta W^2}\right) \equiv 1.58\ R_o \tag{44}$$

at a bias current of:

$$I = 1.40\ I_c. \tag{45}$$

Using the expression for η due to Bardeen and Stephen (1965)[5], one finds:

$$R_o \approx 25\ R_\square \left(\frac{\xi}{W}\right)^2 \tag{46}$$

and:

$$I_c R_{min} = 78.9\ (T_c - T)\left(\frac{\xi^2}{WL}\right) \quad \text{(in millivolts)}. \tag{47}$$

Thus, the theory predicts that the I_cR product is inversely proportional to both the bridge length and the bridge width. At large voltages, the predicted $\bar{V}(I)$ curve is parabolic:

$$\bar{V} = \frac{9}{16\pi}\ \frac{L}{W}\ \frac{R_o}{I_\infty}\ I^2. \tag{48}$$

The effect of a microwave field on the $\bar{V}(I)$ curve may be investigated by adding a sinusoidal ac component to the current bias. Likharev's computer calculations show that both harmonic and subhar-

---

[5] Likharev adds to this expression a term derived from time-dependent Ginzburg-Landau theory to obtain:

$$R_o \approx 10\ R_\square \left(\frac{\xi}{W}\right)^2.$$

monic steps appear, and that the step widths ΔI_n (see Fig. II-3) do not oscillate as a function of microwave amplitude.

The quantitative predictions of the Likharev theory must be viewed with some caution, due to the uncertain approximations made, both in the fundamental model and in the analytic procedure used to obtain the equation of vortex motion. For example, the model prohibits any penetration of vortex currents into the banks (probably correct if $\lambda_\perp >> \lambda_{bank}$), and the solution involves the truncation of an infinite series (probably correct for wide bridges, W >> L, at low voltages). Despite these difficulties, the theory makes some striking qualitative predictions:

(1) The critical current scales with temperature in the same way as the depairing prediction.

(2) The minimum differential resistance for $\bar{V} > 0$ is independent of the bridge length but decreases rapidly with increasing width.

(3) Subharmonic microwave steps should be present.

(4) Widths of microwave steps should be monotonically increasing functions of microwave amplitude.

II.C.2 Method of Conformal Mapping

Many of the difficulties encountered by Likharev (1972) were solved or avoided in a more recent calculation by Aslamazov and Larkin (1975). These authors investigated coherent vortex flow in uniform-thickness bridges (UTBs) consisting of two insulating cuts along the x-axis from +W/2 to +∞ and from -W/2 to -∞. Due to the geometry of the current flow, the results are easily generalized to UTBs of a hyperbolic outline. As before, depairing is neglected and the assumption $\vec{A} \approx 0$, appropriate for $W << \lambda_\perp$, is used to obtain Laplace's

equation for the superconducting phase. The equation is then solved by conformal mapping, which avoids the awkward series encountered when using the physically understandable image-charge method.

The solutions for $\phi(\vec{r})$ show that the current flow through the bridge is not uniform even in the absence of vortices. Rather, current flow is concentrated at the edges of the bridge, according to:

$$\vec{J}_S = \frac{2I}{\pi d} (W^2 - 4x^2)^{-1/2}. \tag{49}$$

This implies that the Lorentz force on a vortex due to its interaction with the transport current is:

$$F_k = - \frac{\hbar I}{e} S_k (W^2 - 4x_k^2)^{-1/2} . \tag{50}$$

The vortex-edge interaction force, derived by conformal mapping of the vortex states, is:

$$F_k = \frac{\pi\hbar}{2e} I_\infty \frac{8x_k}{W^2 - 4x_k^2} . \tag{51}$$

Thus, as $x \to \pm W/2$, the vortex-edge force diverges even more rapidly than the force due to the transport current, and there is an infinite barrier to vortex entry. The value of x at which the forces just balance is given by:

$$x_c = \frac{W}{2} \left(1 + \left(\frac{\pi I_\infty}{I} \right)^2 \right)^{-1/2} \tag{52}$$

This infinite barrier to vortex penetration is an intrinsic feature of models which ignore the vortex core, and occurs because the current density diverges at the center of an isolated vortex. In an actual superconducting vortex, the current density levels off and then decreases at radii less than about one coherence length, due to depairing. Unfortunately, the full Ginzburg-Landau equations are nonlinear and single-vortex solutions may not be superposed. Thus the

vortex-edge interaction is very difficult to evaluate for $|\frac{W}{2} - x| \lesssim \xi$, and the critical current due to vortex flow has not been solved exactly.

AL (1975) obtain a semi-quantitative result by assuming that vortices enter spontaneously when the classical turning point x_c comes within a distance $\xi/2$ of the edge. They find:

$$I_c = \pi I_\infty \frac{(1 - \xi/W)}{[(\xi/W)(2 - \xi/W)]^{1/2}} \approx \pi I_\infty \left(\frac{W}{2\xi}\right)^{1/2} \qquad (53)$$

The latter expression is correct when $W >> \xi$. Assuming viscous damping as before, the equation of vortex motion may be obtained without further approximation, but it is cumbersome and difficult to integrate.

For simplicity, AL (1975) restricted their calculation to the current range $(I - I_c) << I$. In this limit, vortex-vortex interactions are much weaker than the interaction with the transport current and may be neglected in computing the vortex velocity. The vortex-vortex interactions are retained, however, when the rate of vortex entry is computed.

When vortices are present in the bridge, there is a shift in the effective critical current for the entry of a further vortex, given by:

$$\Delta I_c(\tau) = \pi I_\infty \sum_m S_m \left(\frac{W + 2x_m(\tau)}{W - 2x_m(\tau)}\right)^{1/2} \qquad (54)$$

where $x_m(t)$ is the position of the m^{th} vortex at time τ. For periodic vortex motion, with vortices entering the bridge at $\tau = n\tau_o$, we find the condition:

$$I - I_c = \pi I_\infty \sum_m S_m \left(\frac{W + 2x_m(0)}{W - 2x_m(0)}\right)^{1/2} \qquad (55)$$

where

$$x_m(0) = x_o(m\tau_o) \equiv x_m \tag{56}$$

Using the equation of motion based on equations (43) and (50), the period τ_o is given by :

$$m\tau_o = \frac{\eta e W^2}{8\hbar I_c}\left[\frac{\pi}{2} - \arcsin\left(\frac{2x_m}{W}\right) - \frac{2x_m}{W}\left(1 - \left(\frac{2x_m}{W}\right)^2\right)^{1/2}\right] \tag{57}$$

Finally, we recall that the mean voltage $\bar{V}$ is inversely proportional to the period τ_o, obtaining the implicit $\bar{V}(I)$ relation:

$$I = I_c + \pi I_\infty \sum_m S_m \left(\frac{W + 2x_m}{W - 2x_m}\right)^{1/2} \tag{58a}$$

$$\bar{V} = V_o \frac{m\pi}{2}\left[\frac{\pi}{2} - \arcsin\left(\frac{2x_m}{W}\right) - \frac{2x_m}{W}\left(1 - \left(\frac{2x_m}{W}\right)^2\right)^{1/2}\right]^{-1} \tag{58b}$$

where:

$$V_o = \frac{8}{\pi^2} I_c R_o \tag{59}$$

AL (1975) solved this system for small numbers of vortices to compute the low-voltage portion of the $\bar{V}(I)$ curve.

As it is described above, this approximation predicts that $\bar{V} \to V_o \neq 0$ as $I \to I_c$, implying a discontinuous jump as the bias current passes through the critical value. This quirk is the result of neglecting edge interactions in the calculation of vortex velocity. If the equation of motion is integrated using the vortex-edge term alone, the voltage onset is predicted to follow:

$$\bar{V} \to 2I_\infty R_o \left(\ln\left(\frac{I - I_c}{I_\infty}\right)\right)^{-1} \tag{60}$$

as $I \to I_c$. Instead AL (1975) argued that the model as a whole is questionable in this region and suggested on qualitative grounds

that the dependence should be:

$$\bar{V} \propto (I - I_c)^{1/2} . \tag{61}$$

In either case, $d\bar{V}/dI$ is expected to diverge as $I \to I_c$.

The $\bar{V}(I)$ curve predicted by AL (1975) is sketched in Figure II-6. Just above the voltage onset, the curve is predicted to flatten out into a plateau of low differential resistance at about $\bar{V} = V_o$. Thus the minimum differential resistance should occur near this point, but the exact value of the minimum cannot be computed without an accurate treatment of the voltage-onset region. Beyond this voltage plateau, $d\bar{V}/dI$ rises smoothly until voltage $2V_o$ is reached, whereupon it drops discontinuously to a lower value, then starts to climb again. Such discontinuities in $d\bar{V}/dI$ appear at all the voltages nV_o. At each of these voltages, there is an increase in the number of vortices simultaneously present in the bridge, and extra terms must be included in equation (55). The discontinuities become small as n increases, however, and there is a nearly linear region characterized by:

$$\frac{d\bar{V}}{dI} = \frac{2}{\pi} \left(\frac{W}{2\xi} \right)^{1/2} R_o \tag{62}$$

When the bias current becomes very large ($I >> I_c$), both the rate of vortex entry <u>and</u> the vortex velocity will increase with current. Then voltage should increase according to a higher power of I. AL (1975) predicted:

$$\bar{V} = \frac{8}{\pi^3} \frac{R_o}{I_\infty} I^2 \tag{62.5}$$

for this regime.

In the region $I - I_c << I$, where the velocity is nearly independent of current, the microwave steps have a simple dependence on

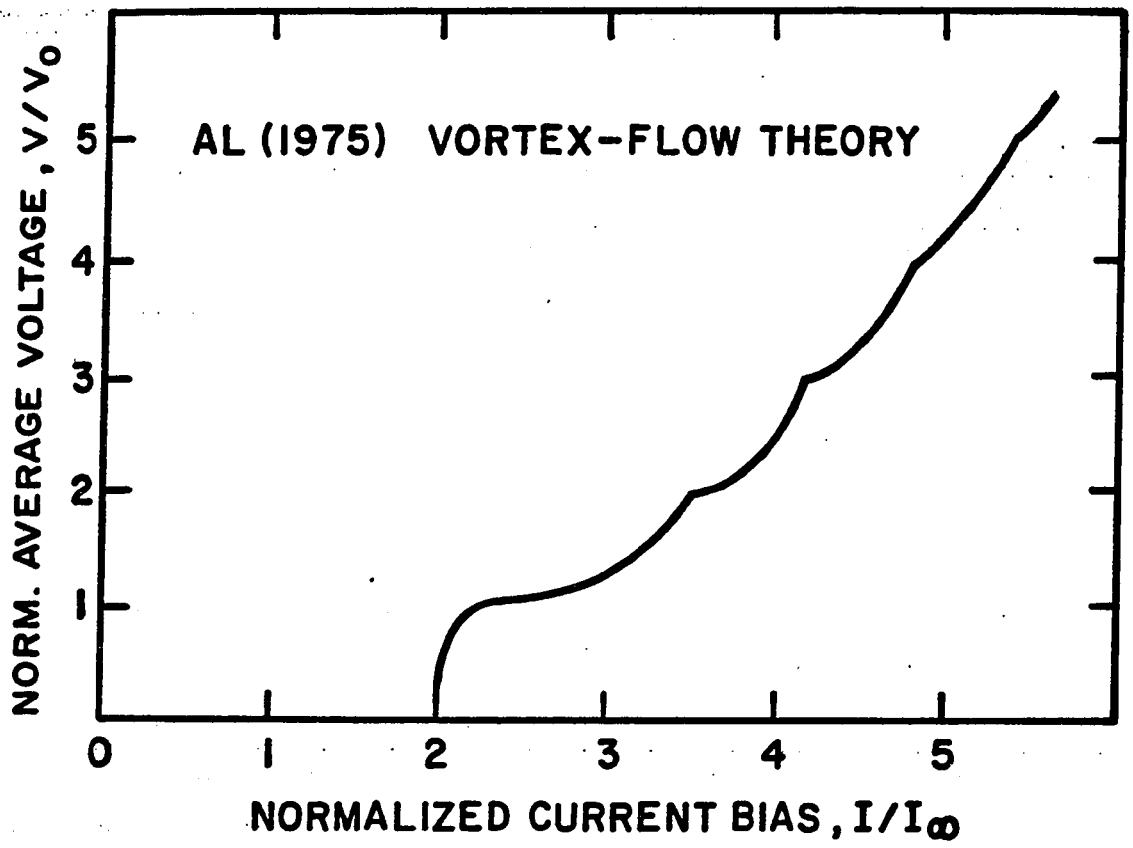

FIG. II-6. $\bar{V}(I)$ curve of a wide uniform-thickness microbridge, as predicted by the vortex-flow theory of Aslamazov and Larkin (1975). Note the discontinuities in $d\bar{V}/dI$ which appear at the periodic voltages $\bar{V} = nV_o$.

the amplitude of the microwave bias current $\tilde{I}$:

$$\Delta I_{step} = 2 \tilde{I} \quad . \tag{63}$$

As in the earlier vortex-flow calculation of Likharev (1972), the step width is found to be monotonic in the microwave amplitude.

The preceding results were derived for a bridge consisting of two insulating cuts in a superconducting plane, which corresponds to the limit $\theta_{max} \to \pi/2$ of a hyperbolic bridge. For a hyperbolic bridge of smaller θ_{max}, AL (1975) find that the results are unchanged except for the critical current. The critical current for a hyperbolic bridge is given by:

$$I_c = \pi I_\infty \left(\frac{W}{2\xi} \right)^{1/2} \quad \text{when} \quad \left(\frac{\pi}{2} - \theta_{max}\right) << \left(\frac{2\xi}{W}\right)^{1/2} \tag{64a}$$

$$I_c = \pi I_\infty \left(\frac{W}{2\xi}\right) \cos\left(\theta_{max}\right) \quad \text{when} \quad \left(\frac{\pi}{2} - \theta_{max}\right) >> \left(\frac{2\xi}{W}\right)^{1/2} \tag{64b}$$

II.D Applicability of Theories; Regimes of Microbridge Behavior

For the sake of computational simplicity, many calculations of microbridge behavior assume rigid boundary conditions. (See Likharev (1979).) That is, $|\psi|$ is equal to its equilibrium value and $\vec{\nabla}\phi = 0$ at all points in the banks. The validity of this rigid boundary assumption is strongly dependent on the geometry of the microbridge to which it is applied.

Rigid boundary conditions are poorly justified for all uniform-thickness microbridges. The two-dimensional spreading of the current leads to a phase shift which diverges as the logarithm of the measurement radius, and Mooij and Dekker (1978) have shown that the current-induced depairing also spreads well beyond the ends of the bridge in a UTB. Rigid boundary conditions are better justified for variable-

thickness microbridges. Assuming that the banks are thick enough to permit three-dimensional current spreading, the phase shift in the banks is finite. The three-dimensional current spreading also reduces the size of the depaired region, although both MD (1978) and Kulik and Omelyanchuk (1976) conclude that there is a depaired region of radius W/2 at the ends of a narrow cylindrical bridge. Rigid boundary conditions are probably best justified for structures which have both current concentration and a material barrier, such as long S-N-S bridges or clean-dirty-clean microbridges. These structures of non-uniform material are discussed briefly in section II.F.

The vortex-flow calculations and the uniform-depairing calculations treat complementary regimes of microbridge size. Therefore, microbridge dimensions, measured in terms of the characteristic superconducting lengths ξ and $\lambda_\perp$, can be used to classify bridges into different regimes of operation, as discussed by Likharev (1972), Klapwijk et. al. (1977a), and Likharev (1979). The details of the transition from uniform-depairing to vortex-flow behavior have not been fully elucidated, but fairly extensive calculations have been made under the assumption of rigid boundary conditions by Likharev (1972), Likharev and Yakobson (1976a), Kuprianov et. al. (1975), and Likharev (1976). The qualitative picture derived from this body of work is sketched in Fig. II-7. (It is assumed that the bridge thickness d is the smallest bridge dimension in the problem and that $\xi \ll \lambda_\perp$; both these conditions reflect the usual experimental situation.)

Microbridges whose widths are small compared to ξ are in the

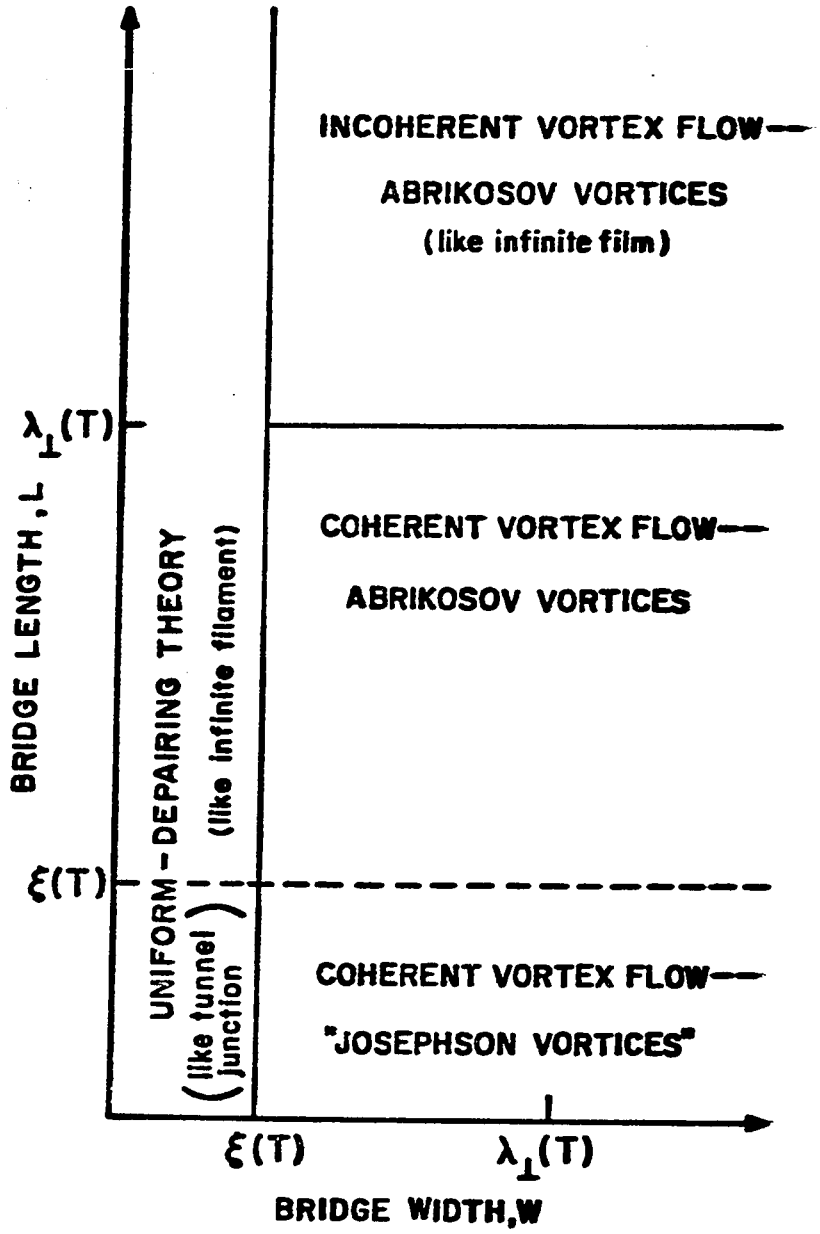

FIG. II-7. Regimes of microbridge behavior (modified from Likharev (1972), (1979)). The exact locations of the transition lines between regimes are known only for the problem with rigid boundary conditions. For rigid boundary conditions, Likharev (1979) gives $L_c = 3.5\xi(T)$ and $W_c = 4.5\xi(T)$ for the critical dimensions.

uniform-depairing regime. That is, $|\psi|$ must be uniform across the bridge cross-section because significant variations on such a small scale would lead to a large gradient term in the GL free energy. In physical terms, a vortex will not fit into the narrow bridge. For bridges in this uniform-depairing regime, the results of LY (1976a) apply. For bridges which are also short ($L << \xi$) as well as narrow, LY (1976a) predict that $I(\Delta\phi)$ is sinusoidal, with $I_c R$ equal to the tunnel junction result, eq. (18). This is the canonical microbridge behavior first predicted by Aslamazov and Larkin (1969). As the bridges are made longer, $I(\Delta\phi)$ becomes skewed and then multivalued (according to LY (1976a)), approaching the behavior of the infinite one-dimensional filament. As noted in section II.B.2, the dynamic state of short, narrow bridges is usually treated in terms of either the RSJ or the TDGL model. The dynamic behavior of long bridges, not studied in this work, is dominated by localized phase-slip centers, discussed by Kadin et. al. (1978).

Microbridges whose widths are large compared to ξ are in the vortex-flow regime. If the bridges are very long ($L >> \lambda_\perp$) as well as wide ($W >> \xi$), there can be many parallel channels of vortex flow, and the flow may not be coherent, especially when the inhomogeneities of real materials are considered. Incoherent vortex flow leads to simple pinning-dominated electrical response similar to that of an infinite two-dimensional film, which has been treated by Tinkham (1975). For bridges which are wide ($W >> \xi$) but moderately short ($L << \lambda_\perp$), coherent vortex flow in a single channel is expected to cause ac

response similar to the Josephson effect.[6]

Kuprianov et. al. (1975) further divide coherent vortex flow into a regime of Abrikosov vortices when $\xi << L << \lambda_\perp$ and a regime of "Josephson" vortices when $L << \xi$. The "Josephson" vortex does not have a nonsuperconducting core in the usual sense, so it should be much less susceptible to pinning, either at impurities or at surfaces. Likharev (1979) argues without detailed calculations that behavior of the "Josephson" vortex regime is similar to that of a wide tunnel junction. The existence of "Josephson"-type vortices in microbridges must be viewed with some skepticism, since detailed solutions for the pseudo-wave function around such a vortex have not been published, and since the phenomenon appears only in very short, very wide bridges for which the rigid boundary conditions are probably invalid.

The regime of Abrikosov vortices ($W >> \xi$, $\xi << L << \lambda_\perp$) is the subject of the two calculations (Likharev (1972) and Aslamazov and Larkin (1975)) discussed in section II.C. These calculations make the additional proviso that $W << \lambda_\perp$, to simplify electromagnetic interactions, so very thin films of type-II superconductors must be used in tests of the theoretical predictions. Among the soft superconductors, Pb alloys are a good choice, since Pb has a fairly large value of the Ginzburg-Landau parameter $\frac{\lambda}{\xi}$, which is increased by reducing the mean free path ℓ.

Since both ξ and $\lambda_\perp$ diverge as $T \to T_c$, all microbridges should

---

6 Unfortunately, the interpretation of the experiments is complicated by the fact that inhomogeneous films may show microwave steps even in the absence of boundaries. See Schmid and Hauger (1973) and Larkin and Ovchinnikov (1974).

be in the uniform-depairing regime over some temperature range near T_c. If the bridge width is larger than about $10\xi(0)$, however, this temperature range will be prohibitively small, so that noise, fluctuations, and material inhomogeneities will tend to smear out the microwave steps and distort the $I_c(T)$ curve. Therefore, practical measurements in the depairing regime require very small bridge dimensions.

Many authors, including Tinkham (1975), have related the Ginzburg-Landau coherence length $\xi_{GL}(t)$ and the GL penetration depth $\lambda_{GL}(t)$ to parameters of the microscopic theory. In terms of the BCS coherence length ξ_{BCS} and the London penetration depth $\lambda_L(t)$, the GL coherence length is:

$$\xi_{GL}(t) = 0.74\ \xi_{BCS}\ \frac{\lambda_L(t)}{\lambda_{GL}(t)}\ (1 - t)^{-1/2} \qquad (65)$$

when $(1-t) << 1$. The dependence of λ_{GL}/λ_L on ξ_{BCS} and ℓ is complicated and numerical methods are required to evaluate it exactly, but the limiting expressions for the clean ($\ell >> \xi_{BCS}$) and dirty ($\ell << \xi_{BCS}$) limits are simple. They are:

$$\lambda_{GL}(t) = \lambda_L(t) \qquad \ell >> \xi_{BCS}, (1-t) << 1 \qquad (66a)$$

$$\lambda_{GL}(t) = \left(0.75\ \frac{\xi_{BCS}}{\ell}\right)^{1/2} \lambda_L(t) \qquad \ell << \xi_{BCS}, (1-t) << 1. \qquad (66b)$$

These expressions lead to simple limits for the GL coherence length:

$$\xi_{GL}(t) = 0.74\ \xi_{BCS}(1-t)^{-1/2} \qquad \ell >> \xi_{BCS}, (1-t) << 1 \qquad (67a)$$

$$\xi_{GL}(t) = 0.855\ (\xi_{BCS}\ell)^{1/2}(1-t)^{-1/2} \qquad \ell << \xi_{BCS}, (1-t) << 1. \qquad (76b)$$

To bridge the gap between these limits, Tinkham (1975) has proposed

the interpolation formula (Tinkham's eq. (2-123b)):

$$\lambda_{GL}(t) = \lambda_L(t)\ \left(1 + 0.75\ \frac{\xi_{BCS}}{\ell}\right)^{1/2} \qquad (1-t)\ll 1 \qquad (68)$$

which implies:

$$\xi_{GL}(t) = 0.74\ \left(1 + 0.75\ \frac{\xi_{BCS}}{\ell}\right)^{-1/2} (1-t)^{-1/2}. \qquad (1-t)\ll 1 \qquad (69)$$

It should be noted that eqs. (68) and (69) are not exact results of microscopic theory, but simply reasonable interpolations between the known clean- and dirty-limit results.

For the cleanest material used in this study (a 3500-Å film of nominally pure In), $\ell/\xi_{BCS} = 0.56$ and the interpolation formula eq. (69) yields a GL coherence length which is 24% lower than the dirty-limit value given by eq. (67b). The uncertainty in ξ_{BCS} is about this large (see Toxen (1962)) and most of the materials used in this study are much dirtier than this In film, so we have used the dirty-limit formulas eqs. (66b) and (67b) for all interpretation of the experimental data.

II.E Joule Heating

All of the calculations discussed above share a fundamental assumption: the phonon and quasiparticle distributions are assumed to remain in equilibrium at the temperature of the banks (i.e. the bath temperature). In fact, this is unlikely as finite voltages lead to power dissipation in the bridge. A simple calculation shows that when our microbridge #S-9 (R = 8 Ω, L,W,d = 400 Å, 500 Å, 400 Å) is biased at 0.2 mA, it is dissipating about 4×10^9 Watt/cm^3. The power is transferred to the phonon system by inelastic scattering of electrons in a characteristic distance λ_Q, the quasiparticle diffusion length

(see Tinkham (1979)). To compute exactly the effects of power dissipation, one would have to solve the coupled Boltzmann equations for the quasiparticle and phonon distributions self-consistently with the superconducting gap equation. For microbridges, which involve both spatial and temporal relaxation, this tremendous task has not been attempted. Instead, one usually introduces the serviceable approximation of Joule heating to deal with the effects of the dissipated energy.

In the Joule heating approximation, it is assumed that the quasiparticles and phonons are in local equilibrium, but at a temperature $T(\vec{r})$ which is not spatially uniform. This temperature is computed from classical heat-flow calculations. Either the full distribution or some average value T_{eff} is substituted into the superconductivity equations to predict the $\bar{V}(I)$ curve or Josephson-effect behavior of the microbridge.

Skocpol, Beasley and Tinkham (1974) were the first to provide a thorough discussion of heating effects in uniform-thickness microbridges. In their model, dissipation leads to formation of a normal hotspot, a region centered around the bridge which is heated above T_c, and in which no supercurrent flows. Heat transfer through the film is characterized by the thermal conductivity κ, while heat transfer to the substrate is limited by the thermal boundary conductance α (see Little (1959)). A characteristic thermal healing length is defined:

$$\eta \equiv \left(\frac{\kappa d}{\alpha} \right)^{1/2} \tag{70}$$

where d, as always, is the bridge thickness. According to the model, power dissipation is confined to the hotspot region and follows the

normal-state law:

$$p = J^2\rho \ . \tag{71}$$

in that region. In this equation, p is the power dissipation per unit volume and J is the current density. The thermal diffusion equation is used to determine self-consistent values of the bridge current and hotspot diameter for both short ($L < \eta$) and long ($L > \eta$) bridges. One-dimensional solutions for distances $x \leq \frac{1}{2}(L + W/2)$ are matched to radial-flow solutions for $r \geq W/2$. The model should be most accurate when the normal hotspot is large, and indeed, SBT (1974) found excellent agreement between the $\bar{V}(I)$ curves obtained from this model and the high-voltage (i.e. $V > 0.2 - 0.5$ mV) part of the experimental curves obtained for Sn UTBs. One feature of particular interest is that the curves include a linear region at high voltage which extrapolates to a finite current at $V = 0$. Thus, Joule heating is a possible explanation for the "excess supercurrent" observed in many microbridges, at least at large voltages.

Joule heating can also lead to hysteresis in the $\bar{V}(I)$ curve of a microbridge when the critical current I_c exceeds the minimum current for hotspot formation I_h. In that case, the bridge remains at the bath temperature as the current is increased to I_c, but as soon as the bridge enters the finite-voltage state, dissipation leads to thermal runaway and the formation of a finite hotspot with a finite voltage across it. The hotspot is self-sustaining, and the bridge remains in the finite-voltage state until the current is reduced to $I_h < I_c$.

Hysteresis can also result from relatively slight heating which does not destroy the superconducting phase coherence. In that case, hysteresis occurs because the effective critical current in the heated

state is less than in the cold (i.e. $V = 0$) state. To investigate the effect of slight heating on a more general $\bar{V}(I)$ curve, we consider a simple model similar to that of Gubankov (1972). The bridge is assumed to be at an effective temperature T_{eff} related to the bath temperature by:

$$T_{eff} = T_B + \Delta T \tag{72}$$

where

$$\Delta T = R_{th}\, I\, \bar{V} \tag{73}$$

and R_{th} is the effective thermal resistance. This should be strictly applicable when the region of current-induced depairing is much smaller than the thermal healing length and $\Delta T << T_B$.

Let us extend Gubankov's model by assuming that the primary effect of changing temperature is a current-dependent translation along the current axis. Specifically:

$$\bar{V}(I) = V'(I - \frac{I_c}{I} \Delta I) \tag{74}$$

where $V'(I)$ represents the curve which would be observed in the absence of heating, and:

$$\Delta I = I_c(T_{eff}) - I_c(T_B) \tag{75}$$

is the difference between the effective critical current in the heated state and the actual critical current of the cold bridge. This expression for $\bar{V}(I)$ is accurate for the RSJ model when $\Delta T << T_B$. In this limit:

$$\Delta I \approx \frac{dI_c}{dT} R_{th} I\, \bar{V} << I_c \tag{76}$$

so the average voltage is:

$$\bar{V}(I) = V' \left(I - R_{th} I_c \left(\frac{dI_c}{dT}\right) \bar{V}\right) \tag{77}$$

and

$$R_D(\bar{V}) = R'_D(\bar{V}) \left[1 + R_{th}\left(\frac{dI_c}{dT}\right) I_c R'_D(\bar{V})\right]^{-1} \tag{78}$$

where $R_D = d\bar{V}/dI$ and $R'_D = dV'/dI$ are differential resistances. Although derived within the RST model, this calculation should be qualitatively correct for any similar $\bar{V}(I)$ curve. The above model demonstrates several features found to be characteristic of the experimental data:

(1) Heating does not generate new structure in the $\bar{V}(I)$ curves; rather it exaggerates existing peaks in R_D.

(2) Hysteresis (marked by infinite or negative R_D) does not appear until I_c becomes large, at low temperature.

(3) Hysteresis first appears wherever the dynamic resistance is highest, regardless of the voltage.

Hysteretic $\bar{V}(I)$ curves are generally considered undesirable in devices for practical SQUID and high-frequency applications, as excess noise and modelling difficulties may result. Heating-induced hysteresis may also be undesirable for digital computer elements, since switching times will be limited by thermal time constants. Biasing conditions are more complicated in hysteretic devices, and Taur et. al. (1974) have observed excess noise associated with hysteresis in point-contact mixers. Lee (1977) has observed excess noise associated with hysteresis in UTBs.

Even if hysteresis is not present, Joule heating may severely limit the Josephson performance of microbridges at high voltages and

frequencies. This limit can be seen in the experimental deviations from the RSJ theory for microwave-induced steps in the $\bar{V}(I)$ characteristic. The RSJ theory, the only theory for which step behavior has been computed in detail, predicts that steps, present at voltages $V = \frac{nhf}{2e}$, appear at increasing values at the integer n as the microwave amplitude is increased. Microbridge experiments, however, show that the number of steps increases only up to a finite microwave power. With further increases in power, the step widths decrease to zero. This reflects a loss of phase coherence caused by heating due to both dc and microwave bias currents. The voltage of the highest observable step, V_{max}, is the parameter most often used to quantify this high-voltage limit.

The model of SBT (1974) does not permit accurate calculation of V_{max}, but some simple scaling properties of UTBs are of interest. When the normal-state electrical resistivity of the device film is increased by alloying ($\rho \sim \ell^{-1}$), the thermal resistivity increases proportionately according to the Wiedemann-Franz law. Both the thermal healing length η and the coherence length ξ (in the dirty limit) decrease as $\ell^{1/2}$. If the bridge length and width are also decreased as $\ell^{1/2}$, so that scaling applies, the voltage limit V_{max} should be unchanged. Thus, alloy materials may be used to increase bridge resistance with no degradation of V_{max} only if L and W are reduced as $\rho^{-1/2}$. If bridge dimensions are held fixed, they appear larger in comparison with the characteristic lengths η and ξ, and V_{max} must decrease. Thus, for fixed microbridge dimensions, there is a trade-off between R and V_{max}: one decreases as the other increases.

One way to reduce the effects of Joule heating in microbridges is to use the variable-thickness geometry. Thicker banks provide three-dimensional cooling at the ends of the bridge, which reduces both the length of the heated region and the maximum temperature at its center. Tinkham, Octavio and Skocpol (1977) have described a heating theory appropriate to small three-dimensional constrictions. Most of their results are derived for the case L = 0, but the generalization to finite length is sketched at the end.

The authors investigate radial flow of current and heat through banks in the form of two intersecting, collinear cones. The temperature profiles derived from the heat-flow calculations are used to compute the effective critical current $I_c(P)$, as a function of the power dissipation P. $I_c(P)$ is a measure of the phase coherence across the bridge. It is argued that the power dissipation is approximately:

$$\frac{V_{rms}^2}{R} \approx \frac{3}{2} \frac{\bar{V}_{max}^2}{R} \tag{79}$$

when the device is biased on the highest observable step, and values of V_{max} are deduced. (The factor 3/2 arises from the substantial ac voltage, $V_{ac} \approx \bar{V}$, needed to generate a significant step.) A small-heating limit ($T_{max} - T_B \ll T_c - T_B$) and a large-heating limit ($T_{max} \gg T_c$) are distinguished.

In the small-heating limit, TOS (1977) use an effective-temperature model to find:

$$I_c(P) = I_c(P = 0)\ (1 - (1-t_B)^{-1/2}\ \frac{2P}{\Omega\kappa(T_B)\,\xi(0)T_c}) \tag{80}$$

where we have substituted the simpler Ginzburg-Landau temperature dependences in place of the two-fluid dependences used by TOS (1977). P is the power dissipation, $t_B \equiv \frac{T_B}{T_c}$ is the reduced temperature of the bath, Ω is the solid angle for cooling subtended by both banks, and κ is the thermal conductivity. One can obtain the same result from equations (73) and (75), using the AL (1969) result for $I_c(T_{eff})$ and:

$$R_{th}^{-1} = \Omega\kappa(T_B)\ \frac{\xi(t_B)}{2}\ . \tag{81}$$

For long bridges ($L >> \xi(0)$), phase coherence will be destroyed as soon as $T_{eff} \gtrsim T_c$, so V_{max} can be roughly estimated by:

$$\frac{3}{2}\ \frac{V_{max}^2}{R} = P_{max} = (1 - t_B)^{1/2}\ \kappa(t_B)\,\xi(0)T_c. \tag{82}$$

In the large-heating limit, there is a region in the center of the constriction which is heated well above T_c. The penetration of the pseudowave function through this region is computed via the WKB approximation. The effective critical current is given by:

$$I_c(P) = I_c(0)\ \exp\ (-2\ c^{banks} - 2c^{bridge}) \tag{83}$$

where the banks term is:

$$c^{banks} = \frac{3}{\sqrt{2}}\ \frac{r_1}{\xi(0)}\ (\frac{e\ V_{rms}}{\pi\ k\ T_c})^2\ (1 - t_B)^{-1/2} \equiv \frac{P}{2P_o} \tag{84}$$

and the bridge term is:

$$c^{bridge} \lesssim (\frac{\sqrt{3}}{2})^{1/2}\ \frac{L}{\xi(0)}\ (\frac{e\ V_{rms}}{\pi\kappa T_c})^{1/2}\ . \tag{85}$$

The dimensional parameter r_1 is roughly equal to W/2, but the exact relation depends on the shape of the microbridge to be compared with the model. The width of microwave steps scales with the effective critical current $I_c(P)$; in practice, V_{max} may be determined from the condition:

$$I_c(P_{max}) \approx 10^{-2} I_c(0). \tag{86}$$

Clearly, the term due to bank heating will always dominate in equation (83) as the voltage becomes arbitrarily large. In practice, the bridge term may be important when the bridge is long, especially in a clean-dirty-clean bridge (see section II.F). The figure of merit P_o is found to be essentially the same for the common elemental superconductors, so improvements in V_{max} are best attained by reductions in width which bring increased resistance.

Use of an alloy material to achieve a high bridge resistance will increase c^{banks} and reduce P_o. However, equation (84) has only a weak dependence on the electron mean free path, leading to:

$$V_{max} \propto P_o^{1/2} \propto \ell^{1/4} \tag{87}$$

Therefore, we have studied the use of alloys to achieve higher electrical resistances, suffering only a small decrease in V_{max}. It must be recalled, however, that the analysis of TOS (1977) assumes that $W, L \ll \xi(t)$, so fabrication limits on microbridge dimensions may become doubly important when alloys are used.

TOS (1977) assume that the temperature distribution is the same as if the whole contact were normal (i.e. nonsuperconducting) and dissipated power everywhere. In fact, at low power levels all of the power dissipation is confined to a region of dimension $\chi = \max\{\lambda_Q, \xi\}$.

Only when $(Wd)^{1/2} << X$ and $X << D$ will the model be accurate. Otherwise, the model will underestimate the temperatures in the bridge region, since the superconducting regions well away from the bridge contribute thermal resistance, but add no electrical resistance. To treat a general variable-thickness microbrdge, with banks of finite thickness, a composite model may be needed. In the dissipative region ($r \leq X$), the model of TOS (1977) would apply with new boundary conditions on $T(r)$. If $X < D$, the intermediate region ($X < r < D$) would involve three-dimensional heat flow without dissipation. Farther out the bank region ($r > \max\{X,D\}$), two-dimensional heat flow and surface heat transfer would be treated as in SBT (1974).

II.F Bridges of Non-Uniform or Clean Materials

So far, we have limited our discussion to microbridges of a single, uniform material in the dirty limit. However, bridges which have different material parameters in the bridge region than they have in the banks can provide an extra degree of design flexibility, usually at the cost of greater complexity in the fabrication process. For example, Likharev and Yakobson (1976a) have shown that a bridge with a normal-metal center (a Super-Normal-Super or SNS bridge) will have a nearly sinusoidal $I(\Delta\phi)$ relation for any bridge length, and several studies of such SNS bridges have recently been performed (e.g. Van Dover et. al. (1979) and Warlaumont et. al. (1979)). Although they have sinusoidal $I(\Delta\phi)$ relations, long SNS bridges have smaller I_cR products than fully superconducting bridges, which reduces the attractiveness of SNS bridges for high-frequency applications.

A fully superconducting structure which promises to overcome many of the practical problems associated with uniform-material microbridges is the clean-dirty-clean ($S_cS_dS_c$) microbridge. In this struc-

ture, the bridge region is composed of a superconductor whose mean free path ℓ_{bridge} is much less than ℓ_{bank}, the mean free path in the (superconducting) banks. For simplicity, we consider the case where the critical temperature T_c, the BCS coherence length ξ_{BCS}, and the London penetration depth λ_L are the same in the bridge as they are in the banks. The GL coherence length ξ_{GL} and penetration depth λ_{GL}, which depend on ℓ, are different. Obviously, such a $S_cS_dS_c$ bridge is not very different from a conventional uniform-material bridge, yet it can have substantially improved properties.

One desirable feature of the $S_cS_dS_c$ bridge is that the dirty bridge provides a material barrier which improves the accuracy of the convenient and well-studied rigid boundary conditions. For elemental superconductors such as Al ($\xi_{BCS} \approx 10{,}000$ Å) and In ($\xi_{BCS} \approx 2600$ Å), it is often possible to describe both the bridge and the banks by the dirty-limit GL theory , even when $\ell_{bank} \approx 10\ell_{bridge}$. Within this dirty limit, the rigid-boundary microbridge theory predicts that the bridge critical current will decrease in proportion to the mean free path in the bridge region:

$$I_c \propto (R_{bridge})^{-1} \propto \ell_{bridge}. \tag{88}$$

Thus, if ℓ_{bridge} is decreased while ℓ_{bank} remains unchanged, currents in the banks ($\approx I_c$) will be reduced, so that phase gradients and depairing in the banks will also be reduced and the rigid boundary conditions will provide a more exact description of microbridge behavior.[7]

---

[7] From the preceding discussion, it may appear that only the <u>self-consistency</u> of the rigid boundary conditions has been improved. Actually, the bulk critical current (eq. (11)), which represents the opposite limit in boundary conditions, also decreases with ℓ ($I_c^{(fil)} \propto \ell^{1/2}$), so the reduced bank depairing and phase gradients obtained with a clean-dirty-clean bridge are quite real.

The clean-dirty-clean bridge also suffers less Joule heating than a uniform-material bridge. As demonstrated by the experimental results of chapters IV and VI, this is a very important factor in both fundamental studies and practical applications of microbridges. In the dirty-limit, rigid-boundary theory, the characteristic power dissipation $I_c^2 R$ will be proportional to ℓ_{bridge}. The thermal resistance, on the other hand, will be dominated by bank parameters, at least for short bridges or large heating. (See section II.E.) Thus, a decrease in ℓ_{bridge}, with ℓ_{bank} held fixed, yields a reduction in the temperature rise at the center of the bridge, leading to improvements in $\Delta T_{no\ hyst}$ and V_{max}.

Since the devices are predicted to improve as the bridge weakness parameter $\gamma \equiv (\ell_{bank}/\ell_{bridge})$ is increased, one may ask how large γ can be made in practice. Usually, the minimum acceptable value of ℓ_{bridge} will be determined by lithographic constraints on the bridge size. Within the rigid-boundary model (for $\ell_{bridge} << \xi_{BCS}$), good performance demands that the bridge length be no more than a few times the GL coherence length in the bridge $\xi_{GL}^{(bridge)}$, which decreases as $(\ell_{bridge})^{1/2}$. Thus a minimum bridge dimension implies a minimum coherence length which in turn implies a minimum ℓ_{bridge}. Consider the concrete example of an In bridge with $\xi_{BCS} = 2600$ Å and $L = 5000$ Å. If $\ell_{bridge} = 25$ Å, then:

$$\xi_{GL}^{(bridge)} = \frac{218\ \text{Å}}{(1-t)^{1/2}} \qquad (89)$$

and the temperature range in which the $I(\Delta\phi)$ relation is single-valued[8]

---

[8] See Likharev and Yakobson (1976a), who show that $I(\Delta\phi)$ is single-valued only for $L \leq 3.5\ \xi_{GL}(T)$.

is only 0.08 K. To obtain a single-valued $I(\Delta\phi)$ relation for the full temperature range down to T = 0, ℓ_{bridge} must be increased to 1100 Å. On the other hand, if it is possible to fabricate a bridge with L = 500 Å, ℓ_{bridge} = 25 Å will yield a single-valued $I(\Delta\phi)$ relation even down to T = 0.[9]

When fabrication limits set a minimum on ℓ_{bridge}, it may be desirable to use the maximum possible ℓ_{bank}. Unfortunately, several complications arise when one tries to extend calculations of microbridge behavior to the clean limit. Even the nomenclature is complicated: a bridge of dirty material ($\ell << \xi_{BCS}$) may be in what Likharev (1979) calls the clean bridge limit if L, W << ℓ. In this work, we will try to be explicit about the relations between ℓ, ξ_{BCS}, and L or W in any case other than the conventional dirty limit ($\ell << \xi_{BCS}$, L).

Consider first the case of a small clean bridge of uniform material (L, W << ξ_{BCS}). If the material is in the clean limit ($\ell >> \xi_{BCS}$), the GL theory, workhorse of microbridge calculations, must be applied with caution. The GL theory is founded on <u>local</u> electrodynamics, so the formulas derived for clean materials (see, for example, Tinkham (1975)) apply only when $\xi_{GL}(t) >> \xi_{BCS}$. This implies applicability over a narrower temperature range than for the dirty-material case ($\ell << \xi_{BCS}$). Whether $\ell >> \xi_{BCS}$ or vice versa, severe complications arise when the bridge width W is less than the mean free path ℓ_o characteristic of the bank material, because increased boundary scattering in the bridge region makes the effective mean free

---

[9] The GL result that the critical length is 3.49 $\xi_{GL}^{(bridge)}$ is strictly accurate only near T_c, but the conclusion is roughly correct even at lower temperatures.

path a function of position. In the normal state, this implies a position-dependent resistivity. In the superconducting state, boundary scattering implies a position-dependent coherence length and superfluid density. As noted by Mooij and Dekker (1978), position dependence in ξ_{GL} requires that an additional term, proportional to $\vec{\nabla}\xi_{GL}$, be added to the GL equation. MD (1978) derived this term from the boundary conditions of Zaitsev (1966) and made numerical calculations for narrow bridges with values of ℓ_o/W in the range 0 to 10. Perhaps surprisingly, they found that the increase in the normal-state resistance exactly balances the decrease in I_c caused by boundary scattering, so that the I_cR product remains constant. That is, the I_cR product is exactly the same for small clean bridges as it is for small dirty bridges. Kulik and Omelyanchuk (1978) have used the more general equations of Eilenberger (1968) to compute the critical current and $I(\Delta\phi)$ relation of small, clean ($W, L << \ell_o, \xi_{BCS}$) bridges at arbitrary temperatures. They, too, find that I_cR (near T_c) equals the dirty-limit result of Aslamazov and Larkin (1969) regardless of the relation between ℓ_o and ξ_{BCS}.

From consideration of the position-dependent mean free path, it is clear that a bridge of uniform material will act like a clean-dirty-clean bridge whenever $W, d << \ell_o$. This means that the advantage of reduced Joule heating can be obtained without the complication of using two separate materials. Still, it should be noted that the two-material $S_cS_dS_c$ bridge can potentially have a sharp boundary between the clean and dirty regions and that the bridge width and thickness need not be as small as in the boundary-scattering dominated bridge.

CHAPTER III. EXPERIMENTAL PROCEDURE

III.A Measurement Techniques

III.A.1 Electrical Measurements

All electrical measurements of microbridges were made in a variable-temperature cryostat designed by Dr. D. E. Prober. Figure III-1 is a schematic diagram of this cryostat. The sample is mounted on a machined copper bar which serves as the controlled-temperature stage. A nylon spacer supports the stage in vacuum and limited thermal contact with the liquid helium bath is provided by the twenty electrical leads of #40 copper wire, plus a thermal link of 0.125-mm copper foil. Current passed through a 1.5-kΩ metal-film resistor embedded in the stage heats the stage to the desired temperature. Thermal response time is a few seconds or less at temperatures below 15 K. Temperature drift is typically less than 10^{-4} K/min, so automatic temperature stabilization is not required. Temperatures down to $\approx$ 4.5 K are achieved with the helium bath at atmospheric pressure. When lower temperatures are needed, a Walker-type regulator (Walker (1959)) is used to control the helium vapor pressure.

The sample temperature is monitored with a Cryo-Resistor[1] germanium resistance thermometer set into the copper stage near the sample. The electrical leads, which carry heat down from room temperature, are carefully heat-sunk on the upper (bath-temperature) copper bar, so that essentially none of the heat reaches the controlled-temperature stage. In any case, the large thermal conductance of the controlled-temperature stage effectively prohibits significant temperature gradi-

[1] Cryo-Cal, Inc., Minneapolis, Minn.

FIG. III-1 Schematic diagram of cryostat probe. For clarity, the parallel-wire sample microwave coil has been rotated 90° and the heater and thermometer leads have been omitted. All leads, including those connected to the heater and thermometer, are heat sunk twice, in multiple-loop coils held down with G.E. 7031 varnish.

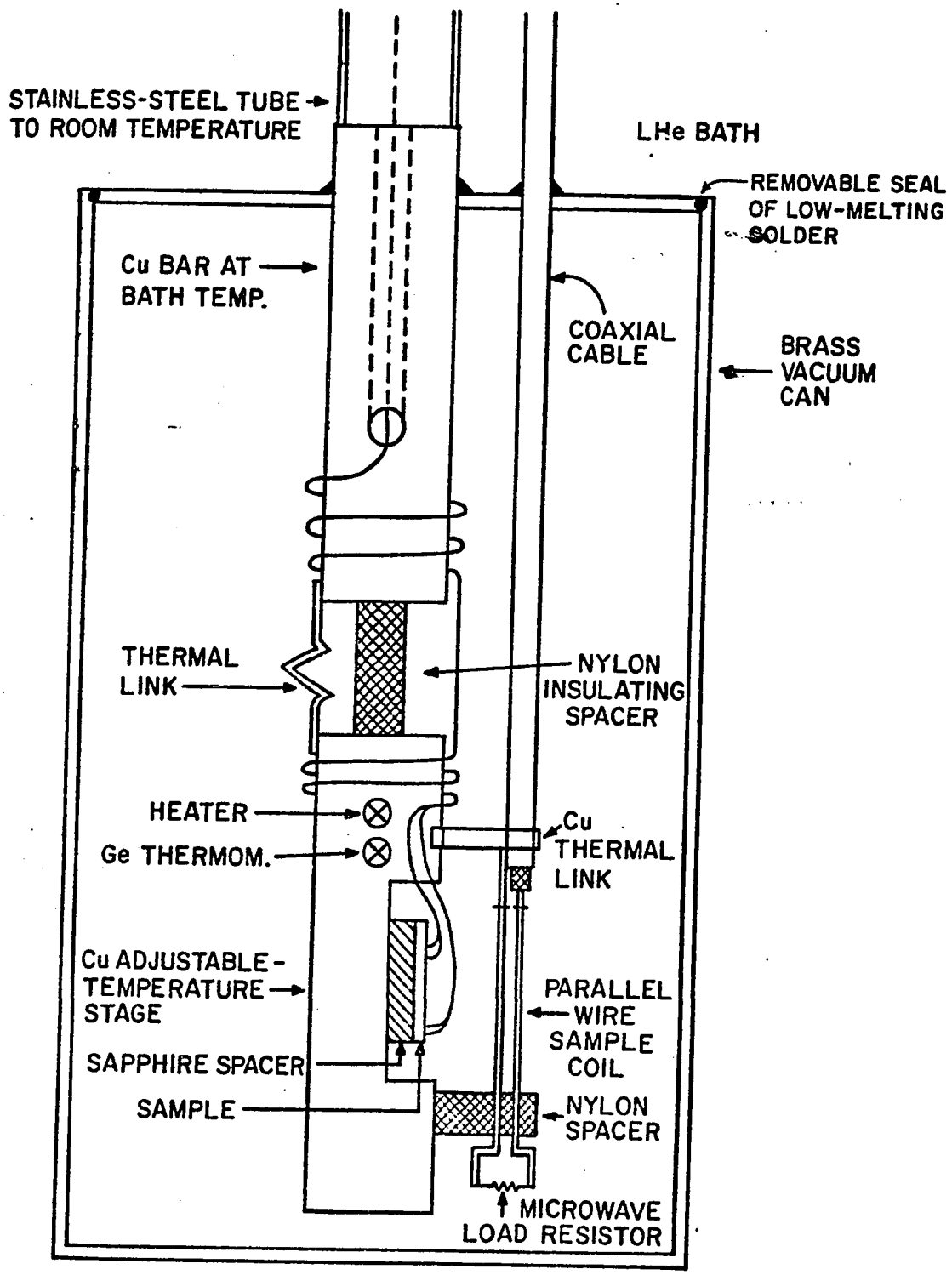
STAINLESS-STEEL TUBE TO ROOM TEMPERATURE
LHe BATH
REMOVABLE SEAL OF LOW-MELTING SOLDER
Cu BAR AT BATH TEMP.
COAXIAL CABLE
BRASS VACUUM CAN
THERMAL LINK
NYLON INSULATING SPACER
HEATER
Ge THERMOM.
Cu THERMAL LINK
Cu ADJUSTABLE-TEMPERATURE STAGE
PARALLEL WIRE SAMPLE COIL
SAPPHIRE SPACER
SAMPLE
NYLON SPACER
MICROWAVE LOAD RESISTOR

ents across it. The thermometer is calibrated to an accuracy of ± 10 mK from 4.5 K to 15 K and its reproducibility should be ± 1 mK. Since not all of the measurements were made using the same thermometer, the larger margin of error should be used in comparing data for different bridges. Cross-calibration of different thermometers confirmed the specified accuracy, and an external check was provided by the T_c of pure In films. This was measured to be within 15 mK of the value for bulk In, which is 3.405 K.

Figure III-2 illustrates the apparatus for $\bar{V}(I)$ measurements. Several kinds of electromagnetic shielding are incorporated into the measurement apparatus to reduce the effects of noise. The sample is enclosed within the brass vacuum can and the leads run up to room temperature within the evacuated stainless-steel support tube, providing isolation from electric fields and high-frequency radiation. The "lid" of this shielded can is formed by a set of monolithic RFI filters[2] inserted into the signal leads. These filters have a cutoff frequency of 5 MHz and provide 80 db of isolation at high frequencies. All cables are shielded and carefully grounded to eliminate 60-Hz pickup. With the setup shown in Figure III-2, the 60-Hz pickup on a 2.5 Ω bridge was measured to be ≲ 30 nV. Low-frequency magnetic shielding is provided by two concentric cylinders of mu-metal which surround the Dewars. A Pb can was available as a superconducting shield, but it was found to be unnecessary for ordinary measurements. This is not surprising since the extremely small dimensions of the devices make them insensitive to static magnetic fields.

---

[2] Part #1212-502, Erie Technological Products, Erie, Pa.

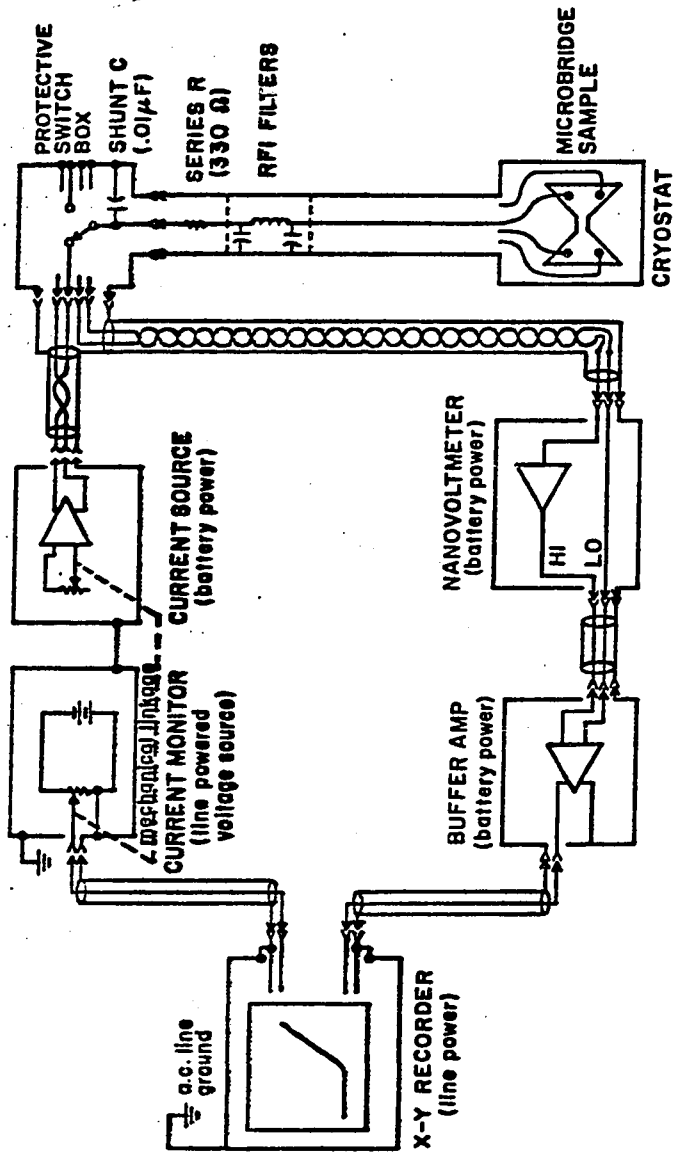

FIG. III-2 Block diagram of $\bar{V}(I)$ measurement apparatus, including shielding. All connections to the microbridge sample are floating and shielded. For $\frac{d\bar{V}}{dI}$ vs. $\bar{V}$ measurements, a lock-in amplifier and a battery-powered, direct-coupled amplifier, in parallel, replace the nanovoltmeter and the buffer amplifier is omitted. Protection from burnout is discussed in detail in the text. The X-Y recorder is Hewlett-Packard type 7047A with common driver input, which does not require a separate guard connection, and we found that connection of the cable shields to the power line ground at the recorder was optional.

All bridge measurements are made under conditions of current bias, provided by the active current source of Figure III-3. The current driver is battery-powered and electrically isolated from the current monitor circuit. The current adjust potentiometer is mechanically coupled by an O-ring pulley to an identical potentiometer which controls the monitor signal. This scheme was suggested by the work of Henkels (1974). In this way, problems due to ground loops, interference carried along the ac power lines, and transients generated by the X-Y recorder are not coupled through the current source to the microbridge. The wire-wound potentiometers which have been used offer low noise and excellent linearity (0.1%), but their intrinsically discrete nature limits resolution to $\gtrsim 10^{-4}$ of full-scale. Conductive-plastic pots could be used to remove this inconvenience. The noise of the current source was measured to be about 1 nA/$(\text{Hz})^{\frac{1}{2}}$, and its output shunt impedance is greater than 10^8 Ω. The transformer-isolated modulation input allows superimposition of small ac currents for $d\bar{V}/dI$ measurements using a lock-in amplifier.

All voltage measurements were made using the four-terminal method to exclude the effects of lead and contact resistance[3]. A battery-powered, chopper-stabilized nanovoltmeter[4] was used for most dc voltage measurements. Due to its 94-Hz chopper frequency, the nanovoltmeter showed a conspicuous 8-Hz component when 60-Hz pickup was present at the sample. This proved to be a convenient check for improper grounding

---

[3] Four separate contacts to the sample were made, but the resistance of the thin-film banks was still common to both voltage and current leads.

[4] Model 147, Keithley Instruments, Inc., Cleveland, Ohio.

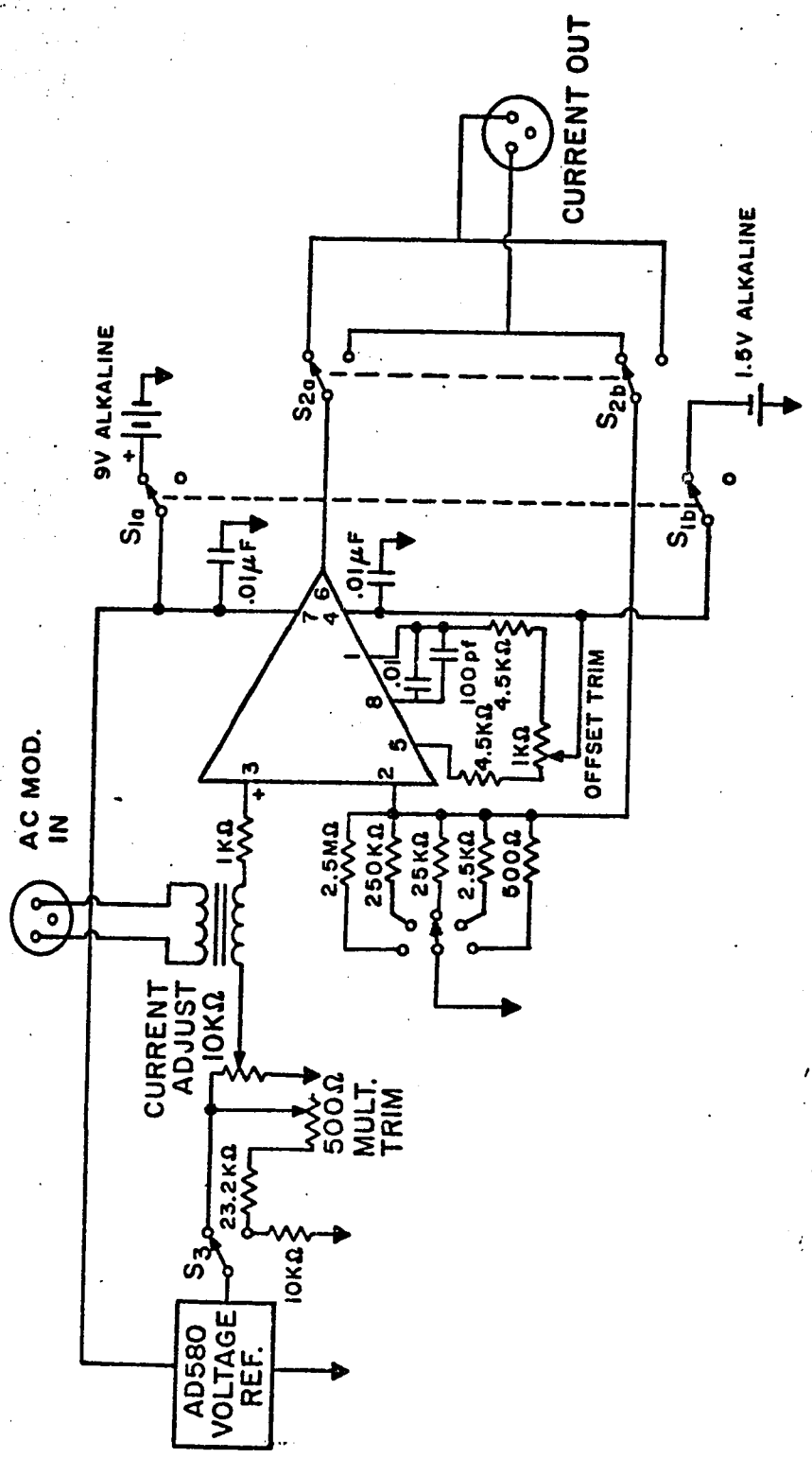

FIG. III-3 Current source for microbridge experiments. Switches S_1, S_2, S_3, and S_4 are the on-off, polarity reverse, range multiplier and current range controls, respectively. Maximum current output is 5 mA. Modulation input transformer is Triad G-101, connected for 17:1 voltage step-down. All resistors are 1% metal-film types, and current-range resistors are selected to within 0.05%.

or broken cable shields. Since the nanovoltmeter was found to present a non-linear input impedance at low ac frequencies, it was not used in measurements of $d\bar{V}/dI$ vs. $\bar{V}$. Instead, it was replaced by a battery-powered, low-noise, direct-coupled preamplifier[5]. Comparison between curves taken with the nanovoltmeter and the direct-coupled amplifiers confirmed that all were accurate to within 2%, though the nanovoltmeter was slightly quieter.

Differential resistance ($d\bar{V}/dI$) measurements were made using a lock-in amplifier[6] operating at a frequency of 224 Hz. With an ac current bias of 0.4 μA, the typical system noise level was equivalent to 0.2 Ω_{p-p}. Larger ac currents yielded more precise values of $d\bar{V}/dI$ at the cost of broadening any sharp peaks.

The time-averaged $\bar{V}(I)$ characteristics of the bridges were also studied in the presence of microwave radiation. Although various microwave sources were tested at least once, a Hewlett-Packard Model 686A backward-wave oscillator was used for most of the X-band measurements (9-12 GHz). Its maximum output power was 10 mW. A 100-mW Gunn-diode oscillator[7] was used for experiments at 25 GHz.

The microwave signal was transmitted down the cryostat via 0.141-inch (3.59-mm) semi-rigid coaxial cable. This coaxial cable remains single-mode up to 30.4 GHz, but there is some attenuation even at

---

5 Model 113, Princeton Applied Research Corp., Princeton, N.J. or the homemade amplifier shown in Fig. III-4.

6 Model 126, with Model 117 preamplifier, Princeton Applied Research Corp., Princeton, N.J.

7 Model CMF-620 AH, Central Microwave Co., St. Charles, Mo.

lower frequencies: the attenuation is 3.0 db/m at 25 GHz. The coaxial cable presented a special problem in thermal design, since the inner conductor could not be heat-sunk in the usual way. The heat leak from room temperature was minimized by choosing a cable with a copper-clad steel core, instead of solid copper, but it was still necessary to keep the sample microwave coupling coil thermally isolated from the temperature stage. When the microwave coil came in physical contact with the dc sample leads, the sample was raised as much as 50 mK above the stage temperature.

The microwave coupling coil was made in the form of a parallel-wire transmission line terminated by a 50-Ω metal-film resistor[8]. Two 0.64-mm-diameter copper wires, separated by 5.0 mm and spaced 2.5 mm above the sample stage, made up a line whose nominal characteristic impedance in vacuum above the copper stage was 145 Ω (see Marchand (1947), p. 17). The copper sample stage acts as a ground plane to suppress tangential fields, so bridges on thin substrates were separated from the stage by a 0.635-mm sapphire spacer plate. The bridge pattern was oriented perpendicular to the direction of propagation to maximize the electric field across the bridge.

The broadband microwave system described above provided satisfactory coupling of microwave power to the bridges at frequencies from 4 to 25 GHz. However, it did not provide accurately calculable source impedance, which might have been helpful in studying the asymmetry behavior discussed in section VI.D.

---

[8] This naive termination is clearly not optimized, but it proved satisfactory.

III.A.2 Protection from Burnout

Due to the strong current concentration and small volume involved, all microbridges are susceptible to electrical burnout. This is not a subtle electronic effect, but a gross melting and evaporation, as vividly demonstrated by Figure III-4. Proper electrical isolation and shielding of the measurement apparatus fulfills a dual role, protecting the bridges against burnout as well as reducing noise. After some early bridges were destroyed, several protective features were incorporated into the circuitry:

(1) Series resistors (330 Ω) and shunt capacitors (0.01 μF) were inserted into the signal leads to smooth out any moderate-to-high-frequency transients. Even at room temperature, these resistors contributed a negligible amount of noise, so it was not necessary to mount them in the liquid helium bath.

(2) A shielded switch box was mounted directly at the top of the cryostat. In the "safe" position, all sample leads were disconnected from the measurement circuitry and shorted to the cryostat body. This permitted adjustments to be made on the measurement circuitry without danger to the sample.

(3) When the output of the nanovoltmeter was used to drive an X-Y recorder, a battery-powered differential amplifier was inserted between them. This was necessary because the low terminal of the nanovoltmeter output is directly connected to the low terminal of its input, which is directly connected (through 330 Ω) to the microbridge. This direct connection could provide a propagation path for destructive transients. The schematic diagram of this differential-input, single-ended output, buffer amplifier is shown

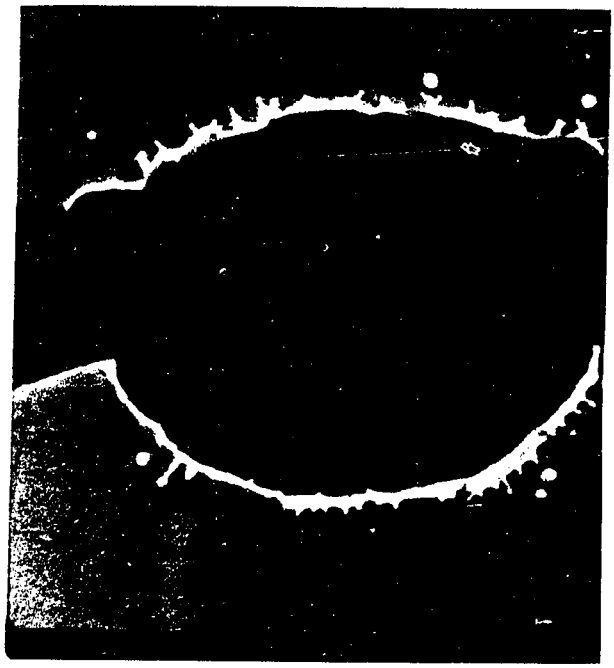

FIG. III-4 Burned-out microbridge. This bridge, #I-5, was apparently burned out by the induction fields of a microscope illuminator transformer. The large diameter of the "blast crater" is apparently due to the thin (250 Å) film. Burnout of a variable-thickness bridge is much less conspicuous because the thick banks reduce the size of the "blast crater".

in Figure III-5.

With these precautions in use, no bridges were burned out by transients during electrical measurements. One bridge of very high resistance, number S-10, was apparently damaged by a severe overload of microwave power.

Processing, handling, and mounting the bridges also required some care to avoid static charge buildup and ac magnetic fields. In particular, the induction fields of soldering irons and power transformers were implicated as troublesome. The bridges were fabricated with integral short circuits which were not removed until the bridges were safely mounted on the cryostat and connected to external short circuits. Cryostat leads were fastened to the substrate with $Sn_{0.5}In_{0.5}$ solder, then final connections to the thin films were made with silver paint. During the mounting procedure, the experimenter and the soldering iron were grounded to the cryostat and the preheated iron was unplugged before use. Candles were burned to produce free ions (M. Octavio, private communication), but a humid day was found to be a better guarantee against static charge buildup. Before the bridges were demounted, they were short-circuited with a drop of silver paint or a bit of indium. When all these procedures were followed, no bridges were burned out during the mounting process.

III.A.3 Scanning-Electron Microscopy

Scanning-electron microscopy was used extensively to investigate fine structure of bridges, metal films, and photoresist patterns. SEM photographs were the primary method of determining the precise dimensions of these submicron microbridges. The microscope used most frequently was an ETEC Autoscan, operated at 10 or 20 kV with a

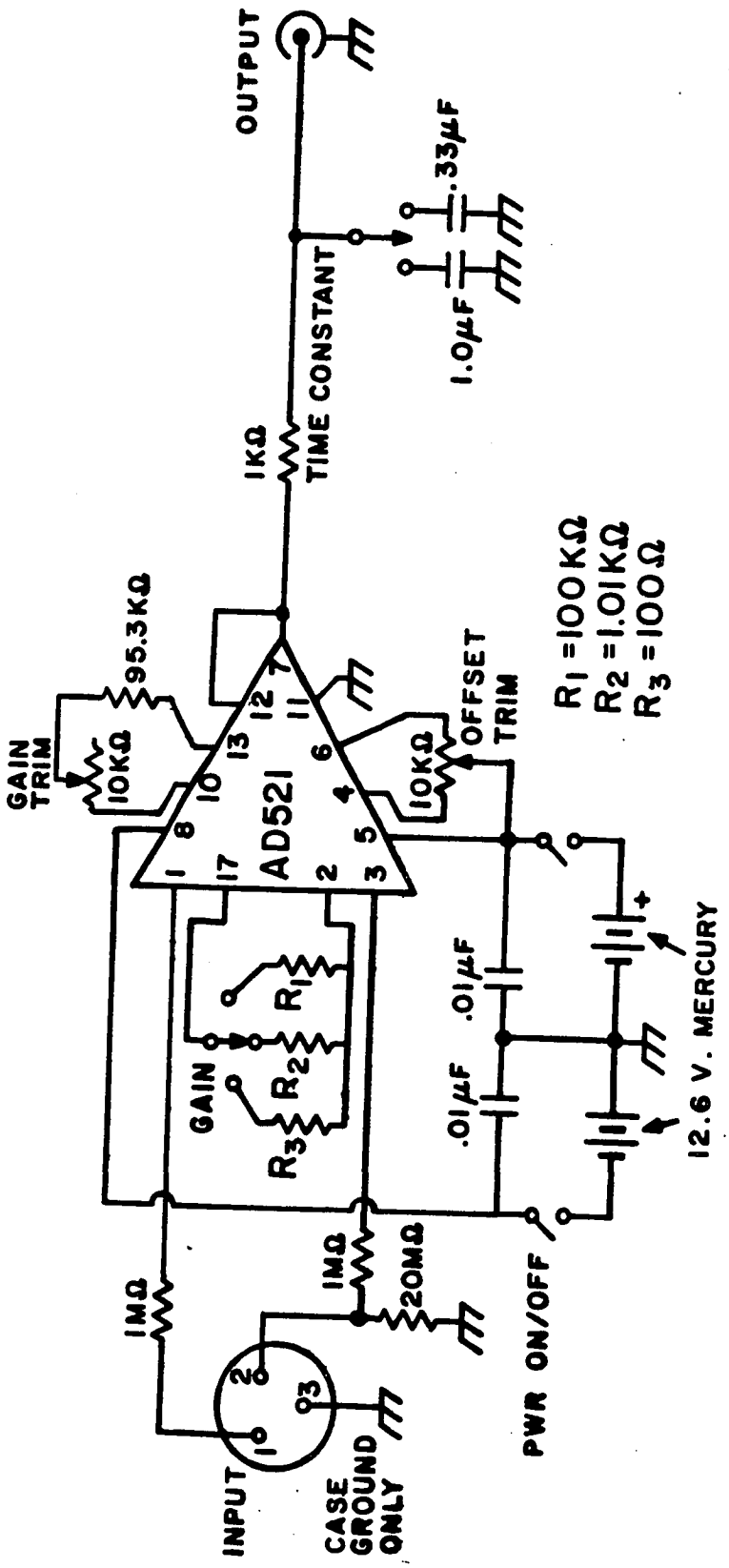

FIG. III-5 Differential-input buffer amplifier. Gain-controlling resistors R_1, R_2, R_3 are selected to within 0.5%. The 20-MΩ current-drain resistor is essential to prevent common-mode overload.

100-μm aperture. Under these conditions, we resolved features as small as 400 Å. For some extra-high-resolution work, a JEOL Model JFSM microscope with a field-emission source was used. The potentially high resolution of this microscope was apparently limited by backscattering from the Pb-alloy films, however. Samples were sputter-coated with a thin layer (typically 40 Å nominal thickness) of $Au_{0.6}Pd_{0.4}$ alloy to prevent charging in the insulating regions. The shunt resistance of this Au-Pd film, measured across an incomplete bridge pattern, was greater than 10^5 Ω, so electron microscopy did not preclude subsequent low-temperature study of the bridges. Electron microscopy of photoresist patterns did preclude subsequent liftoff processing, however, because electron bombardment during either the sputter-coating or the imaging process made the photoresist insoluble in ordinary solvents.

III.B Fabrication Techniques--UTBs

III.B.1 Outline of UTB Fabrication

In order to study high-resistance uniform-thickness microbridges, we first had to develop suitable fabrication processes. Photolithography was chosen over scribing processes (cf. Chiao (1974)) because it could produce sharply-defined, reproducible device geometries. Since sub-micron dimensions ($d \lesssim \xi(T)$) were required, we adopted a microscope projection system using commercial diffraction-limited optics. The liftoff process was chosen for pattern transfer because of its high-resolution capability. There is no chance of overetching, which can occur during wet-chemical processing, and the edge

roughness of the device can be less than 500 Å.[9] A unique feature of this work is through-the-substrate projection exposure, which provides good liftoff yield even for bridges less than 0.5 μm wide.

Although PR liftoff works well with soft superconductors, conventional PR cannot be heated to high ($\gtrsim$ 200 C) temperatures, so our process is not compatible with the heated-substrate deposition required for some high-T_c superconductors such as Nb_3Sn. (See, for example, Hammond (1975) and Beasley (1978).) In addition, successful liftoff by our process is limited to films which are thinner than the PR thickness. Therefore, if device films are to be thicker than 0.2 μm, resolution may be somewhat poorer than that achieved in this work, due to the need for thicker PR.

The materials used for this study were the type-II alloys $Pb_{0.7}Bi_{0.3}$ and $Pb_{0.9}In_{0.1}$. They were chosen for their moderately high resistivities, and because evaporated thin films of these materials show electronic and superconducting properties matching those of bulk materials.

Three examples of our uniform-thickness microbridges are shown in Figure III-6. The mask geometry was a truncated triangular form, but finite resolution of the optical system transformed this to a nearly hyperbolic shape in the narrowest bridges.

---

[9] The intrinsic edge roughness of 1350-type PR may be as small as 50-100 Å, based on results obtained by White and Flanders (1980) in fabrication of fine lines on etched edges defined by photolithography. In our own work on fine lines (Prober and Feuer (1980)), we have observed edge roughness $\leq$ 200 Å. The edge roughness of the metal-film pattern also depends on metallurgical considerations, as discussed in chapter V.

FIG. III-6 Three uniform-thickness microbridges. These scanning-electron micrographs were taken with the electron beam perpendicular to the substrate (i.e. angle of incidence = 90°). Counter-clockwise from the upper left, the widths of the bridges shown are 1.0 μm, 0.45 μm (bridge #I-2) and 0.20 μm (bridge #I-7). Polishing marks are clearly visible in the photo of the 1-μm bridge; the other two bridges are on cover-glass substrates. Note rounded shape of the bridge region, due to limited resolution of the optical projection system.

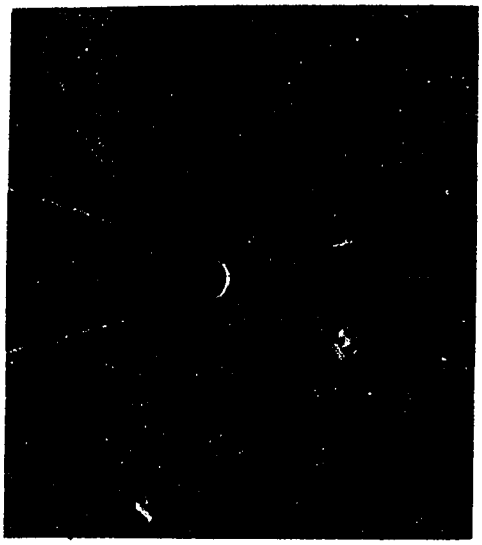

(a) 1 μm

(b) 1 μm

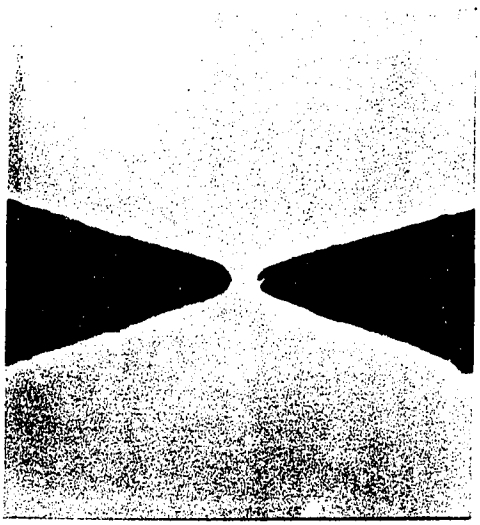

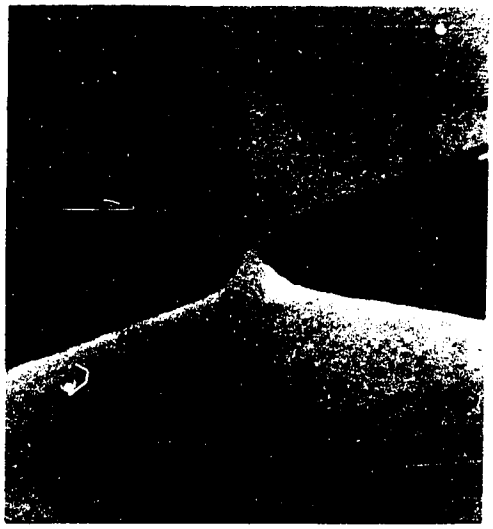

(c) 0.5 μm

The basic fabrication procedure, illustrated in Figure III-7, comprises four steps:

(1) Substrate preparation and cleaning (not shown).

(2) Photolithography-- A layer of photoresist (PR) is applied to a substrate, then exposed and removed in the regions which are to be metallized in the final device (Fig. III-7a,b).

(3) Film Deposition-- A uniform superconducting film is deposited by vacuum evaporation, overlying both bare and PR-covered areas of the substrate (Fig. III-7c).

(4) Liftoff-- The PR is dissolved away, removing the metal which overlies it, while the metal which is in direct contact with the substrate remains (Fig. III-7d).

Detailed process times and parameters are given in Appendix A.

III.B.2 Substrates

Several types of substrates were used, including:

(1) Thick sapphire-- 0.635-mm plates of single-crystal sapphire were obtained from Adolf Meller Co., Providence, R.I. These were mechanically polished to a nominal surface roughness of 250 Å, but many scratches were visible by scanning-electron microscopy. (See Fig. III-6a, for example.)

(2) Thin sapphire-- 0.127-mm plates of single-crystal sapphire were obtained from Insaco, Inc., Quakertown, Pa. These were chemically polished and showed no scratches under the SEM at any magnification.

(3) Microscope cover glasses-- No. 1½ cover glasses (0.17 mm nominal thickness) of Corning type 0211 or equivalent glass were obtained from various suppliers. (Corning 0211 is the glass used

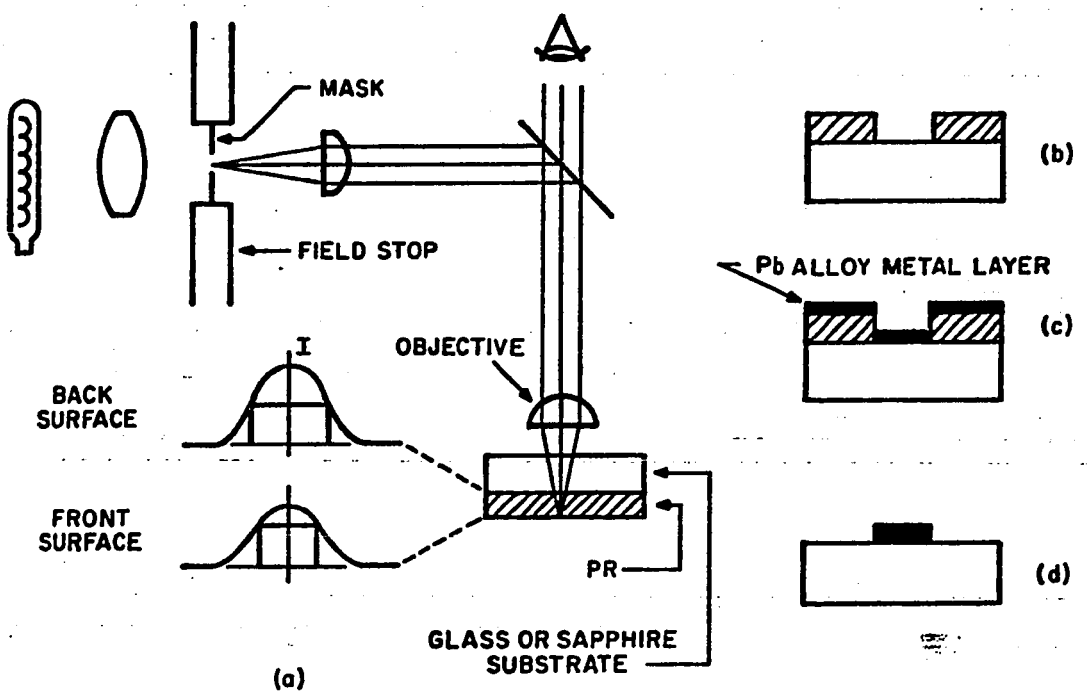

FIG. III-7 Basic fabrication sequence for UTBs. See text for details. (a) Through-the-substrate projection exposure; (b) Developed photoresist pattern with vertical edges; (c) Photoresist pattern coated by vacuum evaporation; and (d) Metal pattern after liftoff.

for standard cover glasses.) These substrates were also scratch-free under the SEM. Their optical properties were optimal for use in through-the-substrate exposure.

(4) SiO-coated glass-- A few cover-glass substrates were coated with thin films of SiO in an attempt to provide improved thermal conductivity at low temperatures. The SiO was evaporated from a tungsten boat to a thickness of 0.25 μm. Judging by its speckled appearance under polarized-light microscopy, the resulting film was polycrystalline. In fact we did not find improved cooling of microbridges on these substrates.

Before the substrates were used for photolithography, they were cleaned by ultrasonic agitation (usa) in acetone and isopropanol to remove surface contamination. Blow-drying the substrates in high-purity-grade nitrogen gas was found to eliminate spotting. Some substrates were reprocessed after one complete fabrication cycle by first etching the device film in chromic acid.

III.B.3 Photolithography

Type AZ-1350B photoresist[10] was used for all photolithography. Substrates were coated with filtered PR by a high-speed spinning process. Coating uniformity was generally satisfactory and coating thickness, checked occasionally by optical interferometry, agreed with manufactorer's data. No adhesion promoter was used before PR coating because adhesion was generally satisfactory. Some episodes of poor adhesion were apparently related to aging of the PR, although low ambient

---

10 Shipley Co., Inc., Newton, Mass.

humidity may have also played a role. Our current practice is to store the PR under refrigeration, at 8 C, for no longer than nine months.

After spin-coating with PR, the substrates were soft-baked to remove any traces of solvent.

Exposure was a two-stage process. First, contact lithography was used to expose all the PR except for a strip 80 μm wide in the center of the substrate. The pattern was then developed to remove the exposed portion of the PR. In the second stage of exposure, projection lithography was used to place several bridge patterns at intervals along the strip of remaining PR. After film evaporation and liftoff, the result was an insulating barrier between two large contact pads which was spanned by several microbridges in parallel. There are two reasons why the projection lithography came last. First, accurate registration is much easier in the projection stage, and second, the fine-scale details which determine the microbridge properties are subjected to development only once, to yield the maximum resolution and reproducibility. A final significant detail is that the insulating barrier does not quite reach the edge of the substrate, so that there is an integral short circuit in parallel with the bridges to protect them from electrical burnout.

We have practiced contact lithography with varying degrees of sophistication. For the earliest devices, a 0.075-mm wire was stretched across the substrate to serve as a mask. This process showed understandably poor reproducibility due to large penumbral spreading at the edges of the pattern. The wire was therefore replaced by an evaporated Al strip on a thick sapphire substrate. This

thin-film mask provided resolution and reproducibility which were satisfactory for the first-stage (coarse) photolithography. Later thin-film masks used a Cr film on a glass substrate for superior abrasion resistance. The Al or Cr mask films were typically $\approx$ 1000 Å thick.

To allow the best possible resolution for tasks such as the replication of masks for the projection stage, we have constructed a system for conformal photolithography. In this technique, pioneered by Smith et al. (1971), the mask is made of a flexible material and pressure is applied to hold the mask and workpiece in intimate contact. If both pieces were rigid, surface irregularities or dust particles could cause a gap between the mask and workpiece leading to penumbral and diffractive spreading of the exposure pattern. However, the flexible mask conforms to the workpiece, leaving a gap only in a small area immediately surrounding a small defect. Figure III-8 is a diagram of the conformal exposure unit constructed for this study. This unit, which incorporates suggestions of Dr. S. K. Decker, relies on atmospheric pressure to hold the mask and workpiece together. The design of Figure III-8 also permits the use of a conformal workpiece and a rigid mask, if desired.

For fine lithography, with details of a few microns or less, we used a microscope projection system similar to that of Palmer and Decker (1973). The system, shown schematically in Figure III-7a, was based on a Zeiss Photomicroscope with 15-watt tungsten illuminator. The Aufl Pol series of strain-free achromats was used for most exposures, but satisfactory results were also obtained in limited tests of some objectives in the Epiplan HD series of planachromats.

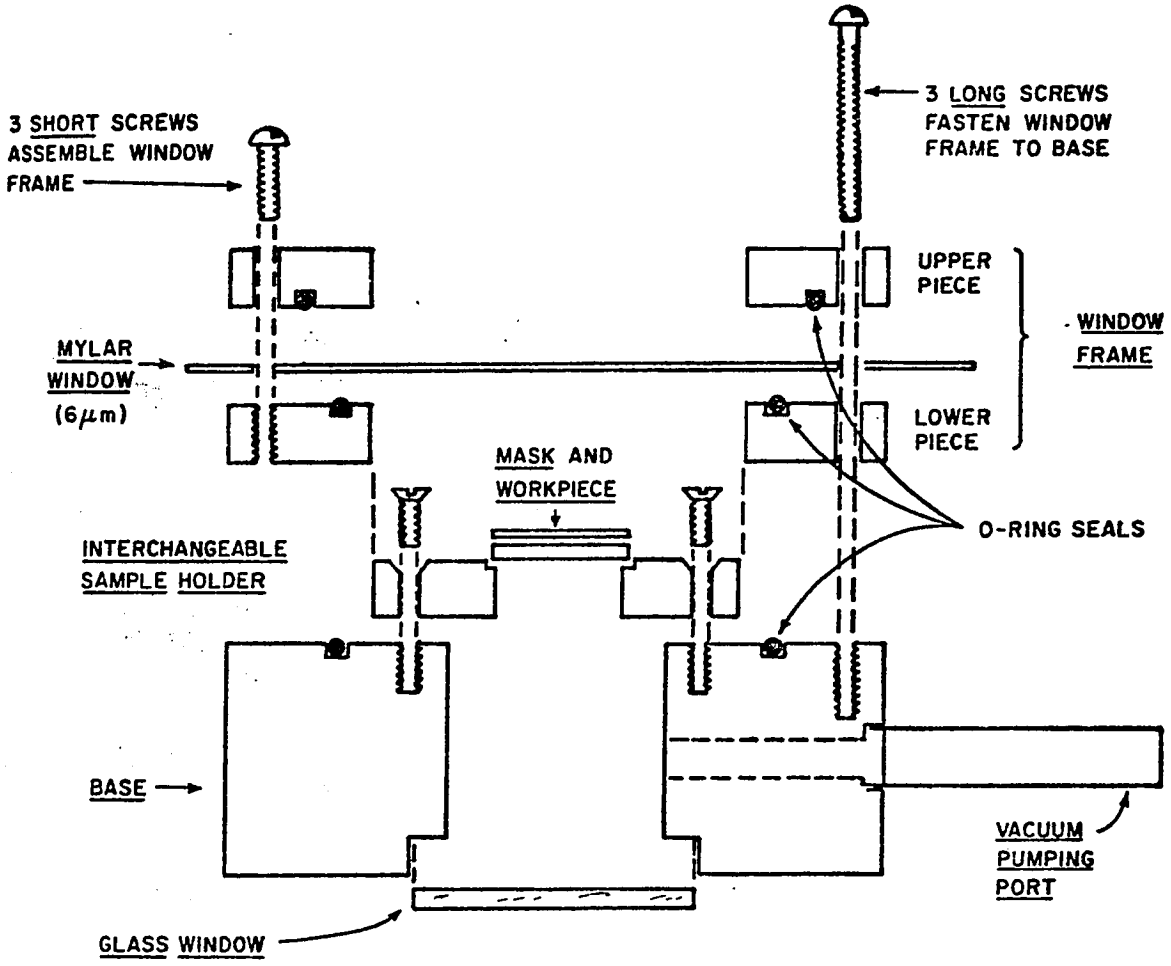

FIG. III-8 Conformal exposure unit — exploded view. When evacuated, atmospheric pressure holds the mylar window, conformal mask and rigid workpiece in intimate contact. The exposing radiation is transmitted through the mylar window in the conformal-mask configuration shown. A glass window is provided on the other side of the unit to permit use in a conformal-workpiece configuration. The latter configuration may be preferable, because transmission is more uniform through the glass window than it is through the mylar window.

As illustrated in the figure, the mask is placed in the plane of the field stop and the microscope is adjusted for Kohler illumination, so that an image of the mask is focussed on the workpiece when the workpiece is in focus to the observer. Both the focus and the registration of the pattern over existing structures can be accomplished to microscopic tolerances (< ½ μm with the 100x objective lens). The image of the mask is demagnified by an amount which depends on the objective chosen--for the 100x objective, the demagnification factor is about 43. Thus a 1-μm microbridge is made using a 40-μm mask which can be a piece of acetate photographic film.

Masks as narrow as 25 μm, with edge definition of 3-5 μm, were made by exposing Kodak type HC-135 high-contrast copy film in an ordinary 35-mm camera. In later experiments, ultra-high-resolution photographic plates were exposed in a commercial reducing projection camera to produce masks with a three-fold improvement in resolution. Figure III-9 shows an example, a mask with a 9-μm bridge gap. Ultra-high-resolution masks were also made by a bootstrapping technique based on the microscope projection system. A large mask on 35-mm film was demagnified and printed into photoresist. Then, via the liftoff process, the PR pattern was transferred to an aluminum or chromium film, yielding a metal-on-glass mask which was smaller than the original. If necessary, the polarity was inverted by conformal printing. Compared with emulsion masks, these bootstrapped masks had improved contrast and edge sharpness, and we used them with good success. Most of our smaller UTBs were made with such a mask.

As stated above, if the mask is precisely positioned, its image should be in focus on the workpiece when the workpiece appears in

10 μm

FIG. III-9 Emulsion mask for 0.2-μm bridges. This optical transmission micrograph shows a mask made by exposing an ultra-high-resolution photographic plate in a commercial projection camera. Note the excellent square corners. The gap between the dark tips is 9 μm, so this mask would project a 0.2 μm bridge pattern.

focus to the observer. Decker (1975) has discussed a first-order correction for imperfect mask position, in the case of specular reflection. In order to achieve the highest possible resolution, we have also included an empirical correction for factors such as chromatic aberration. When the red filter used during focussing and positioning was replaced by the blue filter used during exposure, the focus shifted by a small amount which was not easily calculable. The empirical correction, determined by SEM examination of developed photoresist patterns, did not exceed 2 μm for either conventional or through-the-substrate exposure using the 40x or 100x objective.

Other factors which seriously affected performance of the microscope projection system were aperture diameter and alignment. The choice of aperture diameter represented a compromise between minimizing lens aberrations (and scattering from the lens housing), which favored a small aperture, and minimizing diffraction, which favored a large aperture. Typically, the optimum disc of illumination was found to be 1/2 to 2/3 the diameter of the objective lens. In addition, accurate submicron lithography required that the illuminated disc be accurately centered on the objective lens. Figure III-10a shows the distortion which resulted from a small misalignment of the optical system. It is important to follow the directions for microscope alignment scrupulously.

The exposed PR layers were developed in Shipley AZ developer diluted 1:1 with distilled, deionized water. (As for cleaning and exposure, detailed process parameters for development are given in Appendix A.) Initially, ultrasonic agitation was used during immersion development to ensure proper mixing of developer and dissolving

FIG. III-10 Failures of fabrication. (Counterclockwise from upper left.) (a) Improper microscope alignment leads to distortion of PR patterns and incomplete liftoff; (b) Metal film deposited without oxide undercoat does not have sufficient adhesion to survive liftoff processing; unlike (c) Metal film deposited with oxide undercoat, which lifts off successfully.

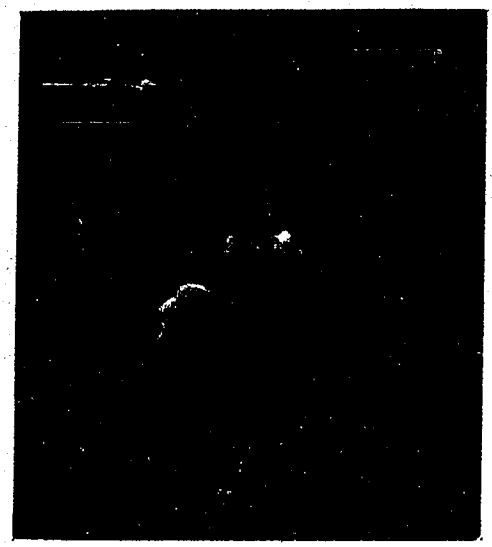

(a)

(b)

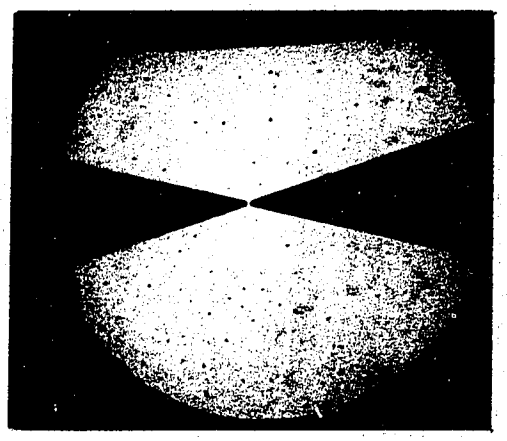

10 µm

(c)

PR. This relatively violent process aggravated any adhesion problems, however, so gentler mixing, with a magnetic stirrer, was used in later processing.

III.B.4 Evaporation of Device Films

The superconducting films were prepared by vacuum evaporation of prealloyed $Pb_{0.70}Bi_{0.30}$ and $Pb_{0.86}In_{0.14}$. The sources were resistively-heated tungsten boats. The Pb-Bi alloy was prepared by heating the weighed components (99.99% pure Pb and 99.999% pure Bi) in an evacuated tube at 450 C for 30 minutes. The Pb-In alloy, specified as $Pb_{.8607}In_{.1393}$, was inherited from the laboratory of Dr. C. T. Lane.

The Pb-Bi alloy was evaporated directly, since Pb and Bi have closely matched vapor pressures in the temperature range of interest (Honig (1962)). Both the low-temperature residual resistivity ρ_4 and the superconducting critical temperature T_c of the evaporated films agreed with data for the bulk alloy (cf. table IV-2). One difficulty encountered with the Pb-Bi films was that they were very prone to oxidation. Though the rate varied strongly with ambient humidity, a typical, unprotected 600-Å film oxidized through in about two weeks. Films which were coated with photoresist remained shiny for several months.

The vapor pressures of Pb and In are not the same at any temperature, so the charge of Pb-In alloy was always evaporated to completion to assure a fixed overall composition. Any composition gradients across the thickness of the film were healed by the interdiffusion of Pb and In, which is extremely rapid even at room temperature. (See Lahiri (1975a).) The residual resistivity and critical temperature of our evaporated Pb-In films agree with data for bulk $Pb_{0.9}In_{0.1}$. For very thin (< 400 Å) films, T_c was found to be slightly higher than

bulk (an increase of $\approx$ 50 mK at 250 Å thickness), possibly because due to scavenging of indium by oxide at the surfaces (see Chou (1975)). The 10% - 90% width of the resistively-measured superconducting transition (bridge plus banks) was typically less than 15 mK, indicating good uniformity for such an alloy.

Some special techniques, originated by Chiao et. al. (1974) and communicated to us by Dr. M. Octavio, were employed during film deposition. First, the substrates were cleaned by exposing them to an oxygen glow-discharge. Typically, the discharge current was 0.8 mA, at a voltage of 1 kV and an oxygen pressure of 80 mTorr. The substrates were shielded so that any material which might be sputtered off the cathode could not reach them, at least by direct line-of-sight. Next, a thin ($\approx$ 40 Å) layer of the device material was evaporated, then oxidized by prolonged exposure to the oxygen glow-discharge. The resulting oxide layer acted as "glue" to ensure good adhesion of the device film which was evaporated subsequently. According to N. Giordano (private communication), samples which are exposed to atmosphere between undercoat and device film evaproation still achieve good adhesion.

Film adhesion was checked by the tape test. A piece of Scotch Magic Transparent tape was applied to the film-coated substrate and then removed. If the film remained on the substrate, adhesion was satisfactory. By this test, the thin oxide undercoat made the difference between satisfactory and unsatisfactory adhesion of the device film. An even more convincing demonstration of the efficacy of the oxide undercoat process is shown in Figure III-10b,c. Liftoff of the bridge pattern shown in Figure III-10b was a complete failure due to

poor film adhesion. The bridge pattern shown in Figure III-10c, which was prepared with an oxide undercoat, had good film adhesion, resulting in a successful liftoff process.

The substrate stage was held at liquid nitrogen temperature (77 K) during deposition of the device films in order to obtain smooth films. Evaporation of a soft material such as Sn, In or Pb onto a room-temperature substrate results in agglomeration and island formation. Though the Pb alloy films form smaller islands than pure Pb, the films are still discontinuous at 400 Å, as shown in Figure III-11a. Evaporation onto substrates at 77 K, however, produces films which are continuous and smooth, as shown in Figures III-11b,c.

When the above techniques of glow discharge cleaning, oxide undercoating, and liquid-nitrogen-temperature deposition were used, we obtained device films with reproducibly good adhesion, smoothness, and electrical proerties.

III.B.5 Liftoff Processing; Through-the-Substrate Exposure

The photoresist pattern was transferred to the device film by the liftoff process, illustrated in Figure III-7d. After exposure and development, the techniques described in the previous section were used to evaporate a uniform film of Pb alloy over the substrate and the PR pattern. Then the sample was ultrasonically agitated in acetone to dissolve the PR, removing the undesired areas of metal film. The ultrasonic agitation assured both solvent penetration and the separation of the loose film areas from the substrate, but it was a relatively violent process which demanded the good film adhesion provided by the oxide undercoat process.

Figure III-12 shows why the PR edge profiles are the critical

FIG. III-11 Surface topography of Pb-alloy films. (Counterclockwise from upper left.) (a) 400-Å Pb-Bi film deposited onto room-temperature substrate is discontinuous; while (b) 1000-Å Pb-Bi film deposited onto substrate held at 77 K is very smooth; and (c) 140-Å Pb-In film deposited onto substrate held at 77 K shows essentially no surface structure, though substrate polishing marks and dust particle indicate good resolution and focus of the SEM. Although this film was not tested for electrical continuity, a 170-Å film had resistivity about twice that of thick films at room temperature.

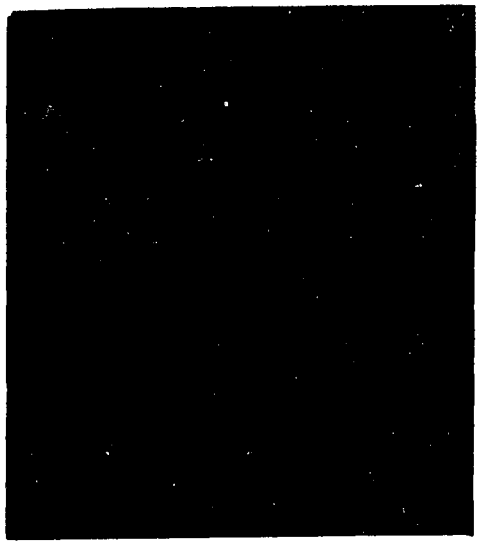

(a)

(b)

(c)

factor in liftoff processing. If the edges are vertical (i.e. perpendicular to the substrate) or undercut, as drawn in Figure III-12a, the evaporated device film will be discontinuous at the edges of the pattern and will lift off freely. If, on the other hand, the edges are sloping, as drawn in Figure III-12b, the film will be continuous and must tear unevenly, creating ragged edges. For submicron microbridges, the most difficult sections to lift off are at the tips of the PR patterns, where the PR edges are most severely rounded by optical diffraction. Here, also, a piece of remanent film may be supported on three sides, making it very difficult to remove. Thus, we found that remanent tips, shown in Figure III-13, were the most common form of liftoff failure when lithographic conditions were nearly correct. Usually this problem was not cured by additional stages of agitation in acetone.

Blurring of the projected image by diffraction, imperfect optics, or other causes results in diffuse contours of exposure energy. The intermediate factors which convert these exposure contours into undesirable sloping or rounded PR edge profiles are limited contrast, which implies a finite development rate in partially exposed regions, and optical absorption within the PR layer. The optical absorption can be surprisingly large. According to Dill et. al. (1975), the extinction length for light at 4047 Å in unexposed PR (Shipley AZ-1350) is 1.08 μm. (The peak sensitivity of this PR is at $\lambda \approx 4000$ Å.) This implies 25% absorption in a layer 3000 Å thick. Unlike the effect of limited contrast, which is always detrimental, the effect of optical absorption can be turned to advantage in controlling the PR edge profiles, by the process of through-the-substrate exposure.

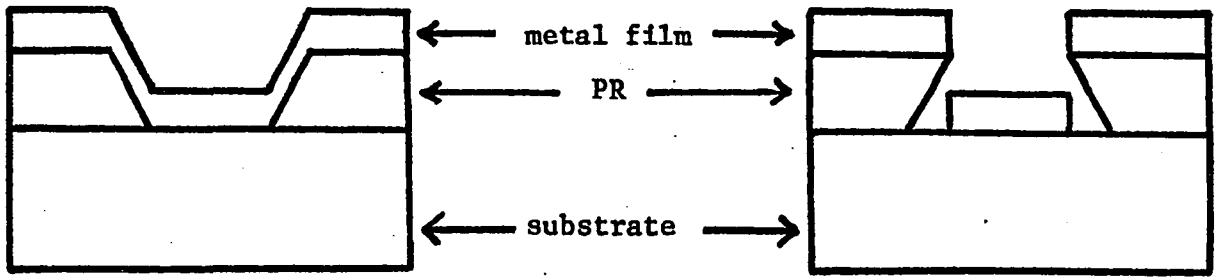

TAPERED PROFILE
POOR LIFTOFF

(b)

UNDERCUT PROFILE
GOOD LIFTOFF

(a)

FIG. III-12 Effect of photoresist edge profiles. (a) If edge profile is undercut, evaporated film will liftoff cleanly; while (b) If edge profile is sloping, evaporated film is continuous and must tear to liftoff, causing ragged edges and poor liftoff yield.

10 μm

FIG. III-13 Unsuccessful liftoff - remanent tips. This optical micrograph was taken with differential-interference-contrast microscopy to give a three-dimensional effect. The central tips of the pattern have failed to liftoff properly, due to rounded PR edge profiles. Additional time in the ultrasonic liftoff bath usually does not cure this problem.

The concept is illustrated in Figure III-14, and actual results are shown in Figure III-15. In conventional exposure (Figure III-14a), the light enters the PR at the air interface and is attenuated by the time it reaches the substrate interface, resulting in exposure energy contours which are widest at the PR-air interface. After development, the PR edges are sloping (Figure III-15a). In through-the-substrate exposure, the workpiece is inverted so that the light passes through the transparent substrate before entering the PR at the substrate interface. Then the exposure energy contours are widest at the PR-substrate interface (Figure III-14b). The PR edge profiles depend on the detailed conditions of exposure and development, but they are usually undercut, as in Figure III-15b, or roughly vertical, as in Figure III-15c.

The practical significance of through-the-substrate exposure was considerable. Our earlier efforts with conventional exposure achieved a liftoff yield of about 50% of 1/2-μm bridges, while the yield for through the substrate exposure was over 90%. These high liftoff yields extended to bridges as narrow as 0.2 - 0.3 μm, dimensions which would probably have been impossible with conventional exposure. The yield from projection exposure of 0.2 - 0.3 μm patterns was typically 15%, due in part to a 10% variation in required exposure time from sample to sample. Since exposure time was fairly critical, we usually exposed six patterns on a single substrate, selected one bridge by optical microscopy, and scratched out the rest. We have used both cover glass and thin sapphire substrates for through-the-substrate lithography, but the results on sapphire were slightly inferior, because the high refractive index of sapphire introduced spherical aberration for which

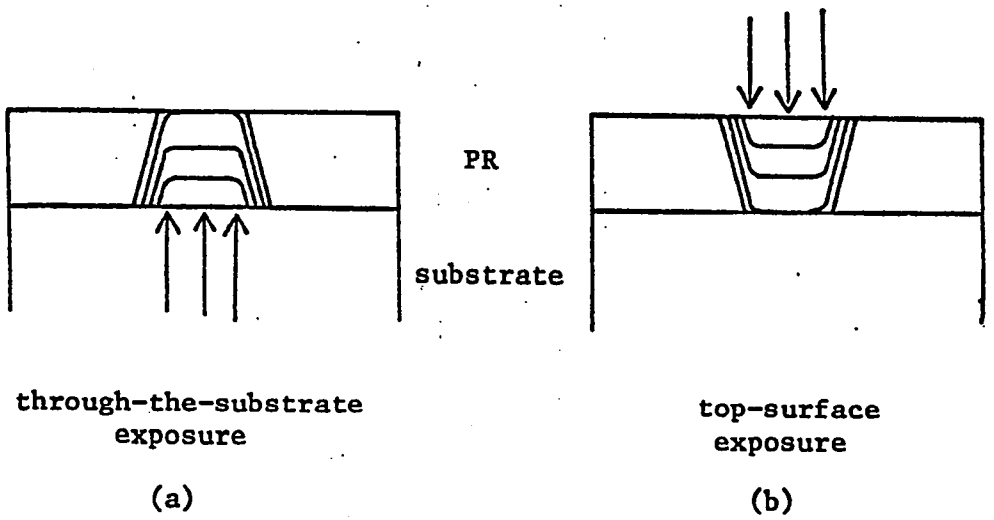

FIG. III-14 Schematic exposure contours. (a) Due to optical absorption in the PR, through-the-substrate exposure leads to undercut exposure contours. With proper development procedures, these can be converted into undercut PR edge profiles. (b) Conventional top-surface exposure leads to sloping exposure contours and undesirable sloping PR edge profiles.

FIG. III-15 Actual PR edge profiles. These scanning-electron micrographs were taken at glancing incidence (i.e. nearly parallel to the substrate) to show the PR edge profiles. (Counterclockwise from upper left.) (a) Conventional top-surface exposure of thin ($\approx$ 250 nm) PR yields sloping edge profile; while (b) through-the-substrate exposure of thicker ($\approx$ 500 nm) PR yields clearly undercut edge profile; and (c) through-the-substrate exposure of thin ($\approx$ 250 nm) PR yields roughly vertical edge profile.

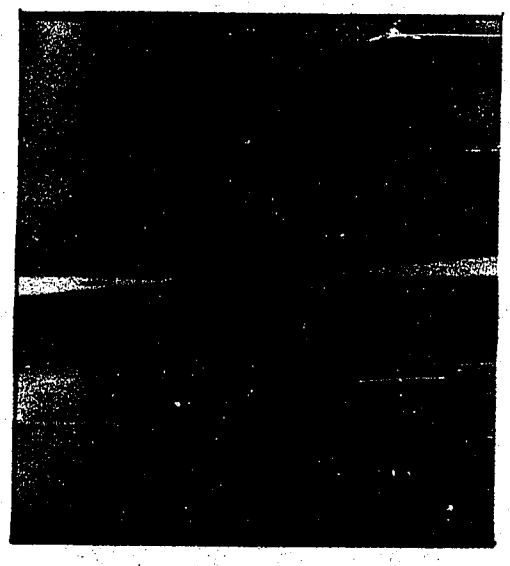

(a)

(b)

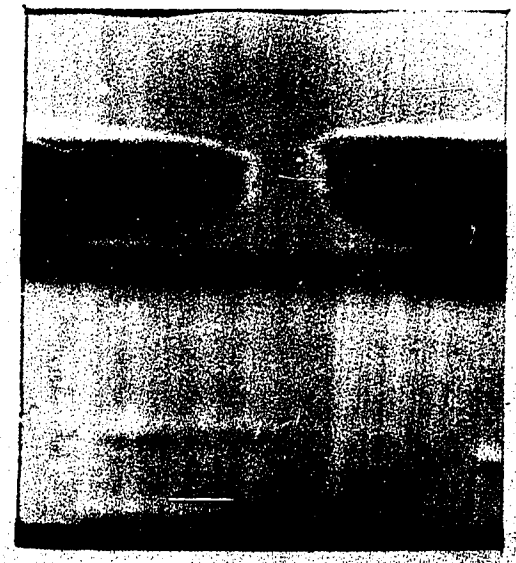

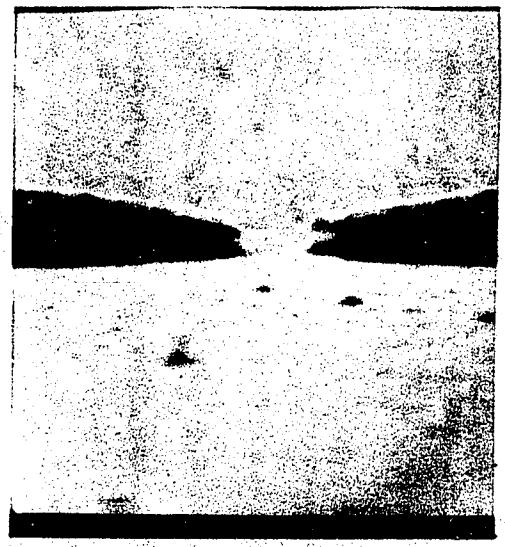

(c)

our standard lenses were not corrected. The 100x objective is corrected to work in immersion oil, which has refractive index n = 1.532 at λ = 4000 Å. Cover glasses (n = 1.533) are very closely matched to this value, but sapphire (n = 1.786) is not. Sapphire slides are acceptable for bridges of $\gtrsim$ 0.4 μm width, but the yield of narrower bridges would be lower than on cover-glass substrates. Sapphire may be preferred, however, for its greater strength and its excellent thermal conductivity at liquid-helium temperatures.

IV. RESULTS AND DISCUSSION-- UTBS

Using the techniques described in the preceding chapter, we fabricated uniform-thickness bridges (UTBs) of $Pb_{0.7}Bi_{0.3}$ and $Pb_{0.9}In_{0.1}$ alloys and studied their electrical properties by recording time-averaged $\bar{V}(I)$ curves both with and without applied microwave radiation. The bridges were roughly hyperbolic in shape, with an asymptotic bank angle (one bank) of $5\pi/6$. Bridge widths ranged from 0.2 μm to 1.9 μm and thicknesses ranged from 250 Å to 900 Å, yielding bridge resistances R_d (cf. section IV.B.1) from 1 Ω to 8 Ω. This range of sizes made it possible to investigate the transition from the uniform-depairing regime to the vortex-flow regime, as discussed in section II.D. The dimensions and basic parameters of the bridges are listed in Table IV-I.

The electrical and superconducting parameters of our alloy films are listed in Table IV-II. As mentioned in the previous chapter, the resistivity and critical temperature of the $Pb_{0.7}Bi_{0.3}$ alloy films match the values for bulk $Pb_{0.70}Bi_{0.30}$ published by Voight (1968) and by Evetts and Wade (1970). The data on bulk Pb-In alloys obtained by Farrell et. al. (1969) were used to identify the exact composition of the $Pb_{0.9}In_{0.1}$ alloy films. For films of ordinary thickness ($\geq$ 400 Å), ρ and T_c indicate a composition of $Pb_{0.89}In_{0.11}$, while for very thin films (250 Å), ρ is slightly lower and T_c is slightly higher, indicating a composition of $Pb_{0.92}In_{0.08}$. For simplicity, both of these material compositions are denoted $Pb_{0.9}In_{0.1}$ (or simply Pb-In) in the following sections.

The GL penetration depth λ_{GL} is derived from the measured resisti-

TABLE IV-I. Parameters of uniform-thickness microbridges. W is the bridge width, d is the bridge (and bank) thickness, I_c is the critical current, and R_d is the device resistance, defined as the minimum differential resistance in the finite-voltage state R_{min}, measured at $T = 0.995\ T_c$ (see section IV.B.)

Bridge #	Material	W (μm)	d (Å)	$I_c(t=0.98)$ (μA)	R_d (Ω)
A	Pb-Bi	1.9	900	(446)[a]	≈ 5[b]
B[c]	Pb-Bi	≈0.9	630	(140)[a]	≈ 9
E	Pb-Bi	0.60	610	149	7.3
F[c]	Pb-Bi	≈0.5	600	69	9.0
I-1[c]	Pb-In	≈0.5	660	229	1.3
I-2	Pb-In	0.45	660	177	1.6
I-4	Pb-In	0.35	440	64	2.8
I-5[c]	Pb-In	≈0.3	250	36	5.9
I-6	Pb-In	0.35	440	57	2.9
I-7	Pb-In	0.20	250	34	5.5

[a] This bridge was tested only very near T_c, so the value tabulated is $2I_c(t=0.99)$. The actual value of $I_c(t=0.98)$ would be larger.

[b] For this very wide bridge, R_{min} is increased by Joule heating even at $t = 0.995$.

[c] Exact width of this bridge is uncertain because it was burned out before scanning-electron microscopy was performed.

TABLE IV-II. Electrical and superconducting properties of the Pb-alloy films studied. T_c is the superconducting critical temperature, ρ is the normal-state resistivity measured just above T_c, $\lambda_{GL}^{(t=0)}$ and $\xi_{GL}^{(t=0)}$ are the Ginzburg-Landau penetration depth and coherence length extrapolated to zero temperature, ℓ is the electron mean free path in the normal state, and ξ_{BCS} is the BCS coherence length calculated from ξ_{GL} and ℓ.

Material	T_c (K)	ρ (Ω-cm)	$\lambda_{GL}(t=0)$ (Å)	$\xi_{GL}(t=0)$ (Å)	ℓ (Å)	ξ_{BCS}[a] (Å)
$Pb_{0.7}Bi_{0.3}$	8.4-8.5	3×10^{-5}	1210	120	33	600
$Pb_{0.9}In_{0.1}$ ($d\geq400$Å)	7.07	7×10^{-6}	640	250	140	610
$Pb_{0.9}In_{0.1}$ ($d=250$Å)	7.12	5×10^{-6}	540	275	200	520

[a] In treatments of the BCS theory, this parameter is usually labeled ξ_o.

vity, using the dirty limit relation:[1]

$$\lambda_{GL}(T) = 6.42 \times 10^{-3} \left(\frac{\rho}{T_c - T} \right)^{1/2} \qquad (T_c - T \ll T_c) \qquad (1)$$

where λ_{GL} is in μm, ρ is in Ω-cm, and T is in K. Strictly speaking, ρ is the resistivity of the material if it is driven into the normal state at temperature T. For the high-resistivity alloys studied, ρ is temperature-independent at low T, so we have used the value of ρ measured just above T_c. The H_{c2} measurements of Evetts and Wade (1970) and Farrell et. al. (1969) are used to compute the GL coherence length ξ_{GL}, according to[2]:

$$\xi_{GL}(T) = \left(\frac{\Phi_o}{2\pi} \, T_c \, \frac{dH_{c2}}{dT} \bigg|_{T=T_c} \right)^{-1/2} (1-t)^{-1/2}. \qquad (2)$$

Finally, the ρℓ product for Pb measured by Chambers (1952), $\rho\ell = 1.0 \times 10^{-11}$ Ω - cm^2, is used to estimate the mean free path ℓ. (Due to the experimental difficulties noted by Chambers, ρℓ may have been overestimated by as much as a factor of two.) The consistency of these independent estimates of λ_{GL}, ξ_{GL}, and ℓ is checked by computing the BCS coherence length ξ_{BCS}, according to equation (4-24) of Tinkham

---

[1] This relation is obtained by combining the isotropic free-electron theory of normal-state resistivity:

$$\rho = \frac{m v_F}{n e^2 \ell}$$

with eqs. (1-9), (2-52), (2-114), (2-120) and (4-26a) of Tinkham (1975). If Tinkham's eq. (2-123b), which connects the clean- and dirty-limit results, is used, λ_{GL} is changed by less than 6%, so we eschew that refinement.

[2] See eq. (4-62) of Tinkham (1975).

(1975). The agreement to better than 20% is acceptable, albeit not outstanding.

IV.A Critical Currents of UTBs

We find that the critical current of a uniform-thickness microbridge is a smooth, reproducible function of the bridge dimensions. Figure IV-1 shows $I_c(t = 0.98)$ for our Pb-In UTBs, versus Wd, the cross-sectional area at the bridge midplane. (The uncertainty in width is large for #I-1 and #I-5 because these bridges were burned out before they could be examined in the SEM.) For comparison, the critical current predicted for a long, one-dimensional filament (eg. (II-11)) is also plotted. The smooth size dependence of I_c observed is not surprising, but it serves as a welcome confirmation of reproducibly good film quality.

Two examples of the temperature dependence of the critical current are shown in Figure IV-2. The critical currents of our UTBs do not exactly fit a power-law dependence, but exponents in the expression:

$$I_c \propto (1-t)^{\beta} \qquad (3)$$

fall in the range $\beta = 1.2$ to $\beta = 1.5$, depending on the bridge and the temperature range fitted. Thus, the observed temperature dependence of the bridges is intermediate between the junction-like dependence ($\beta = 1.0$) predicted for short, narrow bridges and the bulk-like dependence ($\beta = 1.5$) predicted for long filaments.

Since the bridges are nearly hyperbolic in shape, either the uniform-depairing calculation of Mooij and Dekker (1978) or the vortex-flow calculation of Aslamazov and Larkin (1975) should be applicable, depending on the size regime. These calculations were discussed above in

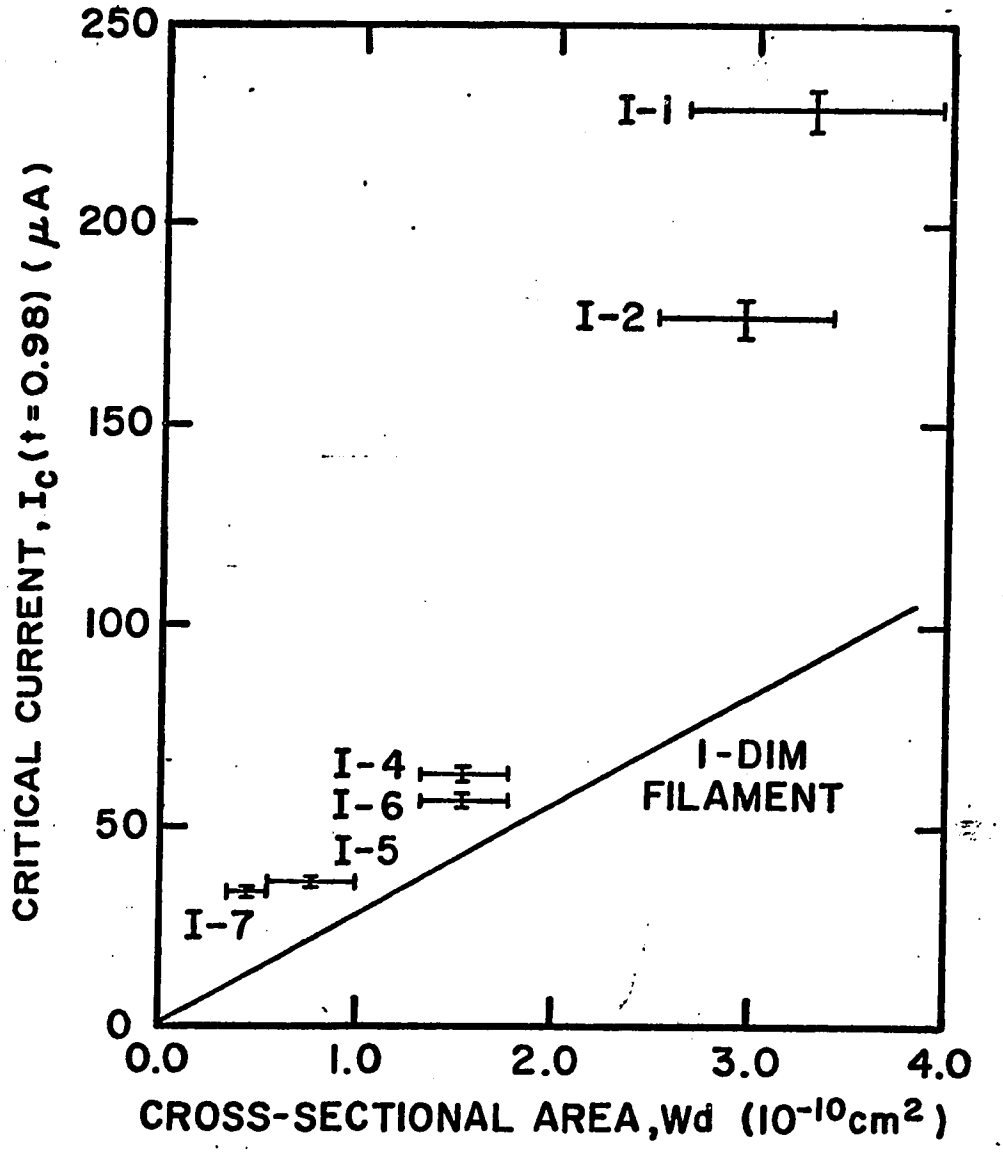

FIG. IV-1. Critical current of uniform-thickness bridges versus cross-sectional area. The dimensions of bridges #I-1 and #I-5 are more uncertain because these bridges were burned out before scanning-electron microscopy. For comparison, we have also plotted $I_c^{(fil)}$, the critical current of a one-dimensional superconducting filament.

FIG. IV-2. Critical current versus temperature for two uniform-thickness bridges. (a) For the narrow Pb-In bridge #I-7, the experimental data fall within 15% of the uniform-depairing theory of Mooij and Dekker (1978). (In a previous work, Feuer and Prober (1979), the theory of MD (1978) was incorrectly applied, leading to a 30% underestimate of $I_c(T)$.) (b) For the wide Pb-Bi bridge #E, the experimental data agree with the vortex-flow theory of Aslamazov and Larkin (1975) very near T_c, but exceed the theoretical predictions at lower temperatures.

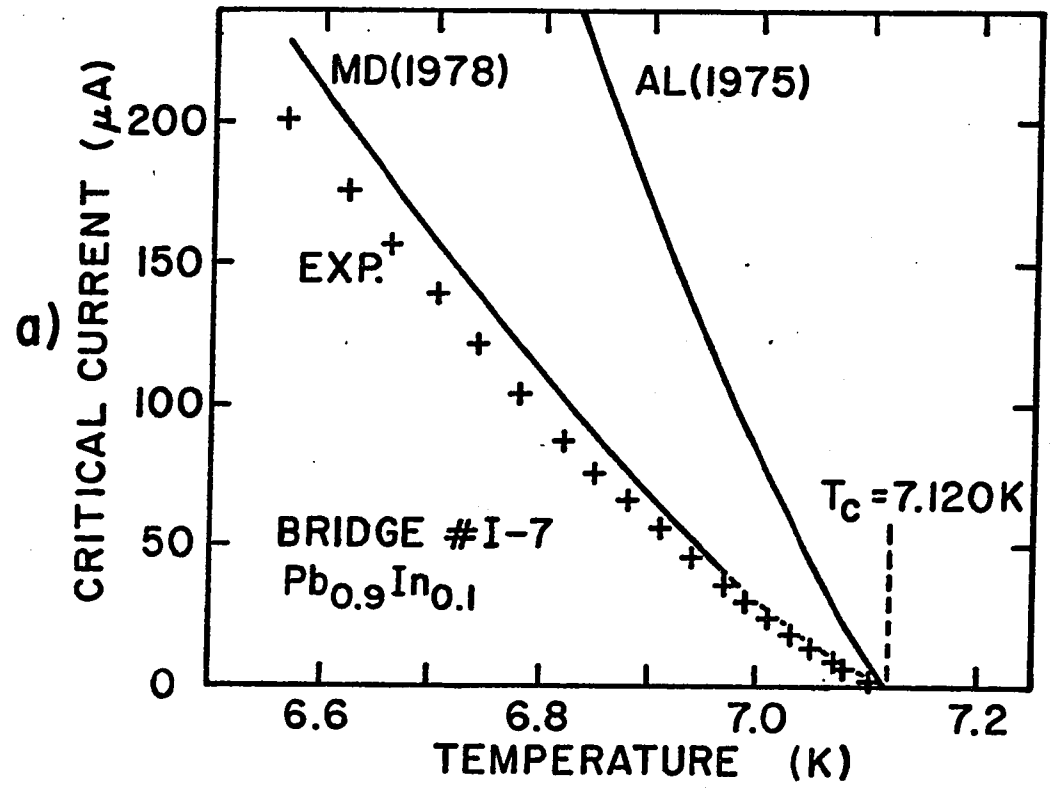
a)
CRITICAL CURRENT (μA)
200
150
100
50
0
MD(1978)
AL(1975)
EXP.
BRIDGE #I-7
$Pb_{0.9}In_{0.1}$
T_c = 7.120K
6.6
6.8
7.0
7.2
TEMPERATURE (K)

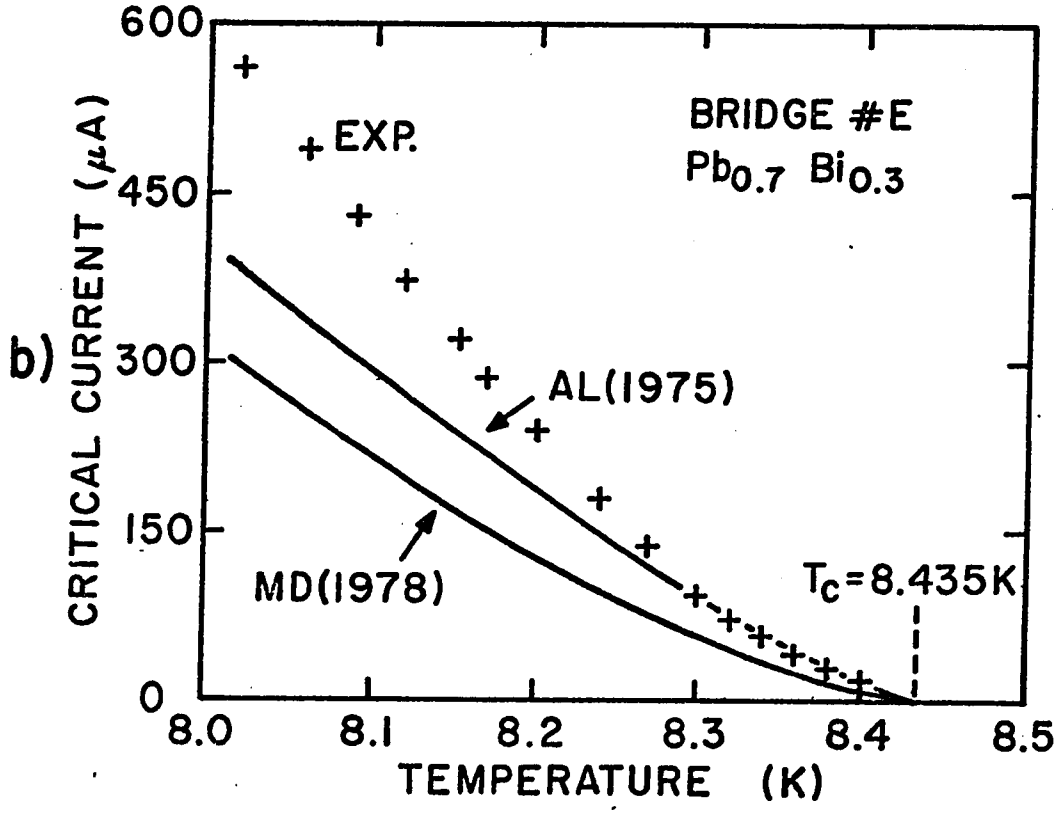
b)
CRITICAL CURRENT (μA)
600
450
300
150
0
EXP.
BRIDGE #E
$Pb_{0.7}$ $Bi_{0.3}$
AL(1975)
MD(1978)
T_c = 8.435K
8.0
8.1
8.2
8.3
8.4
8.5
TEMPERATURE (K)

sections II.B.1 and II.C.1, respectively, and their results are plotted in normalized form in Figure IV-3, assuming an asymptotic bank angle of $5\pi/6$ which applies to our devices. The predicted dependence of I_c on width and temperature is very similar for the two models, but the predicted magnitude of I_c differs by nearly a factor of four when $W \approx 2\xi$. The bulk-like film properties and reproducible shape of our UTBs are thus especially important when the magnitude of I_c is to be compared to these theories.

In Figure IV-2a, the measured critical current of a narrow bridge, #I-7, is compared with the theoretical predictions of both models. The theoretical curves are calculated using the measured resistivity of the film and the value of $\xi_{GL}(0)$ obtained from the bulk H_{c2} data (see Table IV-II). Except the choice of T_c, no fitting to the I_c data was involved, so it is legitimate to compare the magnitude of I_c to the theoretical predictions. Clearly, the uniform-depairing model of MD(1978) is in good agreement with the data, while the vortex-flow result of AL(1975) is much too large.

Data for a wider bridge, #E, are plotted in Figure IV-2b. As before, the theoretical curves are computed independently of the experimental I_c data. For bridge E, the uniform-depairing result of MD(1978) is too small. The vortex flow result of AL(1975) gives the correct order of magnitude, but the $\beta = 1.25$ temperature dependence predicted by AL(1975) is too weak.

The critical-current data plotted in Fig. IV-2 partially confirm the expectations of section II.D. The narrow bridge, for which $W/2 < \xi(T)$ when $T > 6.58$ K ($t > 0.924$), obeys the theoretical predictions of the uniform-depairing regime. The wider bridge, for which $W/2 > \xi(T)$

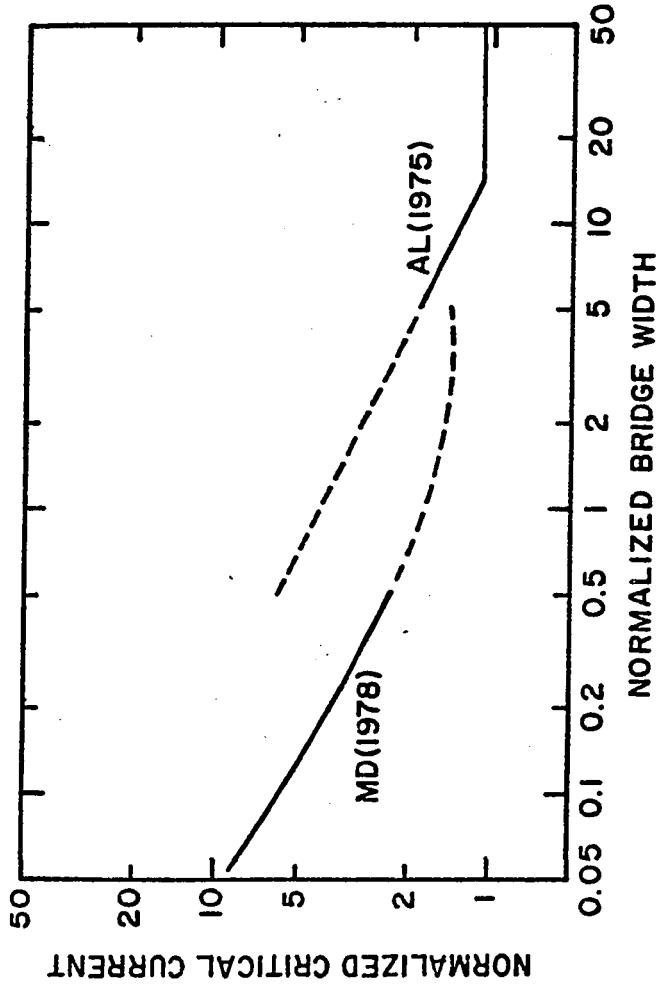

FIG. IV-3 Comparison of critical currents predicted for hyperbolic UTBs by the vortex-flow theory of Aslamazov and Larkin (1975) and the uniform-depairing theory of Mooij and Dekker (1978). This plot is for $\theta_{max} = \frac{5\pi}{12}$ radians. The normalized critical current is $I_c/I_c^{(fil)}$, where $I_c^{(fil)}$ is the critical current of the one-dimensional filament given by eq. (II-12). The normalized bridge width is $W/2\xi(T)$ sin (θ_{max}). The dotted curves show the theoretical predictions in the transition region where the assumed strong inequalities between W and $\xi(T)$ are not strictly satisfied.

when $T < 8.42$ K ($t < 0.998$), comes closer to the theoretical predictions of the vortex-flow regime. However, the vortex-flow theory still needs improvement to obtain the correct temperature dependence. For bridges of intermediate width, the experimental data fall between the two theoretical curves. We have not studied the crossover behavior of I_c in detail.

IV.B $\bar{V}(I)$ Curves of UTBs

IV.B.1 $\bar{V}(I)$ Curves Near T_c

Representative $\bar{V}(I)$ curves of bridge #I-7, plotted in Figure IV-4, are smooth and well-behaved near T_c.

The rounding of the voltage onset, not predicted by the theories discussed in chapter II, is probably the result of intrinsic thermal noise. Theoretical studies of this effect have been carried out by Ambegaokar and Halperin (1969), and extensive experimental studies of noise in UTBs of pure In are discussed by Lee (1977). The rounding observed in our UTBs agrees, at least in order of magnitude, with the results of the above studies and there is no reason to suspect that external interference is smearing out the $\bar{V}(I)$ curves. As discussed in section III.A.1, the agreement of nanovoltmeter and direct-coupled-amplifier measurements and the low level of 60-Hz pickup also indicate that external noise is not distorting the $\bar{V}(I)$ curves.

After an initial peak at the voltage onset, the differential resistance $d\bar{V}/dI$ derived from the $\bar{V}(I)$ curve drops to a nearly constant value which is two to three times the resistance per square in the normal state. The voltage-periodic peaks in $d\bar{V}/dI$ predicted by AL (1975) have not been observed in any bridge. The minimum differential resistance R_{min} is nearly independent of temperature near T_c, as shown in Figure

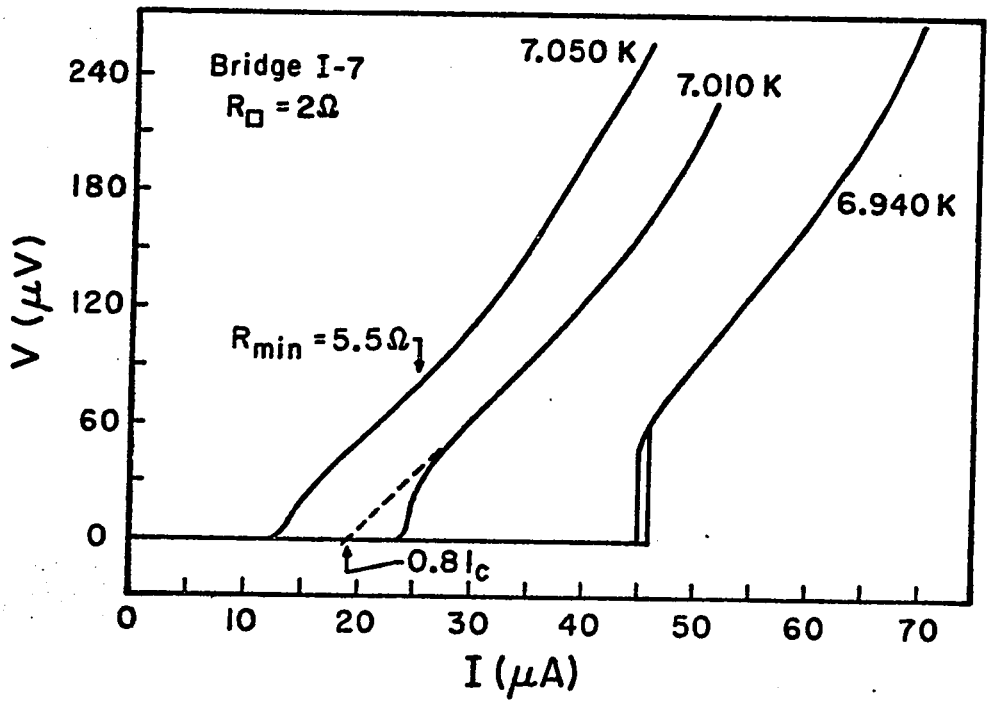

FIG. IV-4 Representative $\bar{V}(I)$ curves of Pb-In bridge #I-7. The dashed extrapolation points out the "excess current" observed at T = 7.010 K. Hysteresis in the voltage onset is visible at T = 6.940 K, just 180 mK below T_c.

IV-5. This is in direct contradiction to the results of both of the vortex-flow models discussed in section II.C, which predict characteristic resistances which diverge as $T \to T_c$. The theory of MD(1978) does not address the finite-voltage state, but on the basis of the two-fluid picture, the normal-state resistance of the depaired region should be characteristic of the $\bar{V}(I)$ curve. MD(1978) conclude that the length of this depaired region is about 2ξ, which leads to a resistance (cf. section II.B.1):

$$R = \frac{\text{arcsinh } (\frac{1}{a})}{\theta_{max}} \; R_D \tag{4}$$

which also diverges as $T \to T_c$, due to the temperature dependence of the normalized width parameter a.

At lower temperatures or higher voltages, $d\bar{V}/dI$ rises, at least partially as a result of Joule heating (see section II.E.1). To avoid heating effects and bank resistance, we define the characteristic device resistance R_d, listed in Table IV-I, as the minimum differential resistance R_{min} measured at $t = 0.995$:

$$R_d \equiv R_{min}(t = 0.995) \tag{5}$$

If one makes a linear extrapolation of the $\bar{V}(I)$ curve from the region of minimum $d\bar{V}/dI$ back to $V = 0$, a substantial "excess current" (see section II.B.2) is observed, as illustrated in Fig. IV-4. Near T_c, we find:

$$I_{ex} = (0.75 - 0.85)I_c. \tag{6}$$

Large excess currents have also been observed in microbridges of type-I materials, by Skocpol et. al. (1974), Yeh and Buhrman (1977), Klapwijk et. al. (1977a), and others, but their origin has not been established with certainty. Likharev and Yakobson (1976b) have ascribed

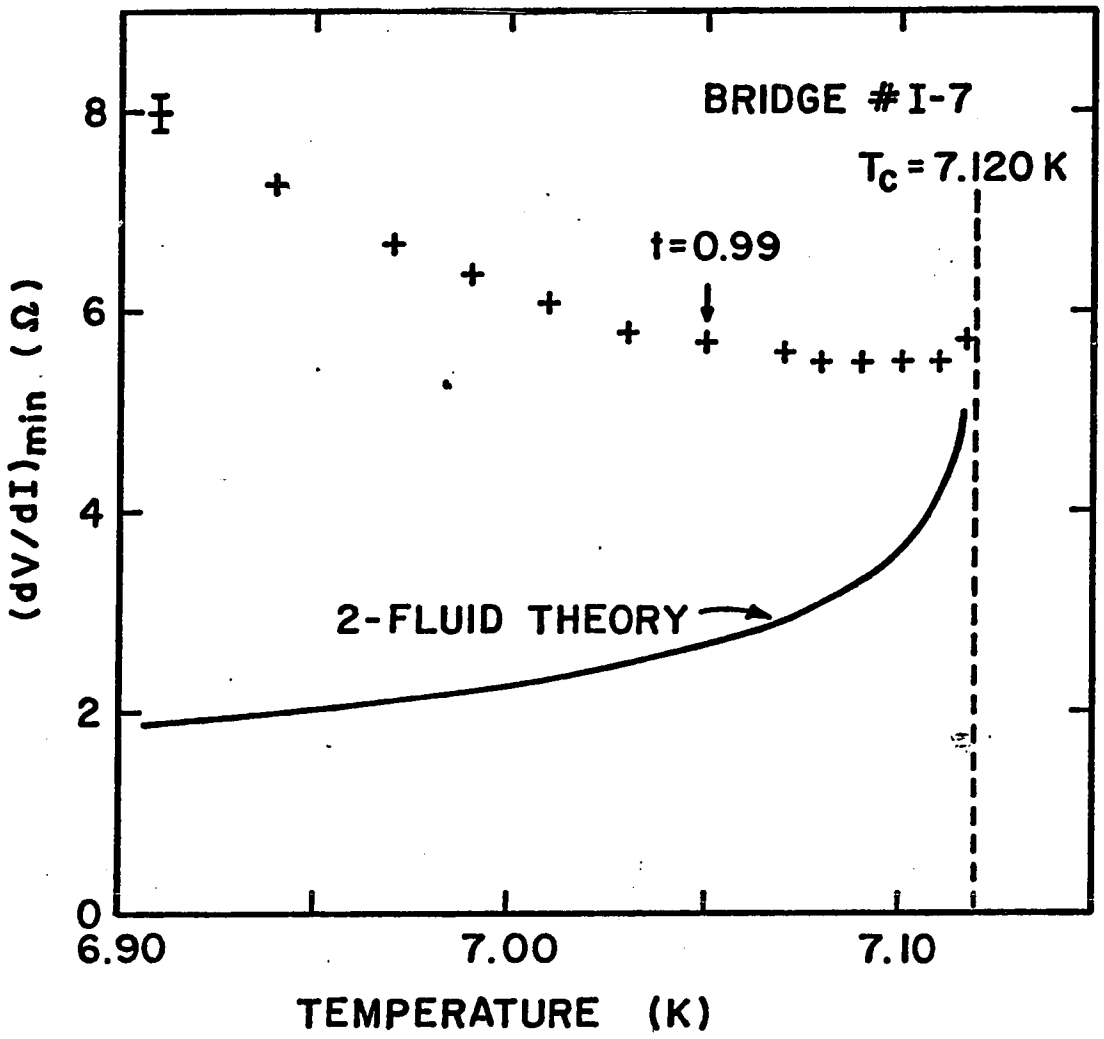

FIG. IV-5. Minimum differential resistance versus temperature for bridge #I-7. The solid curve is the two-fluid result of eq. (IV-4), based on the calculation of Mooij and Dekker (1978). The results of the vortex-flow theories, eqs. (II-44) and (II-62a), are much too large to plot on this scale.

the excess current effect to the finite relaxation time of the Ginzburg-Landau order parameter. The prediction of this theory, which assumes rigid boundary conditions, is that:

$$I_{ex} = 0.75\ I_c \tag{7}$$

for any bridge at any temperature. This approach is almost certainly oversimplified; the rigid boundary conditions are not strictly applicable to UTBs, and time-dependent GL theory has not been shown to explain unambiguously and uniquely any features of microbridge behavior. In any case, we find that I_{ex}/I_c slowly decreases at lower temperatures, but as in the case of the R_{min} data, Joule heating probably has some effect.

No structure was observed in the $\bar{V}(I)$ curves at the energy gap voltage $2\Delta/e$ or at the gap subharmonic voltages $2\Delta/me$, where m is an integer. This topic is discussed in section VI.C.1 below.

IV.B.2 $\bar{V}(I)$ Curves at Low Temperatures; Hysteresis

As the temperature is decreased well below T_c, hysteresis appears in the $\bar{V}(I)$ curve at the voltage onset. As shown in Figure IV-6, the size of the hysteretic region increases smoothly as the temperature is reduced. Such hysteresis has sometimes been attributed to shunt capacitance (Jahn and Kao (1973)) or relaxation-time effects (Song (1976)), but we believe that Joule heating is probably responsible for the hysteresis observed in our UTBs. Skocpol et. al. (1974) have shown that Joule heating can explain quantitatively the I-V curves of hysteretic Sn UTBs, and have pointed out that it may be difficult to distinguish capacitive hysteresis from heating-induced hysteresis. It is almost always possible to fit the data for the downset current I_d of any

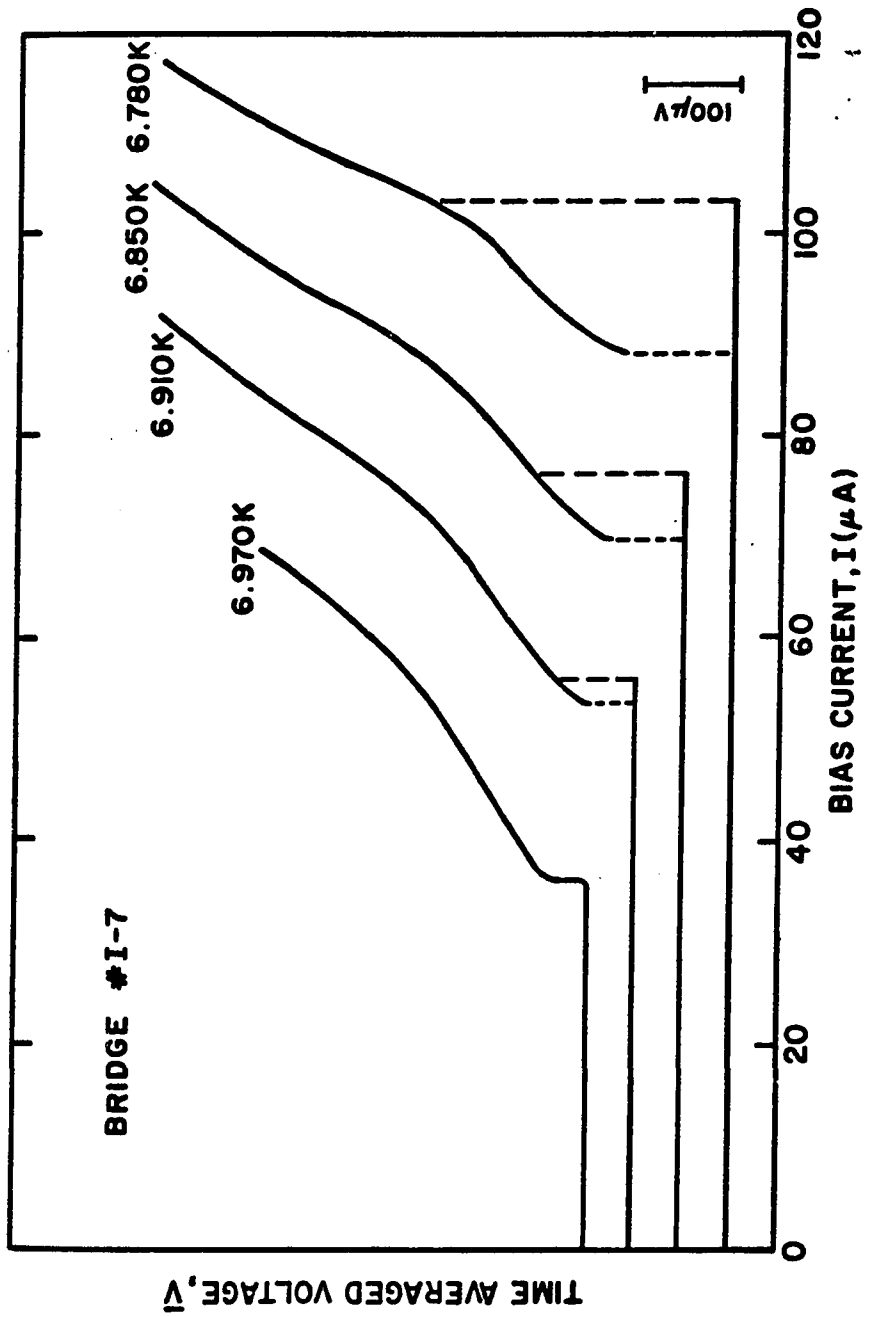

FIG. IV-6 $\bar{V}(I)$ curves of Pb-In bridge #I-7 at lower temperatures. The hysteresis induced by Joule heating dominates an increasing portion of the $\bar{V}(I)$ curve as T is reduced.

single bridge to the curve generated by McCumber (1968), if the capacitance is treated as a free parameter. We find, however, that the capacitance inferred from such a fit is $\sim$ 5 pF, larger than the physical circuit capacitance expected for a microbridge structure (cf. Song (1976)). Moreover, the capacitance inferred for a bridge of Pb-In alloy is a factor of ten larger than that inferred for a Pb-Bi bridge of the same shape and dimensions. In addition, the variable-thickness bridges discussed in the latter part of this work show much less hysteresis, despite a short-gap, thick-bank geometry which must certainly increase the capacitance. Therefore we conclude that shunt capacitance is not the dominant source of hysteresis in the $\bar{V}(I)$ curves of our bridges.

The fact that hysteresis is more severe in Pb-Bi bridges than in Pb-In bridges also argues against the relaxation-time models, since $Pb_{0.7}Bi_{0.3}$ has a larger gap and stronger electron-phonon coupling than $Pb_{0.9}In_{0.1}$ (see Adler et. al. (1967) and Adler and Ng (1965)).

In the simplest effective-temperature model of heating-induced hysteresis, the downset current I_d may be taken to represent the critical current of the bridge at the effective temperature:

$$T_{eff} = T_B + \Delta T \tag{8}$$

For $\Delta T << T_B$, ΔT should be proportional to $I_d\bar{V}(I_d)$, the power dissipation just above the transition back to the zero-voltage state. This linear dependence is observed in all seven UTBs for which sufficient data are available, and an example is shown in Figure IV-7. The constant of proportionality corresponds to the thermal resistance for heat flow out of the bridge. The experimentally-observed values of

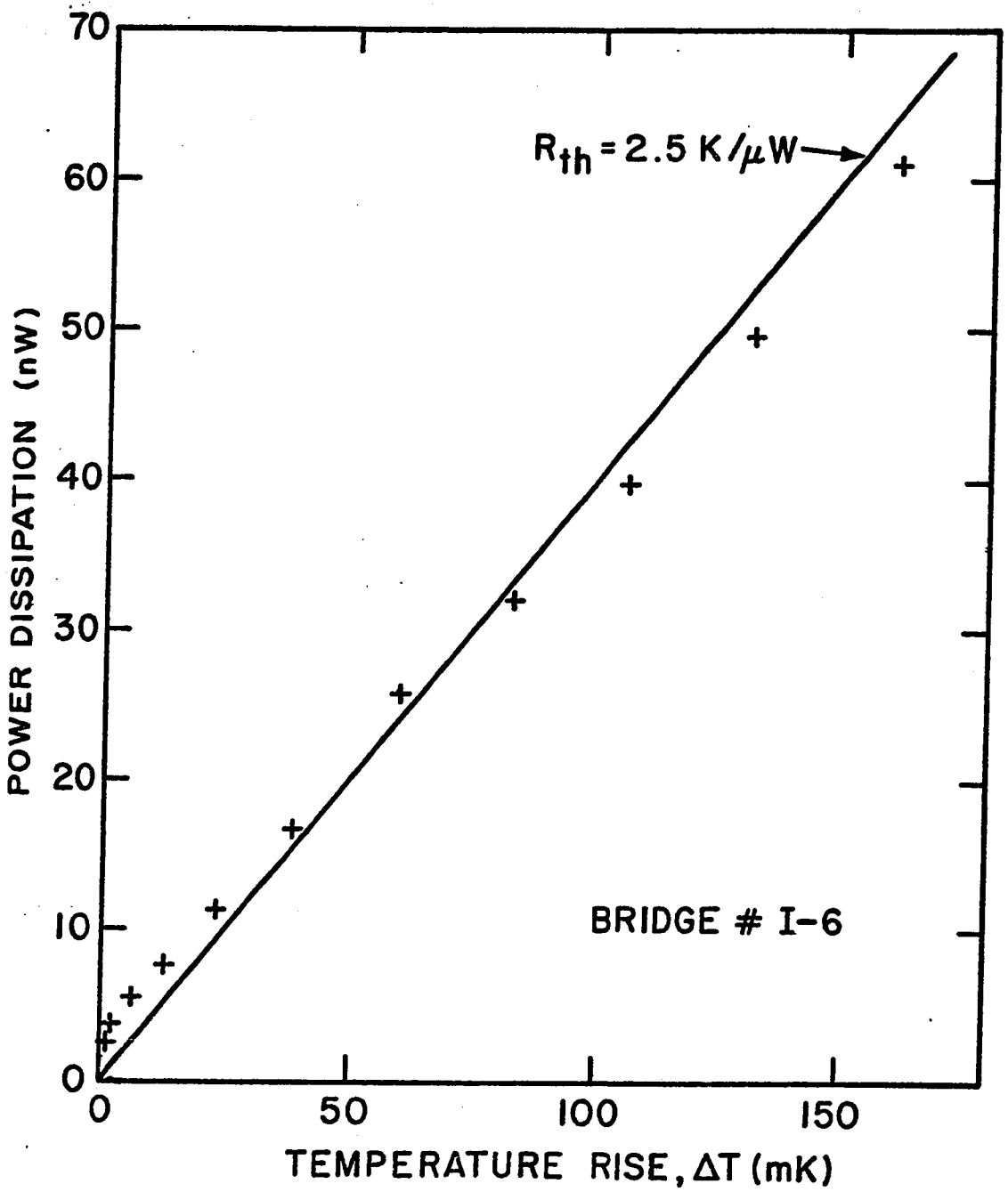

FIG. IV-7. Power dissipation just above the voltage downset, $\bar{V}_d \times I_d$, versus the temperature rise ΔT inferred from the downset current. The linear relationship and the magnitude of the slope confirm the diagnosis of Joule heating.

the thermal resistance are listed in Table IV-III, along with the theoretical values calculated from the radial-heat-flow equations of Skocpol et. al. (1974). In computing the theoretical values, we have used the measured electrical resistivities and the Wiedemann-Franz law to estimate the thermal conductivity, extrapolated the experimental results of Neeper and Dillinger (1964) to obtain the thermal boundary resistance, and chosen an inner radius equal to the bridge width. The agreement between the observed and calculated values of the thermal resistance is quite satisfactory for the simple model involved.

As discussed in section II.E.1, devices with hysteretic $\bar{V}(I)$ curves are generally undesirable for analog applications. Thus, the range of temperature over which the device can be operated without hysteresis, which we call $\Delta T_{no\ hyst}$, is an important performance parameter for applications. Values of $\Delta T_{no\ hyst}$ observed for our UTBs are also listed in Table IV-III. The hysteresis-free operating range is significantly wider for the Pb-In bridges than it is for their Pb-Bi counterparts, but the dependence on bridge width is weak.

IV.C Effects of Microwave Irradiation

IV.C.1 Constant-Voltage Steps; V_{max}

Figure IV-8 shows a typical series of $\bar{V}(I)$ curves obtained for a Pb-In UTB under microwave irradiation. The parameter listed by each curve is the microwave power input to the cryostat, measured in decibels below 1 mW. Constant-voltage steps, predicted by theories discussed in chapter II, are clearly present over a limited range of microwave power. These microwave-induced steps have been observed for all of our Pb-In bridges and for the Pb-Bi bridges which are 0.60 μm wide or narrower.

In Figure IV-9, we have plotted the width (in current) of the nth

TABLE IV-III. Joule heating in uniform-thickness microbridges. $\Delta T_{\text{no hyst}}$ is the hysteresis-free temperature range, V_{max} is the maximum voltage at which microwave steps are observed, and $R_{th}^{(exp)}$ and $R_{th}^{(calc)}$ are the experimental and theoretical values of the thermal resistance for small heating. $R_{th}^{(exp)}$ is determined from thermal hysteresis plots like Fig. IV-7. $R_{th}^{(calc)}$ is calculated according to the radial-heat-flow theory of Skocpol et. al. (1974). In making this calculation, the thermal conductivity of the film is estimated from the Wiedemann-Franz law, the thermal resistance at the film-substrate boundary is extrapolated from the data of Neeper and Dillinger (1964), and the heat source radius is taken to be $r_o = w$.

Bridge #	W (μm)	d (Å)	$R_{th}^{(exp)}$ (K/μW)	$R_{th}^{(calc)}$ (K/μW)	$\Delta T_{\text{no hyst}}$ (K)	V_{max}(t=0.986) (mV)
A	1.9	900	0.45	0.8	0.050	...
B	≈0.9	630	...	...	0.100	<0.020[a]
E	0.60	610	1.5	2.7	0.085	0.150
F	≈0.5	600	2.1	3.3	0.095	0.150
I-1	≈0.5	660	...	...	0.130	0.130
I-2	0.45	660	...	...	0.085	0.130
I-4	0.35	440	2.3	2.4	0.110	0.165
I-5	≈0.3	250	4.4	3.2	0.150	0.190
I-6	0.35	440	2.5	2.4	0.140	0.205
I-7	0.20	250	4.2	4.0	0.150	0.190

[a] No microwave-induced steps were observed in the $\bar{V}(I)$ curves of this bridge.

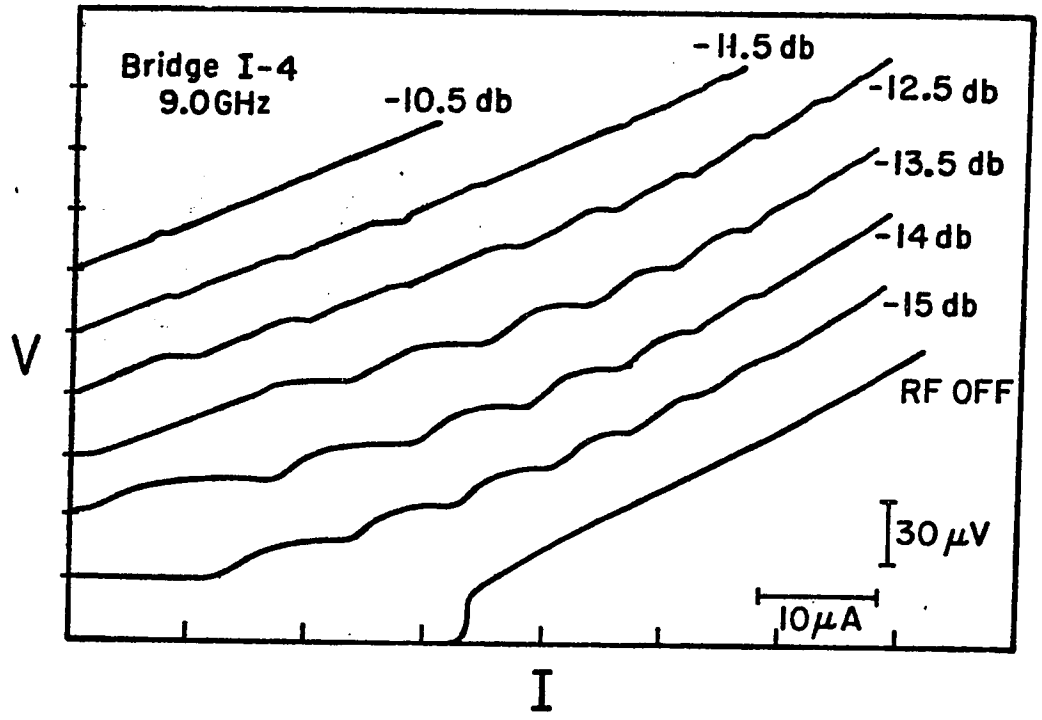

FIG. IV-8. Representative $\bar{V}(I)$ curves of Pb-In bridge #I-4 in the presence of microwave radiation. The microwave power level is in decibels below 1 milliwatt of power input to the cryostat. Note the reappearance of the zeroth step (i.e. the critical current) in the curve for -15 db. These curves were taken at t = 0.987, where the normalized frequency was $(f\Phi_o/I_c R_d) = 0.27$.

microwave step ΔI_n as a function of the microwave amplitude. (The graphical definition of ΔI_n is shown in Fig. II-3.) At low power, the behavior is similar to the predictions of the RSJ model, plotted in Figs. II-3 and II-4. The number of steps increases with microwave amplitude and the width of each individual step has an oscillatory dependence on microwave amplitude. As the power is increased further, however, the steps become progressively narrower. Eventually, they fade out entirely and the $\bar{V}(I)$ curve becomes a smooth line.

In this high-power region, the behavior of the bridge is strongly affected by microwave heating. In order to show significant microwave steps, the bridge must be biased with an ac current which is on the order of the critical current, so microwave power can easily be the dominant power dissipation in the bridge. As discussed in section II.E.1, the growth of a hotspot in the center of the bridge leads to weakening of the superconducting phase coherence, which is characterized by an effective critical current $I_c(P)$. The step width is expected to decrease proportionately with $I_c(P)$ as heating sets in. When the hotspot becomes large enough and hot enough, phase coherence is lost and the steps disappear. Both the theoretical and experimental studies by Tinkham et. al. (1977) and our own experimental results show that the loss of phase coherence occurs over a narrow range of power dissipation.

The voltage of the highest observable microwave step V_{max} is a useful parameter for characterizing the heating limitations on microwave response of a microbridge. Through the Josephson frequency relation ($hf = 2 e\bar{V}$), V_{max} defines a limit on the frequency of device operation as well as a limit on the signal level. For the alloy bridges studied here, we find that V_{max} increases rapidly as the temperature is lowered,

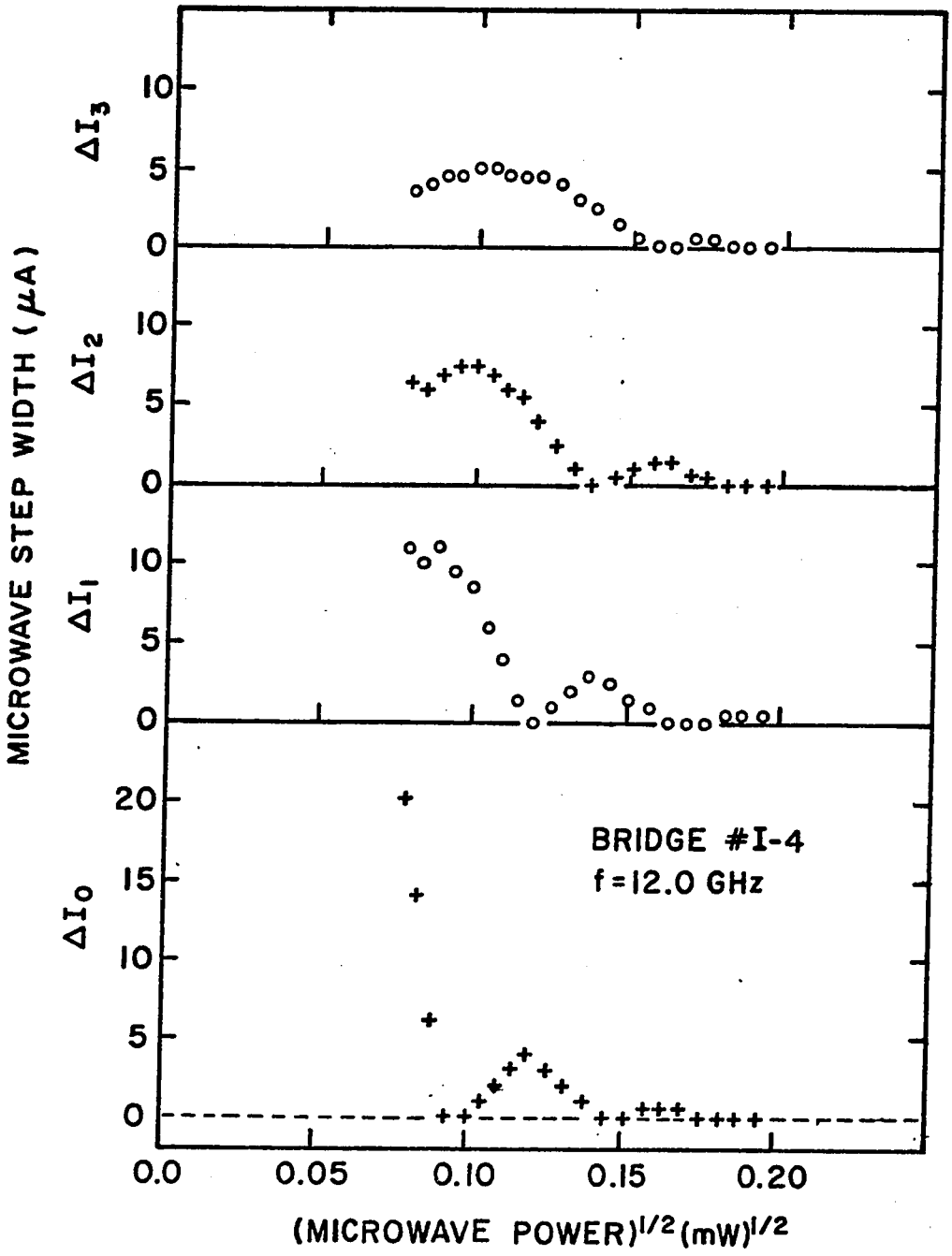

FIG. IV-9. Microwave step width ΔI_n versus (microwave power)$^{1/2}$. The oscillatory dependence of Fig. II-4 is truncated at high power by Joule heating. These data were taken at t = 0.987, where I_c = 33 μA, so that the normalized frequency was $(f\Phi_o/I_cR_d)$ = 0.27.

then saturates at temperatures $T \approx 0.95\ T_c$. This is illustrated in Figure IV-10.

Values of V_{max} ($t = 0.986$) are listed in Table IV-III. There is a general trend toward higher V_{max} in narrower bridges, but it is rather weak, apparently due to the fact that $I_c^2 R_d$ decreases about as rapidly as R_{th} increases when W is reduced. For example, Table IV-I shows that $(I_c(t = 0.98))^2 R_d$ of bridge #I-4 is 1.8 times $(I_c(t = 0.98))^2 R_d$ of bridge #I-7, while Table IV-III shows that R_{th} of bridge #I-7 is 1.8 times R_{th} of bridge #I-4. Since the microwave current required scales roughly as I_c, the result is that V_{max} is similar for the two bridges. The narrower bridges have been tested at lower temperatures, yielding $V_{max} \approx 375\ \mu V$ for #I-6 and #I-7 at $t \approx 0.90$. The magnitude of V_{max} observed for these Pb-alloy UTBs is similar to that observed by Skocpol et. al. (1974) in their study of low-resistance Sn UTBs. Those bridges were larger than ours, but had longer coherence lengths, so that the scaling discussed in section II.E.1 roughly applies.

IV.C.2 Calibration of Absolute Microwave Sensitivity

To maintain a hotspot of constant size and temperature, any increase in the microwave power delivered to the bridge must be compensated by a decrease in the dc power dissipation $I\bar{V}$. Specifically, $I_{max}V_{max}$, the dc power dissipated by the bridge when biased on its highest observable microwave step, must decrease linearly with any increase in the incident microwave power. The rate of decrease corresponds to the coupling constant for microwave power, so it should be independent of temperature. A plot of $I_{max}V_{max}$ versus microwave power at the input to the cryostat is the subject of Figure IV-11. The dependence is indeed linear with a temperature-independent slope, confirming

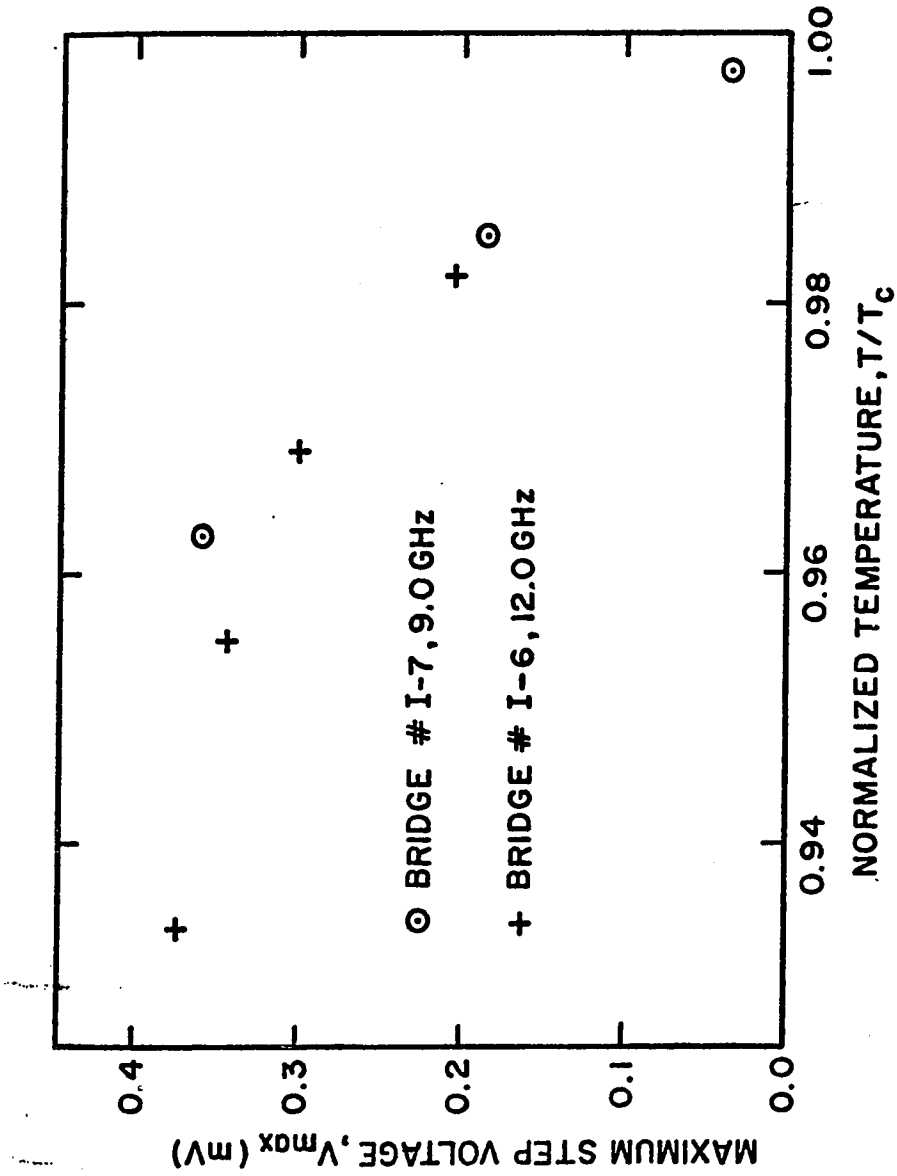

FIG. IV-10 Voltage of the highest observable microwave step, plotted versus normalized temperature for two Pb-In UTBs.

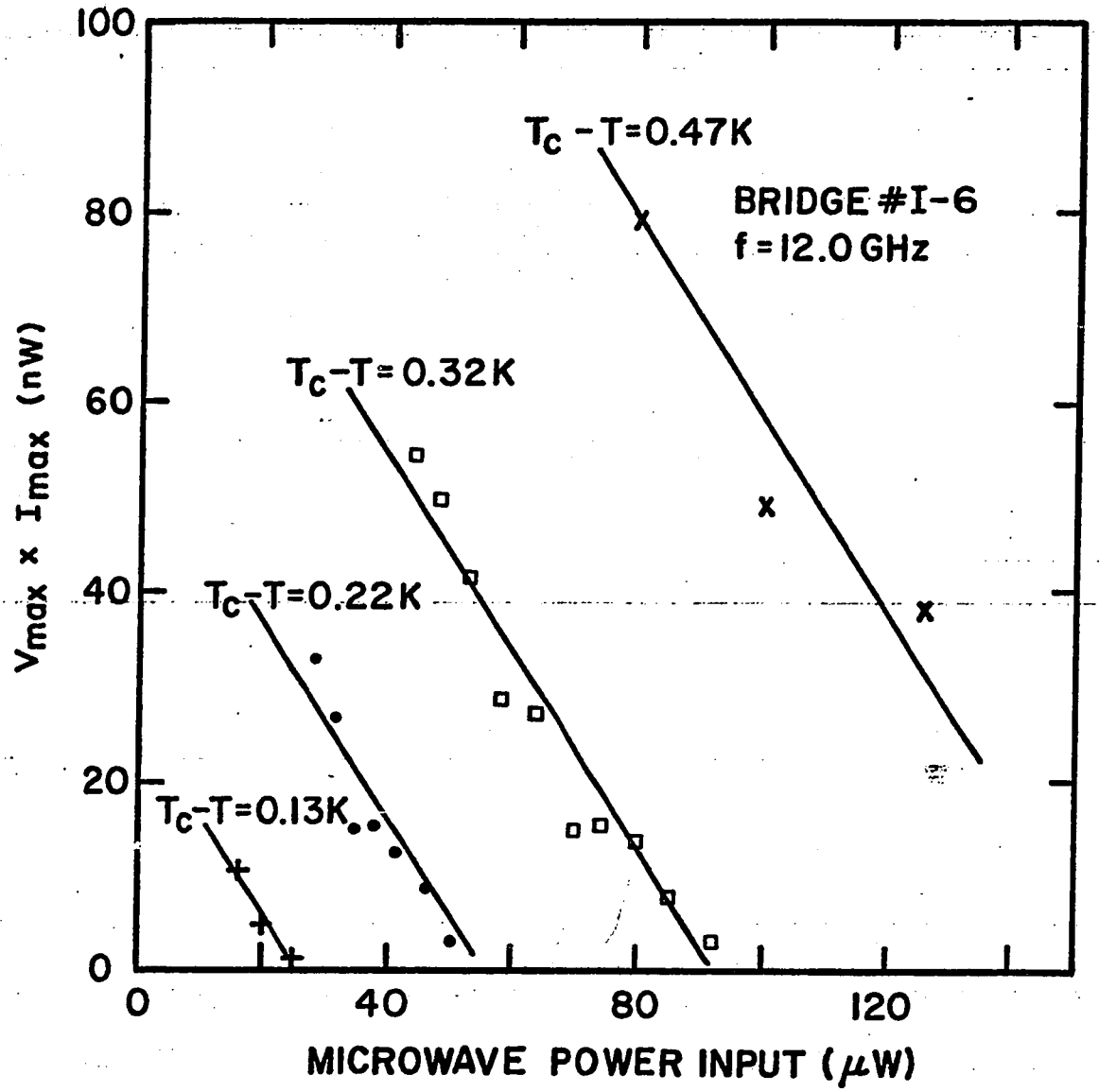

FIG. IV-11. Power dissipation at the highest microwave step versus microwave power input to the cryostat. The linear relationship with temperature-independent slope confirms that Joule heating is limiting the microwave step response. By bolometric arguments, the value of the slope yields a microwave coupling constant of 1.1×10^{-3} W/W for bridge #I-6 at 12.0 GHz.

the diagnosis of heating limitation. Similar plots for other bridges yield the same result. Coupling constants for different bridges at 12 GHz range from 2.4×10^{-4} to 1.2×10^{-3}, with 20% uncertainty in the value for any particular bridge.

The microwave coupling constants derived from the heating model can be used to provide an absolute calibration of the Josephson-effect response of the microbridges. In effect, the bridge is used as a bolometer and the microwave power is determined by the dc substitution method. This method has been used to calibrate the experimental values of $\tilde{I}_1$, the microwave current at the first zero of I_c, for several bridges in the range $0.969 \leq t \leq 0.987$. At this operating point, dc power dissipation is zero and microwave power is low, so heating is minimized. Table IV-IV presents the experimental values of $\tilde{I}_1$ and compares them to the results of the calculations by Russer (1972), which were based on the RSJ model with a current bias:[3]

$$I(\tau) = I_o + \tilde{I} \sin(2\pi f\tau) \qquad (9)$$

The experimental and theoretical values of $\tilde{I}_1$ agree within a factor of two, so calculations of absolute microwave sensitivity based on the current-biased RSJ model are well-justified for these bridges, at least near T_c.

IV.C.3 Noise Rounding and Non-RSJ Effects

Constant-voltage steps, shown in Figs. IV-8 and IV-12, are always rounded at the ends, unlike the simple theoretical curves of Fig. II-3.

---

[3] Since R_d is less than 6Ω for each of the bridges listed in the table, the assumption of current bias through a large source resistance seems appropriate, a conclusion which is supported by the small values of the microwave coupling constant.

TABLE IV-IV. Absolute microwave sensitivity of uniform-thickness microbridges. $\tilde{I}_1$ is the microwave current at the first zero of the n = 0 step (i.e. the first zero of the critical current), I_{co} is the critical current without microwaves, and $\nu \equiv (f\Phi_o/I_{co}R_d)$ is the normalized frequency. Bridge parameters are given in Table IV-I, and f = 12.0 GHz.

Bridge #	T/T_c	ν	$(\tilde{I}_1/I_{co})^{exp}$	$(\tilde{I}_1/I_{co})^{calc}$
I-6	0.969	0.080	1.4	1.05
I-4	0.972	0.081	1.2	1.05
I-5	0.779	0.111	1.4	1.08
I-6	0.982	0.171	1.6	1.11
I-5	0.986	0.183	1.6	1.12
I-4	0.987	0.269	2.6	1.25

This rounding is probably due to noise, since it is less severe at high frequencies and low device resistances. Figure IV-12a demonstrates the effect of microwave frequency on the $\bar{V}(I)$ curves of bridge #E, which has $R_d = 7.3\ \Omega$. At 12 GHz, the change in $d\bar{V}/dI$ associated with the step is much larger than it is at 6 GHz. (Only one step is visible at 12 GHz because of the small value of V_{max}.) At a frequency of 4 GHz, no steps are distinguishable on the $\bar{V}(I)$ curve, although some variation of $d\bar{V}/dI$ might be observed if a lock-in amplifier were used. The effect of device resistance on step rounding is illustrated in Figure IV-12b. The curves, taken at the same normalized temperature with microwave level sufficient to depress I_c to 50% of its unperturbed value, show much sharper steps for the low-resistance bridge. This explains the relatively small amount of rounding observed in most previously-studied microbridges, which usually had $R_d < 1\ \Omega$.

The intrinsic thermal noise of the bridge is sufficient to account for the observed dependence on frequency and device resistance. Likharev and Semonov (1972) have estimated the linewidth of the Josephson oscillation within the framework of the RSJ model. First-order correlation theory is used to calculate the spectral density of the instantaneous voltage in terms of the spectral density of the current fluctuations, assumed to be much smaller than I_c. Likharev and Semonov (1972) find that thermally-induced current fluctuations, which for $T > T_c$ yield the usual Johnson noise, lead to a linewidth:

$$2\Gamma = \frac{3}{2}\ \frac{kTR^2}{\Phi_o^2} \qquad (10)$$

in the voltage signal. Inserting the values $R = 7.3\ \Omega$ and $T = 8.3$ K which are appropriate to the test of bridge #E, one finds:

FIG. IV-12. Effect of frequency and device resistance on noise rounding of microwave steps. (a) Steps are more rounded at lower frequencies. (b) Steps are more rounded in high-resistance devices.

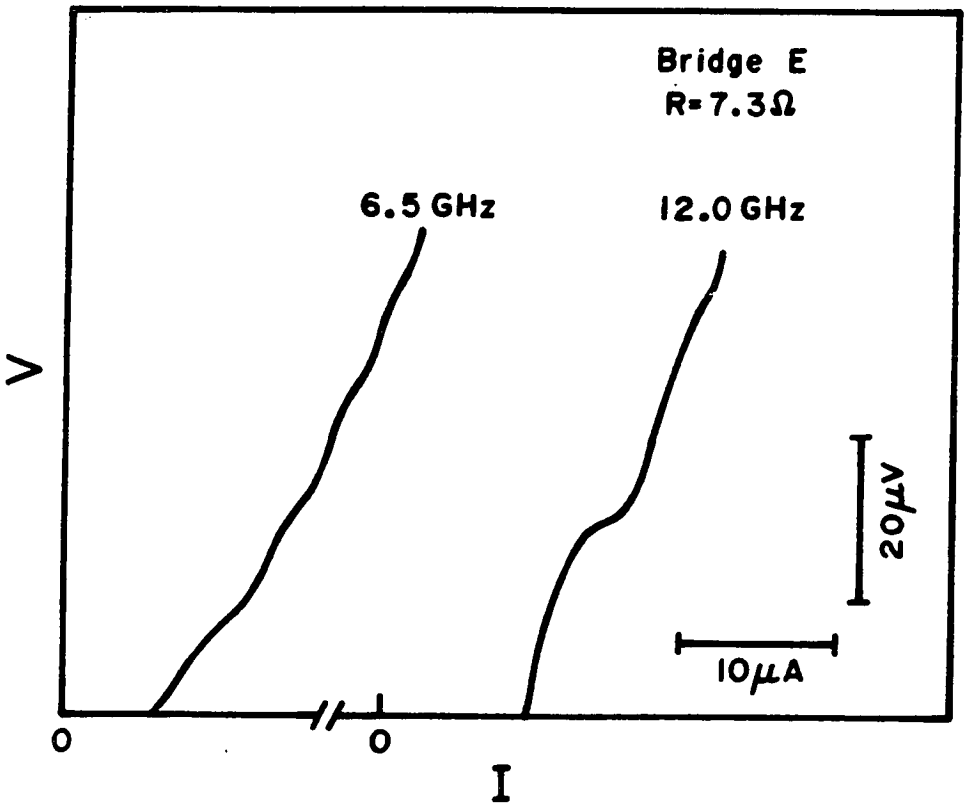
Bridge E
R=7.3Ω
6.5 GHz
12.0 GHz
V
20μV
10μA
0
0
I

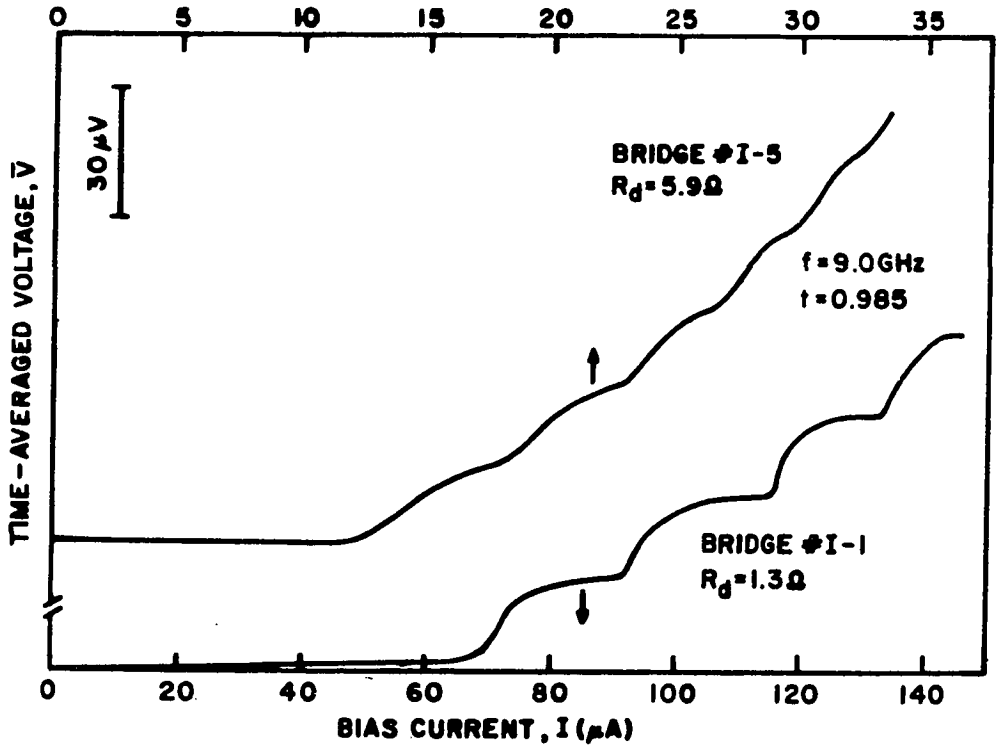
0
5
10
15
20
25
30
35
30μV
BRIDGE #I-5
Rd=5.9Ω
f=9.0GHz
t=0.985
BRIDGE #I-1
Rd=1.3Ω
TIME-AVERAGED VOLTAGE, V̄
0
20
40
60
80
100
120
140
BIAS CURRENT, I (μA)

$$2\Gamma = 4.3 \text{ GHz} \tag{11}$$

in good agreement with the observed low-frequency limit of microwave steps.

Subharmonic steps (i.e. steps at voltages (nhf/2me), where m is an integer greater than 1) have not been observed in any UTB in our study. In terms of the two fluid model of microbridge dynamics, this may imply that the $I(\Delta\phi)$ relation is sinusoidal.[4] The absence of subharmonic steps is in contradiction of the predictions of the vortex-flow models discussed in section II.C.

The Dayem effect (microwave-induced enhancement of the critical current) has not been seen in any of our UTBs. This finding is discussed in section VI.D.2, together with the analogous results for variable-thickness bridges.

Our conclusions about uniform-thickness microbridges, including those concerning operation in the vortex-flow regime, are presented in section VII.A.

---

[4] This has been demonstrated for the voltage-biased case by Gregers-Hansen et. al. (1972). Professor R. W. Henry, working in our lab, has also found subharmonic steps in analog simulations of a current-biased junction with a triangular $I(\Delta\phi)$ relation.

V. FABRICATION OF VARIABLE-THICKNESS BRIDGES

V.A Background

V.A.1 General Aspects of VTB Fabrication

The variable-thickness microbridge (VTB), illustrated in Fig. I-1b, consists of thick banks and a bridge region which is thin as well as narrow. Once a capability for fabricating uniform-thickness microbridges (UTBs) has been established, the capability can be extended to produce VTBs by either adding thick banks to the thin banks of a UTB (accretion method) or thinning down the center of a thick UTB (erosion method). The accretion method offers greater flexibility, since it is at least conceptually straightforward to use different materials for the bridge layer and the thick added banks. Unfortunately, the accretion method is intrinsically prone to problems associated with the interface between the bridge layer and the thick banks. If an oxide layer or other contamination at the interface forms a barrier to electron flow in the immediate vicinity of the bridge, the good electronic cooling and reduced depairing associated with thick banks are lost. The erosion method avoids interface problems, since the bridge and banks are formed in the same film deposition, but it demands an etching process with excellent uniformity and rate control as well as good resolution.

V.A.2 Ion Etching

Ion etching is of central importance in both the accretion and erosion methods. Ion etching offers good uniformity and rate control, at least for common electronic materials such as SiO_2 and Au, and the resolution is much better than conventional wet-chemical

etching.[1] In the accretion method, a brief ion etch can be used to remove surface contamination from the bottom layer immediately before the top layer is deposited in the same vacuum cycle. In the erosion method, ion etching appears to be an appropriate choice for the erosion step which thins the central bridge region.

The ion etching process is analogous to submicroscopic sandblasting: ions accelerated onto the workpiece remove atoms from its surface by sputtering. If the etching is assisted by chemical reactions between the ions or background gas and the workpiece or sputtered atoms, the process is called reactive-ion etching. Various configurations have been used to generate and control the ion flux. In this work, the workpiece is maintained in a relatively high vacuum ($\approx 10^{-4}$ Torr), where it is exposed to a beam of ions produced by a separate ion gun.[2] This configuration, known as ion-beam etching or ion milling, has been treated in a good review article by Melliar-Smith (1976).

The ion gun used in this study was a cold-cathode, hollow-anode type, Commonwealth Scientific[3] model 2-30. In this gun, ions are produced by a dc glow discharge at a gun voltage of 3-10 kV and extracted

---

[1] The resolution of wet-chemical etching is typically greater than or equal to the film thickness, due to etching under the mask. Thus, wet etching is not suitable for patterning on the 0.1-μm size scale.

[2] This is not a scanned, focussed beam which is used to write patterns, as in e-beam lithography. Rather, it provides a roughly unidirectional flux of ions over a disk of ≈ 1-cm radius. The current density of the ion beam falls off rapidly beyond a radius of ≈ 0.5 cm. In our system, the ion gun is attached to the baseplate of the vacuum station.

[3] Commonwealth Scientific Co., Alexandria, Va.

through a single cathode orifice of 4 mm diameter. The gun is insulated from the vacuum chamber and an additional voltage supply is provided so that the ions, produced at energies up to the gun voltage, can be accelerated by an additional 0-5 kV before reaching the workpiece. As discussed by Prober, Feuer and Giordano (1980), the accelerator supply can be reversed so that the ions are decelerated to nominal energies of $\sim$ 1 keV. These low-energy ions are necessary for the wire-fabrication process discussed by the above authors. In this microbridge work, satisfactory etch rates and edge profiles have been achieved with both accelerated and decelerated configurations. In the course of this study, various materials have been tested as masks or workpieces for ion-beam etching, and Table V-I lists etch rates observed for some of these materials. In some cases, interferometry was used to measure the etch depth in a partially-etched film, while in others, a film of known thickness was etched to completion. Unfortunately, the current density of the ion beam is difficult to measure exactly, because of secondary electron emission from the target and ionization of the residual gas in the sample chamber. We have tabulated the estimated beam current density, given by

$$J_b\left(\frac{mA}{cm^2}\right) = \frac{I_b(mA)}{\pi(cm^2)} \qquad (1)$$

where I_b is the current flowing through the accelerator supply. This estimate of J_b is probably more accurate for the accelerated configuration.

As can be seen in the table, we have investigated three types of reactive-ion-beam etching. This reactive-ion etching was necessary because both glass and sapphire substrates etch very slowly in pure Ar,

TABLE V-I. Ion-beam etching rates. The mask: substrate combinations which are marked with an asterisk (*) were used for virtually all of the actual VTB fabrication. The mask: substrate ratios are probably more reproducible than the absolute etch rates.

Mask:Substrate	Etching gas	Background gas[a]	Gun voltage (kV)	Accel. voltage (kV)	Current density[b] ($\mu A/cm^2$)	Rate (nm/min)
···:$Pb_{0.9}In_{0.1}$	Ar	none	6.0	+1.0	33[c]	···:7.3
*Cr:0211 glass	Ar	O_2	8.0	-3.0	45	1.7:4.0
Cr:0211	Ar	CHF_3	8.0	-3.0	35	1.9:4.0
Cr:0211	CHF_3	none	6.0	-0.8	35	1.5:7.5
Cr:0211	CHF_3	O_2	4.6	-0.5	20	0.8:5.3
*Cr:0211	CF_4	none	5.5	-0.7	30	1.4:6.4
Cr:SiO_2	CF_4	none	5.5	-0.7	30	1.3:3.3
Al:0211	CF_4	none	5.5	-0.7	30	1.7:6.0
Ti:0211	CF_4	none	5.5	-0.7	30	0.8:5.8
*Ni-Cr:0211	CF_4	none	5.5	-0.7	30	1.7:5.2
MgF_2:···	CF_4	none	5.5	-0.7	30	2.4:···
C:0211	CF_4	none	5.5	-0.7	30	1.8:4.8
*Ni-Cr:polyimide	O_2	none	4.0	-0.2	10	0.25:6.0

[a] All background gases were fed into the bell jar by continuous leak, at a rate sufficient to provide 1.5-2.0 x 10^{-5} Torr partial pressure. The total pressure in the sample chamber during ion-beam etching was typically 1.0 - 1.5 x 10^{-4} Torr.

[b] As discussed in the text, the nominal current density is estimated to be $1/\pi$ times the current provided by the accelerator supply.

[c] For this test, performed using a large ($\approx$ 25 cm) gun-to-sample distance, the nominal current is estimated to be $1/4\pi$ times the current provided by the accelerator supply.

more slowly than the conventional mask materials such as Cr. Under these conditions, masks must be very thick, which limits the resolution with which they can be patterned, both because of the need to use thick photoresist and the roughness and/or rounded profiles of the edges of thick metal mask films. As shown by Cantagrel and Marchal (1973), the etch rate of certain metallic mask materials, including Cr and Al, can be greatly reduced by including an admixture of O_2 in the background gas. Apparently, the O_2 forms a tough surface layer on the mask which reduces its etching rate. Our ion gun operates in the continuously-pumped mode, so we provided the O_2 in the form of continuous leak into the bell jar. With a leak rate corresponding to 2×10^{-5} Torr of O_2 background, out of a total pressure of $\approx 1 \times 10^{-4}$ Torr, we obtained a differential etch ratio (mask etch rate/substrate etch rate) of about 2.5:1 for Cr masks on substrates of type 0211 glass.[4] Although this differential etch ratio is suitable for shallow structures, a higher ratio as needed to fabricate VTBs with large bank thicknesses by the process described in section V.B. Following the work of Lehmann and Widmer (1978) on reactive sputter etching of SiO_2, we tried the fluorocarbon gases CHF_3 and CF_4 and obtained differential etch ratios of about 4.5:1 for Cr on 0211 glass when either of these gases was used as the sole etching gas.[5] We also tried using these

---

[4] As noted in chapter III, type 0211 glass was used because it is readily available as standard Corning cover glasses, which have a very smooth surface and optical properties well-suited to through-the-substract projection lithography.

[5] This is not nearly as high as the differential etch ratios of 20 or more obtained by Lehmann and Widmer (1978). This is probably because the higher energy of the ion-beam process increases the physical sputtering while the lower background pressure reduces the chemical action.

gases as background gases with an etching beam of Ar, but this approach was not as effective. With 1.5×10^{-5} Torr of CHF_3 gas in the background gas, the differential etch ratio was $\approx$ 2:1. We also found that an O_2 background did not enhance the effectiveness of the CF_4 etch gas. The Cr (mask) - 0211 glass (substrate) - CF_4 (etch gas) system is satisfactory for VTBs with moderately thick banks, and this was the system used in the fabrication of bridges #S-6 and #S-7. For bridges #S-8 through #S-10 and #S-12, Ni-Cr mask films were used, for the reasons discussed in section V.C. However, the highest etch ratios achieved to date were obtained by modifying the substrate. The glass substrate was coated with a layer of polyimide (DuPont Product #PI-2550; see Appendix B for the deposition procedure), which etches very rapidly in O_2. This process was suggested by the work of DeGraff and Flanders (1979). Using O_2 as the etching gas, differential etch ratios of about 25:1 were obtained for Ni-Cr on polyimide. Although some nonuniformity was observed in partially-etched films of polyimide, this was not a problem because the smooth glass substrate served as an etch stop in the actual VTB fabrication process. The Ni-Cr-polyimide-O_2 system was used to fabricate the thick-bank VTBs #S-11, #S-13, #S-14, and #S-15.

V.A.3 Erosion Method

Our first attempt to fabricate VTBs employed the erosion method. First, a thick ($\approx$ 65 nm) UTB of Pb-In alloy was fabricated by the procedures detailed in chapter III. Then a layer of photoresist (PR) was spun onto the Pb-In film and a rectangular window in the PR was exposed by the microscope projection process and developed. The window was 20 μm in length and 0.2 μm in width and it was centered over the narrow part (bridge region) of the UTB. Finally, the sample was subjected to

ion-beam etching for about 1/2 the time needed to completely remove an unmasked film of Pb-In of the same thickness. The PR was then removed by ultrasonic agitation in acetone[6] and the sample was examined in the scanning electron microscope.

The results, shown in Fig. V-1, were disappointing. It had been expected that the ion bombardment would uniformly reduce the thickness of the unprotected region of metal film, producing a narrow trough across the bridge region. Instead, the ion beam drilled a neat, round hole through the bridge, while the thickness in the rest of the bridge was not measurably affected, as is shown by Fig. V-1b, an SEM photo taken at glancing incidence. (In Fig. V-1a, taken at normal incidence, a second semicircular hole can be seen at the edge of the bridge.) This surprising effect might be attributed to incomplete exposure or development of the PR mask, except for the evidence of nonuniform etching of unmasked Pb-In films presented in Figure V-2. When smooth Pb-In films (see Fig. III-11b,c) are subjected to ion etching, small pits and pinholes rapidly form. As etching is continued, these pinholes increase in number and expand in size (Fig. V-2) until only islands of metal are left. Eventually, these islands are also etched away.

---

[6] Although most of the PR was successfully removed, a thin crust remained at some parts of the pattern edges. Apparently, ion bombardment, either due to etching or to the glow-discharge oxidation of the undercoat (see chapter III), hardens the surface of the PR, making it insoluble in ordinary solvents. This is not too surprising, since Shipley type-1350 resist has been used as a negative electron resist by McCarthy and Stanko (1974), and Melliar-Smith (1976) has reported hardening of PR surface due to ion-beam etching. The residual crust, which can be seen in Figs. V-1b and V-12a, is electrically nonconductive.

FIG. V-1 Unsuccessful VTB produced by the ion-erosion method. (a) Viewed at normal incidence; (b) Viewed at glancing incidence. Note the extremely uneven ion-etching, which produces holes at some points before other areas are noticeably thinned. The trough-shaped object in the background of (b) is a crust of ion-hardened photoresist.

(a)

0.2 μm

(b)

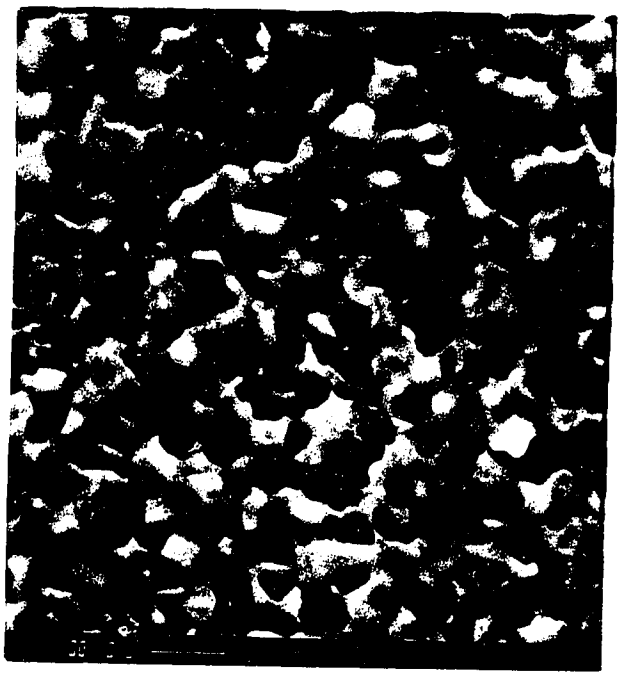

FIG. V-2 Non-uniform ion etching of unmasked Pb-In film.

The nonuniform etching persists when the copper substrate holder is held at 77 K, when an atmosphere of 1.5×10^{-5} of O_2 is added to the background gas in the bell jar, and when the ion beam impinges on the substrate at an angle of 30°, instead of the usual normal incidence (90°). Tests on (nominally) pure Pb films yielded the same results as on Pb-In films.

The nonuniform etching seen in Fig. V-2 is very different from the results obtained when etching SiO_2 or Al_2O_3, materials in which surface roughness can be removed by ion etching. (See Smith (1974).) The cause of the nonuniform etching, which has also been reported in In, is not known. Sandell et. al. (1977) have attributed nonuniform ion-beam etching in In films to etch rates which depend on crystal orientation. We do not believe that such effects are dominant in Pb-In films, since neither the pinholes nor the remanent islands of the partially-etched films show the angular appearance or the uniform size one would expect of crystallites. Whatever its cause, the nonuniform etching of Pb-In films effectively precludes the use of ion-beam erosion as a reproducible method of VTB fabrication in this material.

V.A.4 Early Step-Edge Method

By modifying the standard concept of a strictly planar substrate, one makes possible a third method of VTB fabrication which we call the step-edge method. In the step-edge method, the device film is deposited onto a substrate which has a step etched into it. That is, the substrate is patterned as part of the fabrication process. The film thickness in the vertical step edge and the film thickness on the large planar surfaces can be separately controlled by adjusting the angle of film deposition, which must be unidirectional. First,

suppose that evaporation is carried out normal to the large planar surfaces (defined as an altitude angle of 90°). Then the film thickness on the vertical step edge will be zero, regardless of the film thickness D on the large planar banks. On the other hand, if the evaporation is from an altitude angle slightly less than 90° (and from an azimuth angle pointing into the step), a thin film of thickness $d << D$ will be deposited on the vertical step edge. For an arbitrary altitude angle $(90° - \theta)$, the ratio of the thicknesses will be:

$$d/D = \tan\theta \qquad (2)$$

In this way, the thickness variation along the VTB can be provided with a single film deposition (no interface problems) and no etching.

The simplest step-edge fabrication process, illustrated in Figure V-3, comprises four steps:

(1) Photolithography and liftoff patterning are used to define a half-plane of Cr film with a straight, smooth edge on a glass substrate. This Cr pattern serves as an integral mask during subsequent ion-beam etching.

(2) The exposed regions of the substrate are ion-beam etched to a depth L_s. Although the mask film is of a material which etches more slowly than the substrate, the mask is also somewhat eroded. Then the Cr mask is removed by chemical etching,[7] exposing a glass substrate with a step of depth L_s.

(3) Following the procedures described in chapter III, a PR pattern

---

[7] For mask removal, we used a standard Cr etch, consisting of:
2000 ml distilled H_2O
100 ml HNO_3
330 gm $(NH_4)_2Ce(NO_3)_6$ (ceric ammonium nitrate).

FIG. V-3 Simple step-edge method of VTB fabrication. (a) Half-plane mask for ion-beam etching has been fabricated on flat substrate; (b) After ion-beam etching of the substrate, the metal mask is chemically stripped to expose a substrate with an etched step; (c) A photoresist pattern suitable for UTB liftoff fabrication is centered over the vertical edge of the substrate step; and (d) A superconducting film is evaporated from an altitude angle of slightly less than 90° and the photoresist pattern is lifted off, to complete the VTB. As noted in the text, this process has drawbacks as well as advantages.

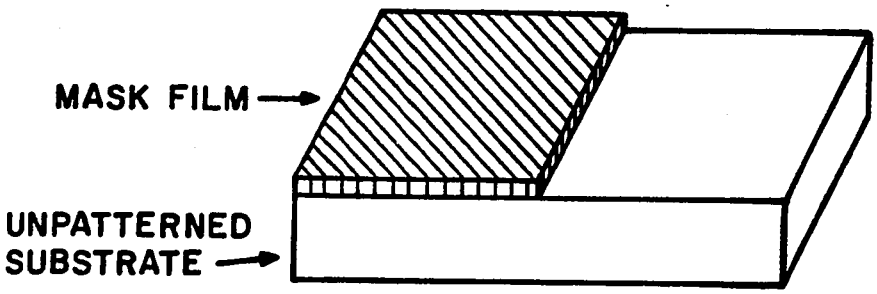

(a)

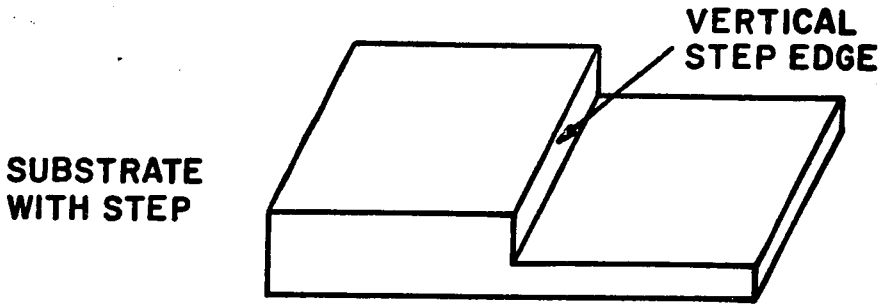

(b)

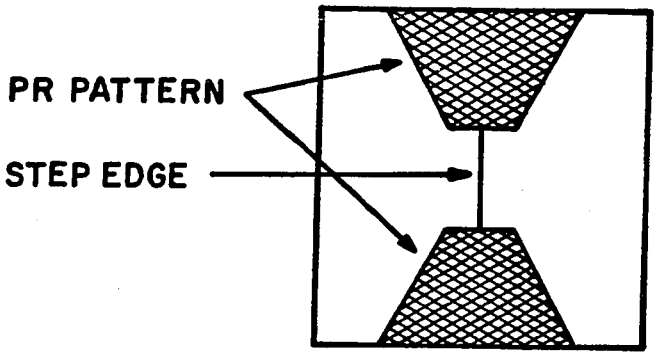

(c)
(TOP VIEW)

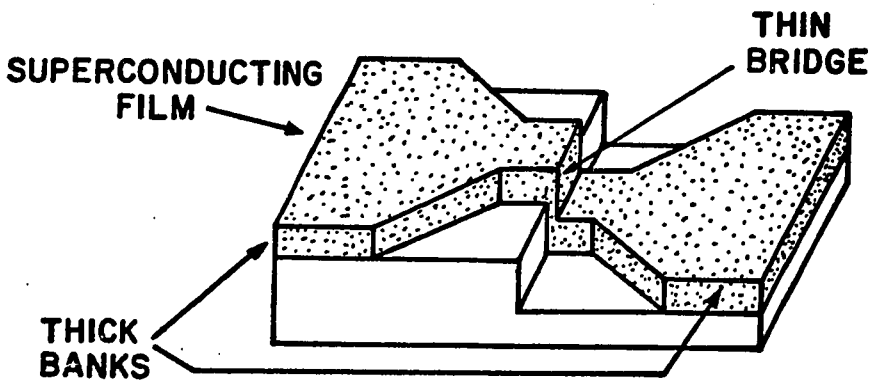

(d)

suitable for liftoff processing of UTBs is formed on the substrate. The narrowest part of the bridge pattern is aligned over the vertical step edge.

(4) A superconducting film is evaporated from an angle slightly less than normal incidence, from an azimuthal direction which allows coating of the vertical step edge. Then the PR and the areas of film overlying it are lifted off in acetone to complete the VTB.

Figure V-4 shows a scanning-electron micrograph of a bridge produced by the above process. The microbridge pattern is not exactly aligned over the substrate step; the width of the UTB pattern at its narrowest point is 0.3 μm, but its width where it crosses the step edge is 0.5 μm. The bank thickness is D = 110 nm, and the bridge thickness is calculated to be d = 20 nm. Three bridges of this type were electrically tested at low temperatures, and it was found that the Joule heating parameters V_{max} and $\Delta T_{no\ hyst}$ were not very different from the values obtained for the UTBs of chapter IV. For example, $V_{max}(t = 0.9) = 0.32$ mV and $\Delta T_{no\ hyst} = 0.10$ K for the bridge shown in Fig. V-4.

The disappointing Joule-heating performance of these single-step bridges is partially due to the misalignment of the PR pattern and partially due to the intrinsic geometry of the microbridges. The misalignment is a rather serious practical difficulty. Although both the substrate step edge and the projected pattern are visible in the microscope during alignment, the optical resolution, $\tilde{>}$ 0.2 μm, simply does not permit sufficiently accurate centering of the bridge pattern over the step. Even if accurate centering could be achieved by a very experienced operator, however, the bridge geometry would be less than

FIG. V-4 VTB fabricated by simple step-edge method. (a) Viewed at normal incidence, the misalignment of the metal pattern over the step is clearly visible. (b) Same bridge, viewed at 45° angle of incidence.

(a)

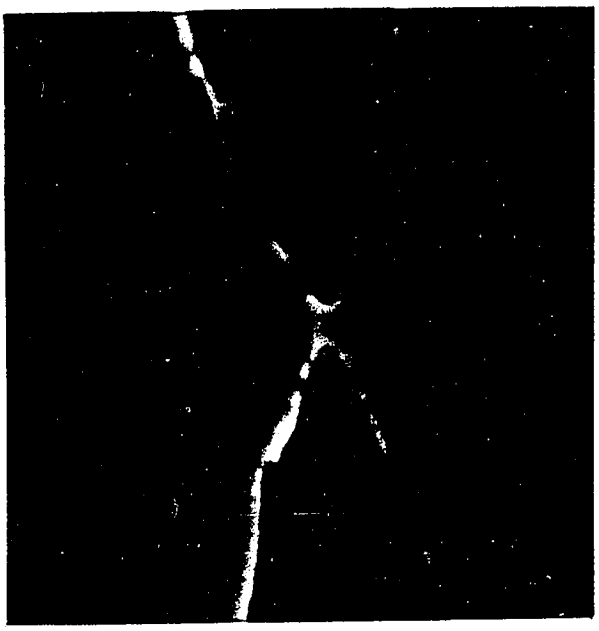

0.2 μm

(b)

ideal. The thin (vertical) region of the bridge, inserted into the center of the structure, increases the overall bridge length compared to that of the UTB. The length of the UTB is already comparable to the coherence length, so an increase in L is not desirable. Also, the expansion of the banks into the width dimension does not occur at the same point as the expansion into the thickness dimension, so the diffusion of electrons out of the bridge (and thus the cooling of the bridge) is never really three-dimensional.

On the other hand, the step-edge method of VTB fabrication offers two significant advantages over the planar methods. First, bridge-bank interface problems are absent, an important aspect for the reasons noted above. The second advantage is the capability of achieving extremely small bridge lengths. Since the length of the thinned region is given by the step depth L_s minus the bank thickness D, it is not limited by the resolution of the optical lithographic process. Under appropriate conditions, both the step depth and the film thickness can be controlled to within 5 nm, and bridges less than 40 nm in length have in fact been fabricated by the advanced step-edge method described in the following section. This advanced step-edge process improves the geometry of the banks, solves the alignment problem, and allows the bridge width to be made small as the bridge length, < 40 nm.

V.B Advanced Step-Edge Method of VTB Fabrication

The advanced step-edge lithography technique utilizes two-dimensional shadowing to produce a metal-film pattern with very fine details. Using this metal film as a mask, the pattern is ion-beam etched into the substrate. As before, the microbridge is deposited on the edge of a substrate step, so that step heights determine micro-

bridge dimensions. The technique may be illustrated by considering the process sequence shown in Fig. V-5 for a bridge 50 nm wide, 25 nm thick, and 100 nm long, with banks 200 nm thick. In this example we shall assume that the evaporated metal atoms stick at the exact point of impact. This idealized ray-optics picture is a standard assumption for most shadowing processes. Deviations from this model and resulting fabrication limits will be discussed in section V.C. Also in Fig. V-5 we assume for simplicity that the chrome masking films are unaffected by the ion etching process. For the measured etching rates this is reasonably accurate.

(a) A 50-nm step is ion etched into the glass substrate. A thin 20-nm chrome film, patterned by conformal-photolithography techniques (see section III.B.3), is used as the etching mask. A CF_4 reactive-ion etching beam is used to enhance the etch rate of the substrate. The chrome film is removed by chemical etching.

(b) A second stage of photolithography, using through-the-substrate projection exposure (see section III.B.3), leaves a half-plane of photoresist whose edge is perpendicular to the initial step. A sharp edge profile is obtained. The top surface of the photoresist is smooth over the step, due to the spin-on application.

(c) A 100-nm chrome film is then evaporated at an angle of 45° from the substrate normal, producing a sharp shadow of the photoresist edge. Because the photoresist is thicker over the bottom of the step, the chrome shadow there falls further back from the photoresist edge than on the top of the step. The edge of the chrome film on the left therefore has a sharp jog in it (Fig. V-5d). The length of the jog is equal to the height of the initial step, 50 nm. Thus a height di-

FIG. V-5 Advanced step-edge process for fabrication of variable-thickness microbridges. (a) A shallow step is ion-beam etched into the glass substrate. (b) A second stage of photolithography leaves a half-plane of photoresist whose edge is perpendicular to the initial step. (c) Evaporation of a Cr mask film at an altitude angle of 45° produces (d) A mask with a small, sharp jog in the edge. (e) Further ion-beam etching produces the fully patterned substrate, and (f) A superconducting film is evaporated from an appropriate angle to complete the variable-thickness microbridge.

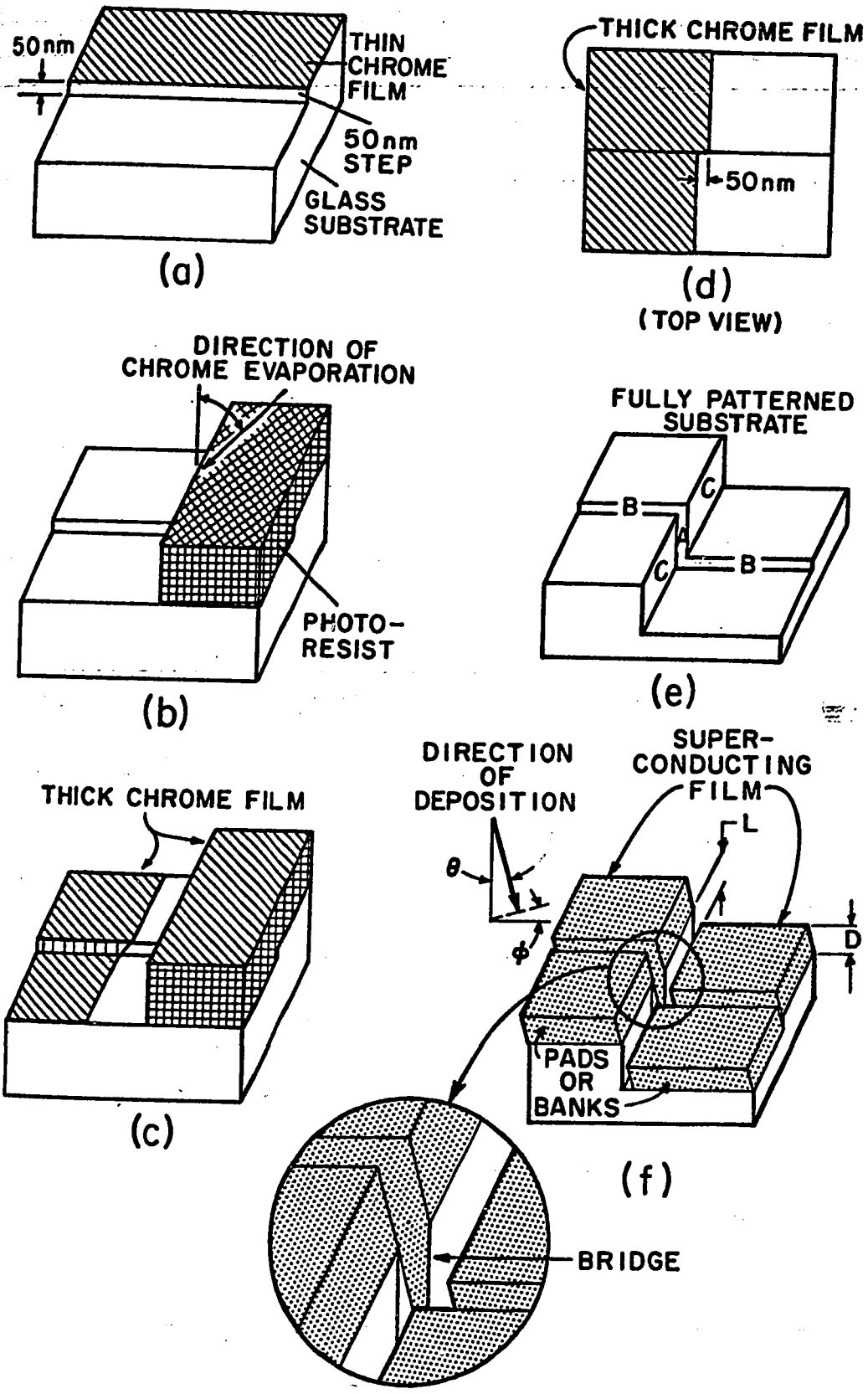
50nm
THIN CHROME FILM
50nm STEP
GLASS SUBSTRATE
(a)
THICK CHROME FILM
50nm
(d)
(TOP VIEW)
DIRECTION OF CHROME EVAPORATION
PHOTO-RESIST
(b)
FULLY PATTERNED SUBSTRATE
B
C
C
B
(e)
THICK CHROME FILM
(c)
DIRECTION OF DEPOSITION
θ
Φ
SUPER-CONDUCTING FILM
L
D
PADS OR BANKS
(f)
BRIDGE

mension has been "folded over" onto the substrate, a key part of the process.

(d) The photoresist and the chrome film overlying it are stripped in acetone, leaving the chrome film on the left half of the substrate.

(e) The half of the substrate unprotected by the chrome pattern is ion-beam etched to a depth of 300 nm. The chrome film is then removed by chemical etching to reveal the fully patterned substrate shown in Fig. V-5e. The microbridge will be formed in region A, the two pads or banks in region B.

(f) A superconducting film is evaporated to coat regions A and B of the substrate (Fig. V-5e), but not regions C. With the evaporation direction as shown, the bridge-film thickness (on the face of the jog, region A) is given by:

$$d = D \tan\theta \sin\phi \qquad (3)$$

with D the bank thickness, θ the coaltitude angle of the evaporation direction, and ϕ the azimuth angle. To form a 25-nm-thick bridge with 200-nm-thick banks, we choose $\theta = 20°$ and $\phi = 20°$. Since coarse lithography is still carried out by liftoff process, the oxide undercoat described in chapter III is used to provide good film adhesion.

With this fabrication technique <u>all</u> microbridge dimensions are determined by step or film heights and the evaporation angle. The bridge width W is approximately equal to the width of the jog and thus to the height of the first step. The vertical bridge length L_v is equal to the height of the deep step minus the pad thickness. The bridge thickness is determined by the evaporation direction and the thickness of the banks. Thus, although optical lithography is em-

ployed, device dimensions are not limited by optical diffraction, and can be extremely small.

A $Pb_{0.9}In_{0.1}$ microbridge produced with this technique, number S-6, is shown in Fig. V-6a. Its dimensions are approximately d=L=60 nm and D=240 nm. W tapers from 90 to 50 nm at the narrowest point. (These SEM photos are taken at a substrate tilt of 45°.) These dimensions, which are typical of the dozen microbridges produced to date, were determined from a series of electron micrographs at different viewing angles.

Determination of the actual microbridge length is complicated by the presence of a small horizontal gap between the banks. This is illustrated by Fig. V-7, which shows bridge #S-6, viewed at normal incidence. Within the ray-optics model, the horizontal gap L_h is proportional to vertical length:

$$L_h = L_v \tan\theta \qquad (\text{for } \phi = 90°) \tag{4}$$

and the overall length:

$$L = ((L_h)^2 + (L_v)^2)^{1/2} \tag{5}$$

is given by:

$$L = L_v/\cos\theta \qquad (\text{for } \phi = 90°) \tag{6}$$

In reality, the film topography can differ from that expected within the ray-optics model, as discussed in the following section, so the overall length was determined from eq. (5) above, using L_h as measured from SEM photographs.

V.C Non-Idealities and Process Refinements

The observed microbridge dimensions and shape are close to those

FIG. V-6 Results of the advanced step-edge process for VTB fabrication. (a) This scanning-electron micrograph of Pb-In VTB #S-6 is taken at a viewing angle of 45°, with an azimuth angle which produces a perspective similar to Fig. V-5(f). (b) Scanning electron micrograph of a bare, 300-nm substrate step, taken at the same viewing angle as part (a), reveals a sharp, square step profile.

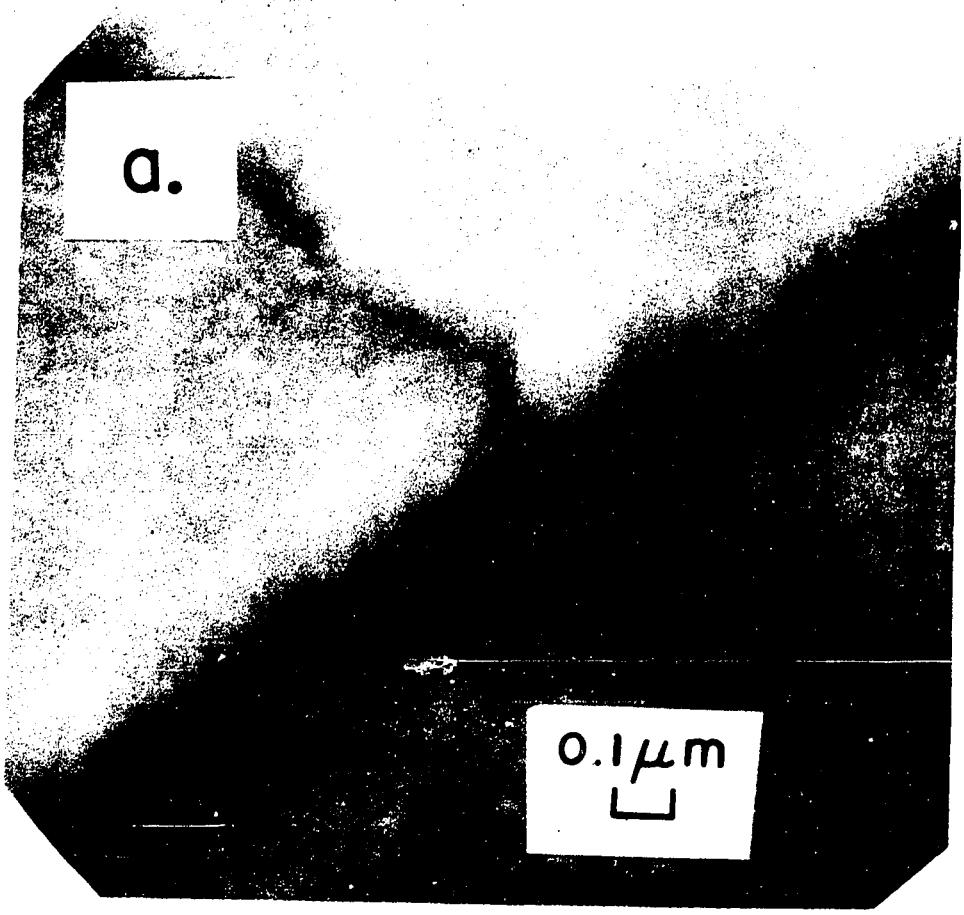
a.
0.1μm

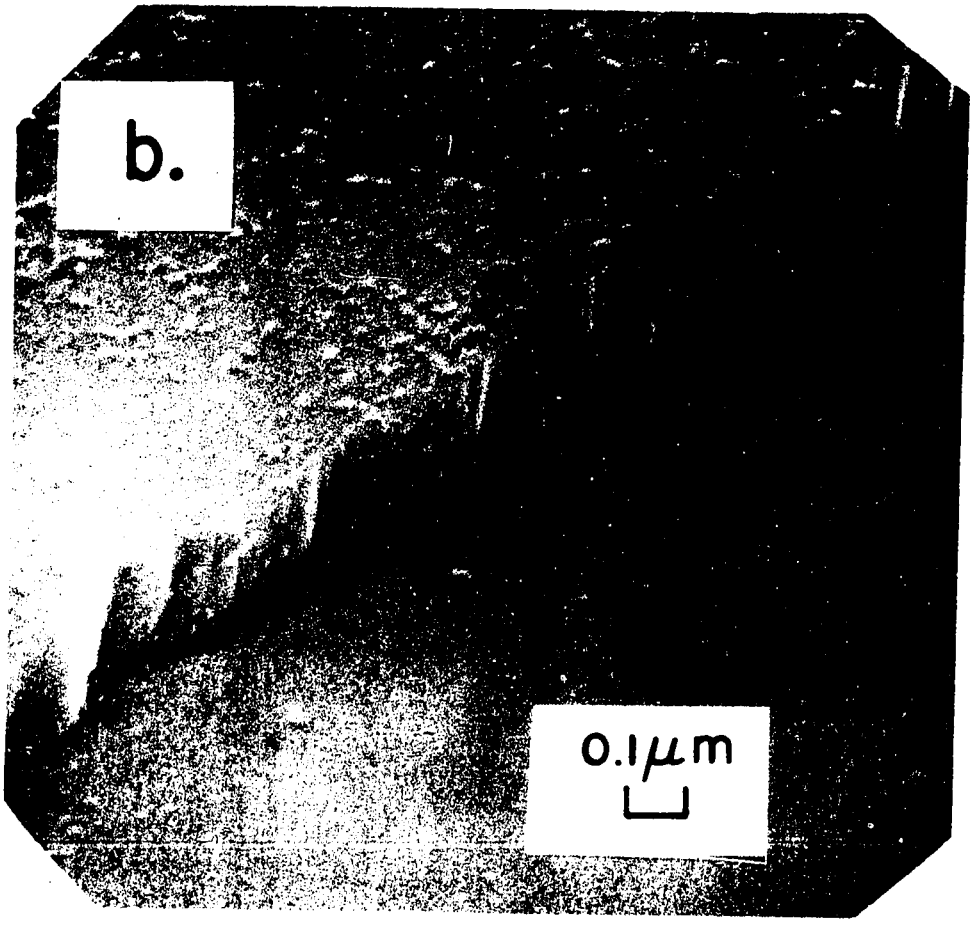
b.
0.1μm

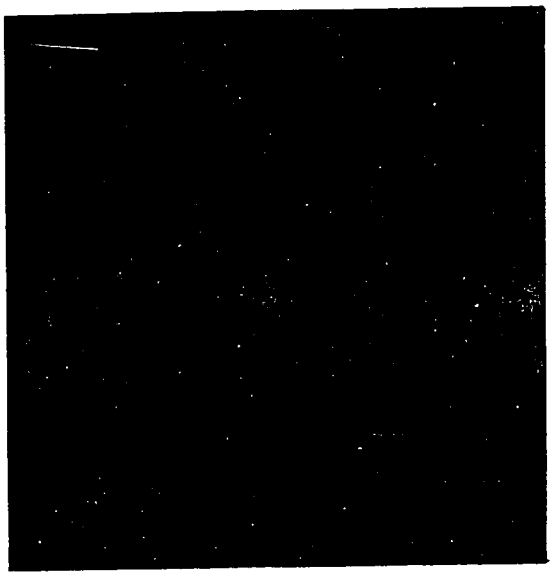

FIG. V-7 Step-edge VTB #S-6, viewed at normal incidence. Note the 60-nm horizontal gap between the banks.

predicted by the idealized deposition assumptions of Fig. V-5, but fine details of film topography, increasingly significant as dimensions are reduced below 100 nm, depend on surface-energy considerations in violation of the ray-optics model. As discussed in section III.B.4, agglomeration of the device film was minimized by the use of an alloy superconductor (Pb-In) and deposition at 77 K. Agglomeration was a problem in the pure In VTBs, as illustrated in Fig. V-8. This is at least partially due to the higher source temperature needed to evaporate In, and we believe that this agglomeration could be controlled with better thermal shielding in the evaporator.

Crystal-growth effects similar to film agglomeration can lead to edge roughness and pattern distortion in the Cr mask films. Figure V-9a shows an example, in which a 100-nm Cr film overhangs a step edge, distorting the sharp jog which should occur in the edge of the Cr pattern where it crosses the step edge. Since defects in the mask film are reproduced in the resulting deep step, Cr masks lead to a poor process yield on small ($W \lesssim 50$ nm) microbridges.

Smoother edges and more accurate shadowing are obtained with mask films of Ni-Cr alloy, as illustrated by Fig. V-9b. The starting material was commercial-grade $Ni_{0.8}Cr_{0.2}$ wire, and it was evaporated from a W boat. Since Ni alloys with W at high temperatures (causing reduced evaporation of Ni), a small charge of Ni-Cr evaporated nearly to completion yielded Cr-rich films, desirable for low etch rates and good adhesion. Our narrowest microbridges, #S-9, #S-13, and #S-14 were all made with Ni-Cr masks. Bridge #S-9, shown in Fig. V-10, has a minimum width of $\approx$ 40 nm. Thinner mask films are also expected to give more accurate shadowing, but the mask must be thick enough to

0.1 μm

FIG. V-8 In VTB #S-14, viewed at the same angle as Fig. V-5a. We believe that the lumpiness of the In films could be controlled by better thermal shielding in the evaporator.

FIG. V-9 Two ion-etching masks, for VTB fabrication, viewed at normal incidence. (a) The Cr mask shown here overhangs the shallow substrate step, distorting the jog in the mask edge; while (b) The NiCr mask shown coats the shallow step more ideally, producing a more accurate pattern. These masks may be compared with the idealized drawing of Fig. V-5d.

(a)

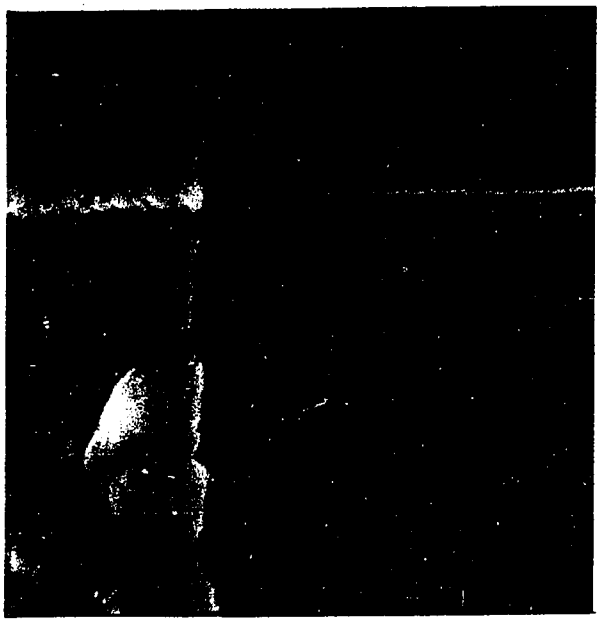

0.1 μm

(b)

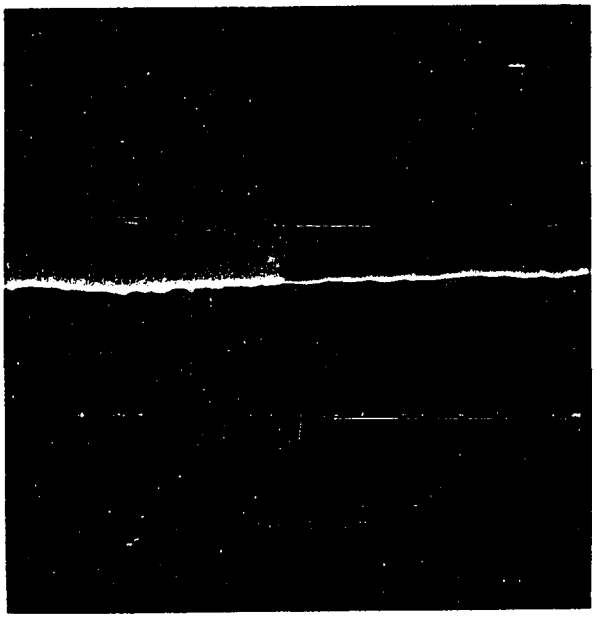

0.2 μm

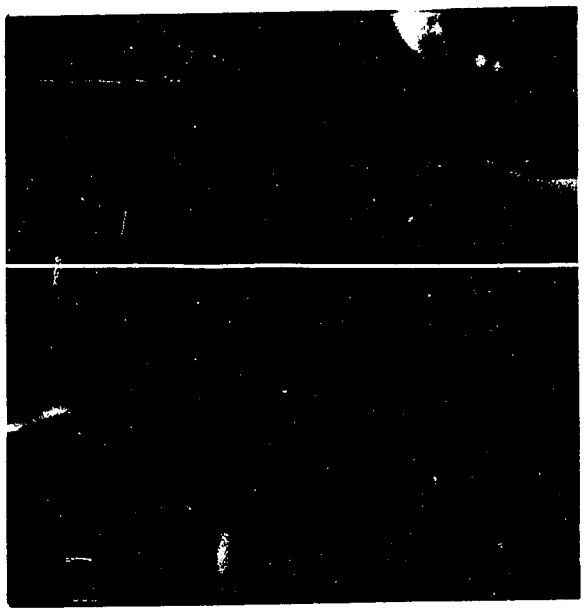

FIG. V-10 Pb-In VTB #S-9, viewed at the same angle as Fig. V-5a. This bridge was fabricated using a fine-grain ion-etching mask of Ni-Cr alloy.

withstand ion-beam etching with little mask erosion.[8] This tradeoff explains the great interest in reactive-ion etching processes which yield high differential etch ratios. Using the Ni-Cr-polyimide-O_2 system described in section V.A.2, a differential etch ratio of 25:1 is achieved, so that a very thin Ni-Cr film of 40 nm is a satisfactory mask for etching a substrate step of 500-nm depth.

Even when agglomeration of the device film is not a problem (i.e. the surface of the film is smooth), the ray-optics picture may be violated in the critical region near the step edge. In particular, the profiles of the film edges may differ from the simple shadowing prediction. Figure V-11a shows the ray-optics prediction of the film cross-section which results from evaporation over a single, straight substrate step. In this idealized case, the edge of the upper film is tapered, while the edge of the lower film is undercut. The actual profiles observed for Pb-In and Sn films evaporated over step edges are quite different, resembling those of Figs. V-11b and V-11c, respectively. The Pb-In film has nearly vertical edges with significant rounding at the top, while the edges of the Sn film slant in the opposite direction from the ray-optics prediction. Figure V-12a shows this phenomenon in a glancing-angle scanning-electron micrograph of an unsuccessful Sn microbridge. This bridge was apparently unsuccesful because the lower film is offset too far to contact the bridge face.

---

[8] Exactly how much mask erosion can be tolerated has been examined theoretically by Cantagrel (1975). Our experimental results are somewhat more optimistic than Cantagrel's theory: we find that erosion of 50% of the mask thickness gives no detectable slope (i.e. $< 15^{\circ}$) to the etched edges.

FIG. V-11 Profiles of metal films evaporated over a step edge. (a) Idealized profile predicted from the ray-optics model (b) Profile with vertical walls and rounding at top is typical of Pb-In films; while (c) Profile with reverse-slanted walls and rounding is typical of Sn films.

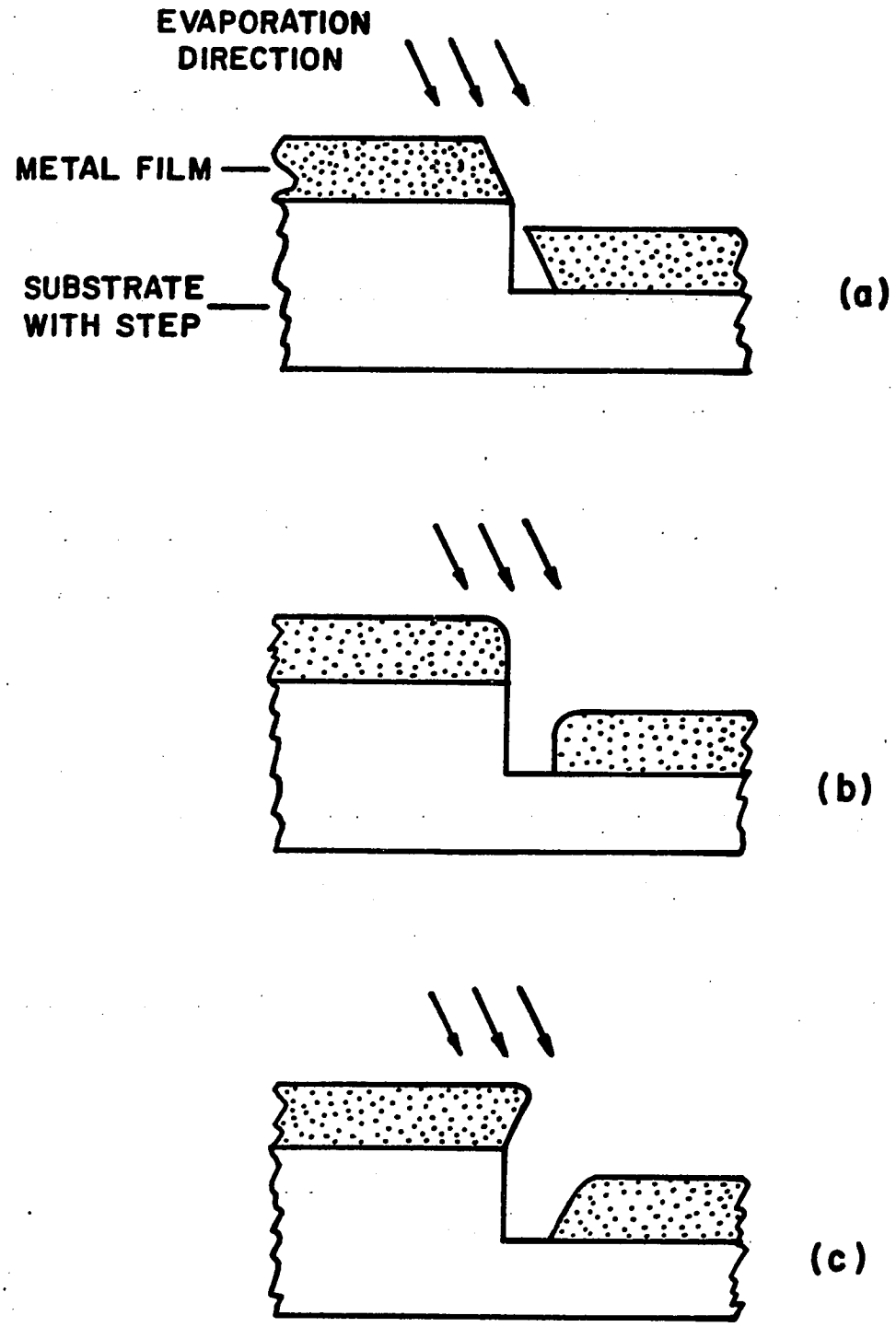
EVAPORATION
DIRECTION
METAL FILM
SUBSTRATE
WITH STEP
(a)
(b)
(c)

Fabrication of Sn microbridges was also made difficult by spontaneous fracture of the Sn films, apparently due to stress induced by the deposition at 77K. This effect is shown in Fig. V-12b. One batch of pure-Pb bridges was fabricated successfully, but hillock growth in the bank films (see Lahiri(1975b)) spoiled these bridges before they were tested at low temperature.

Although a limited number of tests has been performed, the edge profile obtained for a given material appears to be reproducible. If this is so, it should be possible to fabricate step-edge microbridges of any evaporable material by making suitable slight adjustments to the angle of evaporation.

The squareness of the substrate step does not appear to be a limiting factor in obtaining bridge dimensions < 40 nm. In Fig. V-6b, which shows a bare 300-nm step in a glass substrate, the radius of curvature at the top and bottom corners is < 20 nm. There is no evidence of faceting or redeposition (see Melliar-Smith (1976)) which could distort the step profile. Steps produced by etching through a polyimide film on a glass substrate also show excellent square profiles.

In sum, the step-edge technique of VTB fabrication described above has a number of advantages over other current techniques. Fabrication of microbridges in which both the length and width are $\leq$ 50 nm has not been reported by any other lithographic method, so the tiny dimensions possible with step-edge fabrication are a unique advantage. Large aspect ratios of bank thickness to bridge length D/L can be achieved. Device film deposition occurs in a single stage,

FIG. V-12 Unsuccessful Sn VTBs. (a) Viewed at glancing incidence, this Sn film shows a non-ideal profile similar to Fig. V-11c. (b) Viewed at normal incidence, this film shows splitting, apparently due to the stress built up either during evaporation onto a substrate at 77 K or during subsequent warming to room temperature.

(a)

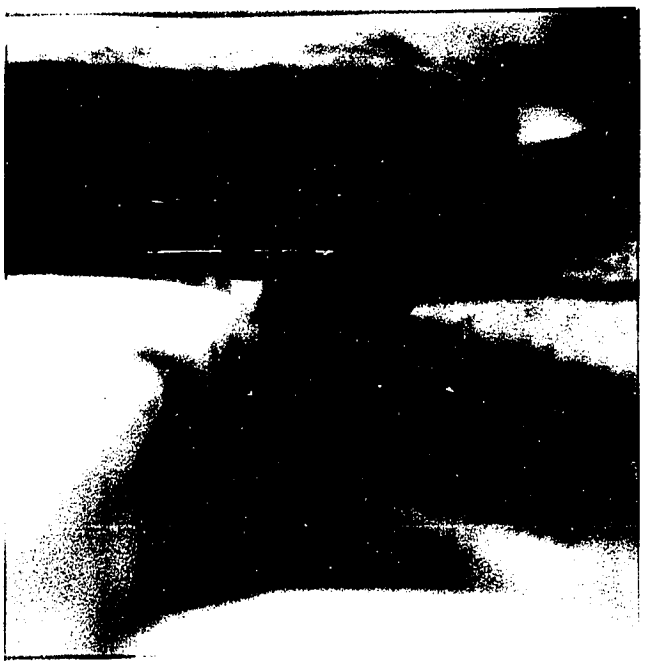

0.1 μm

(b)

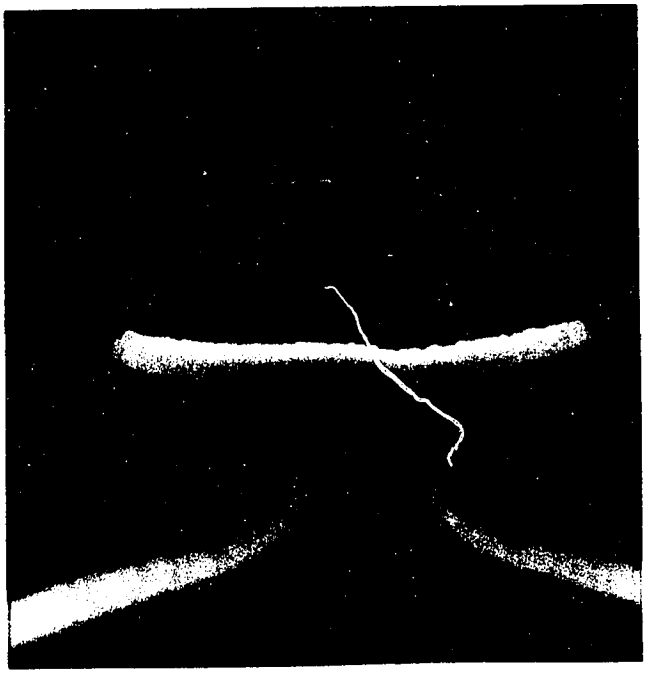

0.5 μm

so no interface problems arise. The technique is self-aligning. The substrate can be heated during deposition, as required for deposition of high-T_c superconductors (see Beasley (1978)). Also, no processing is required after the film deposition, so processing damage to such high T_c films (see Van Dover et. al. (1979)) can be avoided. Finally, the step-edge technique may be implemented with relatively common equipment.

There are many possible extensions of this microbridge fabrication technique to produce more complex structures. For example, bridges and banks of different materials can be produced by deposition from two sources at different angles. One could thus fabricate S N S bridges, which are particularly attractive for use with high-T_c A-15 superconductors, or the clean-dirty-clean structures discussed in section II.F. In another extension of these techniques, one could replace the single deep step with a square-wave grating structure, to produce series microbridge arrays.

CHAPTER VI. RESULTS AND DISCUSSION--VTBS

VI.A Bridge and Material Parameters

Using the procedures described in the preceding chapter, we have fabricated variable-thickness microbridges (VTBs) ranging from <40 nm to 180 nm in width (measured at the narrowest point) and from <40 nm to 200 nm in length. The estimated bridge thickness d ranges from 30 nm to 100 nm,[1] and the bank thickness D ranges from 75 nm to 600 nm. The $\bar{V}(I)$ curves of the microbridges at varying levels of microwave power were recorded by the methods discussed in chapter III. Most of the bridges were of $Pb_{0.9}In_{0.1}$ alloy, but three bridges of pure In were tested to investigate the effect of a long coherence length and mean free path. One impure In bridge, produced by accident, had a composition $In_{0.95}Pb_{0.05}$ and had instructive intermediate properties. All of the VTBs tested in this study were sufficiently narrow to be in the uniform-depairing regime over a fairly wide temperature range near T_c. The device resistances R_d ranged 0.15 Ω to 5.1 Ω for the In bridges and from 3.6 Ω to 8.4 Ω for the Pb-In bridges. The dimensions and basic parameters of these VTBs are listed in Table VI-I.

The superconducting material properties of the Pb-In alloy films used in this study are discussed at the beginning of chapter IV. Comparing the characteristic lengths listed in Table IV-II to the bridge dimensions listed in Table VI-I, it is clear that the Pb-In VTBs dis-

---

[1] The bridge thickness d can deviate from its nominal value given by eq. (V-3) due to the effects described in section V.C. The estimates used here are based on the nominal value, except when SEM photographs indicate otherwise. In that case, the average of the nominal value and the SEM estimate is used.

TABLE VI–I. Parameters of variable-thickness microbridges. Dimensions are estimated by interferometry and scanning-electron microscopy. R_d is defined as the minimum differential resistance at $t = 0.99$ (see section IV.B). while R_{tot} is the total normal-state resistance measured just above T_c.

Bridge #	L (nm)	W (nm)	d (nm)	D (nm)	dI_c/dT (mA/K)	R_d (Ω)	R_{tot} (Ω)	$R_d(dI_c/dT)$ (mV/K)	$R_{tot}(dI_c/dT)$ (mV/K)
$Pb_{0.9}In_{0.1}$ bridges ($\xi(T=0) \approx 25$ nm)									
S-6	60	90–50	60	240	0.163	6.4	9.5	1.04	1.55
S-7	50	90–75	60	240	0.353	3.9	6.3	1.38	2.22
S-8	70	$\approx$70	$\approx$30	75	0.191	6.9	15.4	1.32	2.94
S-9	40	70–50	40	110	0.117	8.4	14.4	0.98	1.68
S-10[a]	40	60–40	40	110	0.035	8.4 (21.5)	10.0	0.30 (0.76)	0.35
S-11	<30	100–80	100	600	0.570	3.6	5.4	2.05	3.08
$Pb_{0.95}In_{0.05}$ bridges ($\xi(T=0) \approx 72$ nm)									
S-12[b]	120	90–60	35	105	0.238	2.6	4.6	0.62	1.09
In bridges ($\xi_{bank}(T=0) \approx 166$ nm)									
S-13[c]	200	100–40	$\approx$50	350	0.292	2.0	2.4	0.58	0.70
S-14[c]	200	90–<40	$\lesssim$40	350	0.116	5.1	6.2	0.59	0.72
S-15[c]	90	230–180	80	350	4.86	0.15	0.21	0.73	1.02

[a]Bridge #S-10 had characteristics of a 21.5-Ω bridge shunted by a 13.8-Ω normal resistance. The values in parentheses are for the inferred bridge resistance of 21.5 Ω. See text for details.

[b]The composition of this impure In bridge was identified by the measured resistivity and critical temperature.

[c]These relatively clean In bridges showed significant boundary scattering in the narrow bridge region. From the measured resistivity ratios, we infer $\xi_{bridge}(T=0) \approx 73$ nm for #S-13, $\xi_{bridge}(T=0) \approx 37$ nm for #S-14, and $\xi_{bridge}(T=0) \approx 152$ nm for #S-15.

cussed below are in the small-bridge, dirty-material limit ($\ell \ll L,W$ and $L,W \ll \xi(T)$) for a range of at least 0.50 K below T_c.

The pure In films used for bridges #S-13, #S-14, and #S-15, have a mean free path ℓ which is comparable to or larger than the bridge dimensions, and the clean limit considerations treated in section II.F are relevant. Using Mathiessen's Rule, the mean free path in the film is:

$$\ell(T = 4) = \ell_\infty(T = 295) \left(\frac{\rho_{295} - \rho_4}{\rho_4} \right) \qquad (1)$$

where ℓ_∞ is the mean free path of perfectly pure bulk In. Chaudhari and Brown (1965) have obtained $\ell_\infty(T = 295) = 11.9$ nm, and we have measured the resistivity of a 350-nm-thick In film at 4 K to be $7.1 \times 10^{-7}\,\Omega$-cm, with a resistivity ratio of $\frac{\rho_{295}}{\rho_4} = 13.2$. This implies a mean free path $\ell = 145$ nm for the 350-nm film at 4 K. Substituting the value $\xi_{BCS} = 260$ nm obtained by Toxen (1962) into the dirty-limit relation:[2]

$$\xi_{GL}(0) = 0.855\ (\xi_{BCS}\ell)^{1/2}$$

We find $\xi_{GL}(0) = 166$ nm for our In film. The three pure In bridges were evaporated at the same time as the test film discussed above, so the parameters obtained for the test film accurately describe the bank material of these three bridges. For each of these three bridges, we find $T_c = 3.425$ K, in reasonable agreement with the bulk value of $T_c = 3.405$ K given by Roberts (1972).

As expected, the effect of boundary scattering is easily dis-

---

[2] Although the pure In bridges are in the clean-bridge limit $W \ll \ell$, the dirty-material formulas still apply because $\ell < \xi_{BCS}$. See discussion, Section II.F.

cerned in the In bridges. The most dramatic case is bridge #S-14, for which the overall resistance ratio of the bridge plus banks is only 3.67, due to boundary scattering in the narrow bridge region. For simplicity, we assume that there is a uniform mean free path ℓ_{bank} in the banks and a different uniform mean free path ℓ_{bridge} in the bridge region. To find the resistivity ratio of the bridge region alone, one must know what part of the total resistance is due to the bridge and what part is due to the banks. Using R_d (defined in section VI.B) as the resistance of the bridge region at 4 K, we obtain $\frac{\rho_{295}}{\rho_4} = 1.60$, $\ell_{bridge} = 7$ nm, and $\xi_{GL}(0) = 37$ nm for the bridge region of #S-14 alone. Following the same procedure for the slightly wider bridge #S-13, we obtain $\frac{\rho_{295}}{\rho_4} = 3.36$, $\ell_{bridge} = 28$ nm, and $\xi_{GL}(0) = 73$ nm for bridge region alone. Using the data for the short, relatively wide bridge #S-15, we obtain $\frac{\rho_{295}}{\rho_4} = 11.2$, $\ell_{bridge} = 122$ nm, and $\xi_{GL}(0) = 152$ nm for the bridge region alone.

Two accidental bridges provide interesting supplementary data. Bridge #S-10, the narrowest Pb-In bridge tested, had values of I_c and R_d appropriate for a 21-Ω bridge in parallel with a 14-Ω nonsuperconducting shunt. When a grossly excessive level of microwave power was accidentally applied to the device, the $\bar{V}(I)$ curve changed permanently to that of a 13.8-Ω resistor, implying that the superconducting bridge had burned out, leaving only the shunt intact. Although no distinct shunt was observed during scanning-electron microscopy carried out a few weeks before the bridge was electrically tested, this sample was cooled to 4 K and warmed to room temperature before cooling for the electrical tests of bridge #S-10. Thus it is conceivable that a stress-induced hillock or whisker of In formed a shunt which was non-

superconducting at 6-7 K. This bridge shows reduced Joule heating due to the small $I_c R$ product.

Bridge #S-12 was intended to be a pure In bridge, but electrical tests revealed that it had a resistivity ratio of 3.29 (despite being relatively wide) and a T_c of 3.685 K, about 0.28 K higher than bulk In. Apparently, Pb-In deposits in the evaporator were re-evaporated during the In evaporation (which takes place at a higher temperature), producing an In-Pb alloy film on the substrate. Comparing the observed resistivity and critical temperature of bridge #S-12 to the bulk-alloy data of Noto et. al. (1966), we find that both of these parameters are consistent with a composition of $In_{0.95}Pb_{0.05}$. The calculational method which was applied to the pure In films above yields ℓ = 27 nm and $\xi_{GL}(0)$ = 72 nm for the impure In film of bridge #S-12. After Pb-alloy deposits were cleaned from parts of the evaporator near the source, the pure In films discussed above were obtained with no further difficulty.

VI.B Critical Currents of VTBs

Unlike the results for UTBs discussed in chapter IV, the critical currents of the VTBs are observed to be a linear function of temperature over a fairly wide range near T_c. $I_c(T)$ for two VTBs is shown in Figure VI-1, which can be compared to the UTB data plotted in Figure IV-2. For narrow VTBs, such as #S-6 and #S-9, the straight line fit to the data near $t = T/T_c = 0.85$ fits all the data from $t = 0.75$ to $t = 0.95$ within a few percent. At lower temperatures, the critical current falls below the linear curve. This is not surprising, since the GL temperature dependences used in deriving the linear $I_c(T)$ curve (eq. (II-17)) are accurate only when $(1-t) \ll 1$. The sign of the

FIG. VI-1 Critical current versus temperature for two variable-thickness bridges. (a) Bridge #S-9, like the other Pb-In VTBs tested, shows a linear temperature dependence of I_c for $0.75 < T/T_c < 0.95$. The experimental data fall slightly above the linear curve very near T_c (inset), and below the linear curve at low temperatures. We have also plotted the theoretical result of Kulik and Omelyanchuk (1975), which applies to short, narrow, dirty VTBs at arbitrary temperatures. However, none of the Pb-In bridges studied by us are actually in the short limit for $t < 0.7$. (b) Bridge #S-14, like the other pure-In tested, shows a linear temperature dependence $0.8 < T/T_c < 1$; there is no visible deviation from linearity near T_c. At low temperatures, the data are in reasonable agreement with the prediction of Kulik and Omelyanchuk (1975), despite the fact that these authors did not consider the effect of boundary scattering in the bridge region, which is quite significant in bridge #S-14.

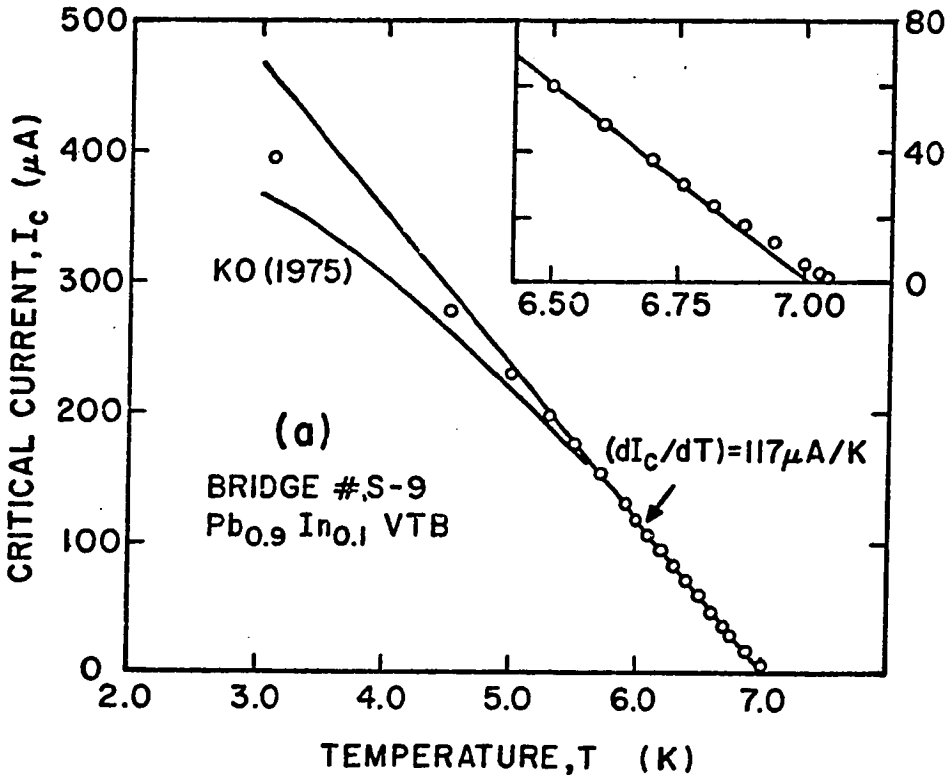
CRITICAL CURRENT, I_c (μA)
TEMPERATURE, T (K)
KO (1975)
(a)
BRIDGE #S-9
$Pb_{0.9}$ $In_{0.1}$ VTB
$(dI_c/dT)=117\mu A/K$
500
400
300
200
100
0
2.0
3.0
4.0
5.0
6.0
7.0
80
40
0
6.50
6.75
7.00

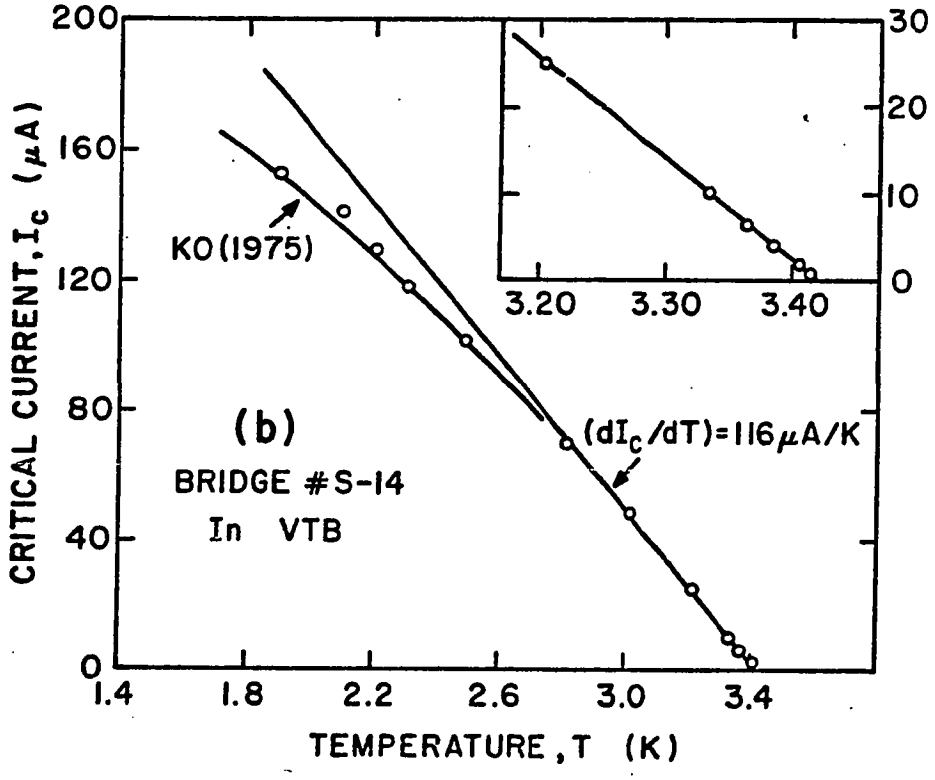
CRITICAL CURRENT, I_c (μA)
TEMPERATURE, T (K)
KO (1975)
(b)
BRIDGE #S-14
In VTB
$(dI_c/dT)=116\mu A/K$
200
160
120
80
40
0
1.4
1.8
2.2
2.6
3.0
3.4
30
20
10
0
3.20
3.30
3.40

deviation from linearity is in agreement with the theory of Kulik and Omelyanchuk (1975) for small, dirty microbridges at arbitrary temperaturs, but the deviation is smaller (i.e. the critical current is larger) in the experimental data. In their calculation, KO (1975) require $\ell << L,W$ and $L,W << \xi(T)$. The latter condition is not quite met by the Pb-In bridges when $t < 0.7$, and KO (1975) do not consider the effect of boundary scattering, which is important in our narrow In bridges.

The $I_c(T)$ curve also deviates from linearity in the region very near T_c. In this temperature range, the experimental data fall above the linear curve. The extent of this deviation may be quantified by the difference between the actual T_c and the T_c extrapolated from the linear portion of the $I_c(T)$ curve. For the narrower Pb-In bridges, this temperature defect is about 50-60 mK. For the wide, short bridge #S-11, however, it is 110 mK. The deviation from linearity near T_c is somewhat surprising, since this is the temperature range in which ξ is largest and in which the GL theory should be most accurate. Inhomogeneities in the T_c of the material do not provide a satisfactory explanation, since the resistive transition of bridge plus banks at low dc or ac current is only $\lesssim$ 25 mK wide. In addition, enhancement or depression of T_c in the bridge region would probably be most pronounced in the narrowest bridges, unlike the effect observed here. The simplest explanation is that the exponent β in the relation:

$$I_c \propto (T_c - T)^{\beta} \qquad (3)$$

is slightly greater than unity and that this is due to the finite width of the bridges. If the exponent β increases with increasing bridge width, the temperature range over which the linear fit is unsatisfactory

would also increase, as is observed. Support for this hypothesis is also provided by the $I_c(T)$ data for the pure In bridges, which show no significant deviation from linearity at temperatures near T_c.

The linear temperature dependence of I_c observed when $0.75 < t < 0.95$ is in good agreement with the small-bridge calculations discussed in section II.B. Within this limit, all the theories predict that

$$R\,(dI_c/dT) = 635\ \mu V/K \qquad (4)$$

regardless of the detailed geometry, dimensions, or material of the microbridge. As discussed in section II.D, the difficulty in applying this relation is in choosing the appropriate value of R. We have chosen R_d, defined for VTBs as the minimum differential resistance at finite voltage, R_{min}, measured at $t = 0.99$. Joule heating is less severe for these VTBs than for the UTBs of chapter IV, so R_{min} is nearly independent of t at $t = 0.99$. The values of R_d for our VTBs are listed in Table VI-I, as are the slopes of the $I_c(T)$ lines, and the product $R_d(dI_c/dT)$ is plotted in Figure VI-2.[3] The table shows that $R_d(dI_c/dT)$ decreases smoothly with decreasing bridge cross-section, and approaches the theoretical limit of 0.64 mV/K for the bridges with the smallest normalized cross-sections. The product $R_{tot}(dI_c/dT)$, where R_{tot} is the total resistance of the bridge plus banks just above T_c, is also plotted. Instead of a smooth trend, $R_{tot}(dI_c/dT)$ shows wide fluctuations which are correlated with variations in the bank

---

[3] Note that R_d is larger than $\frac{\rho L}{Wd}$, the calculated normal-state resistance of the bridge region alone. This probably occurs because the gradients of the quasiparticle potential extend into the banks on either side.

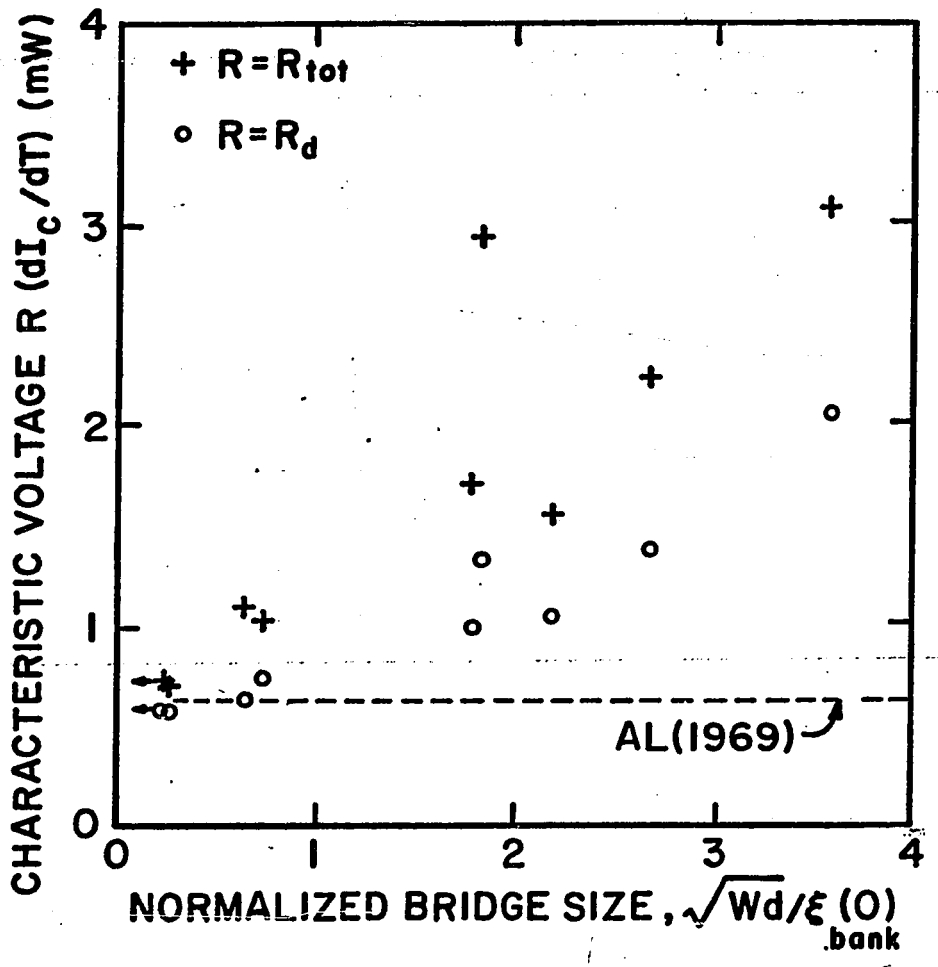

FIG. VI-2 Characteristic voltage versus normalized bridge diameter for the VTBs listed in Table VI-I. When R_d, the minimum differential resistance at t = 0.99, is used to compute the characteristic voltage, a smooth trend is found. The smallest bridges fall close to the small-limit prediction of Aslamazov and Larkin (1969).

thickness D. That is, R_{tot} is a poor predictor of I_c because too much of the bank resistance is included. With the available selection of bridge dimensions, the effect of the bridge length L on the $R_d(dI_c/dT)$ product cannot be clearly established.

VI.C $\bar{V}(I)$ Curves of VTBs

VI.C.1 $\bar{V}(I)$ Curves Near T_c

The $\bar{V}(I)$ curves of our variable-thickness bridges are not dissimilar to those of the uniform-thickness bridges discussed in chapter IV, but more fine structure is observed in the VTB curves. This is at least partially due to three-dimensional cooling in the thick banks, which permits nonhysteretic operation over a wider range of both temperature and power dissipation. Three basic phenomena are discussed in this section:

(1) Temperature-independent peaks in $d\bar{V}/dI$ are observed in all bridges except those with the lowest resistances for each material (i.e. #S-11 and #S-15).

(2) Sharp, temperature-dependent peaks in $d\bar{V}/dI$ are found in some, but not all, of the bridges. In the pure and impure In bridges, the peaks are identified as energy-gap-related structure, occurring at voltages $\bar{V} = 2\Delta/me$ where m = 1,2,3,4,5.

(3) A "foot" structure of low differential resistance $\frac{d\bar{V}}{dI}$ is observed at low voltage for the pure and impure In bridges. The analogous part of the $\bar{V}(I)$ curve for Pb-In bridges does not have low differential resistance, but may still be interpreted as a "foot".

Some representative $\bar{V}(I)$ curves for bridges #S-9 and #S-14 are plotted in Figure VI-3.

The $d\bar{V}/dI$ curves plotted in Figure VI-4 display the temperature-

FIG. VI-3 Representative $\bar{V}(I)$ curves for two VTBs. (a) The $\bar{V}(I)$ curve for Pb-In bridge #S-6 shows no hysteresis down to $T = (T_c - 1.0\ K)$. (b) The $\bar{V}(I)$ curve for In bridge #S-14 shows no hysteresis at the lowest temperature tested ($T \gtrsim 1.3\ K$). The low-voltage foot region is conspicuous in the two lower-temperature curves plotted, and the $n = 1$ peak of the energy-gap-related structure can be seen in the curve taken at $T = 2.10\ K$.

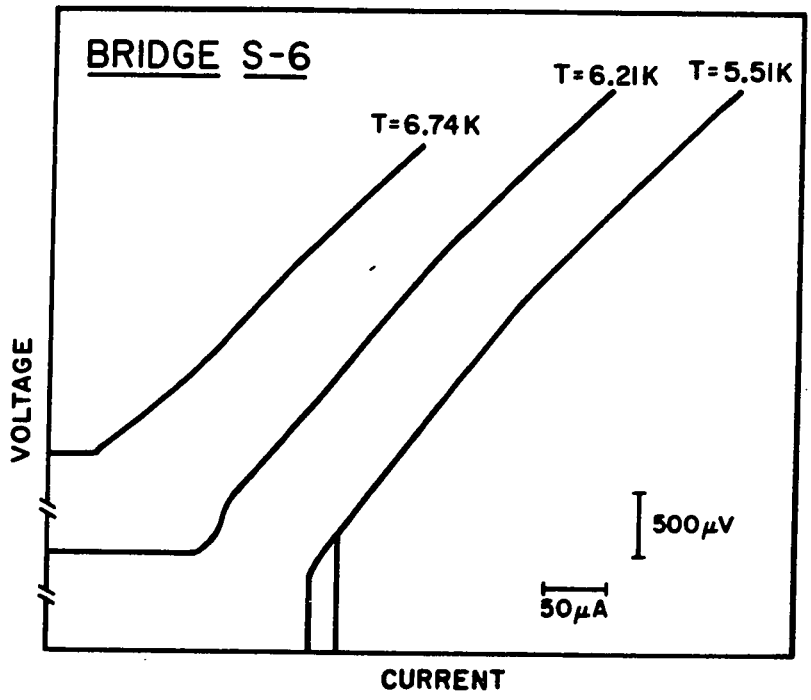
BRIDGE S-6
T=6.74K
T=6.21K
T=5.51K
VOLTAGE
500μV
50μA
CURRENT

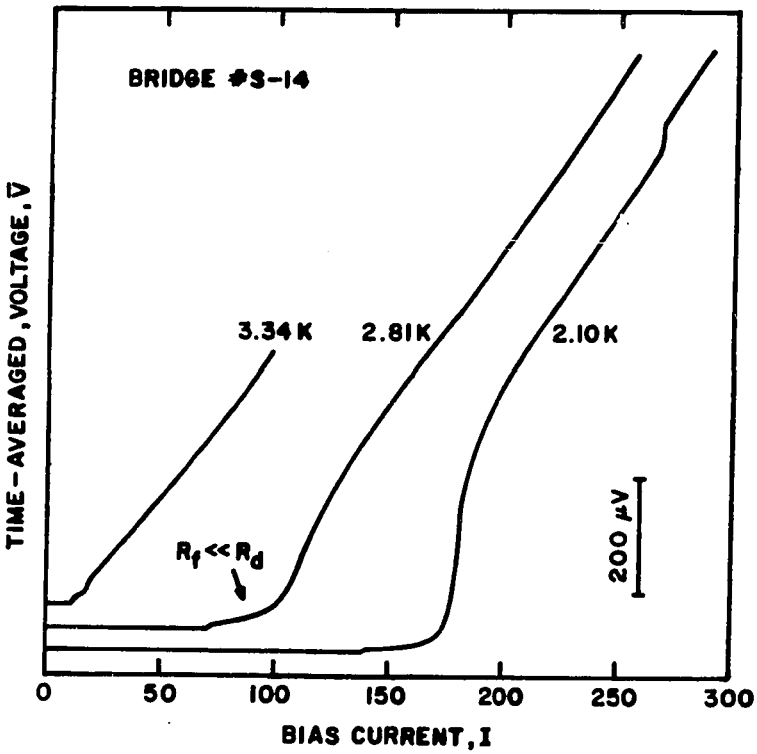
BRIDGE #S-14
3.34K
2.81K
2.10K
TIME-AVERAGED, VOLTAGE, V̄
$R_f \ll R_d$
200 μV
0
50
100
150
200
250
300
BIAS CURRENT, I

independent peaks mentioned in point (1) above. Although the amplitude of the peaks (i.e. the amount of variation in $d\bar{V}/dI$ varies with temperature, the voltage at which each peak occurs remains constant. As $T \to T_c$, the amplitude of the peaks decreases until the peaks become indistinguishable about 20-50 mK below T_c. As temperature is reduced below the range shown in the figure, the relative amplitudes of the individual peaks change, but some of them remain visible until hysteresis at low temperature (discussed in the following section) prohibits stable operation at these voltages. The temperature-independent structure is most pronounced for the high-resistance bridges #S-6 and #S-9. For the moderate-resistance bridges, a few peaks of small amplitude are observed, while the low-resistance bridges #S-11 and #S-15 show no temperature-independent structure at all. The voltages at which the peaks occur are not the same for different bridges, but the peak-to-peak spacing is the same for all Pb-In bridges, about 50 μV. The In bridges show a smaller peak-to-peak spacing, about 15 μV.

We believe that this temperature-independent $d\bar{V}/dI$ structure represents electromagnetic coupling of the bridge to the microwave resonances of the cryostat and measurement apparatus. These cavity-induced steps, which have been previously reported in microbridges (see, for example, Klapwijk et. al. (1977a)), arise because the devices are capable of self-detecting the reflected part of their own Josephson-effect radiation. The voltage of a cavity-induced step, being proportional to the resonance frequency, is usually independent of temperature. High-resistance devices show more pronounced structure because radiation is coupled out of and into them with greater efficiency. Thus, the principal experimental observations listed

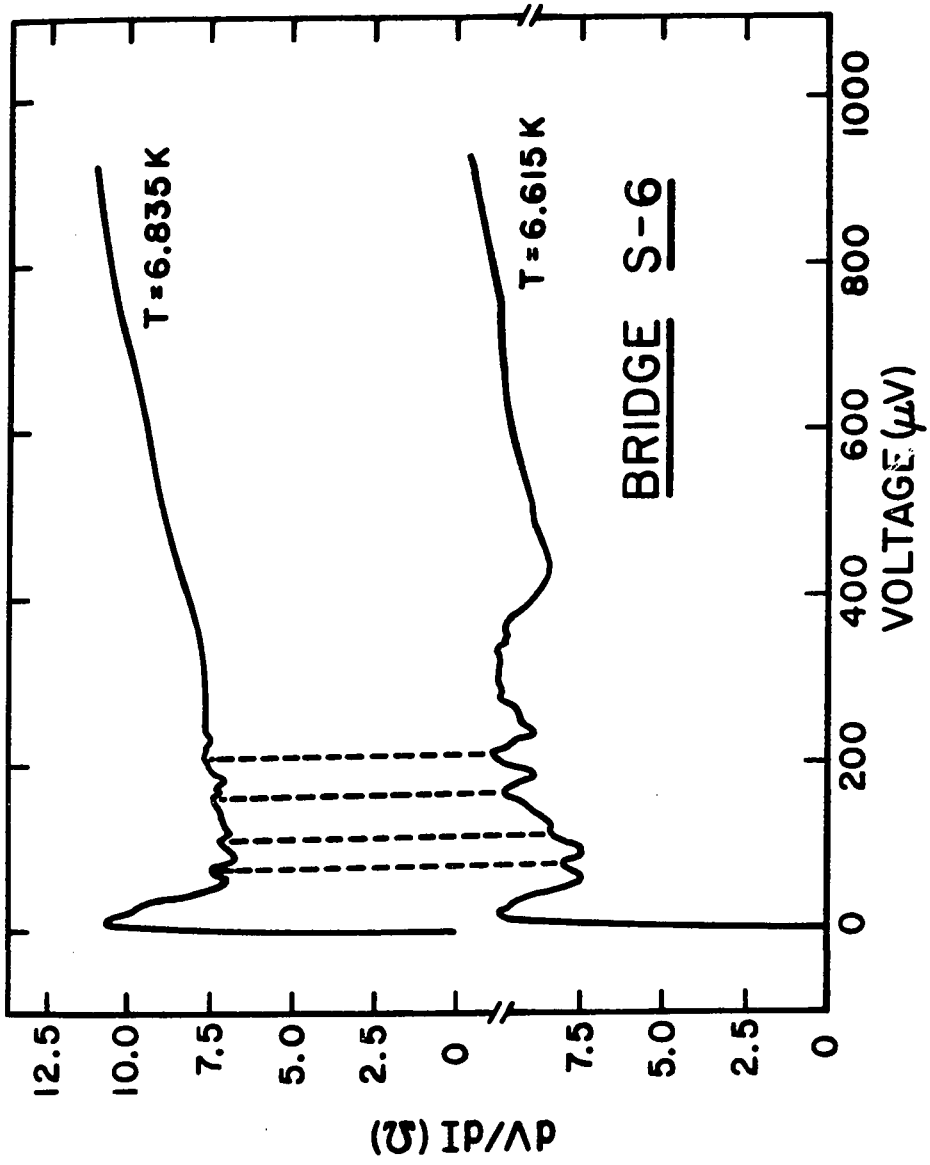

FIG. VI-4 Differential resistance versus time-averaged voltage for a Pb-In VTB. The temperature-independent peaks are attributed to cavity-induced steps (see text).

above are consistent with cavity-induced structure. This hypothesis does not explain why the In bridges show structure with a smaller peak-to-peak spacing, however.

Figure VI-5 shows the energy-gap-related structure in the $d\bar{V}/dI$ curves of the widest In bridge, #S-15. Such structure has been reported previously in In and Sn microbridges (see, for example, Gregers-Hansen et. al. (1973) and Octavio et. al. (1977)), and various theories based on multi-particle tunneling and self-coupling to the Josephson radiation have been proposed to explain it. These theories have been compared to each other by Hasselberg et. al. (1974), who conclude that the distinctions between them are fairly subtle. Bridge #S-15, which has a low resistance, displays subharmonic structure down to the fifth-order peak (i.e. $V_5 = 2\Delta/5e$), but the higher-resistance In bridges #S-13 and #S-14 display only the three lowest-order peaks. As shown in Figure VI-6, the gap value inferred from the third-order peak, which occurs at relatively low voltage, is in good agreement with the energy gap at the bath temperature, computed by applying the BCS temperature dependence to the zero-temperature gap $2\Delta(0) = 3.63\ kT_c$. (The numerical coefficient is the experimental value obtained by Giaever and Megerle (1961).) In bridge #S-15, the gap values inferred from the third-, fourth and fifth-order peaks agree to within 7%. The first- and second-order peaks, however, occur at lower voltages than those predicted on the basis of the bath temperature gap. We believe that this is due to Joule heating. This being so, an effective temperature $T_{eff} = T_B + \Delta T_{sgs}$ may be inferred from each peak of the gap structure. Following Octavio et. al. (1977), we plot the temperature rise ΔT_{sgs} versus $I\bar{V}/\xi(T_B)$ in Figure VI-7. For three-dimensional cooling, the

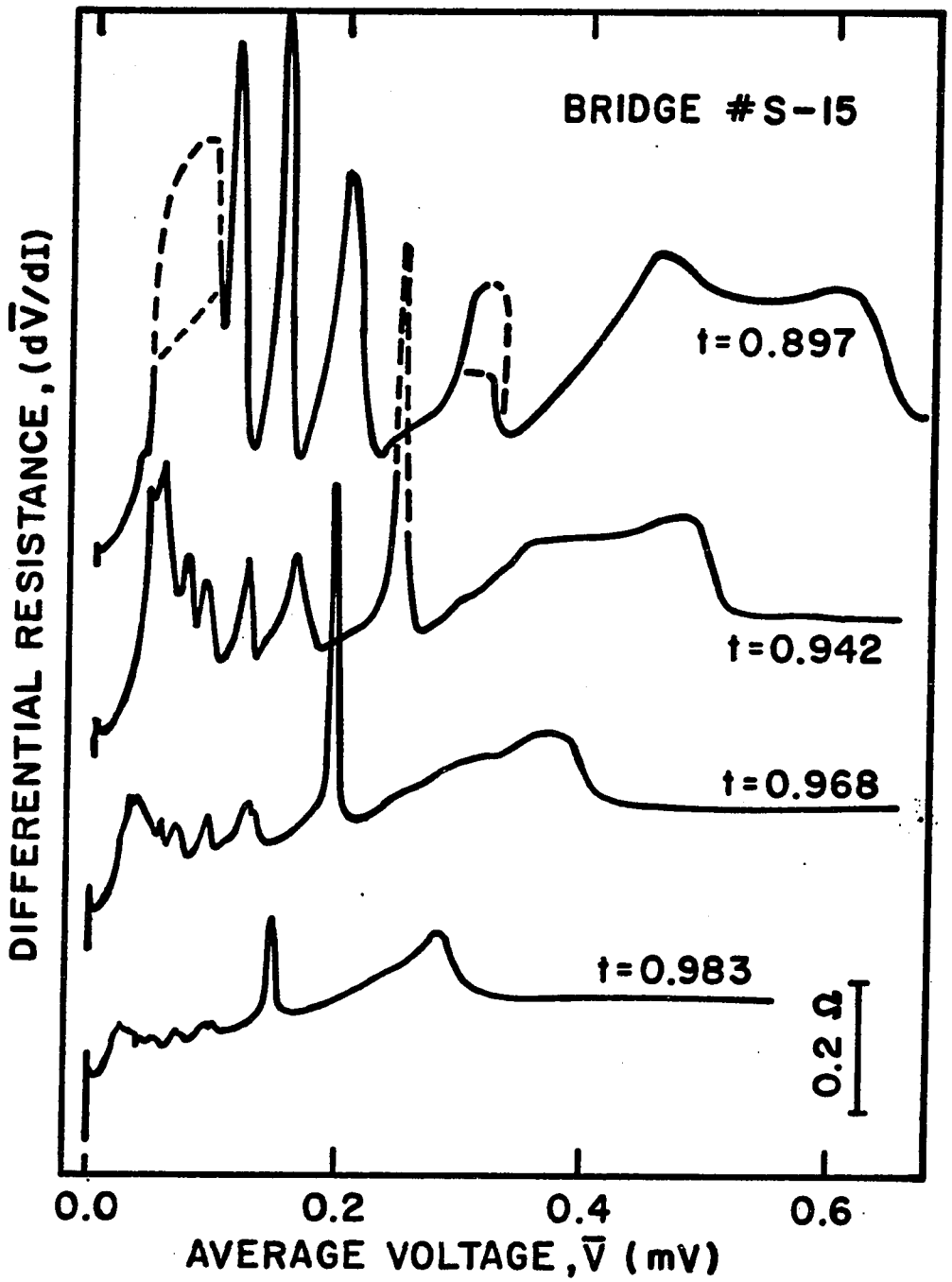

FIG. VI-5 Differential resistance versus time-averaged voltage for an In VTB. For this relatively wide bridge, the n = 1-5 peaks of the energy-gap related structure are clearly visible. The n = 1 peak shows slight hysteresis at the lowest temperature plotted here.

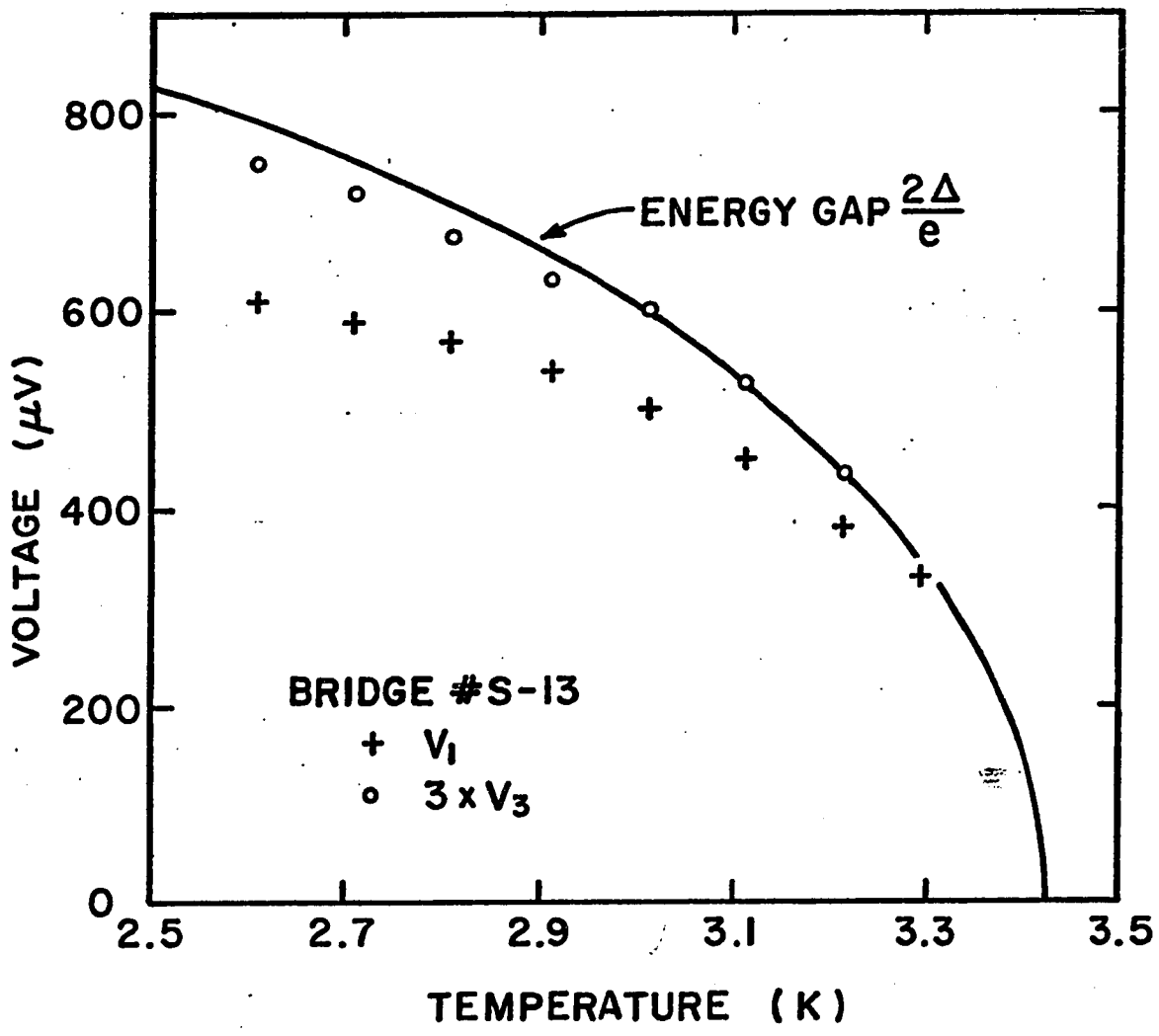

FIG. VI-6 Voltages of temperature-dependent peaks in $d\bar{V}/dI$ versus bath temperature for an In bridge. The voltage of the n = 1 peak falls below the bath-temperature energy-gap voltage, but three times the voltage of the n = 3 peak agrees with the bath-temperature gap.

local temperature rise at a distance r from the bridge is:

$$\Delta T = \frac{I\bar{V}}{\kappa\Omega r} \qquad (5)$$

Thus, the plot of Figure VI-7 should be a straight line if the gap structure is determined by the temperature at a distance $r \approx \xi(T)$ away from the bridge. In fact, the plot is roughly linear and this simple heating argument provides a satisfactory explanation of the depressed peak voltages of the first- and second-order gap structure. However, the slope of the plot implies $\Omega\kappa \approx 2.5 \times 10^{-2}$ W/cm-K, which is an order of magnitude smaller than the result expected from the Wiedemann-Franz law, assuming simple radial cooling.

It is worthy of note that none of the alloy bridges, <u>including</u> the impure In bridge #S-12, display the energy-gap-related structure. This structure <u>is</u> present in the $d\bar{V}/dI$ curves of bridge #S-14, which has a small mean free path only within the bridge region. Thus, it appears that dirty banks ($\ell_{bank} << \xi_{BCS}$) are the critical factor in prohibiting gap-related structure. If confirmed by more extensive experiments, this criterion could be a helpful constraint in selecting the proper theoretical description of this phenomenon.

Several of the alloy bridges (#S-6, #S-8, #S-11, #S-12) show one or two sharp, temperature-dependent peaks in $d\bar{V}/dI$ which are not interpreted as energy-gap-related structure and for which we do not have an explanation. For each of the four bridges listed above, at least one of the aforementioned $d\bar{V}/dI$ peaks occurs at a voltage well above

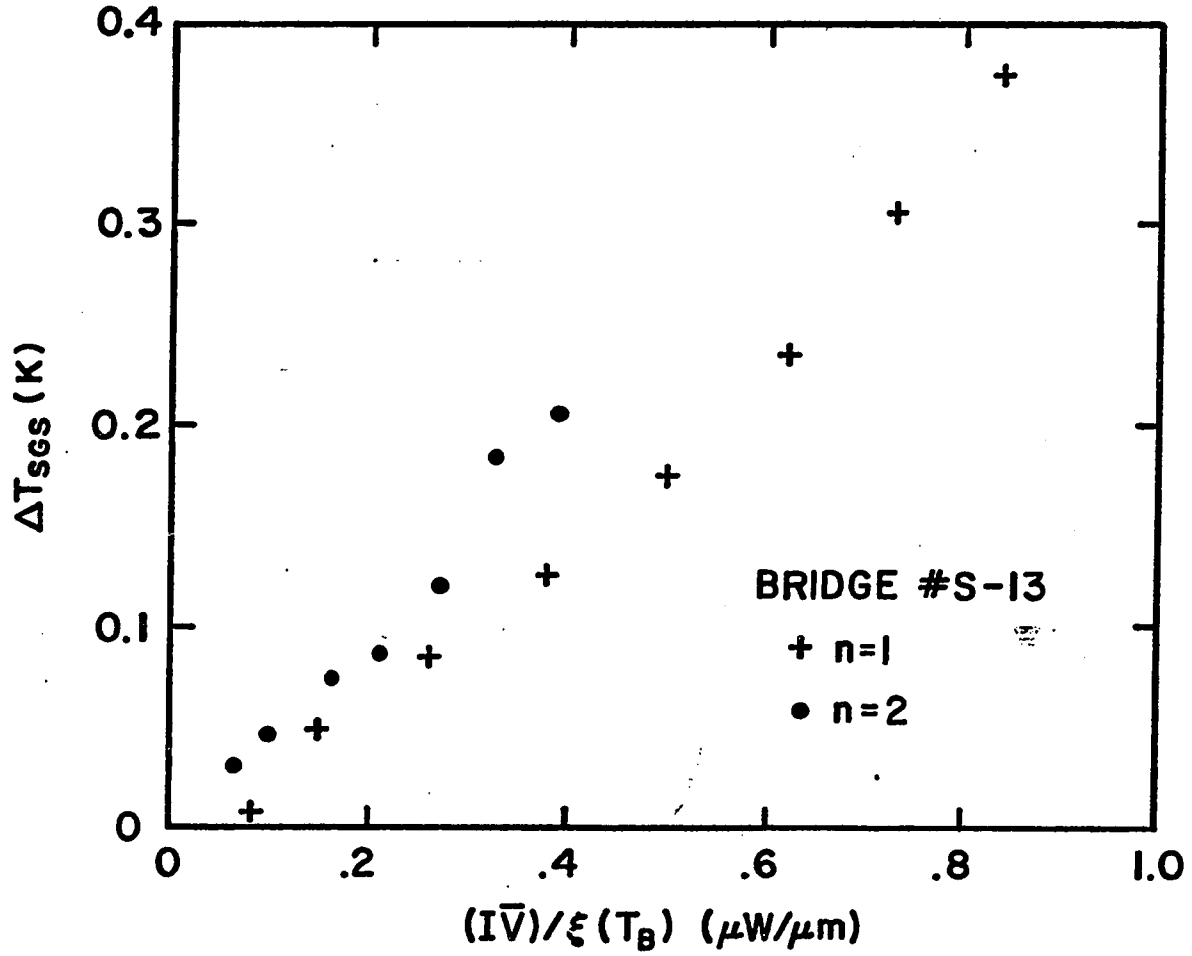

FIG. VI-7 Temperature rise inferred from the energy-gap-related structure, versus $(I\bar{V})/\xi(T_B)$, in an In VTB. As discussed in the text, the linear relationship is in agreement with a simple Joule-heating model.

the bath temperature gap voltage.[4] This is illustrated by Figure VI-8, in which the peak voltage is plotted versus temperature for bridge #S-11. The vortex-flow mechanism introduced by Wang et. al. (1978) cannot explain $d\bar{V}/dI$ peaks in a bridge as narrow as #S-6 ($W/\xi(T) = 0.24$ at $T = T_c - 100$ mK), and the simple heating theory does not give rise to such sharp $d\bar{V}/dI$ structure at high voltages. Since it is not even clear what distinguishes the four bridges which show such structures from the six bridges which do not, the origin of these features of the $\bar{V}(I)$ curve must remain a mystery, at least for the present.

At low voltages, the $\bar{V}(I)$ curves of Sn and In microbridges show a region of low differential resistance, variously referred to as a shoulder, bump, or foot. (We will use the term "foot" exclusively.) Detailed studies of this foot region have been made in In UTBs by Jensen and Lindelof (1976) and in Sn VTBs by Octavio et. al. (1978). Both studies concentrated on the temperature dependence of the differential resistance of the foot region R_f. Jensen and Lindelof used an analytic approximation to the time-dependent Ginzburg-Landau (TDGL) theory (discussed briefly in section II.B.2) to predict a foot region with:

$$(R_f)^{-1} = (R_d)^{-1} + \frac{1}{15}\left(\frac{L}{\xi}\right)^2 \left(\frac{2e\tau_\Delta}{\hbar}\right) I_c \quad . \tag{6}$$

Subsequent numerical calculations by Baratoff and Kramer (1977) have shown, however, that the exact TDGL theory does not predict any foot

---

[4] As we have seen, Joule heating can decrease the gap, but heating cannot explain the shift of gap structure to increased voltages. Gregers-Hansen et. al. (1973) have apparently observed gap enhancement due to the Eliashberg mechanism discussed below, but to introduce such an enhancement to explain our results be speculative, to say the least, as the enhancement would have to be as large as 60%.

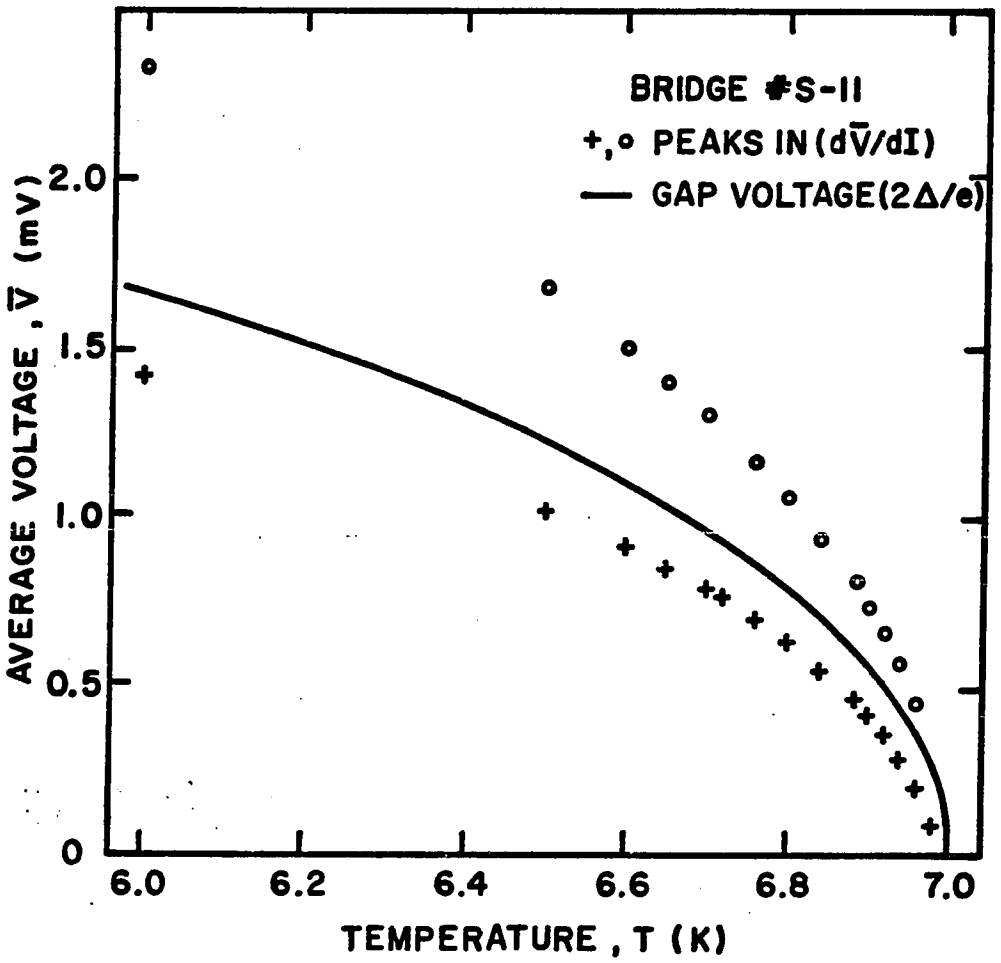

FIG. VI-8 Voltages of temperature-dependent peaks in $d\bar{V}/dI$ versus bath temperature in PbIn bridge #S-11. Since the voltage of the higher peak exceeds the energy-gap voltage, we do not identify these peaks as energy-gap-related structure.

structure. Octavio et. al. introduced a description of the foot region in terms of the more sophisticated relaxation models of Golub (1976) and Aslamazov and Larkin (1976). Recently, Schmid et. al. (1980) have presented a corrected calculation based on the same physical picture as Octavio et. al. (1978). In brief, the quasiparticle distribution as a function of energy cannot adjust rapidly enough to follow the oscillation of the order parameter when the bridge is biased at a finite voltage. The resulting nonequilibrium distribution of quasiparticles in the bridge in turn affects the energy gap. In this way, the slow relaxation of the quasiparticles affects the supercurrent flowing in the bridge.

The effect of quasiparticle relaxation depends on the frequency of the Josephson oscillation $f_J = \frac{2e\bar{V}}{h}$, which is proportional to the time-averaged voltage across the bridge. When $\bar{V} < \hbar/2e\tau_E$ $(2\pi f_J < 1/\tau_E)$, where τ_E is the inelastic electron scattering time, the model of Schmid et. al. (1980) predicts that the finite quasiparticle relaxation time will cause a decrease in the differential resistance of the bridge, yielding a foot resistance R_f given by:

$$\left(\frac{R_f}{R_d}\right) = \frac{10.8\,\hbar}{kT_c\tau_E}\left(\frac{kT_c}{\Delta(T)}\right)^2 \left[1 + 0.052\left(\frac{\Delta(T)}{kT_c}\right)\left(\frac{L}{\xi(T=0)}\right)^2\right]^{-1} \qquad (7)$$

which is lower than the device resistance. As usual, k is Boltzmann's constant and $2\Delta(T)$ is the superconducting energy gap. (In comparisons with experimental results we identify R_d with the minimum differential resistance on the $\bar{V}(I)$ curve <u>above the foot region</u>, measured at $t = 0.99$.) Using the standard BCS result for the temperature-dependent energy gap, eq. (7) becomes:

$$\left(\frac{R_f}{R_d}\right) = \frac{8.78\times10^{-12}}{T_c \tau_E} (1-t)^{-1}\left[1 + 0.160 \left(\frac{L}{\xi(0)}\right)^2 (1 - t)^{1/2}\right]^{-1} \qquad (8)$$

with T_c measured in degrees Kelvin and τ_E in seconds. The low-resistance foot is predicted to terminate at a voltage:

$$V_f = \frac{2.76\,\hbar}{e\,\tau_E} = 1.817 \times 10^{-15} (\tau_E)^{-1}. \qquad (9)$$

In the latter expression, τ_E is in seconds and V is in volts. Both equations (7) and (9) were confirmed by the experiments of Octavio et. al. (1978) on Sn VTBs.

The low-resistance foot is clearly observed in the $\bar{V}(I)$ curves of our In VTBs (see Fig. VI-3b). The normalized foot resistances R_f/R_d for bridges #S-14 and #S-15 are plotted as functions of temperature in Figure VI-9. The result of eq. (8) is also plotted, using the normalized length $(L/\xi_{bridge}(0)) = 0.592$ deduced for bridge #S-15 in section VI.A. The theoretical curve has been fitted to the data at $t = 0.95$, yielding the inelastic scattering time $\tau_E = 1.8 \times 10^{-10}$ seconds. The agreement with the value $\tau_E = 9.5 \times 10^{-11}$ seconds computed from the tables of Kaplan et. al. (1976)[5] is fair.

The data for the longer bridge, #S-14, are in clear disagreement with the length dependence predicted by the theory of Schmid et. al. (1980). Bridge #S-14 is longer than #S-15 and has a shorter coherence length in the bridge, leading to $(L/\xi_{bridge}(0)) = 5.41$. Using eq. (8),

---

[5] Actually, Kaplan et. al. (1976) tabulate the related parameter τ_o, which Clarke et. al. (1979) have shown to be:

$$\tau_o = 8.4\ \tau_E.$$

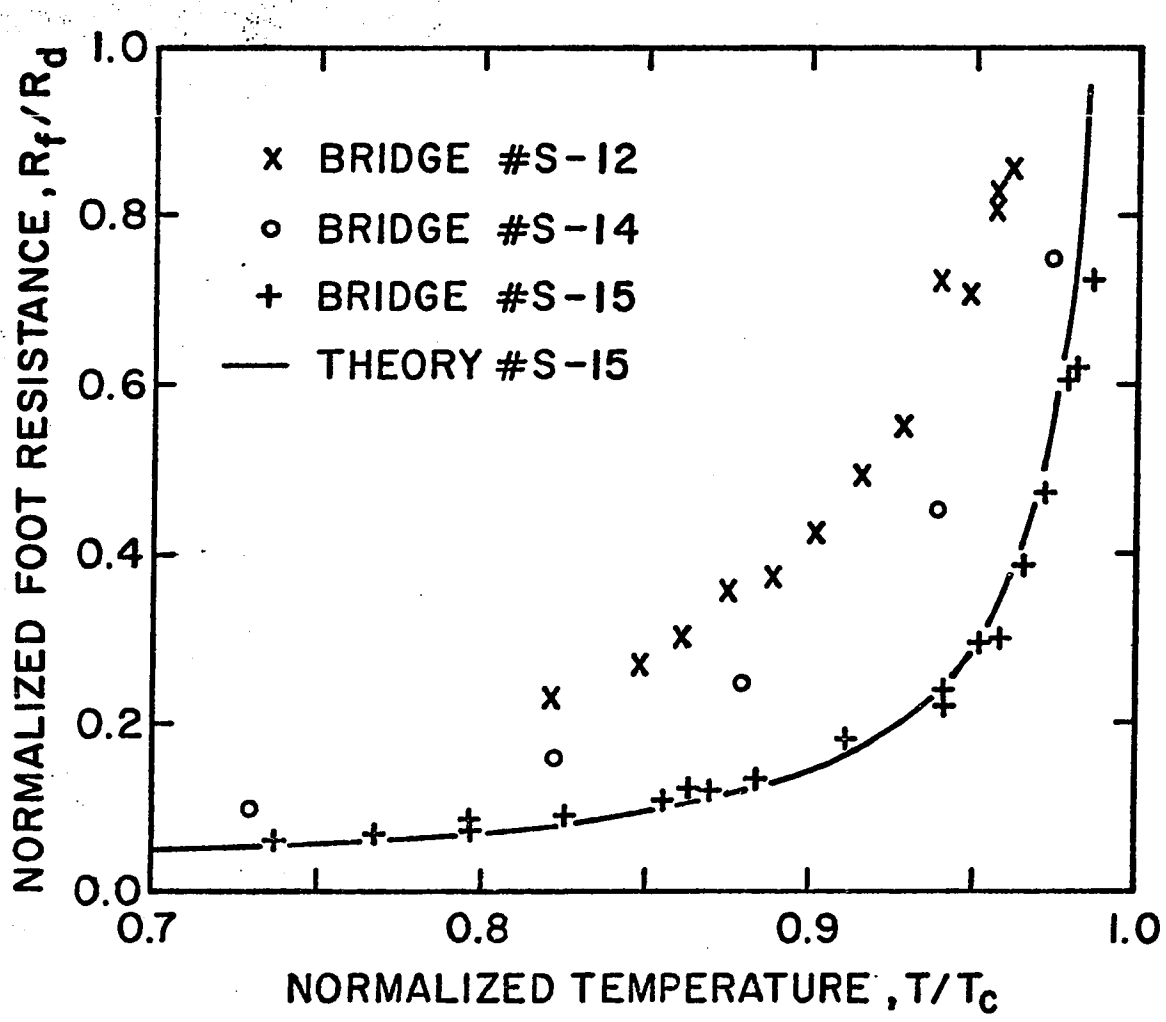

FIG. VI-9 Normalized foot resistance versus normalized temperature for pure and impure In VTBs. The solid line is the theory of Schmid, Schön and Tinkham (1980), fitted to the data for bridge #S-15 at t = 0.95.

this implies that (R_f/R_d) at t = 0.95 should be 50% lower than for #S-15 at the same temperature. In fact, (R_f/R_d) at t = 0.95 is 70% higher for #S-14 than for #S-15, in sharp disagreement with the theory. Although the requirement $L << \xi(0)(1 - t)^{-1/4}$ for rigorous application of the theory may not be met at this temperature, the qualitative conclusion appears to be unchanged at higher temperatures. The value of τ_E derived from the foot resistance of bridge #S-14 at t = 0.95 is $\tau_E = 5.1 \times 10^{-11}$ seconds, about half the value deduced from Kaplan et. al. The disagreement may arise because an effective length should be used in place of the geometrical length, or because boundary scattering, not considered in the theory, affects the results. Most likely, however, the discrepancy results from a width dependence of the effect which is not considered in this (one-dimensional) model. The R_f data for the intermediate-width bridge #S-13 fall between those for #S-14 and #S-15, but this could be explained by any of the above ideas.

The upper voltage limit of the foot region V_f, defined as the inflection point in the $\bar{V}(I)$ curve, is found to be 15-20 μV, with no apparent temperature dependence, for our In VTBs. Using eq. (9), this implies an inelastic scattering time of $\tau_E = 9 - 12 \times 10^{-10}$ seconds, in good agreement with the data of Kaplan et. al. (1976).

Neither Octavio et. al. (1978) nor Yeh and Buhrman (1977) noted a low-voltage foot in the $\bar{V}(I)$ curves of pure Pb VTBs. In the $\bar{V}(I)$ curves of our very narrow Pb-In bridges (#S-6, #S-9, #S-10), however, we find the low-voltage feature shown in Figure VI-10, which may be interpreted as a foot. The increase in differential resistance at the end of the foot occurs at a voltage $V_f \approx 100$ μV, in reasonable agreement with the value 80 μV obtained from eq. (9), using the data of Kaplan et. al. (1976) In the Pb-In bridges, the normalized foot resistance is $R_f/R_d = 1$ at all temperatures where the foot is observed. The foot is not observed very near T_c (t > 0.96 for bridge #S-9)

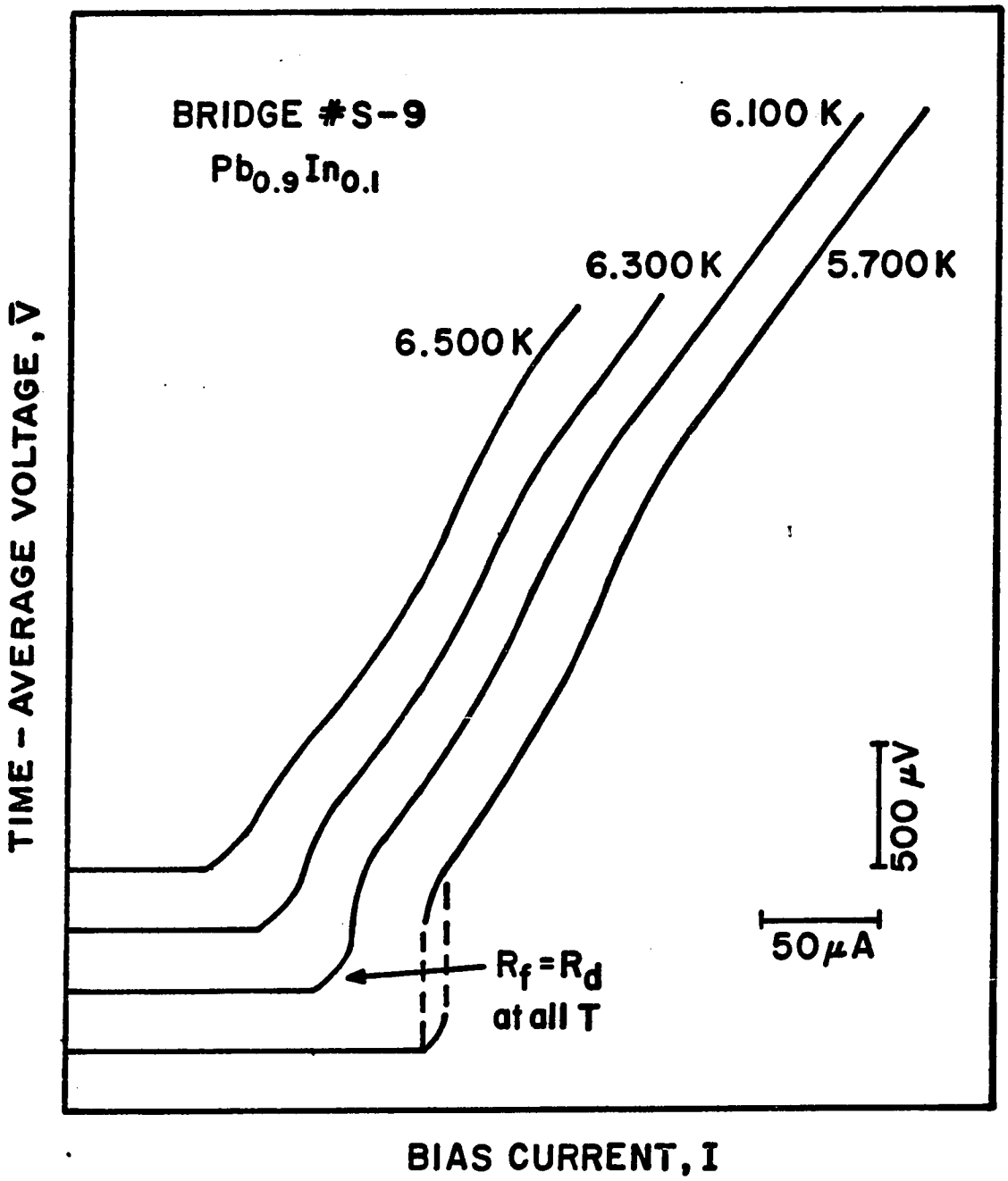

FIG. VI-10 $\bar{V}(I)$ curves of Pb-In VTB #S-9 at intermediate temperatures. Note the foot-like feature at low voltage, which has a (temperature-independent) differential resistance $R_f = R_d$.

or at low temperatures where heating-induced hysteresis is severe (e.g. $t < 0.75$ for bridge #S-9). Both Pb and $Pb_{0.9}In_{0.1}$ are moderately strong coupling, with $2\Delta(0)/kT_c = 4.35$ (Adler et. al. (1967)). If this constant is combined with the BCS temperature dependence of the energy gap, and the value $\tau_E = 2.3 \times 10^{-11}$ sec (obtained from the Pb data of Kaplan et. al. (1976)) is used in eq. (7), one finds that R_f/R_d is predicted to be less than 1 for $t < 0.97$, in contradiction to the observed data.

The low-voltage foot is also observed in the $\bar{V}(I)$ curves of the impure In bridge #S-12. The normalized foot resistance, plotted in Fig. VI-9, is larger than the values observed for pure In. This suggests that a smooth progression from pure In to $Pb_{0.9}In_{0.1}$ may exist, and tests of R_f/R_d for a sequence of alloy compositions might be informative.

VI.C.2 $\bar{V}(I)$ Curves at Low Temperatures--Hysteresis

Figure VI-11 illustrates the development of hysteresis in a narrow Pb-In VTB at low temperature. Due to the foot structure, the hysteresis first appears at a small finite voltage ($\sim$ 150 μV), rather than at the voltage onset $V \to 0$. The hysteresis-free temperature range $\Delta T_{\text{no hyst}}$ is listed in Table VI-II. The series of Pb-In bridges clearly shows that there is a strong inverse correlation between Wd and $\Delta T_{\text{no hyst}}$ (e.g., compare #S-6 to #S-7). On the other hand, there is no strong correlation between large D (i.e. thick banks) and large $\Delta T_{\text{no hyst}}$. The single exception to this rule is bridge #S-8 for which $D \gtrsim W$. Since D certainly has a strong effect on the thermal resistance of the two-dimensional cooling in the banks (see Skocpol et. al. (1974)), it must be that three-dimensional heat flow in the region near

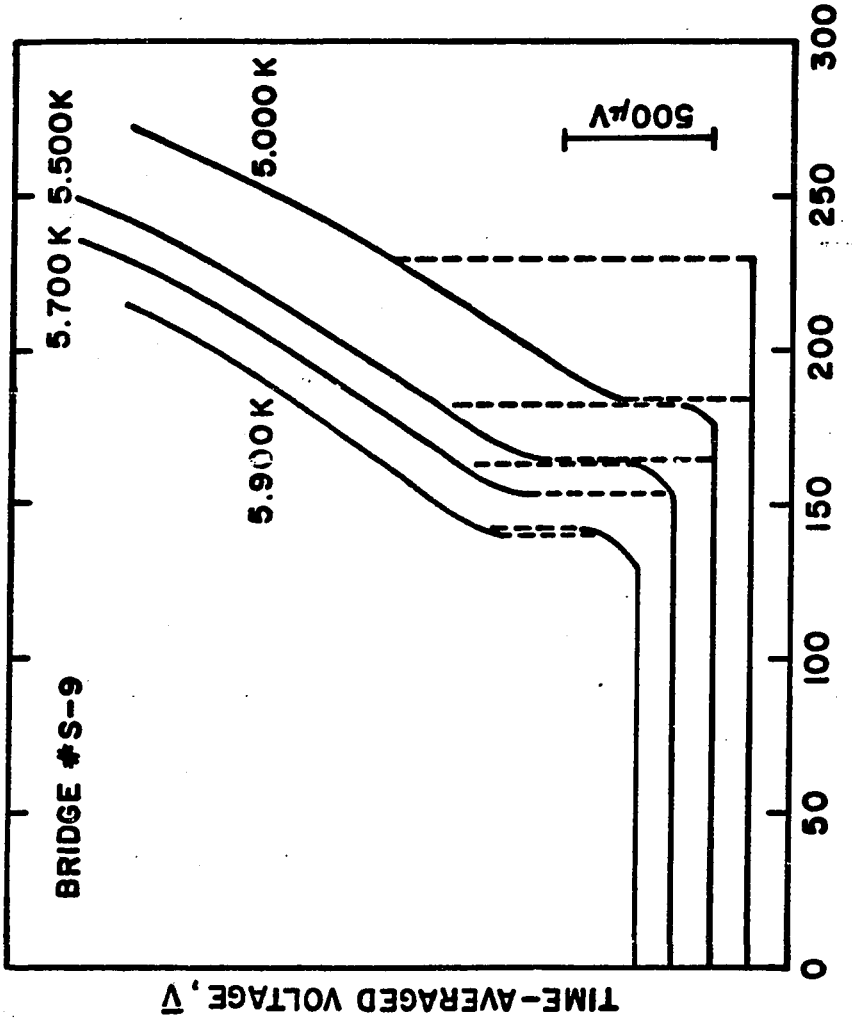

FIG. VI-11 $\bar{V}(I)$ curves of Pb-In VTB #S-9 at low temperatures. Note that the hysteresis initially appears above the foot region, rather than at $\bar{V} = 0$.

TABLE VI-II. Joule heating in variable-thickness microbridges.

$\Delta T_{no\ hyst}$ is the hysteresis-free temperature range, V_{max} is the maximum voltage at which microwave steps are observed, and $P_o(t\to 0)$ is the characteristic power level defined by Tinkham et. al. (1977). The tabulated values of P_o are computed from $V_{max}(t = 0.90)$ and extrapolated to $t = 0$.

Bridge #	Wd (10^{-12} cm^2)	R_d (Ω)	$\Delta T_{no\ hyst}$ (K)	$V_{max}(t=0.90)$ (mV)	$V_{max}(t_{min})$ (mV)	$P_o(t\to 0)$ (μW)
$Pb_{0.9}In_{0.1}$ bridges						
S-6	30	6.4	0.98	1.04	1.40[a]	.16
S-7	45	3.9	0.48	0.94	...	.22
S-8	$\approx$21	6.9	0.64	0.70	...	.07
S-9	20	8.4	1.17	1.02	1.50[b]	.12
S-10[c]	16	8.4	$\approx$3.9	>1.0	...	.12
S-11	80	3.6	0.20	0.73	...	.15
$In_{0.95}Pb_{0.05}$ bridge						
S-12	21	2.6	0.48	0.48	...	.09
In bridges						
S-13	20	2.0	1.0	0.59	...	.17
S-14	$\lesssim$16	5.1	>2.0	$\gtrsim$1.05	1.85[d]	.21
S-15	144	0.15	0.30	0.30	...	.59

[a] $t_{min} = 0.72$

[b] $t_{min} = 0.78$

[c] Bridge #S-10 behaves as a shunted bridge. As discussed in the text, the shunt can increase $\Delta T_{no\ hyst}$.

[d] $t_{min} = 0.47$.

the bridge is the dominant source of thermal resistance when the bridge is biased just above its critical current.

The shunted bridge #S-10 demonstrates that a small I_cR product can be of value in reducing Joule heating (e.g. increasing $\Delta T_{no\ hyst}$). We have argued above that for bridge #S-10, R_d was determined by the parallel combination of a 21-Ω microbridge and a 14-Ω normal shunt. For this bridge, the product $R_d(dI_c/dT)$ is 0.30 mV/K, about 1/3 the value for the unshunted bridge #S-9, and $\Delta T_{no\ hyst}$ is 3.9 K, about 3 times as large as for the unshunted bridge. When a normal shunt is added in parallel with a bridge, both the power dissipation and the differential resistance at a given bias current are reduced. As shown in section II.E, the former effect reduces the temperature rise of the bridge, and the latter effect means that a larger temperature rise is tolerated before hysteresis sets in. If the shunt resistance is physically separated from the bridge, heating will be further reduced, since part of the power dissipation will not be raising the temperature of the bridge region. If a normal shunt resistor is to be used to reduce heating-induced hysteresis, however, it should be remembered that the reduced I_cR product will usually lead to degraded signal-to-noise ratio and curtailed frequency response.

The In bridges show the same general trend as the Pb-In bridges. The boundary scattering in the bridge region may make the dependence on cross-sectional area even stronger for the small In bridges than for the small alloy bridges. For In bridges #S-14, we observed no hysteresis over the entire temperature range studied, implying $\Delta T_{no\ hyst} > 2.1$ K. This bridge is nonhysteretic over a wider temperature range than any unshunted Pb-In bridge, despite the smaller T_c of

In. As discussed in section II.F, the boundary scattering increases R_d, thus decreasing the power dissipation V^2/R_d, without proportionately increasing the thermal resistance of the banks.

VI.D Effects of Microwave Irradiation

VI.D.1 Microwave Steps and V_{max}

The $\bar{V}(I)$ curves of all of our VTBs show many constant-voltage steps under microwave irradiation, as shown in Fig. VI-12. The plots of step width ΔI_n vs. microwave amplitude for VTBs are qualitatively similar to those obtained for UTBs in chapter IV. An example of such a plot, for bridge #S-6 , is shown in Fig. VI-13. $\Delta I_n(\sqrt{P})$ is initially oscillatory and qualitatively similar to the prediction of the RSJ model (see Fig. II-4), but ΔI_n gradually vanishes as the microwave power becomes large. A comparison of Fig. VI-13 to Fig. IV-9 shows that the RSJ-like response extends over a wider range of microwave power for the VTB than it does for the UTB.

The improved microwave response is due to the thick banks which reduce Joule heating. As before, the effect of Joule heating on microwave response is gauged by the parameter V_{max}, the voltage of the highest observable microwave step. $V_{max}(t=0.90)$ for each VTB is listed in Table VI-II. All of the VTBs, without exception, have larger V_{max} than the value observed for the best UTBs, #I-6 and #I-7.[6] Some of the best VTBs were not tested at high enough microwave power to establish V_{max} exactly, so a lower bound is tabulated. As with $\Delta T_{no\ hyst}$, there is an inverse correlation between V_{max} and the cross-sectional area Wd, but unlike

---

[6] The VTBs, fabricated by the newer technique of step-edge lithography, all have widths which are less than the narrowest UTB, #I-7, but some of the VTBs, such as #S-11, have larger cross-sectional areas Wd. Thus we conclude that the variable-thickness geometry is the critical factor in the improvement.

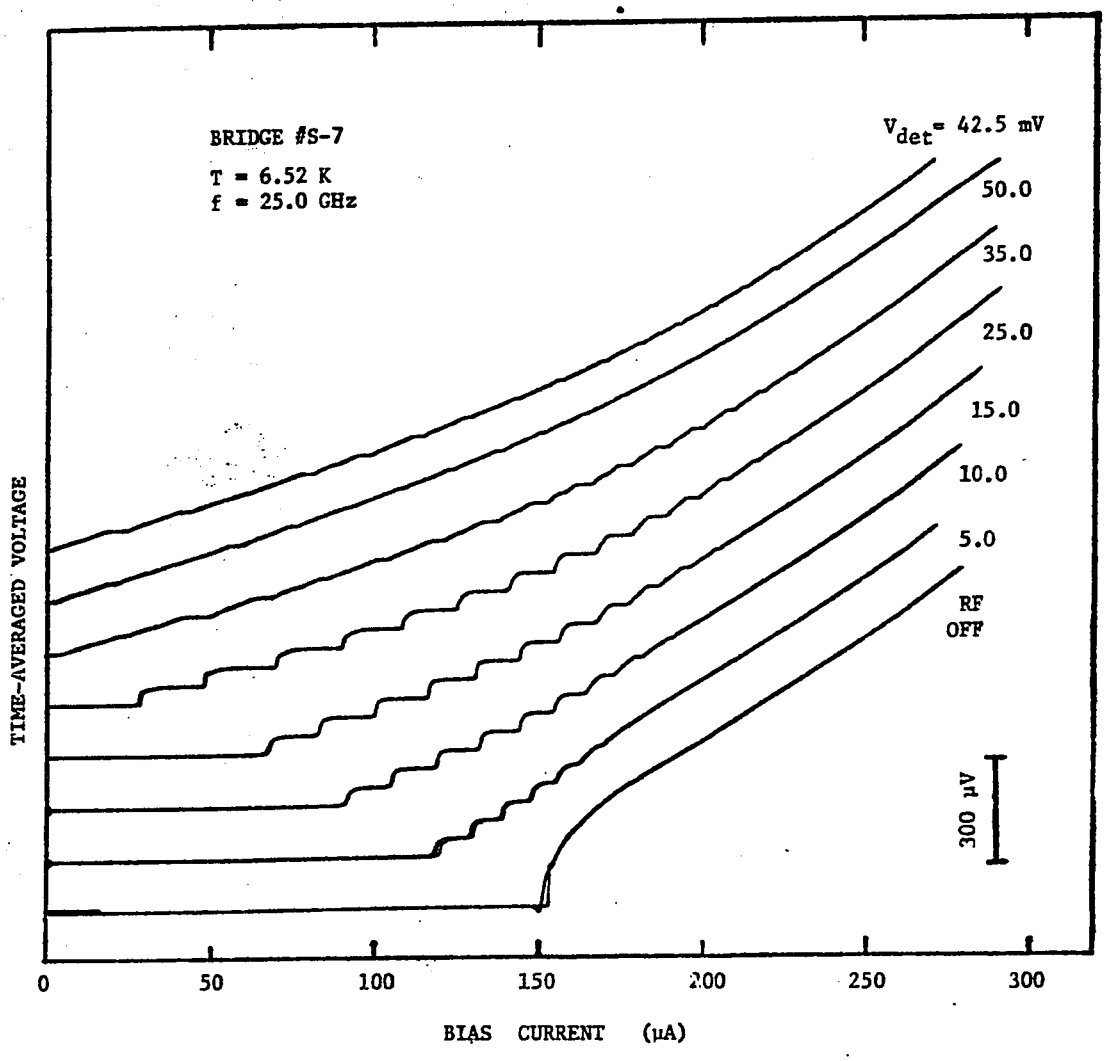

FIG. VI-12 $\bar{V}(I)$ curves of Pb-In VTB #S-7 under 25-GHz microwave irradiation. The microwave-induced steps are present up to $\bar{V} \approx 750\,\mu V$, much higher than the best result obtained for any of the UTBs of chapter IV. The diode detector voltage V_{det} is roughly proportional to microwave power. At this temperature, the normalized frequency is $(f\Phi_o/R_dI_c) = 0.088$.

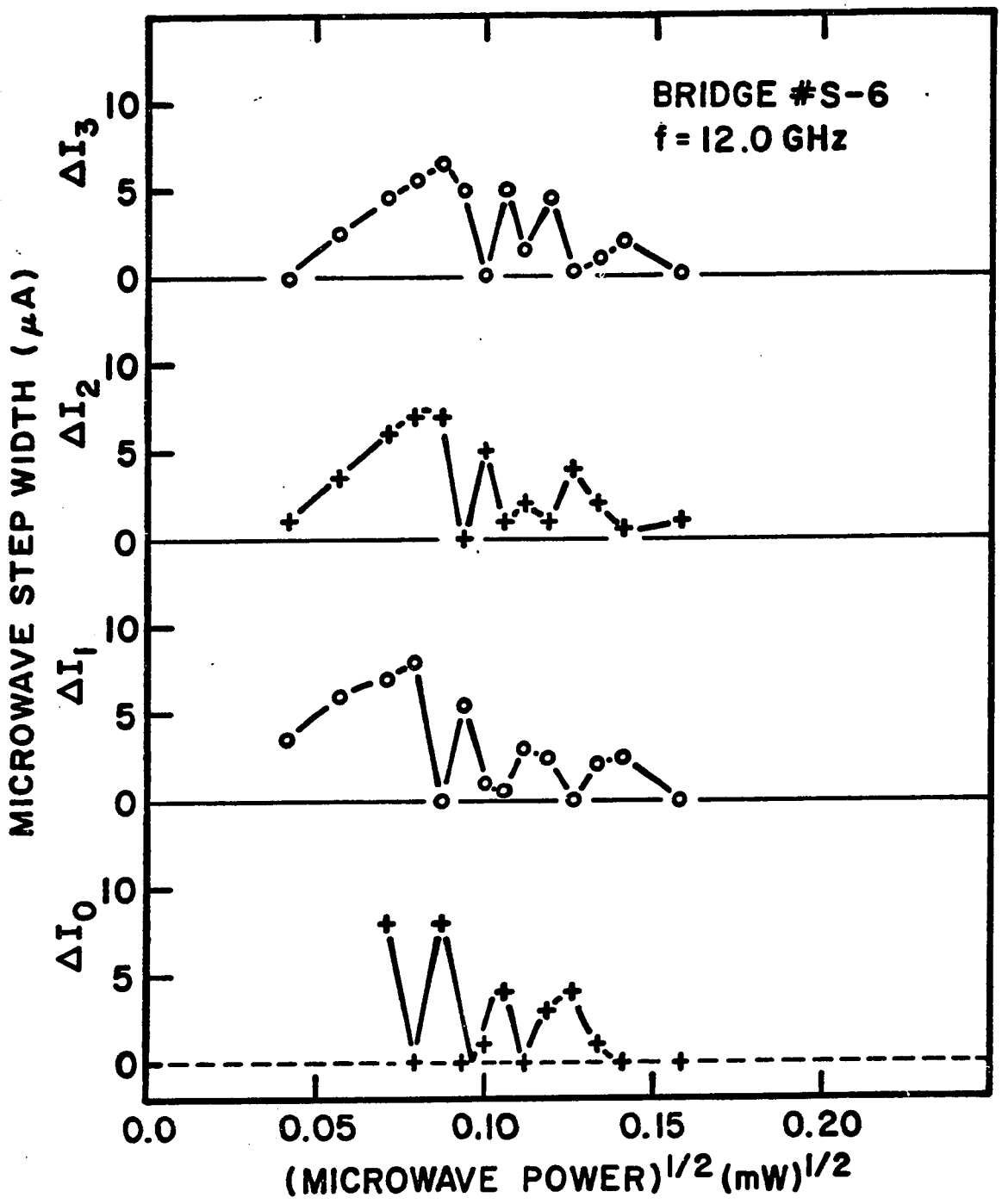

FIG. VI-13 Microwave step widths ΔI_n versus (microwave power)$^{1/2}$, for Pb-In VTB #S-6. The line segments are included as guides to the eye. These data are for t = 0.970, where I_c = 28 μA, so that the normalized frequency is $(f\Phi_o/R_dI_c)$=0.14.

$\Delta T_{no\ hyst}$, V_{max} is quite sensitive to the bank thickness D. For example, the wide bridge #S-11 has V_{max} as large as the narrow bridge #S-8; the large cross-sectional area of #S-11 is successfully compensated by its thick banks. In their study of Sn VTBs, Octavio et. al. (1977) also found that V_{max} increased with increasing bank thickness.

As the bath temperature is reduced, V_{max} increases to a saturation level which depends on bridge cross-section. As shown in Figure VI-14, V_{max} for the wide bridge #S-11 has nearly reached saturation at t = 0.90, while V_{max} for the narrow bridge #S-6 is still increasing at that temperature. In both bridges, the ratio of bank thickness to bridge thickness $D/d \gtrsim 5$, so that both bridges have three-dimensional cooling. Very near T_c, V_{max} is nearly equal for the two bridges.

Experimental values of P_o, the characteristic heating power introduced by Tinkham et. al. (1977), are listed in the final column of Table VI-II. To determine P_o, equation (II-84), which assumes that the solid angle for cooling in one bank is π, is applied to the measured value of $V_{max}(t = 0.90)$. It is estimated that V_{max} corresponds to $I_c(P)/I_c(0) = 0.03$, and values for $P_o(t = 0)$ are deduced. The theoretical value of P_o, found by inserting the material parameters of $Pb_{0.9}In_{0.1}$ alloy listed in Table IV-II into the theoretical expression eq. (II-84), is $P_o = 1.0 \times 10^{-6}$ W. For our In films, discussed at the beginning of the current chapter, the theoretical value $P_o = 4.7 \times 10^{-6}$ is computed. Clearly, the experimentally observed values of P_o are about an order of magnitude smaller than the theoretical predictions. This may occur because the banks are not sufficiently thick for three-dimensional cooling in the large-heating

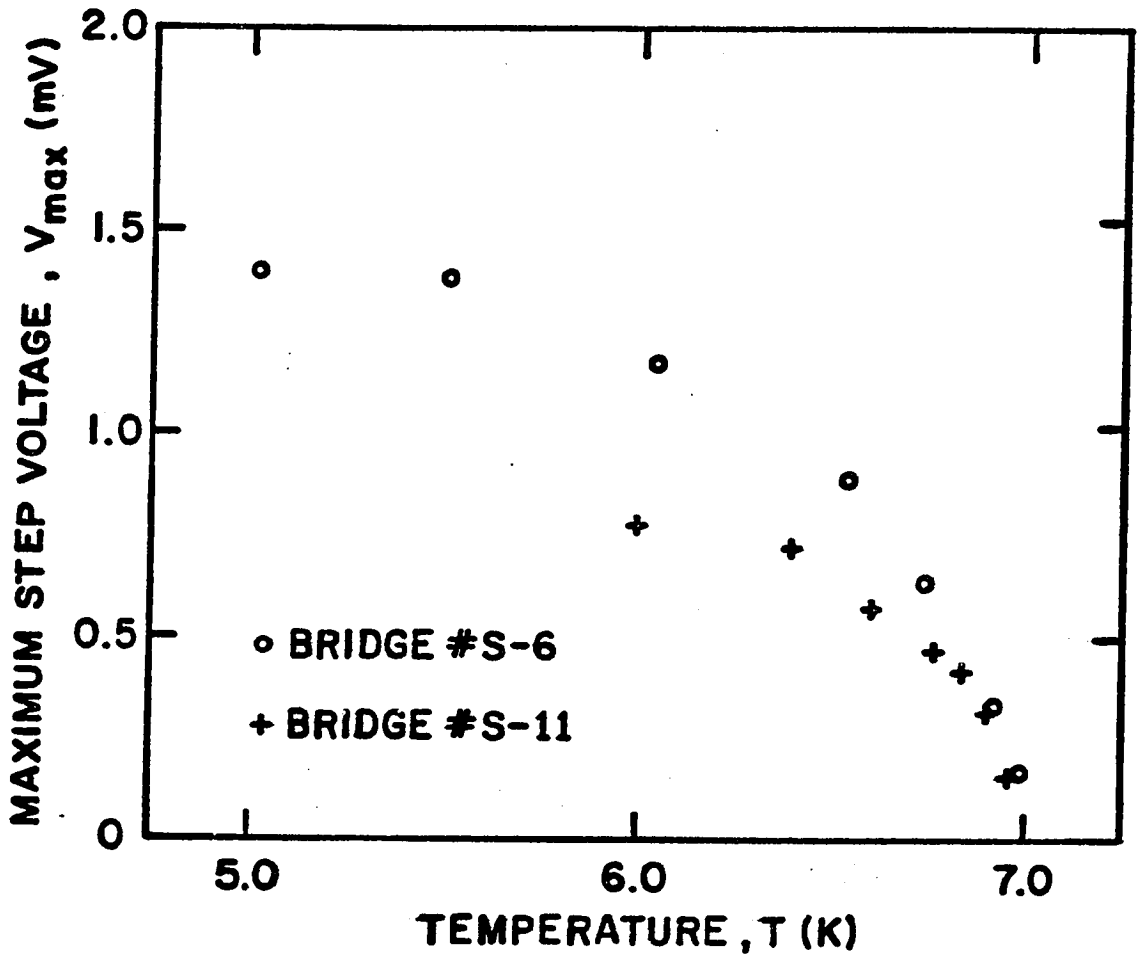

FIG. VI-14 Voltage of the highest observable microwave step V_{max} versus temperature for two Pb-In VTBs. Near T_c, V_{max} for the wide bridge #S-11 is similar to V_{max} for the narrow bridge #S-6. At low temperatures, however, V_{max} for the narrow bridge is much larger.

regime. Another possible source of discrepancy is that the theory of Tinkham et. al. (1977) assumes that the temperature distribution is the same as if the whole constriction (bridge plus banks) were nonsuperconducting. As discussed in section II.E, this can lead to an underestimate of the temperature in the bridge region and a consequent overestimate of V_{max}. The underestimate of T will be particularly severe in bridges such as #S-13 and #S-14, in which boundary scattering confines the power dissipation to the bridge region alone. Also, in these two bridges, the limitation on V_{max} due to the bridge term eq. (II-85) may also be significant. Thus, the clean-dirty-clean effect produced by boundary scattering does provide reduced Joule heating, but the improvement is not as great as one might expect from a simplistic application of the formulas of Tinkham et. al. (1977).

VI.C.2 Other Microwave-Induced Effects

Three types of microwave-induced behavior which are not predicted by the RSJ model or simple Joule heating theories are discussed in this section. Microwave-induced enhancement of the critical current, sometimes referred to as the Dayem effect, was observed in the pure In bridges. Subharmonic steps (i.e. constant-voltage steps at $\bar{V}$=nhf/2me with m an integer greater than 1) were observed in both the pure and impure In bridges. Microwave-induced asymmetry of the $\bar{V}(I)$ curve was observed for all VTBs tested.

Microwave-induced enhancement of the critical current was not observed for any of our alloy VTBs, but it was observed for the bridges of pure In. A sensitive test for I_c enhancement was made by biasing the bridge at a dc current slightly larger than I_c and monitoring the voltage while varying the microwave power. We estimate that an en-

hancement of 0.2% could be readily detected by this method, yet no enhancement was found for the alloy bridges, including the impure In bridge. The bridges of pure In, in contrast, showed enhancements of about 10% at $t \approx 0.90$. Most of the VTB tests were made at a frequency of 25 GHz, though some of the negative results were duplicated at 12 GHz as well. None of the Pb-In or Pb-Bi UTBs discussed in chapter IV showed microwave enhancement of I_c at 12 GHz.

The different behavior of Pb-In and In bridges is explained, at least qualitatively, by the Eliashberg model of gap enhancement. Following early experimental studies of critical current enhancement by Wyatt et. al. (1966) and Dayem and Wiegand (1967), Eliashberg (1970) proposed an explanation based on nonequilibrium superconductivity. The experimental significance of the Eliashberg model has been discussed in a recent article by Klapwijk et. al. (1977b). Within this model, microwave irradiation excites quasiparticles to higher energies, creating a nonthermal distribution of quasiparticles. When the frequency of the exciting radiation is less than the gap frequency $2\Delta/h$, little pairbreaking takes place, so the total number of quasiparticles is not greatly increased. In fact, because recombination is more rapid for high-energy quasiparticles, the number of quasiparticles may actually decrease. In either case, the nonequilibrium distribution of quasiparticles gives rise to a nonequilibrium value of the energy gap which can be larger than the equilibrium value. The enhanced critical current then occurs as a reflection of the enhanced energy gap. This picture predicts a low-frequency cutoff f_{min} for microwave enhancement which varies inversely with the inelastic electron scattering time τ_E. Thus, bridges of Pb alloy do not show microwave enhancement of I_c be-

cause the short τ_E of Pb alloys gives rise to a large f_{min}, larger than the measurement frequency.[7] Support for this argument can be found in the results of Yeh and Buhrman (1977) and Octavio (1978). Neither study found gap enhancement in VTBs of pure Pb which were exposed to microwave radiation at 10, 15, or 35 GHz.

The absence of I_c enhancement in the impure In bridge #S-12 is not immediately obvious from the Eliashberg gap-enhancement mechanism, as formulated by Klapwijk et. al. (1977b). The impure In film had a T_c close to that of pure In, and the lowest order can be treated as simply In with a short mean free path. From eq. (7) of Klapwijk et. al. (1977b), it can be shown that the only effect of a decrease in the (elastic-scattering) mean free path ℓ is a decrease in the microwave current needed to achieve a given amount of gap enhancement. That is, gap enhancement should occur regardless of the value of ℓ. One must consider, however, that gap enhancement and I_c enhancement are not equivalent in a short microbridge. As shown by the low-power part of Fig. II-4, the Josephson-effect response of a short bridge causes a microwave-induced <u>decrease</u> in I_c if the gap remains constant. Thus, the gap enhancement must be large enough to overcome this Josephson-effect decrease if I_c enhancement is to be observed. For a dirty-limit bridge, current biased at a frequency much less than $2\Delta/h$, the microwave scale current for gap enhancement is proportional to $\ell^{1/2}$, while the microwave scale current for Josephson-effect

---

[7] It must be noted that this explanation is not fully satisfactory in <u>quantitative</u> terms. Klapwijk et. al. (1977) estimate theoretically that $f_{min} \gtrsim 1$ GHz for Sn, while Kaplan et. al. (1976) find that $\tau_E(Sn)/\tau_E(Pb) \gtrsim 12$, so one would not expect f_{min} for Pb to be greater than 12 GHz on the basis of the theory.

response is I_c, which is proportional to $R^{-1} \propto \ell$. This implies that the Josephson-effect depression of I_c overcomes the gap enhancement and prevents I_c enhancement in short, dirty bridges with ℓ sufficiently small. Since Joule heating adds further complication to the ℓ-dependence of I_c enhancement, a quantitative calculation based on the published model, which neglects heating, is not justified.

Another non-RSJ effect which has been previously observed in microbridges is the development of constant-voltage steps at the subharmonic voltages $V = nhf/2me$. We find that subharmonic steps are not present in Pb-alloy UTBs or VTBs, but are present in pure and impure In VTBs. Noise rounding of the microwave steps is much more severe for In bridge #S-14 than it is for most of the Pb-In bridges, so noise rounding cannot explain the absence of subharmonic steps in the Pb-In bridges. The step with $(n/m) = \frac{1}{2}$ is generally the largest subharmonic step, but $(n/m) = 1/4, 1/3, 2/3, 3/4, 4/3, 3/2, 7/2$, etc. have also been observed. Gregers-Hansen et. al. (1972) reported that subharmonic steps in Sn UTBs were prominent in larger bridges and attributed them to a nonsinusoidal $I(\Delta\phi)$ relation caused by the magnetic self-inductance of the bridge structure. We find, however, that the subharmonic steps are only slightly less prominent in the very narrow bridge #S-14 than they are in the relatively wide bridge #S-15. Specifically, the maximum value of $\Delta I_{1/2} \approx 0.11 I_c$ for bridge #S-14 at $t = 0.975$, while the maximum value of $\Delta I_{1/2} \approx 0.23 I_c$ for bridge #S-15 at $t = 0.982$. Furthermore, the sharp distinction between Pb-alloy and In-based bridges suggests that weak electron-phonon coupling, associated with large τ_E, may be fundamentally connected with the subharmonic steps found in the pure and impure In bridges. This idea is not sup-

ported by the results of Yeh and Buhrman (1977) who found subharmonic steps "of very small amplitude" in some of their Pb VTBs, but a systematic study of subharmonic steps in alloys of the Pb-In or Pb-Tl system might therefore be useful in clarifying the origin of the subharmonic steps.

The third non-RSJ, microwave-induced effect observed in our VTBs is microwave-induced asymmetry of the $\bar{V}(I)$ curves. This effect has not, to our knowledge, been previously reported in microbridges, although the microwave-induced dc voltages observed in "bad" tunnel junctions by Langenberg et. al. (1966) and Chen et. al. (1972) may be a related phenomenon. A set of $\bar{V}(I)$ curves of bridge #S-9 showing microwave-induced asymmetry are reproduced in Figure VI-15. The voltage and current scales have been inverted for the negative half of the curve to facilitate comparison between the curves obtained for the two polarities. These $\bar{V}(I)$ curves illustrate several characteristic features of the microwave-induced asymmetry:

(i) No asymmetry is observed for any bridge in the absence of microwave radiation.

(ii) No asymmetry is observed at high levels of microwave power, where Joule heating begins to destroy steps.

(iii) No asymmetry is observed at high dc voltages, beyond the maximum step voltage V_{max}.

(iv) The microwave step voltages are not shifted, but the step widths ΔI_n are sometimes different on the positive current (+) and negative current (-) curves. For this reason, we describe the asymmetry in terms of a current shift $\delta I(\bar{V}) \equiv I^+(\bar{V}) - I^-(\bar{V})$.

(v) Both the magnitude and the polarity of the asymmetry depend on

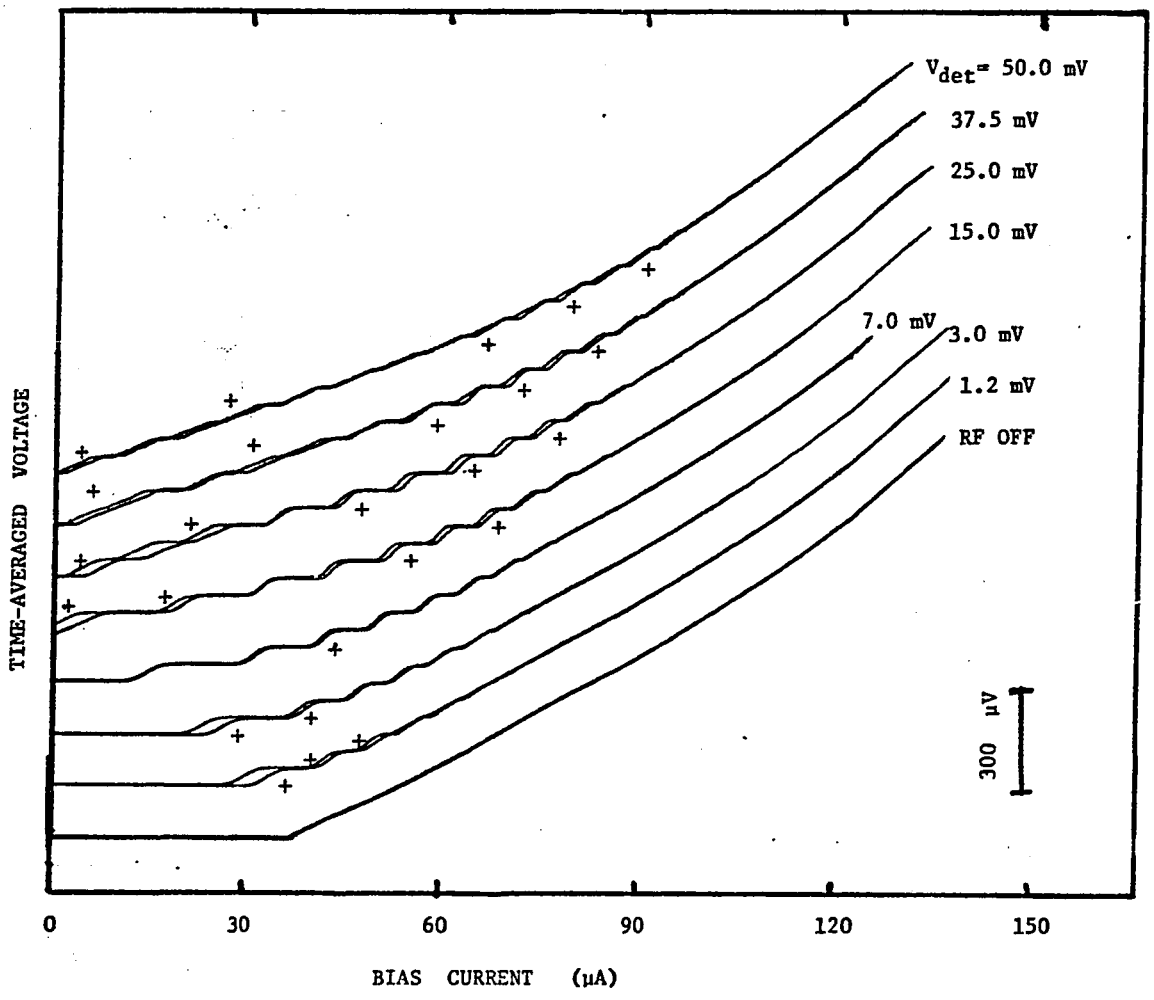

FIG. VI-15 Asymmetrical $\bar{V}(I)$ curves of Pb-In VTB #S-9. The microwave-induced asymmetry, discussed in detail in the text, has not been previously reported in microbridges.

the microwave power and the dc (time-averaged) voltage across the bridge.

(vi) When ΔI_o is small due to the Josephson-effect response of the bridge to applied microwave power, the asymmetry appears as a self-bias voltage (i.e., a time-averaged voltage across the bridge is present even when the dc bias current is zero).

(vii) The curves can be traced in either direction without hysteresis, except where the $\bar{V}(I)$ curve with no microwaves shows Joule-heating hysteresis.

When asymmetry studies on various bridges at different temperatures are compared, several systematic features stand out:

(a) No microwave-induced asymmetry is observed in the (linear) $\bar{V}(I)$ curves of bridges in the normal state (i.e. above T_c).

(b) Microwave-induced asymmetry is observed for <u>all</u> of the step-edge VTBs tested, including pure and impure In bridges as well as Pb-In bridges. (Tests of this kind were not performed on the UTBs.)

(c) The asymmetry is most pronounced in the very narrow bridges which have the least Joule heating and the highest R_d.

(d) The magnitude and polarity of the asymmetry observed for a given bridge at a given microwave power level and temperature depends on the configuration of microwave components used at room temperature. Presumably, this is due to changes in the source impedance driving the bridge, though it is possible that the harmonic content of the oscillator output is affected by the load impedance being driven.

(e) If no changes are made in the apparatus, asymmetric $\bar{V}(I)$ curves can be repeatedly retraced, even after the bridge has been

warmed to room temperature (but not removed from the cryostat) and stored for two weeks.

(f) Microwave-induced asymmetry has only been observed at a source frequency of 25 GHz; tests at 9.0 and 12.0 GHz have not revealed asymmetry. In view of point (d) above, the absence of the effect at 9 and 12 GHz cannot be firmly attributed to direct frequency dependence.

In Figure VI-16, the asymmetry current at the voltage onset $\delta I(V \to 0)$ is plotted as a function of microwave power[8] for bridge #S-9 at several temperatures. At low power, $\delta I(V \to 0)$ is essentially independent of temperature, and the data for all temperatures fall on a single universal curve. As the power P increases, $\delta I(V \to 0)$ rises to a peak, then decreases and changes polarity at power P_1. As P is increased further, the data for various temperatures separate from the universal curve and smoothly approach zero asymmetry. The high-temperature data are the first to separate from the universal curve. The implication is that Joule heating limits the microwave response of the bridge, including the microwave-induced asymmetry, above a threshold of microwave power which increases as the bath temperature is decreased.

The universal curve observed at low power levels is somewhat surprising, since one might expect the asymmetry current δI to be proportional to $I_c(T)$ or the power P_1 to be proportional to $(I_c(T))^2$.

Although the step-edge variable-thickness bridges are structur-

---

[8] Actually, the abcissa is millivolts of output from a diode detector, which is only approximately linear in microwave power.

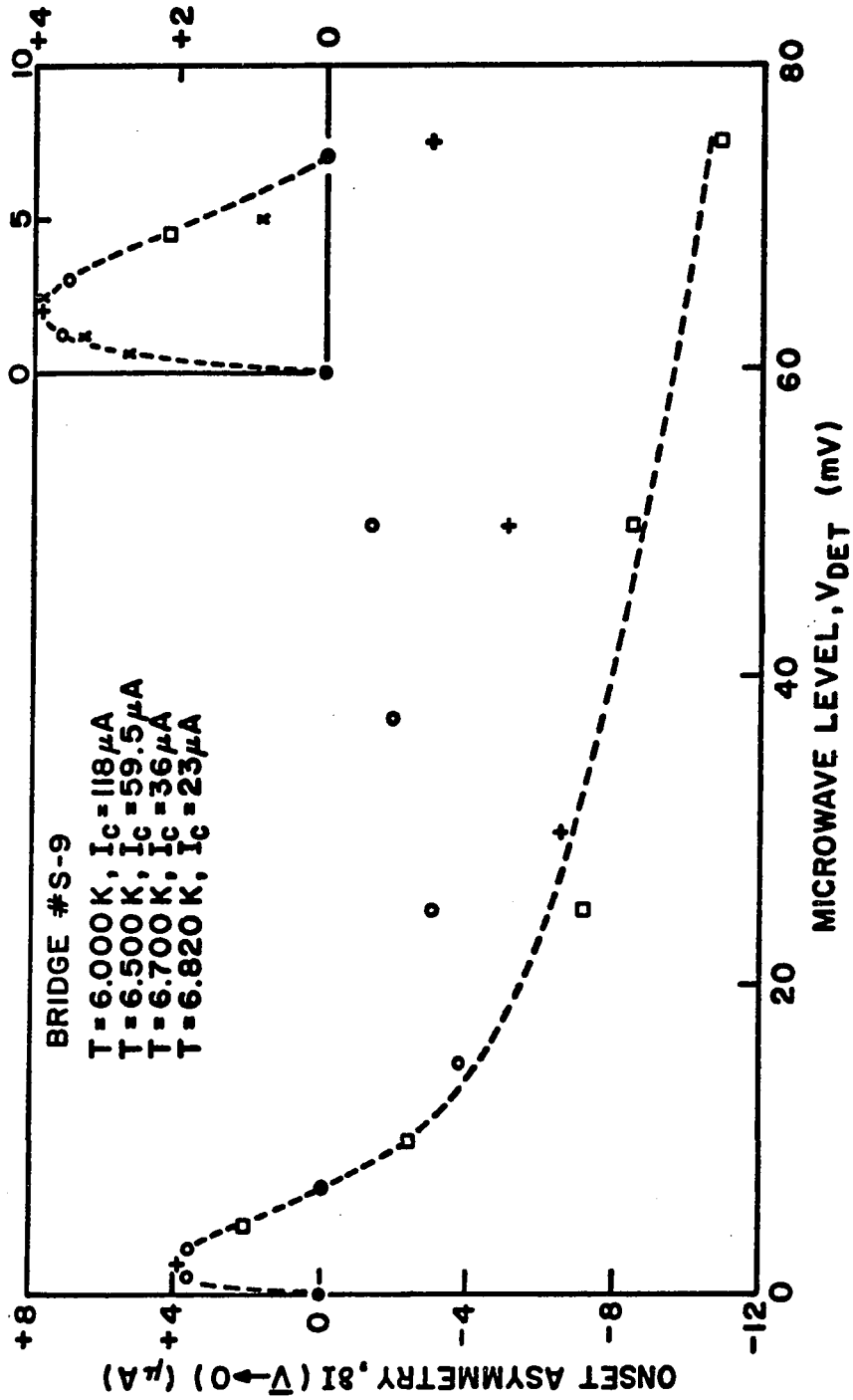

FIG. VI-16 Zero-voltage asymmetry current versus microwave detector voltage. Perhaps surprisingly, the asymmetry current observed at low microwave power levels does not depend on temperature. However, the power level at which the data leave the universal curve (dashed curve) increases with decreasing temperature.

ally asymmetrical, it is difficult to find a detailed mechanism which satisfactorily explains the above observations of asymmetry in $\bar{V}(I)$ curves. Points (ii), (iii), (v), and (a) rule out the possibility that the measurement circuitry itself is picking up and rectifying the microwave signal. Indeed, points (ii) and (iii) strongly suggest that the microwave-induced asymmetry is directly connected with the Josephson effect in the microbridges. Trapped flux, which can cause asymmetry in the I-V curves of wide tunnel junctions, cannot be responsible for the asymmetry observed here, because the bridges are too narrow. For example, the effect is observed in bridge #S-9 just 10 mK below T_c, where $(W/\xi(T)) < 0.1$. Reproducibility of the curves after warming above T_c also argues against a mechanism based on trapped flux. Both heat flow and quasiparticle diffusion are asymmetrical in an asymmetrical bridge, so nonequilibrium mechanisms are possible candidates. However, it is difficult to explain why there is no asymmetry in the curves without external microwaves, since the Josephson oscillation provides an internal microwave source.

We believe that the microwave-induced asymmetry is an intrinsic phenomenon of Josephson-effect microbridges which deserves further study. The effect may possibly have been overlooked in previous studies, or it may be clearly evident only in higher-resistance microbridges with good Josephson-effect response, which have not been previously studied. If the latter, microwave-induced asymmetry will take on increasing importance as microbridges are improved for practical application. The asymmetry is very sensitive to changes in the microwave source apparatus, so it would probably be informative to perform tests in a waveguide cryostat where the impedances and electromagnetic

field configurations are well known.

We summarize the conclusions to be drawn from these VTB studies, and compare them to the conclusions obtained for UTBs, in the following chapter.

VII. SUMMARY OF TRENDS AND CONCLUSIONS

VII.A Uniform-Thickness Bridges

At low voltages and temperatures near T_c, the $\bar{V}(I)$ curves obtained for the UTBs are qualitatively similar to those of the RSJ model, although substantial excess currents ($\approx 0.8\ I_c$) are extrapolated from the quasi-linear region. The differential resistance R_{min} of this quasi-linear region is nearly independent of temperature near T_c.

At higher voltages and lower temperatures, Joule heating becomes significant. Hysteresis which appears in the voltage onset is the most dramatic effect of heating. The hysteresis-free temperature range $\Delta T_{no\ hyst}$ is typically 85 mK for Pb-Bi bridges and 140 mK for Pb-In bridges. Joule heating also leads to a limit in the microwave response, characterized by the voltage of the highest observable microwave step V_{max}. V_{max} increases (improves) slightly as the bridge width is decreased; the largest value observed was 375 μV, for bridge #I-7 at $t \approx 0.90$.

The critical currents and microwave step data for narrow ($W<\xi(T)$) UTBs are reasonably well described by the uniform-depairing and resistively-shunted-junction (RSJ) theories, supplemented by straightforward calculations of Joule heating. Both the magnitude and temperature dependence of the critical current agree with the predictions of Mooij and Dekker (1978). However, the temperature dependence of R_{min} does not agree with the two-fluid result. When narrow bridges are exposed to microwave radiation, the $\bar{V}(I)$ curves show constant-voltage steps at the appropriate Josephson-relation voltages. The RSJ model correctly predicts the oscillatory dependence of step width on microwave amplitude which is observed at low power, but microwave heating causes the

steps to fade out at high power levels. Using heating effects to calibrate the microwave current in the bridge, the absolute microwave sensitivity at low power is found to be in good agreement with the RSJ calculation. An intrinsic noise calculation based on the RSJ model also agrees with the data on step rounding, and the absence of subharmonic steps indicates a nearly sinusoidal current-phase relation.

Interpretation of the data for wide UTBs is less straightforward. Although the magnitude of the critical current is in agreement with the vortex-flow result of Aslamazov and Larkin (1975), the temperature dependence of the experimental data is stronger. The experimental $\bar{V}(I)$ curves do not show the periodic $d\bar{V}/dI$ peaks predicted by AL (1975), and the temperature dependence of R_{min} is also different from the vortex-flow result. Microwave steps were observed in the $\bar{V}(I)$ characteristics of all bridges for which $(W/\xi(0)) \leq 50$. These observations were made at temperatures which imply $(W/\xi(T)) \leq 7$.

One major distinction between the RSJ model and the vortex-flow models is that the latter predict a monotonic dependence for step width ΔI_n as a function of microwave amplitude, while the former predicts the oscillatory dependence shown in Fig. II-4. Since the oscillatory behavior is truncated at high power levels by heating, it is identified at relatively low power by the vanishing and reappearance of the n = 0 and n = 1 steps. Using this criterion, the oscillatory dependence is observed for all of the bridges which show steps except for bridge #E, which is the widest of these. For example, bridge #F shows the oscillatory dependence at temperatures as low as 8.39 K, where its relative width is $(W/\xi(T)) = 5$. Since bridge #E shows steps over such a narrow

range of microwave power, it appears that heating truncates the oscillatory dependence even before the first zero has been reached. In brief, the evidence does not favor the monotonic dependence predicted by the vortex-flow theories of Likharev (1972) and AL (1975), even for bridges with $(W/\xi(T)) \gtrsim 5$ and $(W/\xi(0)) \gtrsim 40$.

No microwave steps were observed for the widest microbridge tested (1 μm Pb-Bi bridge #B). Judging by the trends evinced by the narrower bridges, heating probably restricted the steps to very narrow ranges of temperature and microwave power, so that they were missed in the limited number of measurements performed. It is also possible that generation of steps in such wide bridges would require levels of microwave power which exceed the Joule heating threshold, prohibiting steps entirely.

Conventional scaling assumptions are that the Wiedemann-Franz law holds and that $I_c R$ is a constant independent of material for given values of $(W/\xi(T))$, T, and T_c. Then one expects the power dissipation I^2R to scale with the thermal resistance if the material is changed, and the limitations due to Joule heating should apply to wide UTBs of any material. Indeed, Harris and Laibowitz (1977), in their study of Nb UTBs fabricated by electron-beam lithography, found that microwave induced steps were observed only in bridges for which $W \leq 0.5$ μm. These Nb bridges had superconducting parameters ($\xi_{GL}(0) = 135$ Å and $\lambda_{GL}(0) = 430$ Å) similar to our Pb-Bi bridges, and the steps were observed down to temperatures which implied $(W/\xi(T)) = 5.9$. Harris and Laibowitz (1977) speculated that Joule heating might have been the factor which prohibited observation of steps in wider bridges, but no data for V_{max} or $\Delta T_{no\ hyst}$ were published.

Janocko et. al. (1972) obtained rather different results, ob-

serving microwave-induced steps in Mo-Re bridges as wide as $(W/\xi(T)) \approx 250$. The resolution of the apparent conflict is that Janocko et. al. (1972) used Mo-Re films whose properties were very different from the bulk material. Film resistivities were fifteen times larger than those of the bulk alloy and there were large variations ($\approx$ 3 K) in the critical temperature of the bridges. These anomalies, together with a very complicated pattern of step spacing, suggest that film inhomogeneities may have played a significant role in these experiments (cf. Schmid and Hauger (1973) and Larkin and Ovchinnikov (1974)).

Gubankov et. al. (1977) have investigated the transition from uniform depairing to vortex flow in variable-thickness bridges (VTBs). In their studies of Sn VTBs, Gubankov et. al. (1977) found that $I_c(T)$ for a relatively narrow bridge ($(W/\xi(0)) \approx 18$) near T_c agreed with the uniform-depairing prediction of Aslamazov and Larkin (1969), while $I_c(T)$ for a very wide bridge ($(W/\xi(0)) \approx 500$) near T_c agreed with the vortex-flow result of Likharev (1972). The very wide bridge showed microwave-induced steps at a temperature which implied $(W/\xi(T)) \approx 90$, but it <u>did not</u> show an oscillatory dependence of step width ΔI_n on microwave amplitude. (As in the present work, the steps faded out at high power, so the oscillatory dependence was identified by the reappearance of the zeroth and first steps.) Measurements at various temperatures on one particular bridge spanned the vortex-flow boundary $(L/\xi(T)) = 3.49$ computed by Kuprianov et. al. (1975), and it was found that the oscillatory dependence disappeared near the predicted boundary temperature. However, the published data are also compatible with heating-induced

truncation of the oscillatory dependence.[1] Wang et. al. (1978) observed microwave-induced steps in a Nb VTB with $(W/\xi(0)) = 60$. They found that even-numbered steps were present under some operating conditions, which was attributed to the coherent flow of two vortices simultaneously. The observation of microwave-induced steps in very wide VTBs is almost certainly related to the thick banks used. Thick banks may help to keep vortex flow confined to a single channel and they definitely reduce the effects of Joule heating.

As described in the preceding paragraphs, our observations on moderately wide UTBs do not confirm the vortex-flow theory of the dynamic state presented by AL (1975). In particular:

(1) The magnitude and temperature dependence of R_d do not agree with the theory.

(2) No voltage-periodic peaks in $d\bar{V}/dI$ are observed in the absence of microwave radiation.

(3) Microwave steps show an oscillatory dependence on microwave amplitude.

(4) No subharmonic steps are observed.

It must be pointed out, however, that the theoretical prediction for the critical current is roughly correct in magnitude, and that no allowance for Joule heating was made in the theory.

---

[1] If the RSJ theory is applied to the data taken at the higher temperature (just above the predicted vortex-flow transition temperature), one can compute the microwave power level at which the zeroth step should reappear at the lower temperature (below the predicted transition). Since this power level exceeds the heating threshold shown in the data at the higher temperature, heating may obliterate the step reappearance at the lower temperature.

In any case, it is clear from these studies that the uniform-thickness microbridges based on the vortex-flow mechanism do not have great promise for device applications, despite early optimism in the mid-1970s. It appears that the initially promising results were obtained with films that were not homogeneous materials. While the use of inhomogeneous films for practical devices is not necessarily precluded, our studies of microbridges of homogeneous films show significant heating problems for devices which should be in the vortex-flow regime. Our results for UTBs indicate clearly the need for the variable-thickness, small-bridge configuration studied in the second part of the thesis.

VII.B Variable-Thickness Bridges

The VTBs studied here are both shorter and narrower than one coherence length for at least 0.5 K below T_c. Although both the Pb-In alloy and the "pure" In are moderately dirty materials ($\ell_{bank} < \xi_{BCS}$), two of the In bridges are clean bridges in the sense that $W < \ell_{bank}$. All of the VTBs tested show the linear temperature dependence of I_c near T_c which is predicted by the small-microbridge theories of Aslamazov and Larkin (1969) and Likharev and Yakobson (1976a). Very near T_c ($(1-t) < 0.015$), the Pb-In bridges show a deviation from linearity which is correlated with bridge width; the pure In bridges, for which $W/\xi(0) << 1$, do not show a deviation very near T_c. At low temperatures ($t < 0.7$, below the range of applicability of the GL theory), I_c falls between the linear curve and the result of Kulik and Omelyanchuk (1975). The product $R_d(dI_c/dT)$ is a smooth function of the bridge cross-sectional area which decreases to 0.6 mV/K for the narrowest bridges. This limiting value is close to the AL (1969) pre-

diction. The minimum differential resistance at t = 0.99, which we denote R_d, is found to be a more useful measure of the device resistance than the total resistance measured above T_c. In brief, the I_c data for the Pb-In and In VTBs form a consistent picture which confirms the key results of the small-bridge calculations based on the GL theory as the bridges are made very narrow.

The $\bar{V}(I)$ curves of the VTBs show more structure than those of the Pb-alloy UTBs discussed in chapter IV. Cavity-induced steps indicate the efficient microwave coupling which can be achieved in the higher-resistance bridges. Energy-gap-related structure appears only in the pure In bridges, which have a long mean free path in the banks. The role of the mean free path is not considered explicitly in the gap-structure theory of Hasselberg (1974), but may be treated in future work by T. M. Klapwijk and G. Blonder (private communication). A low voltage foot structure is observed in the $\bar{V}(I)$ curves of the pure and impure In bridges, and a possibly analogous structure is described in the $\bar{V}(I)$ curves of narrow Pb-In bridges. The upper voltage limit of the foot V_f for In and Pb-In bridges is compared to the theoretical prediction of Schmid, Schon, and Tinkham (1980) that:

$$V_f = \frac{2.76\,\hbar}{e\,\tau_E} \qquad (1)$$

and this relation is approximately confirmed. Though not conclusive, this supports the idea that the foot is intimately connected with quasiparticle relaxation. The foot resistance of the In bridges is in rough agreement with the theory. However, the foot resistance decreases weakly with decreasing bridge length, while the theory of Schmid et. al. predicts the opposite (weakly increasing) length de-

pendence. However, more bridges should be tested to separate out the effects of length and width. The foot resistance of the Pb-In bridges does not agree with the theory.

As expected, the variable-thickness geometry provides improved finite-voltage performance (as compared to the UTB geometry) due to reduced Joule heating. Both $\Delta T_{no\ hyst}$ and $V_{max}(t = 0.90)$ are 3-5 times larger for the best Pb-In VTBs than they are for the best UTBs of chapter IV. The highest values of V_{max} observed were 1.50 mV for bridge #S-9 at $t = 0.78$ and 1.85 mV for bridge #S-14 at $t = 0.47$. Both $\Delta T_{no\ hyst}$ and V_{max} increase as the cross-sectional area of the bridge decreases, but only V_{max} increases with increasing bank thickness D. This probably occurs because the heating when biased on a high step at V_{max} involves a high power level and a larger hotspot than the heating which causes hysteresis at the voltage onset. If the hotspot radius is >D, the cooling is quasi-two-dimensional and depends strongly on D. On the other hand, $\Delta T_{no\ hyst}$ involves low-level heating and a small hotspot, so the thermal resistance is dominated by the three-dimensional spreading resistance near the bridge unless the banks are very thin ($D \lesssim \sqrt{Wd}$).

The systematic trends of the V_{max} data agree qualitatively with the theory of Tinkham, Octavio and Skocpol (1977), but the quantitative agreement is relatively poor. V_{max} of the Pb-In bridges varies roughly as $\sqrt{R_d}$, except for bridge #S-8 which has relatively thin banks ($D \lesssim \sqrt{Wd}$). As predicted by the theory, the pure In bridge #S-15 has P_o about 5 times as large as P_o for Pb-In bridge #S-9, which has a comparable normalized width $W/\xi(0)$. However, for both bridges the magnitude of P_o is only about 1/10 the theoretical prediction. This may

reflect the difference between the actual spatial distribution of the power dissipation and the spatial distribution assumed in the theory. Alternatively, the bank thickness may be insufficient to justify the assumption of fully three-dimensional cooling in the banks. Finally, we note that our bridges are not really in the limit $eV_{max} >> \pi kT_c$ assumed by Tinkham et. al. (1977). This may lead to an underestimate of the bridge term eq. (II-85).

The pure In bridges #S-13 and #S-14 show dramatic effects of boundary scattering. For bridge #S-14, the overall resistance ratio of the bridge plus banks is $\rho_{295}/\rho_4 = 3.67$ and the inferred resistance ratio of the bridge region alone is $\rho_{295}/\rho_4 = 1.60$, despite clean banks with $\rho_{295}/\rho_4 = 13.2$. The high resistance of the bridge region reduces the dissipated power at a given voltage, improving both $\Delta T_{no\ hyst}$ and V_{max} substantially over the results obtained for wide In bridges. The improvement in V_{max} is somewhat less than one would predict assuming a constant P_o, however.

Table VII-I summarizes our observations on effects which are <u>not</u> predicted by the RSJ model augmented by Joule-heating calculations. All of these effects, except the microwave induced asymmetry of the $\bar{V}(I)$ curves, show a marked dependence on the microbridge material. The cavity-induced structure and the microwave-induced asymmetry appear to be more prominent in the higher-resistance bridges.

The very small Pb-In VTBs tested in this study display most of the characteristics desired for device applications. In Table VII-II, we have listed several key performance parameters of bridge #S-9 and compared them to those of In bridge S-14 and best-case results reported for other microbridge structures. One major advantage of the alloy

TABLE VII-I. Summary of non-RSJ effects in variable-thickness microbridges.

Bridge #	R_d (Ω)	Cavity-induced steps	Energy-gap structure	Low-voltage foot	I_c enhancement	Subharmonic steps	Microwave-induced asymmetry
$Pb_{0.9}In_{0.1}$ bridges							
S-6→11	3.6-8.4	Yes, except #S-11 strong when $R_d > 5\Omega$	No	Maybe $R_f = R_d$ $V_f \approx 100\mu V$	No ($<0.002I_c$)	No	Yes $\leq 0.3I_c$
$In_{0.95}Pb_{0.05}$ bridge							
S-12	2.6	Yes	No	Yes $R_f << R_d$ $V_f \approx 25\mu V$	No ($<0.002I_c$)	Yes $\Delta I_{1/2} \leq 0.1I_c$ at t=0.966	Yes
In bridge							
S-15	0.15	No	Yes n = 1-5	Yes $R_f << R_d$ $V_f \approx 15-20\mu V$	Yes $\approx 0.1I_c$ at t=0.9	Yes $\Delta I_{1/2} \leq 0.2I_c$ at t=0.982	Yes
In bridges with strong boundary scattering in bridge region							
S-13,14	2.0,5.1	Yes	Yes n=1-3	Yes $R_f << R_d$ $V_f \approx 15-20\mu V$	Yes $\approx 0.1I_c$ at t=0.9	Yes $I_{1/2} \leq 0.1I_c$ at t=0.975	Yes

TABLE VII-II. Key parameters for application of microbridges as high-frequency detectors.

Bridge	R_d (Ω)	V_{max} at (mV)	t	Reference
Uniform-thickness bridges				
Sn	$\lesssim$ 0.15	0.4	0.55	Skocpol et. al. (1974)
Pb-In	5.5	0.4	0.90	this work, #I-7
Variable-thickness bridges				
Pb	...	1.6	...	Yeh and Buhrman (1977)
Nb	0.39	0.4	0.94	Li-Kong Wang et. al. (1978)
Sn	$\lesssim$ 0.44	3.7	0.40	Octavio and Skocpol (1979)
(uniform material)				and Octavio (1978)
Sn	$\lesssim$ 2.5	4.2		Octavio and Skocpol (1979)
(clean-dirty-clean)				and Octavio (1978)
Pb-In	8.4	1.5	0.78	this work, #S-9
In	5.1	1.9	0.47	this work, #S-14

bridge is the high device resistance provided by the high-resistivity material. As noted by Richards (1977), device resistance must be $\gtrsim$10 Ω if efficient, low-noise coupling of radiation is to be achieved at frequencies above 100 GHz.[2] The value of the variable-thickness geometry is also clearly demonstrated by the table. For the uniform-thickness bridges, V_{max} is never greater than 0.4 mV, corresponding to a fundamental Josephson frequency of 200 GHz. This means that the UTBs will not operate well, if at all, at the sub-millimeter wavelengths where the small RC times of microbridge-type devices are most attractive. By contrast, all of the VTBs listed in the table have $V_{max} \geq 1$ mV, and thus should be capable of Josephson-effect detection at frequencies above 500 GHz. In addition to larger V_{max}, the VTBs show larger $\Delta T_{no\ hyst}$, permitting application at lower normalized temperatures, where the energy gap is larger and I_c is not so sensitive to temperature variations.

The best performance (i.e. the largest values of $\Delta T_{no\ hyst}$ and V_{max}) listed in the table is for bridges in which $\ell_{bridge} < \ell_{bank}$. As discussed at the beginning of this chapter, boundary scattering causes such an effect in our narrow In bridges, and the narrowest of these bridges is indeed the best. Tinkham et. al. (1977) also concluded that boundary scattering made an important contribution to the resistance of their narrow VTBs of (moderately) pure Sn. Recognizing the importance of the clean-dirty-clean effect in reducing Joule heating (see section

---

[2] Resonant coupling may be used to provide an impedance transformation at frequencies < 100 GHz, but above $\gtrsim$ 100 GHz, resonant coupling is impractical for most device applications (P. L. Richards, private communication).

II.F), Octavio and Skocpol (1979) made a deliberate attempt to produce a bridge with dirtier Sn in the center region, and succeeded in obtaining one bridge with $R_{tot} = 2.5\ \Omega$ and V_{max} higher than any uniform-material bridge.

In this work, we have surveyed the properties of high-resistance, variable-thickness microbridges, and found many opportunities for future work involving the physics of ultrasmall microbridges. Several of the dynamic-state effects were observed to show conspicuous dependence on the electron mean free path or on the base material (In vs. Pb). Thus we believe that detailed studies of subharmonic steps, microwave-induced enhancement of the critical current, energy-gap-related structure in $\bar{V}(I)$ or low-voltage "feet" for a series of alloys with different compositions would help to confirm or develop satisfactory theories of these phenomena. The microwave-induced asymmetry of the $\bar{V}(I)$ curves does not show such a conspicuous material dependence, and the next logical step in explicating this asymmetry is a study using a waveguide cryostat with precisely known field configurations. Of course, future experiments need not be limited to the simple variable-thickness microbridge geometry studied here. For example, a structure combining a microbridge with an integral, oxide-barrier tunnel junction could be used to study directly the quasiparticle distribution function in an operating microbridge.

This work also has significant implications for superconducting device applications. Using advanced fabrication techniques, such as those described in this work, it should soon be possible to fabricate clean-dirty-clean bridges with smaller dimensions and higher resistivity in the bridge center than those produced to date. Whether

boundary scattering or alloy materials are used to enhance the bridge resistivity, the result will be devices with both high device resistance and large V_{max} which permit the use of optimized Josephson-effect microbridges in a variety of high-frequency applications.

APPENDIX A. PROCESS PARAMETERS FOR PHOTOLITHOGRAPHY

A.1. Substrate Cleaning

a) Ultrasonic agitation (usa) in acetone bath for $\gtrsim$ 180 sec.

b) Spray-bottle rinse in acetone.

c) Blow dry with high-purity-grade nitrogen gas.

d) If spotty, give successive rinses in acetone, distilled, deionized water, and isopropanol, then blow dry with high-purity-grade nitrogen gas.

e) usa in isopropanol bath for $\gtrsim$ 180 sec.

f) Spray-bottle rinse in isopropanol

g) Blow dry with high-purity-grade nitrogen gas.

A.2. Preparation of photoresist (PR) layer

a) Center substrate on chuck of high-speed spinner, spin at 10,000 revolutions per minute (rpm) for 250-nm layer, 4000 rpm for 350-nm layer, or 2000 rpm for 500-nm layer.

b) Drop three drops of filtered PR onto center of spinning slide. Shipley type AZ-1350B PR was used for all photolithography. Pre-filter was Millipore microfiber glass type AP 2502200, and absolute filter was Millipore type FALP 02500, a 1-μm filter of polytetrafluoroethylene.

c) Spin for 30 seconds after last drop.

d) Check for uniformity; clean and repeat if necessary.

e) Softbake samples on a hotplate for 15 min. at 90°C.

A.3. Exposure of PR pattern

a) Contact exposures were made using an unfiltered 100-watt high-pressure mercury-vapor arc lamp. With a lamp-to-workpiece distance of $\gtrsim$ 20 cm, typical exposure times were $\sim$ 30 sec.

b) Projection exposures were made using a Carl Zeiss Photomicroscope equipped with type II-C epi-illuminator incorporating a 15-Watt tungsten lamp. Centerable objectives of the "Aufl Pol" series of achromats were used for all bridge exposures, although a series of tests with the "Epiplan HD" series of planachromats also yielded satisfactory results. A red filter with a low-pass cutoff of 620 nm (Corning type CS2-60) was used during focusing and registration of patterns, and a blue filter with a single transmittance peak at 400 nm (Corning type CS5-58) was used during exposure. Exposure times were adjusted to fit the objective lens used:

objective	demagnification	aperture (mm)	lamp brightness	typical exposure (sec)	focus correction[1] (µm)
100x	1/43x	1	VII	40	0
40x	1/17x	1 $\frac{1}{2}$	VIII	60	-2
6.3x	1/2.7x	4	X[2]	115	+150

[1] Focus correction is for exposure through a standard cover glass, No. 1 $\frac{1}{2}$ thickness.

[2] No blue filter was used during exposures with the 6.3x objective, to minimize exposure time.

A voltage-regulating (Sola) transformer was used in the AC power line of the microscope lamp.

A.4. Development at exposed PR

We used Shipley type AZ developer, diluted 1:1 with distilled, deionized water.

a) Immerse sample in developer solution at 21 $\pm$ 1 C; 25-second immersion for a 250-nm PR layer, or 30-second immersion for a 500-nm layer.

b) Developer is continuously mixed during immersion, either by usa or by magnetic stirrer. The latter, gentler process does not aggravate any adhesion problems.

c) Rinse for $\gtrsim$ 60 sec in flowing distilled, deionized water.

d) Blow dry in high-purity-grade nitrogen gas.

The developed PR patterns were used with no postbake.

APPENDIX B. PREPARATION OF POLYIMIDE LAYERS

Films of a polyimide precursor (DuPont product #PI-2550, diluted in DuPont #T-8035 thinner) were formed on glass substrates by a high-speed spinning process, as for photoresist layers. These precursor films were cured to polyimide by subsequent baking.

a) Center substrate on vacuum check of spinner, and flood substrate with dilute precursor. One part precursor was thoroughly mixed with one part thinner to obtain 550-nm layers.

b) Wait 60 seconds for any bubbles to rise.

c) Spin at 6000 rpm for 120 sec.

d) Bake on hotplate for 60 minutes at 300 C.

REFERENCES

Adler, J. G., and S. C. Ng (1965) Can. J. Phys. 43, 594.

Adler, J. G., J. E. Jackson, and T. A. Will (1967) Phys. Lett. 24A, 407.

Ambegaokar, V., and B. I. Halperin (1969) Phys. Rev. Lett. 22, 1364.

Anderson, P. W., and J. M. Rowell (1963) Phys. Rev. Lett. 10, 230.

Anderson, P. W., and A. H. Dayem (1964) Phys. Rev. Lett. 13, 195.

Aslamazov, L. G., and A. I. Larkin (1969) JETP Lett. 9, 87.

Aslamazov, L. G., and A. I. Larkin (1975) Sov. Phys. - JETP 41, 381.

Aslamazov, L. G., and A. I. Larkin (1976) Sov. Phys. - JETP 43, 698.

Auracher, F., and T. Van Duzer (1973) J. Appl. Phys. 44, 848.

Baratoff, A., and L. Kramer (1977) in SQUID--Superconducting Quantum Interference Devices and their Applications, edited by H. D. Hahlbohm and H. Lubbig (Walter de Gruyter, Berlin), p. 51.

Bardeen, J., and M. J. Stephen (1965) Phys. Rev. 140, A1197.

Beasley, M. R. (1978) AIP Conf. Proc. 44, 389.

Cantagrel, M. (1975) IEEE Trans. ED-22, 483.

Cantagrel, M., and M. Marchal (1973) J. Mater. Sci. 8, 1711.

Chambers, R. (1952) Proc. Roy. Soc. (London) A215, 481.

Chaudhari, R. D. and J. B. Brown (1965) Phys. Rev. 139, A1482.

Chen, J. T., R. J. Todd, and Y. W. Kim (1972) Phys. Rev. B5, 1843.

Chiao, R. Y., M. J. Feldman, M. Ohta, and P. T. Parrish (1974) Rev. Phys. Appl. 9, 183.

Chimenti, D. E., and R. P. Huebener (1977) Solid State Comm. 21, 467.

Chou, N. J., S. K. Lahiri, R. Hammer, and K. L. Komarek (1975) J. Chem. Phys. 63, 2758.

Claassen, J. H. (1980) Appl. Phys. Lett. 36, 771.

Claassen, J. H., and P. L. Richards (1978) J. Appl. Phys. 49, 4117.

Clarke, John, Ulrich Eckern, Albert Schmid, Gerd Schön, and Michael Tinkham (1979) Phys. Rev. B20, 3933.

Dayem, A. H., and J. J. Wiegand (1967), Phys. Rev. 155, 419.

Dean, R. H., and R. J. Matarese (1975) IEEE Trans. ED-22, 358.

Decker, Stephen K. (1975) Ph.D. Thesis, California Institute of Technology, unpublished.

DeGraff, P. D., and D. C. Flanders (1979) J. Vac. Sci. Technol. 16, 1906.

Dill, Frederick H., William P. Hornberger, Peter S. Hauge, and Jane M. Shaw (1975) IEEE Trans. ED-22, 445.

Dolan, G. J. (1977) Appl. Phys. Lett. 31, 337.

Eilenberger, G. (1968) Z. Phys. 214, 195.

Eliashberg, G. M. (1970) JETP Lett. 11, 114.

Evetts, J. E., and J. M. A. Wade (1970) J. Phys. Chem. Solids 31, 973.

Farrell, D. E., B. S. Chandrasekhar, and Harvey V. Culbert (1969) Phys. Rev. 177, 694.

Fulton, T. A., and R. C. Dynes (1970) Phys. Rev. Lett. 25, 794.

Giaever, Ivar, and Karl Megerle (1961) Phys. Rev. 122, 1101.

Giordano, N. (1980) Phys. Rev. B21, 2008.

Giordano, N., W. Gilson, and D. E. Prober (1979) Phys. Rev. Lett. 43, 725.

Golub, A. A. (1976) Sov. Phys. - JETP 44, 178.

Gorkov, L. P. (1959) Sov. Phys.- JETP 9, 1364.

Gorkov, L. P., and G. M. Eliashberg (1968) Sov. Phys.-JETP 27, 328.

Gregers-Hansen, P. E. ,M. T. Levinsen, and G. Fog Pedersen (1972) J. Low Temp. Phys. 7, 99.

Gregers-Hansen, P. E., E. Hendricks, M. T. Levinsen, and G. R. Pickett (1973) Phys. Rev. Lett. 31, 524.

Gubankov, V. N., K. K. Likharev, and N. M. Margolin (1972) Sov. Phys.- Solid State 14, 819.

Gubankov, V. N., V. P. Koshelets, and G. A. Ovsyannikov (1975) JETP Lett. 21, 226.

Gubankov, V. N., V. P. Koshelets, and G. A. Ovsyannikov (1977) Sov. Phys.- JETP 44, 181.

Guthmann, C., J. Maurer, M. Belin, J. Bok, and A. Libchaber (1974) Phys. Rev. B11, 1909.

Hammond, R. H. (1975) IEEE Trans. MAG-11, 201.

Harris, E. P. and R. B. Laibowitz (1977) IEEE Trans. MAG-13, 724.

Hasselberg, L.-E., M. T. Levinsen, and M. R. Samuelsen (1974) Phys. Rev. B9, 3757.

Havemann, R. H. (1978) J. Vac. Sci. Technol. 15, 389.

Heiblum, M., S. Y. Wang, J. R. Whinnery, and T. K. Gustafson (1978) IEEE J. Quantum Electronics QE-14, 159.

Henkels, Walter Harvey (1974) Ph.D. Thesis, Cornell Univ., unpublished.

Henry, R. W., D. E. Prober, and A. Davidson (unpublished). Submitted to Am. J. Phys., 1980.

Hcnig, R. E. (1962) RCA Review 23, 567.

Jahn, M. T., and Y. H. Kao (1973) J. Low Temp. Phys. 13, 175.

Janocko, M. A., J. R. Gavaler, and C. K. Jones (1972) Proc. 1972 Applied Superconductivity Conf., Annapolis, Md., p. 608.

Jensen, H. Hojgaard, and P. E. Lindelof (1976) J. Low Temp. Phys. 23, 469.

Josephson, B. D. (1962) Phys. Lett. 1, 251.

Kadin, A. M., W. J. Skocpol, and M. Tinkham (1978) J. Low Temp. Phys. 33, 481.

Kaplan, S. B., C. C. Chi, D. N. Langenberg, J.-J. Chang, S. Jafarey, and D. J. Scalapino (1976) Phys. Rev. B 14, 4854.

Klapwijk, T. M., and J. E. Mooij (1975) IEEE Trans. MAG-11, 858.

Klapwijk, T. M., M. Sepers, and J. E. Mooij (1977a) J. Low Temp. Phys. 27, 801.

Klapwijk, T. M., J. N. van den Bergh, and J. E. Mooij (1977b) J. Low Temp. Phys. 26, 385.

Kramer, L., and A. Baratoff (1977) Phys. Rev. Lett. 38, 518.

Kulik, I. O. and A. N. Omelyanchuk (1975) JETP Lett. 21, 96.

Kulik, I. O., and A. N. Omelyanchuk (1976) Sov. Phys.-JETP 41, 1071.

Kulik, I. O., and A. N. Omelyanchuk (1978) Sov. J. Low Temp. Phys. 4, 142.

Kuprianov, M. Yu., K. K. Likharev, and L. A. Maslova (1975) in Proceedings of the 14th International Conference on Low-Temperature Physics, edited by M. Krusius and M. Vuorio (North-Holland, Amsterdam), vol. 4, p. 104.

Lahiri, S. K. (1975a) Thin Solid Films 28, 279.

Lahiri, S. K. (1975b) J. Appl. Phys. 46, 2791.

Laibowitz, R. B., A. N. Broers, J. T. C. Yeh, and J. M. Viggiano (1979) Appl. Phys. Lett. 35, 891.

Langenberg, D. N., D. J. Scalapino, B. N. Taylor, and R. E. Eck (1966) Phys. Lett. 20, 563.

Larkin, A. I., and Yu. N. Ovchinnikov (1974) Sov. Phys.-JETP 38, 854.

Lee, Tsung-Wen (1977) Ph.D. Thesis, S.U.N.Y. Stony Brook, unpublished.

Lehmann, H. W., and R. Widmer (1978) Appl. Phys. Lett. 32, 163; also J. Vac. Sci. Technol. 15, 319.

Likharev, K. K. (1972) Sov. Phys. JETP 34, 906.

Likharev, K. K. (1976) Sov. Phys.-Solid State 17, 1856.

Likharev, K. K. (1979) Rev. Mod. Phys. 51, 101.

Likharev, K. K. and V. K. Semenov (1972) JETP Lett. 15, 442.

Likharev, K. K., and L. A. Yakobson (1976a) Sov. Phys.-Tech. Phys. 20, 950.

Likharev, K. K., and L. A. Yakobson (1976b) Sov. Phys.-JETP 41, 570.

Little, W. A. (1959) Can. J. Phys. 37, 334.

Lukens, J. E., R. D. Sandell, and C. Varmazis (1978) AIP Conf. Proc. 44, 298.

Marchand, Nathan (1947) Ultrahigh Frequency Transmission and Radiation (John Wiley and Sons, New York), p. 17.

McCarthy, S. L., and J. Stanko (1974) Rev. Sci. Instrum. 45, 335.

McCumber, D. E. (1968) J. Appl. Phys. 39, 3113.

Melliar-Smith, C. M. (1976) J. Vac. Sci. Technol. 13, 1008.

Mooij, J. E., and P. Dekker (1978) J. Low Temp. Phys. 33, 551.

Neeper, D. A., and J. R. Dillinger (1964) Phys. Rev. 135, A1028.

Noto, Koshichi, Yoshio Muto, and Tadao Fukuroi (1966) J. Phys. Soc. Japan 21, 2122.

Octavio, Miguel (1978) Ph.D. thesis, Harvard University, unpublished.

Octavio, M., W. J. Skocpol, and M. Tinkham (1977) IEEE Trans. MAG-13, 739.

Octavio, M., W. J. Skocpol, and M. Tinkham (1978) Phys. Rev. B17, 159.

Octavio, M., and W. J. Skocpol (1979) J. Appl. Phys. 50, 3505.

Palmer, D. W., and S. K. Decker (1973) Rev. Sci. Instr. 44, 1621.

Parks, R. D., and J. M. Mochel (1964) Rev. Mod. Phys. 36, 284.

Pearl, J. (1964) Appl. Phys. Lett. 5, 65.

Prober, D.E., and M. D. Feuer (1980) Bull. Am. Phys. Soc. 25, 197. See also Prober et. al. (1980).

Prober, D. E., M. D. Feuer, and N. Giordano (1980) Appl. Phys. Lett. 37, 94.

Richards, P. L. (1977) in Semiconductors and Semimetals, edited by R.K. Willardson and A. C. Beer (Academic Press, New York), vol. 12, p. 395.

Roberts, B. W. (1972) Properties of Selected Superconductive Materials, National Bureau of Standards Technical Note 724 (U.S. Govt. Printing Office, Washington).

Russer, P. (1972) J. Appl. Phys. 43, 2008.

Sandell, R. D., G. J. Dolan, and J. E. Lukens, in SQUID--Superconducting Quantum Interference Devices and their Applications, edited by H. D. Hahlbohm and H. Lubbig (Walter de Gruyter, Berlin), p. 93.

Schmid, A., and W. Hauger (1973) J. Low Temp. Phys. 11, 667.

Schmid, Albert, Gerd Schön, and Michael Tinkham (1980) Phys. Rev. B21, 5076.

Skocpol, W. J., M. R. Beasley, and M. Tinkham (1974) J. Appl. Phys. 45, 4054.

Smith, H. I., F. J. Bachner, and N. Efremow (1971) J. Electrochem. Soc. 118, 821.

Smith, Henry I. (1974) IEEE Proc. 62, 1361.

Song, Y. (1976) J. Appl. Phys. 47, 2651.

Stewart, W. S. (1968) Appl. Phys. Lett. 12, 277.

Taur, Y., J. H. Claassen, and P. L. Richards (1974) Appl. Phys. Lett. 24, 101.

Tinkham, M. (1975) Introduction to Superconductivity (McGraw-Hill, New York).

Tinkham, M. (1978) AIP Conf. Proc. 44, 269.

Tinkham, M. (1979) Festkörperprobleme 19, 363.

Tinkham, M., M. Octavio, and W. J. Skocpol (1977) J. Appl. Phys. 48, 1311.

Toxen, A. M. (1962) Phys. Rev. 127, 382.

van Dover, R. B., R. E. Howard, and M. R. Beasley (1979) IEEE Trans. MAG-15, 574.

Volkov, A. F. (1973) Sov. Phys.-Solid State 15, 925.

Voss, R. F., R. B. Laibowitz, A. N. Broers, S. I. Raider, and J. M. Viggiano (1980) Proc. 1980 Appl. Superconductivity Conf., to be published in IEEE Trans. Magnetics, early 1981.

Walker, E. J. (1959) Rev. Sci. Instr. 30, 834.

Wang, Li-Kong, Dae-Jin Hyun, and B. S. Deaver, Jr. (1978) J. App. Phys. 49, 5602.

Warlaumont, John, J. C. Brown, T. Foxe, and R. A. Buhrman (1979) Phys. Rev. Lett. 43, 169.

White, Alice E., and D. C. Flanders (1980) Bull. Am. Phys. Soc. 25, 197.

Wyatt, A. F. G., V. M. Dmitriev, W. S. Moore, and F. W. Sheard (1966) Phys. Rev. Lett. 16, 1166.

Yeh, J. T. C., and R. A. Buhrman (1977) J. Appl. Phys. 48, 5360.

Zaitsev, R. O. (1966) Sov. Phys.-JETP 23, 702.